IMPEDANCE SPECTROSCOPY FOR CELLULAR AND BIOMOLECULAR ANALYSIS

By

Daniele Malleo

A thesis submitted for the degree of Doctor of Philosophy

School of Electronics and Computer Science,

University of Southampton,

United Kingdom.

April 2009

UNIVERSITY OF SOUTHAMPTON

ABSTRACT

FACULTY OF ENGINEERING
SCHOOL OF ELECTRONICS AND COMPUTER SCIENCE

Doctor of Philosophy

IMPEDANCE SPECTROSCOPY FOR CELLULAR AND BIOMOLECULAR ANALYSIS

By Daniele Malleo

The application of microfabrication technology to molecular and cell biology has motivated the rapid development of a novel class of microdevices collectively known as 'Lab On a Chip' devices.

Impedance spectroscopy is a non-invasive, label-free, analytical technique that is amenable to miniaturization, electronic integration, automation, and scalability within 'LOC' devices.

This thesis describes a microfabricated device for performing continuous impedance analysis of individual cells held in an array of hydrodynamic traps. This device enables continuous long-term analysis of cells and time-dependent measurement of changes elicited by cytotoxic agents and drug compounds. Finite element models are employed to predict the response to changes in the captured single cells (cell position in the trap, cell size, membrane conductivity). The system is used to assay the response of HeLa cells to the effects of the surfactant Tween 20 and Streptolysin-O, a bacterial pore-forming toxin.

Novel electrode materials that reduce the parasitic effect of electrode polarisation are described and characterised. These are iridium oxide and PPy/PSS (polypyrrole/poly(styrenesulphonate)). Impedance data is analysed in terms of equivalent circuit models. The findings presented suggest that iridium oxide and PPy/PSS could be used as alternative materials to platinum black and plain platinum. PPy/PSS electrodes offer the highest electrode/electrolyte interface area and least variation with time.

Finally, a silicon-based capacitive sensor with nanometric plate separation (nano-gap capacitor), is characterized by impedance spectroscopy, and used to explore the behaviour of double layers constrained in cavities of dimensions comparable to the Debye length.

DECLARATION OF AUTHORSHIP

I, DANIELE MALLEO, declare that the thesis entitled IMPEDANCE SPECTROSCOPY FOR CELLULAR AND BIOMOLECULAR ANALYSIS and the work presented in the thesis are both my own, and have been generated by me as the result of my own original research. I confirm that:

- This work was done wholly or mainly while in candidature for a research degree at this University;
- Where I have consulted the published work of others, this is always clearly attributed;
- Where I have quoted from the work of others, the source is always given. With the exception of such quotations, this thesis is entirely my own work;
- I have acknowledged all main sources of help;
- Where the thesis is based on work done by myself jointly with others, I have made clear exactly what was done by others and what I have contributed myself;
- None of this work has been published before submission

Signed: ……..

Date:……

External contributions to Chapter 3.

- The work presented in chapter 3, "Hydrodynamic cell trapping array for impedance analysis of single cells ", is the result of a collaborative project carried out in part with J. Tanner Nevill (JTN) in the laboratory of Prof. Luke Lee at the University of California, Berkeley.
- JTN's contribution consisted of microfabrication of electrodes and advice in the design of the lithography masks. The fabrication of the polymer layers, and assembly of the devices were carried out wholly by myself at the University of Southampton.
- The device geometry builds on the published cell traps of Dino Di Carlo.
- The polyelectrolyte capsules were a gift from Catia Bernabini in Southampton.

External contributions to Chapter 4.

- The work presented in chapter 4, "Electrode polarization and the double layer", is the result of a collaborative project carried out in part with J. Tanner Nevill at the University of California, Berkeley, specifically, the measurements presented in sections 4.8 to 4.10. The data analysis and interpretation was carried out by myself in Southampton.

External contributions to Chapter 5.

- The work presented in chapter 5, "Novel electrode materials", is the result of a collaborative project carried out in part with J. Tanner Nevill at the University of California, Berkeley and Andre Van Ooyen at the University of Aachen, Germany.
- Andre Van Ooyen fabricated the un-activated iridium oxide electrodes and provided the protocol for the electrochemical activation.
- SEM was carried out by Liz Wu at Berkeley.
- The majority of the measurements were carried out by myself at Berkeley. JTN performed the 'ageing' measurements. Data analysis and interpretation was carried out by myself jointly with JTN at Berkeley.

External contributions to Chapter 6.

- The work presented in chapter 6, "Nanogap sensor" is based on a device designed and fabricated by K.H. Jeong at the University of California, Berkeley.
- The experimental setup was designed by J. Tanner Nevill (JTN), Dino Di Carlo (DDC) and Cristian Ionescu Zanetti (CIZ) at Berkeley.
- The dry characterization was carried out mostly by CIZ, DDC and JTN.
- The initial 'dry' circuit model, presented in section 6.5, was devised by CIZ. I completely altered the MATLAB code used in the model and wrote new code for parametric optimization of the circuit model that allowed systematic improvement to the final model.
- The measurements in KCl, presented in section 6, were carried out by myself. The equivalent circuit model was developed by me, based on previous work in collaboration with JTN and CIZ.
- The experimental design for measurements of a constrained double layer was done jointly with CIZ.
- Data interpretation (section 6.6.4) was done in collaboration with JTN.
- Measurements of sensitivity to proteins in solution were performed by myself, and data interpretation jointly with JTN.

Acknowledgements

Thanks go to Prof. Hywel Morgan, my supervisor, for gracefully accommodating my somewhat whimsical research style, for granting me the freedom to explore issues which were not always relevant to the core topic of my doctoral research, and of course for letting me fly away to the US only nine months into my PhD.

At the University of Southampton, thanks go to Nicolas Green, David Holmes, Sun Tao and Beppe Benazzi.

At UC Berkeley, I've met the most incredible people, many of which I now consider great friends. Thanks go to Prof. Luke Lee who let me work in his lab and with his supervision shaped my way of looking at bioengineering issues and more in general at science and technology.

My heartfelt thanks go to Cristian Ionescu-Zanetti and Dino Di Carlo with whom I have had the pleasure to work on the nanogap sensor project. The challenge was great and the learning curve steep, but I have treasured every moment of working with them, and I can honestly say that I've never learned so much in so little time.

David Breslauer, Michelle Khine, Eunice Lee, Mimi Zhang, and the rest of the BioPoets should be thanked for sharing their knowledge of all things 'bio' with me, and in general for making the work environment so much fun.

Special thanks to Tanner Nevill who is my friend and has to be, hands down, the smartest person I've ever met. Maybe some of that magic in his thinking has rubbed off on me; I've loved bouncing crazy ideas ranging from that elusive cheap portable diagnostic device that will alleviate some of the 3rd world problems to that invention-factory that we have envisioned on a lazy Sunday afternoon. Working together has been the most satisfying endeavour of this PhD. Of course, skiing the powdery double-diamonds in Utah and free climbing granite walls wasn't too shabby either. I would be remiss if I didn’t extend my thanks also to Stephanie for her hospitality and friendship, and to Hazel who joined us only recently but made the last months I have spent in Berkeley so much fun.

Last but not least, thanks go to my family who supported me throughout. My mom, who's always been there for me, my late father and of course, my sisters.

Table of Contents

List of Figures

List of Tables

I.Introduction

"What I want to talk about, is the problem of manipulating and controlling things on a small scale"

Richard P. Feynman

Richard Feynman on December 29th, 1959 gave a talk, entitled "*There's Plenty of Room at the Bottom*", at the annual meeting of the American Physical Society at the California Institute of Technology.

The talk had far-reaching and potent implications that sound prescient today, almost fifty years later: in it, Feynman touched on many different aspects of science and technology, ranging from information theory to physical chemistry, from quantum mechanics to cell biology, from computer science to micro- and nano-fabrication.

A general *tenet* emerges from his lecture: biology as a scientific field would benefit more than anything else, from the introduction of novel tools, capable of probing cells, proteins and biomolecules. In particular, Feynman envisioned *very interesting possibilities for relatively small machines*. For example: "*it would be interesting in surgery if you could swallow the surgeon. You put the mechanical surgeon inside the blood vessel and it goes into the heart (…) It finds out which valve is the faulty one and takes a little knife and slices it out. Other small machines might be permanently incorporated in the body to assist some inadequately-functioning organ.*"

It's not easy to narrowly define how small is 'small': in the field of biology characteristic lengths range many orders of magnitude- the scale in Figure I-1 offers some insight: to enable biological work to take place at cellular and sub-cellular level, tools should be in the 100nm – 100μm dimension range: it is in this spirit that novel technologies and devices have been developed under the new paradigm of 'Lab on a

chip".

The field of Lab-on-a-chip technology is one that has been rapidly evolving since its inception in the 1990's when the term "LOC" was first introduced. The benefits and advantages of miniaturizing conventional analytical tools and using microfluidic platforms to study biological systems have been reviewed in a number of articles ([1-13]): the ability to perform laboratory operations on a microscopic scale is compelling as small volumes reduce the time taken to synthesize and analyze a compound (see Table I-1); the unique behaviour of fluids at the microscopic scale allows greater control of molecular concentrations and interactions; reagent costs can be reduced and chemical waste minimized.

Parameter	**Macroscopic example**	**Factor change**	**Microscopic example**
Length of edge	1 mm	d	1 μm
Surface	1 mm^2	d^2	1 μm^2
Volume	1 μl	d^3	1 fl
Number of molecules	10	d^3	1
Diffusion time ($D = 10^{-6} cm^2/s$)	15 min	d^2	1 ms
Example: in flowing systems			
Linear flow rate	1 μm/s	d	1 mm/s
Separation time	10^5s (>1 day)	d^2	100 ms
Example: in planar array			
N. of vol. per microwell plate	96	d	10^8

Table I-1 Various opportunities can emerge from miniaturization of reaction systems simply considering scaling laws giving the dependence of reaction parameters on the size of the system. Due to the short distances in microfluidic channels, the transport times of mass and heat are shortened. Fast and controlled heat supply as well as cooling is facilitated due to high surface to volume ratio. Taken from [1]

Moreover, miniaturized units or stages can be designed in a modular fashion, and later coupled or integrated so that an analyte can be detected, separated, purified and analyzed on a single integrated platform.

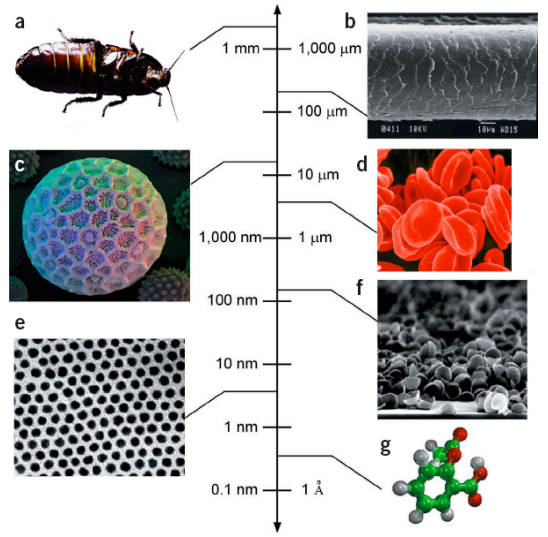

Figure I-1 (a) a cockroach. (b) a human hair. (c) Polygonum Pollen grain. (d) Red blood cells. (e) Cobalt nanocrystalsuperlattice. (f) half-shells of Palladrium. (g) Aspirin molecule. Taken from [14]

The range of applications that can now be performed on *LOC* devices is now immense: cell culture handling[15-18], point of care diagnostics [19-32], immunoassays [25, 33-38], proteins extraction and separation [39, 40], DNA Separation analysis and sequencing [34, 41-51], polymerase chain reaction [52-59].

Additionally, miniaturized devices can be cheaper and can be made portable, hence allowing samples to be analyzed "in the field". This expands the appeal of these devices to scientists looking to develop point-of-care diagnostic and analytical tools.

Perhaps most alluring is the potential of this novel class of devices to go beyond the simple miniaturization of macroscopic scale instruments, furthering research and discovery by enabling the devising of experiments otherwise impossible to realize. For example, presenting cells with cues in a controllable and reproducible fashion is a feat that would not otherwise be achieved by standard tissue culture techniques and tools. Moreover analytical devices could be integrated to probe the biochemical processes that govern cell behaviour

The cell is the core of human biology; from a molecular point of view it is a "compartment of compartments" within which multiple reactions occur. The cell by itself "lives", in the sense that it has the ability to move, replicate or self-destroy, harvest energy from chemical reactions, apply forces, transmit signals, transceive information and sense its environment.

It is not surprising therefore that there is an enormous interest in directing the application potential of microfabricated devices to the study of cell biology at the

single-cell level given the newly-enabled ability to handle single cells as well as to manipulate laminar flows with sub-cellular precision to provide chemical and physical stimuli (See for example [60-62]).

There are now numerous examples of on-chip cell manipulation (trapping and sorting by electrical, optical and mechanical means)[63-69], single cell electroporation [70-74], and single cell optical [75-85] and electrical analysis [86-90].

The main focus of this thesis is the novel use of impedance spectroscopy as a tool for single cell analysis. Impedance spectroscopy is a non-invasive, label-free, analytical technique that has found widespread use in disparate scientific and technological fields, but, until now, has been a somewhat neglected tool for the analysis of single cells, mainly due to the technological difficulties intrinsic to the fabrication of microelectrodes and the bio-compatible microenvironments within which the cells under study need to be trapped and isolated.

Impedance spectroscopy is particularly attractive because it's an all electrical sensing method, which, contrary to the most traditionally used optical-based analytical tools, holds enormous potential for miniaturization, electronic integration, automation, and scalability. These advantages translate to great untapped potential for this technique to be used as the basis of devices for medical diagnostics as well as for drug discovery and toxin screening.

Scope of the work

The thesis begins with a comprehensive literature review and an introductory chapter to the theoretical foundations of impedance spectroscopy. A novel device that can perform continuous differential impedance spectroscopic analysis of single cells hydrodynamically captured in an array inside a microfluidic channel is introduced. On this platform long-term transient and steady state analyses can be carried out. Individually addressable electrodes and micrometer-sized traps are integrated in a microfluidic platform to provide a non-invasive, label-free tool for single cell analysis.

Additionally electrode polarization - a critical issue in impedance spectroscopy of biological samples (cells, single and in bulk suspension, as well as suspended biomolecules)- is investigated from a theoretical and experimental perspective. Iridium oxide and polyelectrolyte coatings are studied as a novel electrode material for impedance spectroscopy, and their advantages are explored in comparison with metals commonly used in microfabricated devices, such as gold or platinum. Finally, by employing impedance spectroscopy, a nanogap capacitive sensor designed for the detection of protein folding events is characterized.

Chapters overview

Chapter 1

The theoretical foundations of impedance spectroscopic methods are described: fundamentals of polarization mechanisms, measurement of complex permittivity of biological materials and interpretation of dielectric relaxations. Impedance spectroscopy measurements are compared, from a theoretical standpoint to alternative methods for dielectric spectroscopy such as dielectrophoresis, electroorientation and electrorotation.

Chapter 2

Recent progresses in the field of impedance spectroscopy of cells are reviewed: papers on the impedance spectroscopy of cells in bulk are quickly reviewed. Single cell impedance spectroscopy contributions in the context of cytometry are presented, followed by studies of cell cultures performed with electrode-cell-impedance sensors. Finally, contributions on single cell impedance spectroscopic techniques are reviewed, using both dielectrophoretic based measurements, and direct impedance measurements

Chapter 3

A microfabricated device engineered to perform continuous impedance analysis on individual cells using an array of hydrodynamic traps is presented. Design, fabrication, simulation and experimental steps are presented. It is shown that the device is ideally and uniquely suited to non-invasively quantify the effect of surfactants and pore-forming toxins on captured cells without the aid of fluorescent or radioactive labels. Additionally, we showcase the capability of this device to analyze the transient behaviour of the polyelectrolyte microcapsules engineered for drug delivery as they undergo changes induced by the perfusion of media of varying conductivity and pH.

Chapter 4

The phenomenology of the electrode polarization is explored: the classical theoretical model of the double layer (Gouy – Chapman – Stern model) is explained. Then, a detailed explanation of the constant phase element, a distributed circuit element commonly employed to fit double layer impedance data acquired to equivalent circuit models, is given. Finally experimental measurements on metal and semiconductor electrodes at different regimes of solution concentration and applied excitation voltage are presented. Observations are made with regard to discrepancies found between experimental results and classical theory predictions, and hypotheses are discussed to explain said discrepancies.

Chapter 5

Impedance spectroscopy has been used to characterize three different electrode materials that give high effective surface areas thus reducing the effect of electrode polarisation. The three materials are platinum black, iridium oxide, and PPy/PSS (polypyrrole/poly(styrenesulphonate)) conducting polymer. All three materials are compared with a reference material platinum electrode. The impedance data is analysed in terms' of a equivalent circuit models and the ultrastructure of the metal electrode is imaged using electron microscopy. The results suggest that iridium oxide and PPy/PSS lead to an increase in the effective capacitance of 77x and 854x respectively.

Chapter 6

A nano-gap dielectric sensor engineered for the study of conformational changes in proteins has been characterized by impedance spectroscopy and used as a tool to study the impedance response of overlapping ionic double layers.

Chapter 7

The main contributions of this thesis are summarized and possible directions for future research based on the findings presented, are laid out.

References

[1] P. S. Dittrich, and A. Manz, "Lab-on-a-chip: microfluidics in drug discovery," *Nature Reviews Drug Discovery,* vol. 5, no. 3, pp. 210-8, Feb 28, 2006.

[2] N. T. Nguyen, and Z. G. Wu, "Micromixers - a review," *Journal of Micromechanics and Microengineering,* vol. 15, pp. R1-R16, 2005.

[3] D. J. Laser, and J. G. Santiago, "A review of micropumps," *Journal of Micromechanics and Microengineering,* vol. 14, no. 6, pp. R35-R64, Jun, 2004.

[4] E. Verpoorte, "Chip vision - optics for microchips," *Lab on a Chip,* vol. 3, no. 3, pp. 42N-52N, 2003.

[5] H. Becker, and C. Gartner, "Polymer microfabrication methods for microfluidic analytical applications," *Electrophoresis,* vol. 21, no. 1, pp. 12-26, Jan, 2000.

[6] J. C. McDonald, D. C. Duffy, J. R. Anderson *et al.*, "Fabrication of microfluidic systems in poly(dimethylsiloxane)," *Electrophoresis,* vol. 21, no. 1, pp. 27-40, Jan, 2000.

[7] P. S. Dittrich, and A. Manz, "Single-molecule fluorescence detection in microfluidic channels - the Holy Grail in mu TAS?," *Analytical and Bioanalytical Chemistry,* vol. 382, no. 8, pp. 1771-1782, Aug, 2005.

[8] Y. N. Xia, and G. M. Whitesides, "Soft lithography," *Annual Review of Materials Science,* vol. 28, pp. 153-184, 1998.

[9] D. R. Reyes, D. Iossifidis, P. A. Auroux *et al.*, "Micro total analysis systems. 1. Introduction, theory, and technology," *Analytical Chemistry,* vol. 74, no. 12, pp. 2623-2636, Jun, 2002.

[10] P. A. Auroux, D. Iossifidis, D. R. Reyes *et al.*, "Micro total analysis systems. 2. Analytical standard operations and applications," *Analytical Chemistry,* vol. 74, no. 12, pp. 2637-2652, Jun, 2002.

[11] T. Vilkner, D. Janasek, and A. Manz, "Micro total analysis systems. Recent developments," *Analytical Chemistry,* vol. 76, no. 12, pp. 3373-3385, Jun, 2004.

[12] T. M. Squires, and S. R. Quake, "Microfluidics: Fluid physics at the nanoliter scale," *Reviews of Modern Physics,* vol. 77, no. 3, pp. 977-1026, Jul, 2005.

[13] H. A. Stone, A. D. Stroock, and A. Ajdari, "Engineering flows in small devices: Microfluidics toward a lab-on-a-chip," *Annual Review of Fluid Mechanics,* vol. 36, pp. 381-411, 2004.

[14] G. M. Whitesides, "The 'right' size in nanobiotechnology," *Nature Biotechnology,* vol. 21, pp. 1161-1165, 2003.

[15] L. Kim, Y. C. Toh, J. Voldman *et al.*, "A practical guide to microfluidic perfusion culture of adherent mammalian cells," *Lab on a Chip,* vol. 7, no. 6, pp. 681-694, 2007.

[16] A. Rosenthal, A. Macdonald, and J. Voldman, "Cell patterning chip for controlling the stem cell microenvironment," *Biomaterials,* vol. 28, no. 21, pp. 3208-3216, 2007.

[17] S. Petronis, M. Stangegaard, C. B. V. Christensen *et al.*, "Transparent polymeric cell culture chip with integrated temperature control and uniform media perfusion," *Biotechniques,* vol. 40, no. 3, pp. 368-376, 2006.

[18] D. Di Carlo, L. Y. Wu, and L. P. Lee, "Dynamic single cell culture array," *Lab on a Chip,* vol. 6, no. 11, pp. 1445-1449, 2006.

[19] L. J. Kricka, "Microchips, microarrays, biochips and nanochips: personal laboratories for the 21st century," *Clinica Chimica Acta,* vol. 307, no. 1-2, pp. 219-223, May, 2001.

[20] V. Srinivasan, V. K. Pamula, and R. B. Fair, "An integrated digital microfluidic lab-on-a-chip for clinical diagnostics on human physiological fluids," *Lab on a Chip,* vol. 4, no. 4, pp. 310-315, 2004.

[21] C. H. Ahn, J. W. Choi, G. Beaucage *et al.*, "Disposable Smart lab on a chip for point-of-care clinical diagnostics," *Proceedings of the IEEE,* vol. 92, no. 1, pp. 154-173, Jan, 2004.

[22] M. Toner, and D. Irimia, "Blood-on-a-chip," *Annual Review of Biomedical Engineering,* vol. 7, pp. 77-103, 2005.

[23] K. K. Jain, "Nanodiagnostics: application of nanotechnology in molecular diagnostics," *Expert Review of Molecular Diagnostics,* vol. 3, no. 2, pp. 153-161, Mar, 2003.

[24] N. Christodoulides, S. Mohanty, C. S. Miller *et al.*, "Application of microchip assay system for the measurement of C-reactive protein in human saliva," *Lab on a Chip,* vol. 5, no. 3, pp. 261-269, 2005.

[25] A. E. Herr, A. V. Hatch, D. J. Throckmorton *et al.*, "Microfluidic immunoassays as rapid saliva-based clinical diagnostics," *Proceedings of the National Academy of Sciences of the United States of America,* vol. 104, no. 13, pp. 5268-5273, Mar, 2007.

[26] P. Fortina, S. Surrey, and L. J. Kricka, "Molecular diagnostics: hurdles for clinical implementation," *Trends in Molecular Medicine,* vol. 8, no. 6, pp. 264-266, Jun, 2002.

[27] J. G. E. Gardeniers, and A. van den Berg, "Lab-on-a-chip systems for biomedical and environmental monitoring," *Analytical and Bioanalytical Chemistry,* vol. 378, no. 7, pp. 1700-1703, Apr, 2004.

[28] A. D. Sheehan, J. Quinn, S. Daly *et al.*, "The development of novel miniaturized immuno-sensing devices: A review of a small technology with a large future," *Analytical Letters,* vol. 36, no. 3, pp. 511-537, 2003.

[29] T. M. H. Lee, and I. M. Hsing, "DNA-based bioanalytical microsystems for handheld device applications," *Analytica Chimica Acta,* vol. 556, no. 1, pp. 26-37, Jan, 2006.

[30] H. Gardeniers, and A. Van den Berg, "Micro- and nanofluidic devices for environmental and biomedical applications," *International Journal of Environmental Analytical Chemistry,* vol. 84, no. 11, pp. 809-819, Sep, 2004.

[31] A. Rasooly, "Moving biosensors to point-of-care cancer diagnostics," *Biosensors & Bioelectronics,* vol. 21, no. 10, pp. 1847-1850, Apr, 2006.

[32] C. P. Price, and L. J. Kricka, "Improving healthcare accessibility through point-of-care technologies," *Clinical Chemistry,* vol. 53, no. 9, pp. 1665-1675, Sep, 2007.

[33] B. H. Weigl, R. L. Bardell, and C. R. Cabrera, "Lab-on-a-chip for drug development," *Advanced Drug Delivery Reviews,* vol. 55, no. 3, pp. 349-377, Feb, 2003.

[34] L. Bousse, C. Cohen, T. Nikiforov *et al.*, "Electrokinetically controlled microfluidic analysis systems," *Annual Review of Biophysics and Biomolecular Structure,* vol. 29, pp. 155-181, 2000.

[35] J. Wang, A. Ibanez, M. P. Chatrathi *et al.*, "Electrochemical enzyme immunoassays on microchip platforms," *Analytical Chemistry,* vol. 73, no. 21, pp. 5323-5327, Nov, 2001.

[36] M. Zimmermann, E. Delamarche, M. Wolf *et al.*, "Modeling and optimization of high-sensitivity, low-volume microfluidic-based surface immunoassays," *Biomedical Microdevices,* vol. 7, no. 2, pp. 99-110, Jun, 2005.

[37] A. M. Dupuy, S. Lehmann, and J. P. Cristol, "Protein biochip systems for the clinical laboratory," *Clinical Chemistry and Laboratory Medicine,* vol. 43, no. 12, pp. 1291-1302, Dec, 2005.
[38] J. H. Ng, and L. L. Ilag, "Biomedical applications of protein chips," *Journal of Cellular and Molecular Medicine,* vol. 6, no. 3, pp. 329-340, Jul-Sep, 2002.
[39] A. Ros, W. Hellmich, J. Regtmeier *et al.*, "Bioanalysis in structured microfluidic systems," *Electrophoresis,* vol. 27, no. 13, pp. 2651-2658, Jul, 2006.
[40] O. Schmut, J. Horwath-Winter, A. Zenker *et al.*, "The effect of sample treatment on separation profiles of tear fluid proteins: Qualitative and semi-quantitative protein determination by an automated analysis system," *Graefes Archive for Clinical and Experimental Ophthalmology,* vol. 240, no. 11, pp. 900-905, Nov, 2002.
[41] A. T. Woolley, K. Q. Lao, A. N. Glazer *et al.*, "Capillary electrophoresis chips with integrated electrochemical detection," *Analytical Chemistry,* vol. 70, no. 4, pp. 684-688, Feb, 1998.
[42] J. Wang, "From DNA biosensors to gene chips," *Nucleic Acids Research,* vol. 28, no. 16, pp. 3011-3016, Aug, 2000.
[43] G. J. M. Bruin, "Recent developments in electrokinetically driven analysis on microfabricated devices," *Electrophoresis,* vol. 21, no. 18, pp. 3931-3951, Dec, 2000.
[44] D. Figeys, and D. Pinto, "Lab-on-a-chip: A revolution in biological and medical sciences," *Analytical Chemistry,* vol. 72, no. 9, pp. 330A-335A, May, 2000.
[45] D. Erickson, and D. Q. Li, "Integrated microfluidic devices," *Analytica Chimica Acta,* vol. 507, no. 1, pp. 11-26, Apr, 2004.
[46] C. A. Emrich, H. J. Tian, I. L. Medintz *et al.*, "Microfabricated 384-lane capillary array electrophoresis bioanalyzer for ultrahigh-throughput genetic analysis," *Analytical Chemistry,* vol. 74, no. 19, pp. 5076-5083, Oct, 2002.
[47] R. Lenigk, M. Carles, N. Y. Ip *et al.*, "Surface characterization of a silicon-chip-based DNA microarray," *Langmuir,* vol. 17, no. 8, pp. 2497-2501, Apr, 2001.
[48] J. S. Bader, R. W. Hammond, S. A. Henck *et al.*, "DNA transport by a micromachined Brownian ratchet device," *Proceedings of the National Academy of Sciences of the United States of America,* vol. 96, no. 23, pp. 13165-13169, Nov, 1999.
[49] B. M. Paegel, R. G. Blazej, and R. A. Mathies, "Microfluidic devices for DNA sequencing: sample preparation and electrophoretic analysis," *Current Opinion in Biotechnology,* vol. 14, no. 1, pp. 42-50, Feb, 2003.
[50] M. Krishnan, V. Namasivayam, R. S. Lin *et al.*, "Microfabricated reaction and separation systems," *Current Opinion in Biotechnology,* vol. 12, no. 1, pp. 92-98, Feb, 2001.
[51] R. G. Blazej, P. Kumaresan, and R. A. Mathies, "Microfabricated bioprocessor for integrated nanoliter-scale Sanger DNA sequencing," *Proceedings of the National Academy of Sciences of the United States of America,* vol. 103, no. 19, pp. 7240-7245, May, 2006.
[52] T. B. Christensen, C. M. Pedersen, K. G. Grondhal *et al.*, "PCR biocompatibility of lab-on-a-chip and MEMS materials," *Journal of Micromechanics and Microengineering,* vol. 17, no. 8, pp. 1527-1532, 2007.
[53] Y. K. Cho, J. Kim, Y. Lee *et al.*, "Clinical evaluation of micro-scale chip-based PCR system for rapid detection of hepatitis B virus," *Biosensors & Bioelectronics,* vol. 21, no. 11, pp. 2161-2169, 2006.

[54] P. Hawtin, I. Hardern, R. Wittig *et al.*, "Utility of lab-on-a-chip technology for high-throughput nucleic acid and protein analysis," *Electrophoresis,* vol. 26, no. 19, pp. 3674-3681, 2005.

[55] J. G. Lee, K. H. Cheong, N. Huh *et al.*, "Microchip-based one step DNA extraction and real-time PCR in one chamber for rapid pathogen identification," *Lab on a Chip,* vol. 6, no. 7, pp. 886-895, 2006.

[56] C. S. Zhang, and D. Xing, "Miniaturized PCR chips for nucleic acid amplification and analysis: latest advances and future trends," *Nucleic Acids Research,* vol. 35, no. 13, pp. 4223-4237, 2007.

[57] S. Mondal, and V. Venkataraman, "Novel fluorescence detection technique for non-contact temperature sensing in microchip PCR," *Journal of Biochemical and Biophysical Methods,* vol. 70, no. 5, pp. 773-777, 2007.

[58] A. Alonso, C. Albarran, P. Martin *et al.*, "Usefulness of microchip electrophoresis for the analysis of mitochondrial DNA in forensic and ancient DNA studies," *Electrophoresis,* vol. 27, no. 24, pp. 5101-5109, 2006.

[59] J. Felbel, A. Reichert, A. Kielpinski *et al.*, "Reverse transcription-polymerase chain reaction (RT-PCR) in flow-through micro-reactors: Thermal and fluidic concepts," *Chemical Engineering Journal,* vol. 135, pp. S298-S302, 2008.

[60] H. Andersson, and A. VanDenBerg, "Lab-on-Chips for Cellomics: Micro and Nanotechnologies for Life Science," *Lab-on-Chips for Cellomics: Micro and Nanotechnologies for Life Science*, 2004.

[61] H. Andersson, and A. van den Berg, "Microfluidic devices for cellomics: a review," *Sensors and Actuators B-Chemical,* vol. 92, no. 3, pp. 315-325, 2003.

[62] E. M. Lucchetta, J. H. Lee, L. A. Fu *et al.*, "Dynamics of Drosophila embryonic patterning network perturbed in space and time using microfluidics," *Nature,* vol. 434, no. 7037, pp. 1134-1138, Apr, 2005.

[63] G. Medoro, C. Nastruzzi, R. Guerrieri *et al.*, "Lab on a chip for live-cell manipulation," *Ieee Design & Test of Computers,* vol. 24, no. 1, pp. 26-36, 2007.

[64] P. U. Arumugam, H. Chen, A. M. Cassell *et al.*, "Dielectrophoretic trapping of single bacteria at carbon nanofiber nanoelectrode arrays," *Journal of Physical Chemistry A,* vol. 111, pp. 12772-12777, 2007.

[65] J. Voldman, "Electrical forces for microscale cell manipulation," *Annual Review of Biomedical Engineering,* vol. 8, pp. 425-454, 2006.

[66] C. Q. Yi, C. W. Li, S. L. Ji *et al.*, "Microfluidics technology for manipulation and analysis of biological cells," *Analytica Chimica Acta,* vol. 560, no. 1-2, pp. 1-23, 2006.

[67] D. H. Kim, A. Haake, Y. Sun *et al.*, "High-throughput cell manipulation using ultrasound fields," *Proceedings of the 26th Annual International Conference of the Ieee Engineering in Medicine and Biology Society, Vols 1-7,* vol. 26, pp. 2571-2574, 2004.

[68] D. Holmes, H. Morgan, and N. G. Green, "High throughput particle analysis: Combining dielectrophoretic particle focussing with confocal optical detection," *Biosensors & Bioelectronics,* vol. 21, no. 8, pp. 1621-1630, 2006.

[69] D. Holmes, and H. Morgan, "Cell sorting and separation using dielectrophoresis," *Electrostatics 2003*, no. 178, pp. 107-112, 2004.

[70] C. Ionescu-Zanetti, A. Blatz, and M. Khine, "Electrophoresis-assisted single-cell electroporation for efficient intracellular delivery," *Biomedical Microdevices,* vol. 10, pp. 113-116, 2008.

[71] M. Khine, C. Ionescu-Zanetti, A. Blatz *et al.*, "Single-cell electroporation arrays with real-time monitoring and feedback control," *Lab on a Chip,* vol. 7, no. 4, pp. 457-462, 2007.

[72] C. Bae, and P. J. Butler, "Automated single-cell electroporation," *Biotechniques,* vol. 41, no. 4, pp. 399-+, 2006.
[73] T. P. Hunt, and R. M. Westervelt, "Dielectrophoresis tweezers for single cell manipulation," *Biomedical Microdevices,* vol. 8, no. 3, pp. 227-230, 2006.
[74] H. Y. Wang, and C. Lu, "High-throughput and real-time study of single cell electroporation using microfluidics: Effects of medium osmolarity," *Biotechnology and Bioengineering,* vol. 95, no. 6, pp. 1116-1125, 2006.
[75] Z. Palkova, L. Vachova, M. Valer *et al.*, "Single-cell analysis of yeast, mammalian cells, and fungal spores with a microfluidic pressure-driven chip-based system," *Cytometry Part A,* vol. 59A, no. 2, pp. 246-253, Jun, 2004.
[76] Y. Sun, and X. F. Yin, "Novel multi-depth microfluidic chip for single cell analysis," *Journal of Chromatography A,* vol. 1117, no. 2, pp. 228-233, Jun, 2006.
[77] S. V. Kyriacou, M. E. Nowak, W. J. Brownlow *et al.*, "Single live cell imaging for real-time monitoring of resistance mechanism in Pseudomonas aeruginosa," *Journal of Biomedical Optics,* vol. 7, no. 4, pp. 576-586, Oct, 2002.
[78] X. J. Gao, T. S. Chen, D. Xing *et al.*, "Single cell analysis of PKC activation during proliferation and apoptosis induced by laser irradiation," *Journal of Cellular Physiology,* vol. 206, no. 2, pp. 441-448, Feb, 2006.
[79] L. M. Shaner, and P. R. Brown, "Single cell analysis using capillary electrophoresis," *Journal of Liquid Chromatography & Related Technologies,* vol. 23, no. 7, pp. 975-997, 2000.
[80] W. E. Huang, K. Stoecker, R. Griffiths *et al.*, "Raman-FISH: combining stable-isotope Raman spectroscopy and fluorescence in situ hybridization for the single cell analysis of identity and function," *Environmental Microbiology,* vol. 9, no. 8, pp. 1878-1889, Aug, 2007.
[81] J. Vitecek, J. Petrlova, V. Adam *et al.*, "A fluorimetric sensor for detection of one living cell," *Sensors,* vol. 7, no. 3, pp. 222-238, Mar, 2007.
[82] H. Zhang, and W. R. Jin, "Single-cell analysis by intracellular immuno-reaction and capillary electrophoresis with laser-induced fluorescence detection," *Journal of Chromatography A,* vol. 1104, no. 1-2, pp. 346-351, Feb, 2006.
[83] G. H. Xiong, Y. Chen, and E. A. Arriaga, "Measuring the doxorubicin content of single nuclei by micellar electrokinetic capillary chromatography with laser-induced fluorescence detection," *Analytical Chemistry,* vol. 77, no. 11, pp. 3488-3493, Jun, 2005.
[84] T. Vo-Dinh, "Nanobiosensors: Probing the sanctuary of individual living cells," *Journal of Cellular Biochemistry*, pp. 154-161, 2002.
[85] T. Miyashiro, and M. Goulian, "Single-cell analysis of gene expression by fluorescence microscopy," *Two-Component Signaling Systems, Pt B*, Methods in Enzymology, pp. 458-475, 2007.
[86] L. S. Jang, and M. H. Wang, "Microfluidic device for cell capture and impedance measurement," *Biomedical Microdevices,* vol. 9, no. 5, pp. 737-743, 2007.
[87] E. Nascimento, T. Silva, and A. Oliva, "Identification, characterization and manipulation of Babesia bovis infected red blood cells using microfluidics technology," *Parassitologia (Rome),* vol. 49, no. Suppl. 1, pp. 45-52, 2007.
[88] T. Sun, S. Gawad, C. Bernabini *et al.*, "Broadband single cell impedance spectroscopy using maximum length sequences: theoretical analysis and practical considerations," *Measurement Science & Technology,* vol. 18, no. 9, pp. 2859-2868, 2007.

[89] S. Gawad, T. Sun, N. G. Green *et al.*, "Impedance spectroscopy using maximum length sequences: Application to single cell analysis," *Review of Scientific Instruments,* vol. 78, no. 5, 2007.
[90] A. Han, and A. B. Frazier, "Ion channel characterization using single cell impedance spectroscopy," *Lab on a Chip,* vol. 6, no. 11, pp. 1412-1414, 2006.

Chapter 1 Theory and Overview

1.1 Introduction and outline

Impedance spectroscopy of cells and biomolecules involves the investigation of their dielectric parameters by applying an AC field of variable frequency and measuring the current. This chapter outlines the theoretical foundations and fundamental concepts of dielectric and impedance spectroscopy. It begins with a description of impedance spectroscopic methods, starting from the fundamentals of polarization, measurement of the complex permittivity of biological materials and the interpretation of dielectric relaxations. Impedance spectroscopy measurements are compared with alternative methods for measuring the dielectric properties of particles, such as dielectrophoresis, electro-orientation and electrorotation. The issue of electrode polarization is also presented in the context of impedance spectroscopy and the phenomenon of the electrical double layer is explained.

1.2 Dielectric materials and polarization

An ideal dielectric material is defined as a material that has only bound charges and no mobile carriers. An external electric field applied to a slab of dielectric induces polarization of bound charges. Polarization is a term used to describe the response of the charges in a material to the application of an electric field. In vector notation

$$\vec{P} = \alpha \vec{E} \tag{1-1}$$

where $\vec{E}$ is the electric field and α the polarisability. $\vec{P}$ is the electrical dipole moment per unit volume. (C-m/m^3).

The dipole moment (C-m) is defined as

$$\vec{p} = q\vec{d} \tag{1-2}$$

where $\vec{d}$ is the vector separating two charges, ±q of opposite sign.

1.3 Polarization mechanisms

There are five distinct polarization mechanisms (refer to [1-5] for theory of the various polarization processes).

- Electronic
- Atomic
- Orientational
- Interfacial
- Counterion

Electronic, atomic and orientational polarizations are attributed to slight movements or reorientation of localised charges in response to an external electric field. In the context of impedance spectroscopy of biomolecules and cells, electronic and atomic polarization mechanisms are of little consequence and are therefore only briefly described here.

For heterogeneous dielectric materials, interfacial and counterion polarization mechanisms involve movement of charge carriers on a larger scale. Each polarization process results in a dielectric relaxation with a characteristic time constant or frequency response.

1.3.1 Electronic polarization

Electronic polarization results from the displacement of the centre of negative charge (the electron cloud) from the centre of positive charges (atomic nucleus) by the application of an external electric field; this polarization process occurs at excitation frequencies in excess of 10^{14} Hz.

1.3.2 Atomic polarization

Atomic polarization occurs when atoms experience a slight displacement from their equilibrium position in a molecule. Atomic polarization occurs in the frequency range of 10^{12}-10^{14} Hz.

1.3.3 Orientational polarization

Orientational polarization occurs for polar molecules. For example H_2O, represented in Figure 1-1 has a permanent dipole with which an externally applied electric field interacts [6]. The polar molecule experiences a torque that tends to align the dipole to the field.

$$\vec{\tau} = \vec{p} \times \vec{E} \tag{1-3}$$

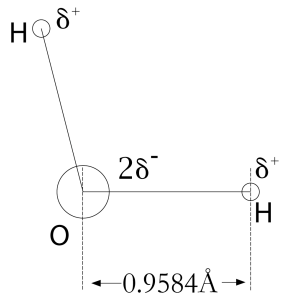

Figure 1-1 Schematic representation of a water molecule; the oxygen at the vertex has a higher electro-negativity than the hydrogen at the tip: the side of the molecule with the oxygen atom has a partial negative charge. A molecule with such a charge difference is called a dipole. Adapted from http://upload.wikimedia.org/wikipedia/commons/e/ea/Dipole_water.png

Orientational polarization of water occurs at frequencies in the range of 10^9-10^{12} Hz, depending on temperature. The relaxation frequency is around 2 GHz at room temperature [7-9]. The total polarisability of a material is the sum of these components.

The time constant for dipolar relaxation ranges from microseconds for large globular proteins, to picoseconds for smaller polar molecules such as water.

1.3.4 Interfacial polarization

Interfacial polarization, also called Maxwell-Wagner polarization [4, 10], occurs in heterogeneous dielectric materials, as charges which get trapped at internal interfaces cause macroscopic distortions of the field [1] which cause a frequency dependent polarization. This polarization mechanism is of particular relevance in the study of biological cells and it is further expanded upon in section 1.4

1.3.5 Counterion polarization

Counterion polarization occurs when clouds of ions move along and around the surface of polyelectrolytes [11]. This effect is responsible for the dispersion in the kHz frequency range of the solutions of biological particles and long chain macromolecules such as DNA.

1.4 Complex Permittivity

The permittivity of a material is a measure of the extent to which its charge distribution is polarised by an external electric field, or more precisely the dipole moment induced by an electric field.

By defining the vector fields $\vec{E}$ (electric field) and $\vec{D}$ (dielectric displacement) such that, according to Maxwell's equations:

$$\nabla \times \vec{E} = 0 \tag{1-4}$$

$$\nabla \cdot \vec{D} = \rho \tag{1-5}$$

Where ρ is the charge density, it is defined in [12] that

$$\vec{D} - \vec{E} = \vec{P} \tag{1-6}$$

From this, since $\vec{P}$ is proportional to $\vec{E}$, as described in (1-1) :

$$\vec{D} = (\alpha + 1)\vec{E} = \varepsilon\vec{E} \tag{1-7}$$

where ε is the permittivity.

For a non-ideal dielectric, materials where free charge carriers are found as well as bound polarisable charges, it is useful to resort to equivalent circuit analysis, modelling the physical mechanisms of conductivity and polarisability using networks of resistors and capacitors. A non-ideal dielectric material is modelled as a lossy parallel plate capacitor, with geometrical parameters area A and plate separation d, with an AC potential V of angular frequencies ω applied between the two plates (Figure 1-2).

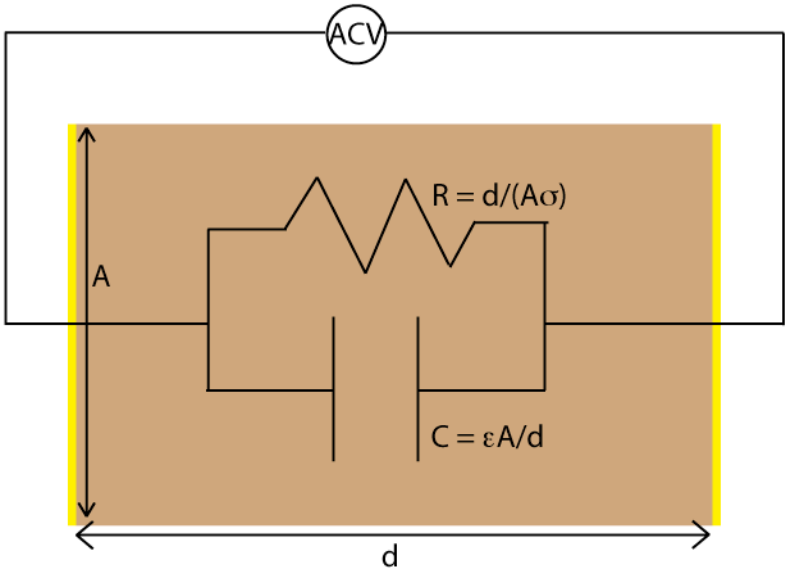

Figure 1-2. Two-dimensional representation of a non-ideal capacitor (a). A distance d separates two conducting plates (drawn in yellow) of area A. The dielectric material separating the plates has permittivity ε and conductivity σ. (b) Equivalent circuit model of the non-ideal capacitor. Both the capacitor and the resistor element in the model are proportional to the cell constant (A/d).

For the parallel circuit above, it is convenient to define the admittance of the system as

$$Y^* = G + j\omega C \tag{1-8}$$

Where the capacitance *C*, is a measure of the ability of the system to store energy and is a function of the geometrical dimensions of the capacitor:

$$C = \varepsilon_r \varepsilon_0 \left(A/d\right) \tag{1-9}$$

and G is the conductance (*1/R*), related to the conductivity as

$$G = \sigma \left(A/d\right) \tag{1-10}$$

Introducing the definitions of complex conductivity and permittivity, to include the effect of both the resistive and capacitive elements in the dielectric, as:

$$\sigma^* = \sigma' + j\sigma'' \tag{1-11}$$

$$\varepsilon^* = \varepsilon' - j\varepsilon'' \tag{1-12}$$

Equation (1-8) can be re-written as:

$$Y^* = \left(A/d\right)\left(\sigma + j\omega\varepsilon_0\varepsilon_r\right) \tag{1-13}$$

Also introducing a generalized complex capacitance C*:

$$Y^* = j\omega C^* \tag{1-14}$$

where

$$C^* = \left(A/d\right)\varepsilon^* \tag{1-15}$$

From this it follows

$$C^* = \frac{Y^*}{j\omega} \tag{1-16}$$

From (1-12) and (1-15):

$$C^* = \left(A/d\right)\left(\varepsilon_0\varepsilon_r - \frac{j\sigma}{\omega}\right) \tag{1-17}$$

Therefore from (1-15) and (1-17):

$$\varepsilon^* = \left(\varepsilon_0\varepsilon_r - \frac{j\sigma}{\omega}\right) \tag{1-18}$$

Which, refering to (1-12), yields:

$$\varepsilon' - j\varepsilon'' = \left(\varepsilon_0\varepsilon_r - \frac{j\sigma}{\omega}\right) \tag{1-19}$$

i.e.:

$$\varepsilon' = \varepsilon_0\varepsilon_r \tag{1-20}$$

$$\varepsilon'' = \left(\frac{\sigma'}{\omega}\right) \tag{1-21}$$

Similarly, admittance can be considered in terms of complex conductivity,

$$Y^* = \left(A/d\right)\left(\sigma + j\omega\varepsilon_0\varepsilon_r\right) = \left(A/d\right)\sigma^* \tag{1-22}$$

i.e.

$$\sigma^* = \sigma + j\omega\varepsilon_0\varepsilon_r \tag{1-23}$$

$$\sigma^* = j\omega\varepsilon_0\varepsilon^* \tag{1-24}$$

If a DC current flows in the system, this will have a form $\frac{\sigma_{dc}}{\varepsilon\omega_0}$, i.e. diverging as frequencies approach 0 Hz, and is added to the ε" (ω) term.

When two slabs of different dielectric properties are placed in series between two electrodes as illustrated in Figure 1-3, interfacial polarization arises.

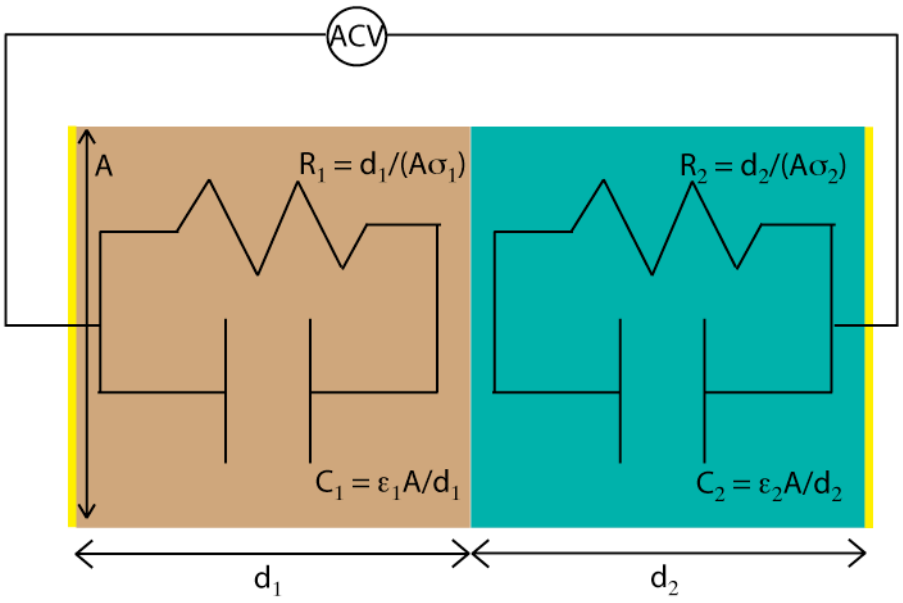

Figure 1-3 Two slabs of materials with characteristic dielectric and geometric parameters in series, between two measuring electrodes give rise to interfacial polarization if $\varepsilon_1\sigma_1 \neq \varepsilon_2\sigma_2$

The impedance of the system is equal to the sum of the impedances of the two slabs:

$$Z = Z_1 + Z_2 \tag{1-25}$$

The admittance, Y, is

$$Y = \left(\frac{1}{Y_1} + \frac{1}{Y_2}\right)^{-1} = \left(\frac{Y_1 + Y_2}{Y_1 Y_2}\right)^{-1} = \frac{Y_1 Y_2}{Y_1 + Y_2} \tag{1-26}$$

where

$$Y_1 = \frac{1}{R_1} + j\omega C_1 = \frac{R_1 + j\omega R_1 C_1}{R_1} \tag{1-27}$$

$$Y_2 = \frac{1}{R_2} + j\omega C_2 = \frac{R_2 + j\omega R_2 C_2}{R_2} \tag{1-28}$$

Equation (1-26) can be expanded to:

$$Y = \frac{(1 + j\omega R_1 C_1)(1 + j\omega R_2 C_2)}{R_1 + R_2 + j\omega R_1 R_2 (C_1 + C_2)} \tag{1-29}$$

By substituting

$$\tau_1 = R_1 C_1$$
$$\tau_2 = R_2 C_2 \tag{1-30}$$

Equation (1-29) becomes

$$Y = \frac{(1 + j\omega\tau_1)(1 + j\omega\tau_2)}{R_1 + R_2 + j\omega R_1 R_2 (C_1 + C_2)} \tag{1-31}$$

and after setting

$$\tau = \frac{R_1 R_2 (C_1 + C_2)}{R_1 + R_2} \tag{1-32}$$

equation (1-31) becomes

$$Y = \frac{(1 + j\omega\tau_1)(1 + j\omega\tau_2)}{R_1 + R_2 + j\omega\tau (R_1 + R_2)} = \frac{1}{R_1 + R_2} \frac{(1 + j\omega\tau_1)(1 + j\omega\tau_2)}{1 + j\omega\tau} \tag{1-33}$$

The expression can be further manipulated to give:

$$Y = \frac{1}{R_1 + R_2} \frac{(1 + j\omega\tau_1)(1 + j\omega\tau_2)}{1 + j\omega\tau} \tag{1-34}$$

$$Y = \frac{1}{R_1 + R_2} \frac{1 + j\omega\tau_1 + j\omega\tau_2 - \omega^2\tau_1\tau_2}{1 + j\omega\tau} \frac{1 - j\omega\tau}{1 - j\omega\tau} \tag{1-35}$$

$$Y = \frac{1}{R_1 + R_2} \frac{(1 + j\omega\tau_1 + j\omega\tau_2 - \omega^2\tau_1\tau_2)(1 - j\omega\tau)}{1 + \omega^2\tau^2} \tag{1-36}$$

$$Y = \frac{1}{R_1 + R_2} \frac{1 + j\omega\tau_1 + j\omega\tau_2 - \omega^2\tau_1\tau_2 - j\omega\tau + \omega^2\tau\tau_1 + \omega^2\tau\tau_2 + j\omega^3\tau_1\tau_2\tau}{1 + \omega^2\tau^2} \tag{1-37}$$

$$Y = \frac{1}{R_1 + R_2} \frac{1 - \omega^2\tau_1\tau_2 + \omega^2\tau(\tau_1 + \tau_2) - j\omega\tau(1 - \omega^2\tau_1\tau_2) + j\omega(\tau_1 + \tau_2)}{1 + \omega^2\tau^2} \tag{1-38}$$

The equation can be expressed in terms of complex dielectric constant as in general case of (1-14)

$$Y = j\omega C^* = j\omega \left(A/d\,\varepsilon_0\right)\varepsilon^* = j\omega \left(A/d\,\varepsilon_0\right)(\varepsilon' - j\varepsilon'') = \left(A/d\,\varepsilon_0\right) j\omega\varepsilon' + \omega\varepsilon'' \tag{1-39}$$

It is convenient to define

$$C_0 = \frac{A}{d}\varepsilon_0 \tag{1-40}$$

so the real and imaginary part of (1-38) and (1-39) can be equated to yield:

$$\varepsilon' = \frac{1}{C_0 (R_1 + R_2)} \frac{(\tau_1 + \tau_2) - \tau(1 - \omega^2\tau_1\tau_2)}{1 + \omega^2\tau^2} \tag{1-41}$$

$$\varepsilon'' = \frac{1}{\omega C_0 \left(R_1 + R_2\right)} \frac{1 - \omega^2 \tau_1 \tau_2 + \omega^2 \tau \left(\tau_1 + \tau_2\right)}{1 + \omega^2 \tau^2} \tag{1-42}$$

When $\omega \to 0$, i.e. in the limit of a DC applied signal, (1-41) reduces to:

$$\varepsilon_{dc} = \frac{\tau_1 + \tau_2 - \tau}{C_0 \left(R_1 + R_2\right)} \tag{1-43}$$

When $\omega \to \infty$, i.e. for high frequencies

$$\varepsilon_{\infty} = \frac{\tau_1 \tau_2}{\tau} \frac{1}{C_0 \left(R_1 + R_2\right)} \tag{1-44}$$

Substituting (1-43) and (1-44) back into (1-41):

$$\varepsilon' = \varepsilon_{\infty} + \frac{\varepsilon_{dc} - \varepsilon_{\infty}}{1 + \omega^2 \tau^2} \tag{1-45}$$

Substituting (1-43) and (1-44) back into (1-42):

$$\varepsilon'' = \frac{1}{\omega C_0 \left(R_1 + R_2\right)} + \frac{\omega \tau \left(\varepsilon_{dc} - \varepsilon_{\infty}\right)}{1 + \omega^2 \tau^2} \tag{1-46}$$

Equation (1-45) gives the characteristic permittivity dispersion of two dielectric slabs in series, termed ‘Debye dispersion’. This results from interfacial polarization and is discussed further in the next section. Equation (1-47) consists of two terms: the first one to the dc conductivity of the medium and its dominant in the limit of ω→0; the second term is again a ‘Debye’ type dispersion.

1.5 Dielectric relaxations, permittivity dispersions and dielectric loss

Because the motion of charges is intrinsic to the polarization phenomenon, the polarization mechanisms depend on frequency, as reorientation of electrons, ions and dipoles cannot occur instantaneously. Taking for example rotational polarization, at excitation frequencies lower than the characteristic frequency, the dipoles have enough time to align with the field. As the frequency increases, the dipoles no longer can follow the field and the polarization decreases. The fall in polarizability results in a decrease in energy storage (and a *dispersion* in permittivity ε'). This change is termed dielectric relaxation. When the phase lag between the driving field and the dipole orientation develops, energy is drawn from the electrical source by the material, and is dissipated.

Dielectric loss, as indicated by the equations (1-46) and (1-50), has two terms: the first (DC conductivity) term indicate that energy is lost through Joule heating, while the second term indicates that energy is also lost due to the electrical conductivity that arises from the relaxation mechanism: this loss, represented by ε", reaches a maximum at the characteristic angular frequency or $\omega = 1/\tau$ when the time required for maximum orientation of the dipoles is exactly equal to the one half cycle of the applied ac field. At higher frequencies and in the limit of $\omega=\infty$, the applied field is oscillating too quickly for the dipoles to orient with the field and no energy is stored. At lower frequencies the dipoles are oriented and work is done in moving the dipoles in a viscous medium. The power lost per cycle of AC field increases with frequency, as the number of cycles per second increases.

It is therefore useful to characterize dielectric materials by recording their values of permittivity (real and imaginary) against the excitation frequency of an externally applied electric field as shown in Figure 1-4.

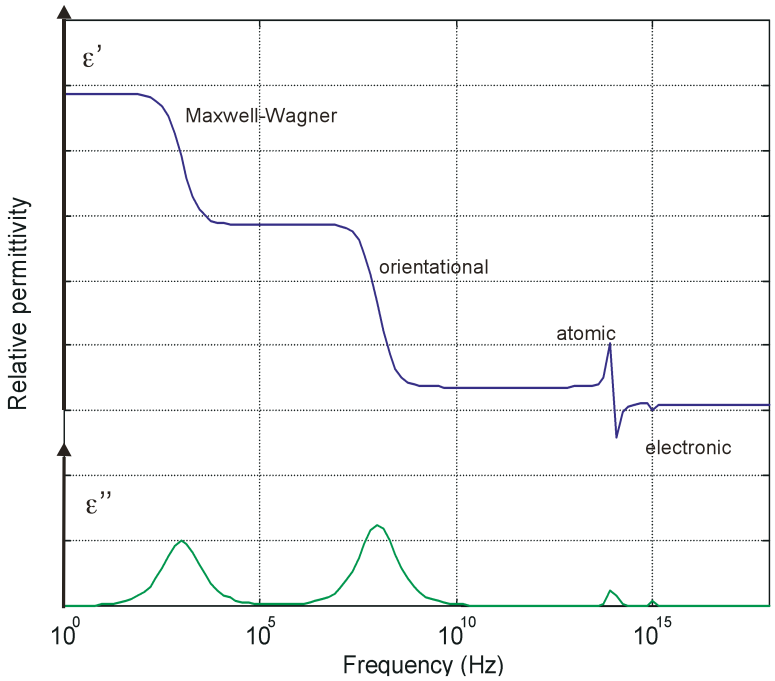

Figure 1-4. Simplified representation of dielectric dispersions due to four kinds of relaxation mechanisms across a wide frequency spectrum: Maxwell-Wagner, orientational, atomic, electronic. Courtesy of J. Tanner Nevill

Schwan named the relaxations caused by counterion and Maxwell-Wagner polarization the α and β relaxations respectively. Relaxations caused by orientational polarization of water molecules are termed γ. Orientation of bound water is termed the δ dispersion [13].

1.5.1 Debye Dispersions

A dielectric system that exhibits a single relaxation due to Maxwell-Wagner interfacial polarization will have a permittivity spectrum as plotted in Figure 1-5

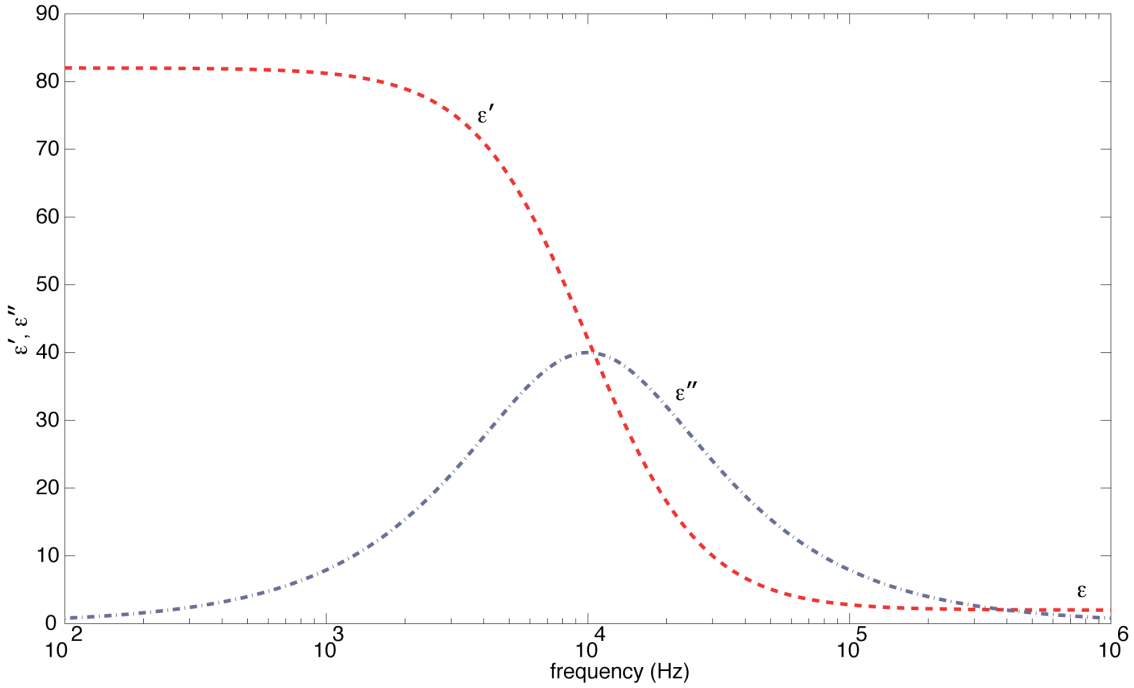

Figure 1-5 Complex permittivity spectrum for a dielectric exhibiting Maxwell-Wagner polarization. The parameters used for this simulation are as follow: The relaxation frequency is 10 kHz, $\varepsilon_\infty = 2$, $\varepsilon_s = 82$, and $\Delta\varepsilon = 80$.

In the plot, ε' decreases from a value of DC or 'static' permittivity, ε_s, at low frequencies to a value of ε_∞ at high frequencies; the decrement is termed Δε. The frequency at which ε" peaks is f_0, the characteristic frequency, and $\tau = \frac{1}{2\pi \cdot f_0}$ is the relaxation time. The Debye relaxation is described as:

$$\varepsilon^* = \varepsilon_\infty + \frac{\Delta\varepsilon}{1 + j\omega\tau} \tag{1-47}$$

From (1-47) the real and imaginary components are:

$$\varepsilon' = \varepsilon_\infty + \frac{\Delta\varepsilon}{1 + (\omega\tau)^2} \tag{1-48}$$

$$\varepsilon'' = \frac{\Delta\varepsilon\omega\tau}{1 + (\omega\tau)^2} \tag{1-49}$$

The inclusion of an extra term to equation (1-47) to account for DC conductivity results in an expression for the complex permittivity of:

$$\varepsilon^* = \varepsilon_\infty + \frac{\Delta\varepsilon}{1 + j\omega\tau} - j\frac{\sigma_{dc}}{\omega\varepsilon_0} \tag{1-50}$$

When the loss factor ε" is plotted against the permittivity ε' in a complex plane (known as Cole-Cole plot) as in Figure 1-6, a single Debye relaxation gives a semicircle with the origin on the axis.

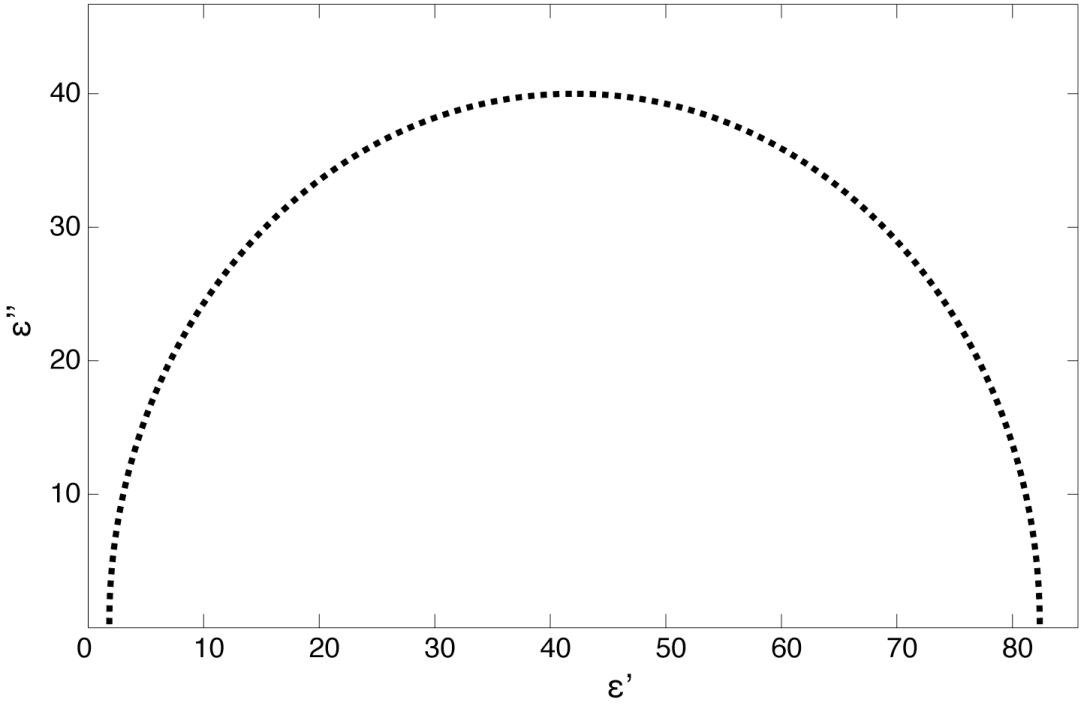

Figure 1-6. Cole-Cole plot of a single Debye-type relaxation. The same simulation parameters were used as described in Figure 1-5.

1.5.2 Non-ideal dispersions

Complex plane plots obtained from experimental data often deviate from a semicircle. The deviation can be accounted for by various empirical equations [14-19], some of which are summarized by Asami [20]. Generally the non-ideal behaviour is due to a combination of several relaxations with different characteristic frequencies. To model the 'spread' in the response, the Debye equation was generalized, by Cole and Cole as [14]:

$$\varepsilon^* = \varepsilon_\infty + \frac{\Delta\varepsilon}{1+(j\omega\tau)^\alpha} \tag{1-51}$$

where α characterizes the spread. If α = 1, the Cole-Cole expression reduces to the Debye expression. Figure 1-7 and 1-8 illustrate the effect of α on the permittivity and loss factor of a dielectric system. In the frequency spectrum, the permittivity decrement is spread as the loss factor peak. In the complex plane, the semicircle is depressed.

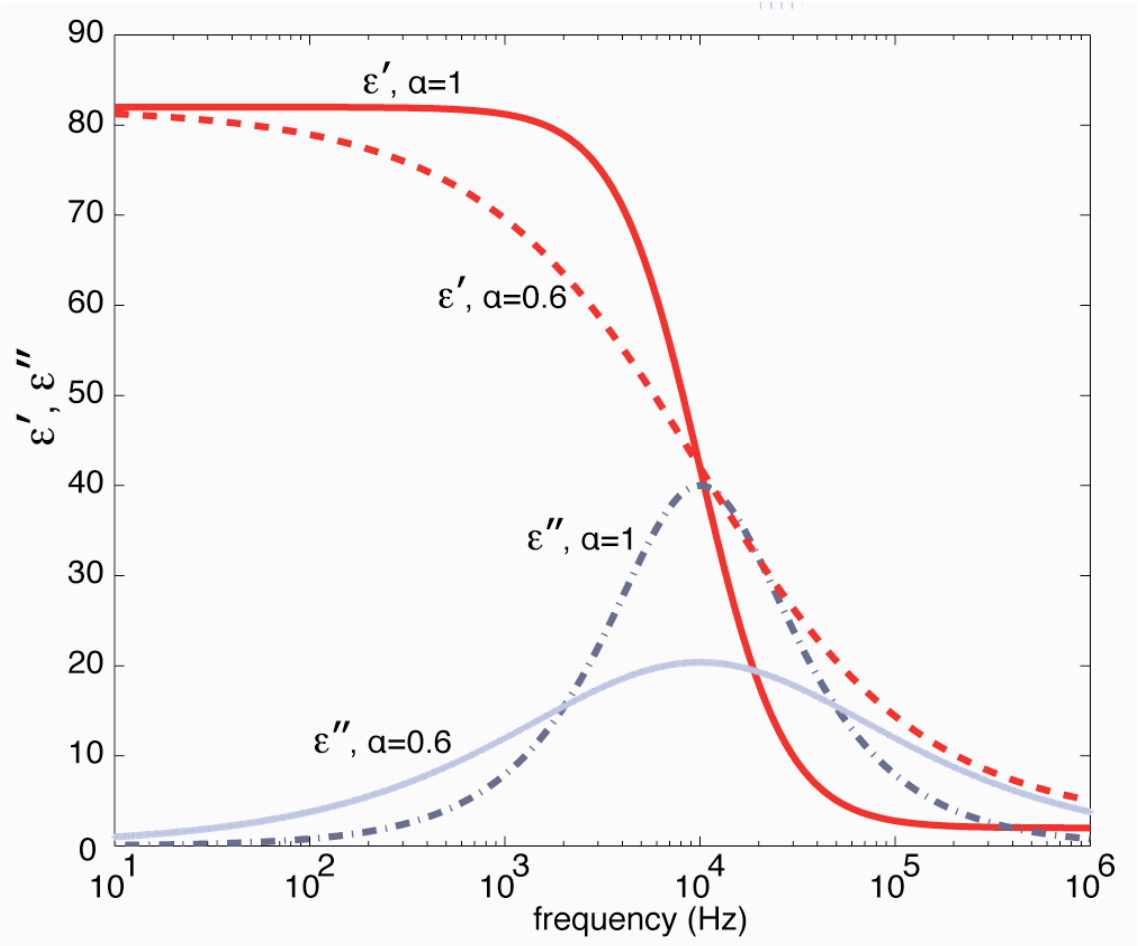

Figure 1-7. Complex permittivity plot of a single Debye-type relaxation compared to a Cole-Cole relaxation with α =0.6. The relaxation frequency is 10 kHz, is ε_∞= 2, ε_s = 82, resulting in a Δε = 80.

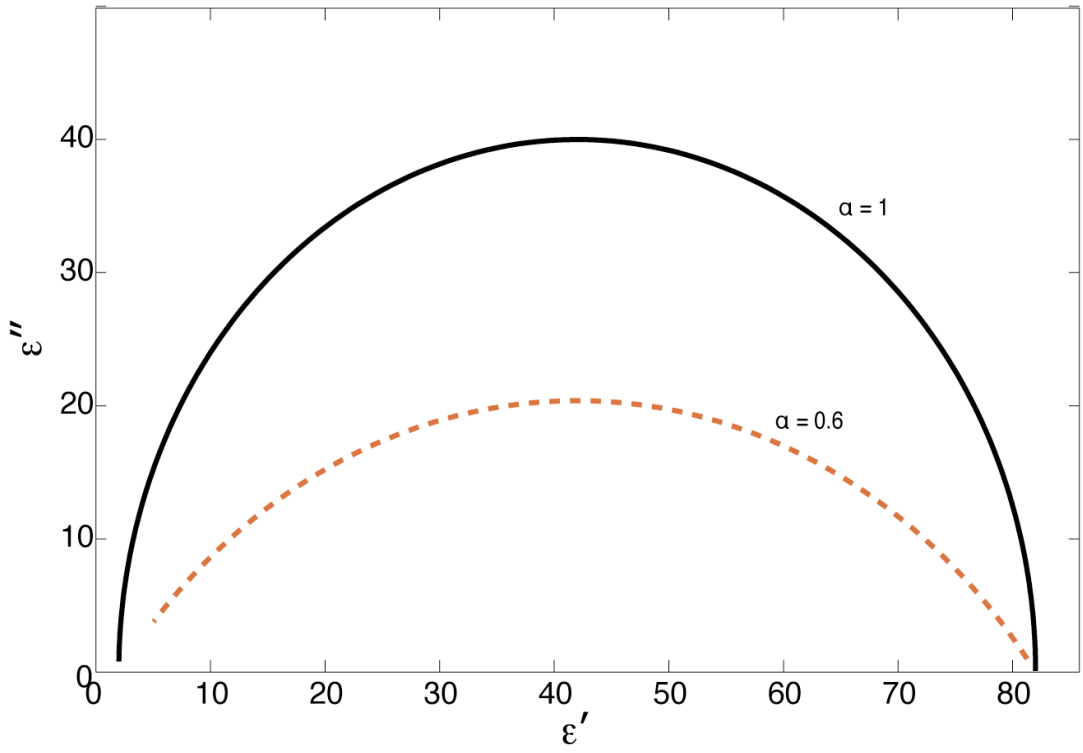

Figure 1-8. Cole-Cole plot of a single Debye-type relaxation compared to a Cole-Cole relaxation with α =0.6. The relaxation frequency is 10 kHz, is ε_∞= 2, ε_s = 82, resulting in $\Delta\varepsilon$ = 80.

In 1967 the model was further generalized by Havriliak and Negami [16] as

$$\varepsilon^* = \varepsilon_\infty + \frac{\Delta\varepsilon}{\left(1+\left(j\omega\tau\right)^{\alpha}\right)^{\beta}} \tag{1-52}$$

Simulations results showing the effect of varying β are shown in Figure 1-9 and Figure 1-10.

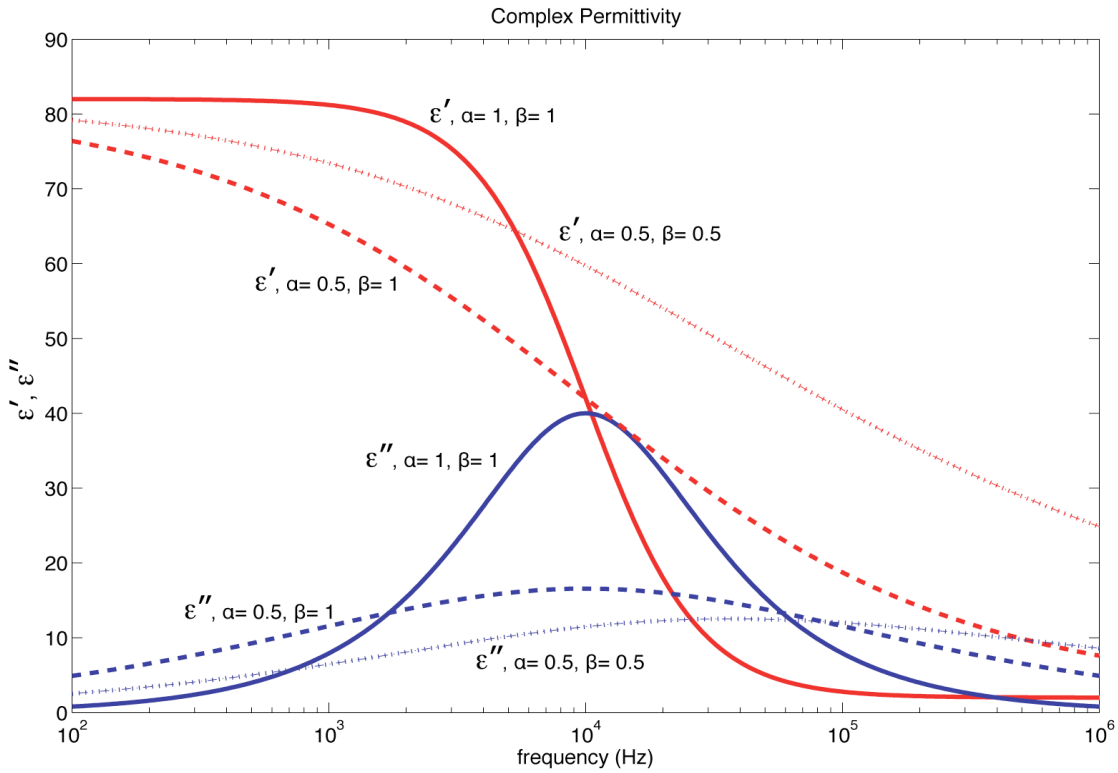

Figure 1-9 Complex permittivity plot of a single Debye-type relaxation compared to a Cole-Cole relaxation with α =0.5 and a Havriliak-Negami relaxation with α =0.5 and β = 0.5.

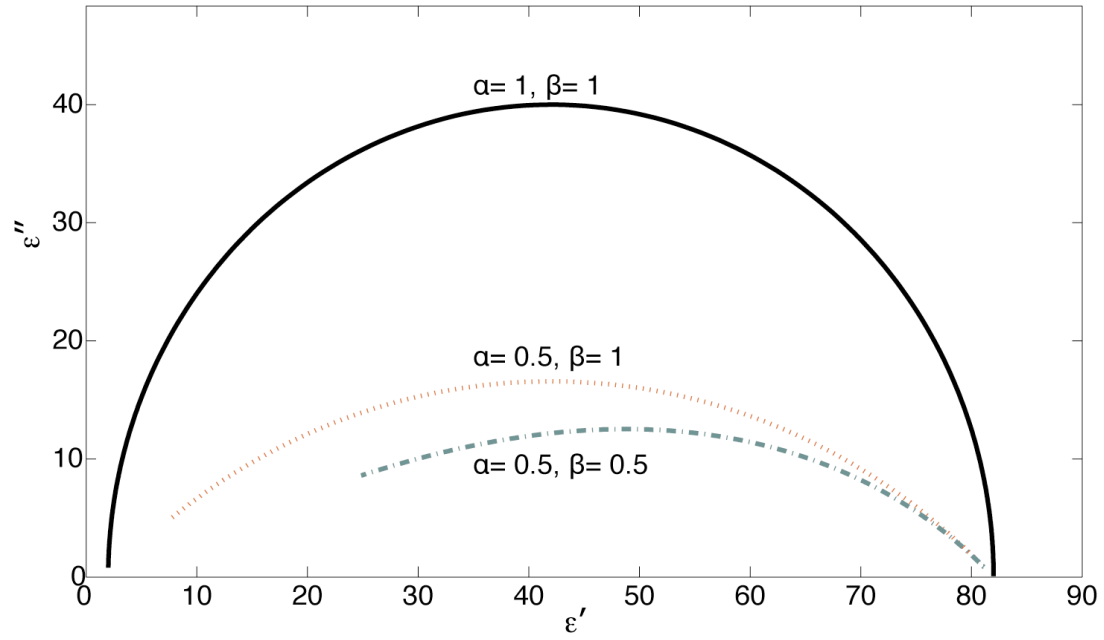

Figure 1-10 Cole-Cole plot of a single Debye-type relaxation compared to a Cole-Cole relaxation with α =0.5 and a Havriliak-Negami relaxation with α =0.5 and β = 0.5.

It can be seen from Figure 1-10, that the parameter β not only depresses the semicircle in the complex plane but also introduces an asymmetry with respect to f_0 in the frequency spectrum for both the real and imaginary representation of the complex

permittivity. The permittivity from several polarization mechanisms is summed across the spectrum, hence the permittivity function exhibits a behaviour generally modelled as:

$$\varepsilon^* = \varepsilon_\infty + \frac{\Delta\varepsilon_1}{\left(1+\left(j\omega\tau_1\right)^\alpha\right)^\beta} + \frac{\Delta\varepsilon_2}{\left(1+\left(j\omega\tau_2\right)^\alpha\right)^\beta} + \ldots + \frac{\Delta\varepsilon_n}{\left(1+\left(j\omega\tau_n\right)^\alpha\right)^\beta} \qquad (1\text{-}53)$$

Such a summation of Debye relaxations is plotted in Figure 1-11

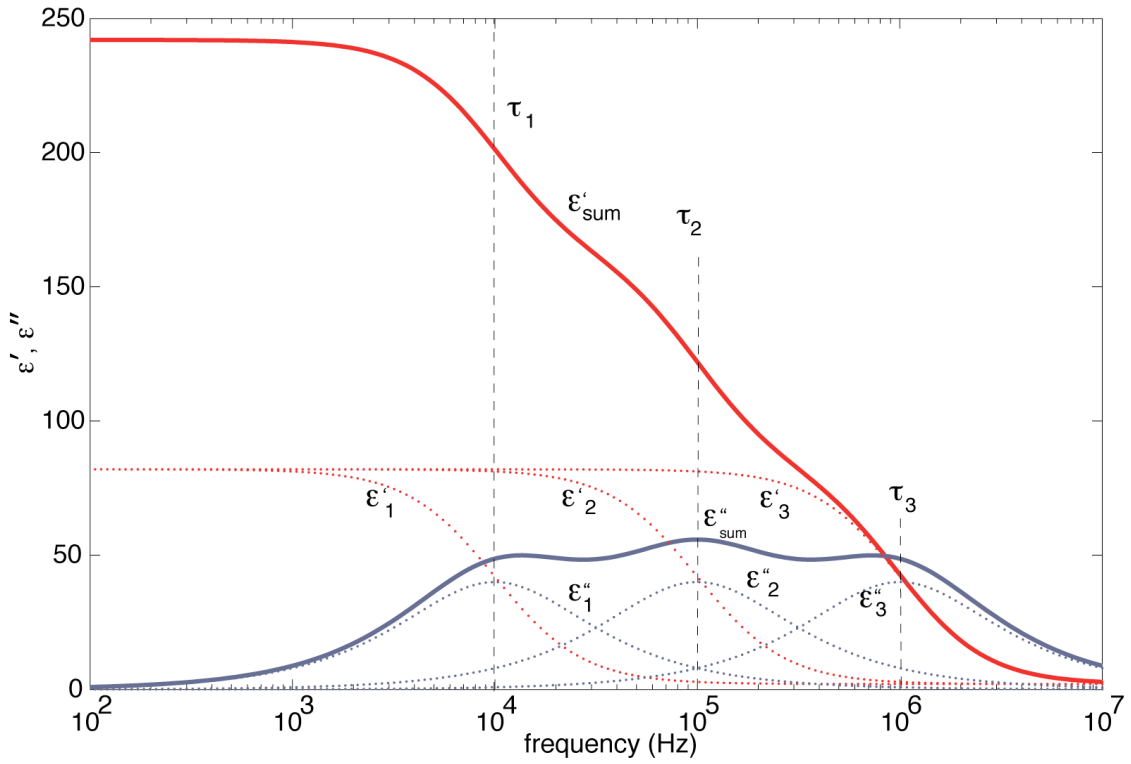

Figure 1-11. Complex permittivity plot of multiple Debye relaxations (broken lines) and their sum total (lines). The following parameters were used: Relaxation 1: $\varepsilon_\infty = 2$, $\varepsilon_s = 82$, relaxation frequency 10 kHz. Relaxation 2: $\varepsilon_\infty = 2$, $\varepsilon_s = 82$, relaxation frequency = 100 kHz. Relaxation 3: $\varepsilon_\infty = 2$, $\varepsilon_s = 82$, relaxation frequency = 1 MHz.

1.6 Impedance and Dielectric Spectroscopy

The impedance spectrum of a system is measured by applying a frequency-dependent excitation signal and measuring the current. From the impedance spectrum and the geometrical parameters of the system, the complex permittivity or dielectric

spectrum is derived. Conventionally, a small AC voltage, $V^*(j\omega)$, swept over a range of frequencies is applied. The electrical current response, $I^*(j\omega)$, is measured and the complex impedance $Z^*(j\omega)$, of the system is:

$$Z^*(j\omega) = \frac{V^*(j\omega)}{I^*(j\omega)} = Z_{RE}(j\omega) + jZ_{IM}(j\omega) \tag{1-54}$$

Here $Z_{RE}(j\omega)$, and $Z_{IM}(j\omega)$ are the real and imaginary parts of the complex impedance, respectively. The magnitude and phase angle of the complex impedance are

$$\left|Z^*(j\omega)\right| = \sqrt{\left[Z_{RE}(j\omega)\right]^2 + \left[Z_{IM}(j\omega)\right]^2} \tag{1-55}$$

and

$$\angle Z^*(j\omega) = \arctan\frac{Z_{RE}(j\omega)}{Z_{IM}(j\omega)} \tag{1-56}$$

respectively.

1.6.1 Maxwell's mixture equation

For a dilute suspension of particles, like a suspension of biological cells, the impedance of the system can be described by Maxwell's mixture equation [4]. The equivalent complex permittivity of the mixture containing the particle and the suspending medium is given by:

$$\varepsilon^*_{mix} = \varepsilon^*_m \frac{1 + 2\Phi f_{cm}}{1 - \Phi f_{cm}} \tag{1-57}$$

where ε^*_{mix} is the complex permittivity of the mixture and Φ is the volume fraction (ratio of the particle volume to the detection volume). f_{cm} is the Clausius-Mossotti factor, defined as

$$f_{cm} = \frac{\varepsilon^*_p - \varepsilon^*_m}{\varepsilon^*_p + 2\varepsilon^*_m} \tag{1-58}$$

ε^*_p and ε^*_m are the complex permittivities of the particle and medium.

Equation (1-57) fails when the particle concentration is high. Hanai et al. modified the model for suspensions with high volume fractions [21, 22] by defining

$$1 - \Phi = \frac{\varepsilon^* - \varepsilon^*_p}{\varepsilon^*_m - \varepsilon^*_p}\left(\frac{\varepsilon^*_m}{\varepsilon^*}\right)^{1/3} \tag{1-59}$$

The complex impedance of the system, Z^*_{mix}, is then:

$$Z^*_{mix} = \frac{1}{j\omega C^*_{mix}} \tag{1-60}$$

Where C^*_{mix} is the complex capacitance of the system. Measurement of the complex impedance or admittance of a cell suspension can be used to derive the average dielectric properties of the cells.

1.6.2 Shelled Model for cells

Biological cells can be modelled electrically as 'shelled' particles (Figure 1-12).

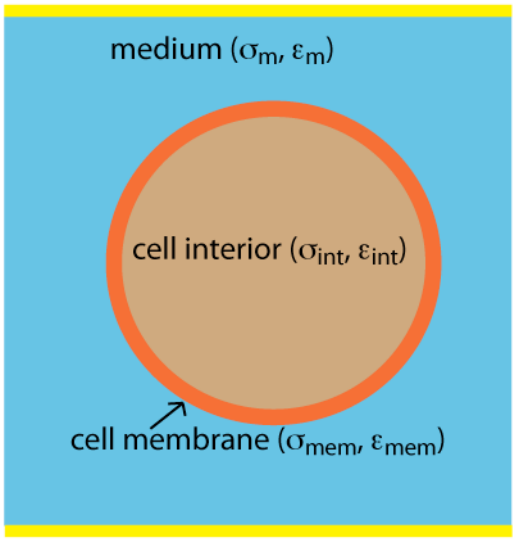

Figure 1-12. Single model for a cell. Each layer has a conductivity and permittivity σ and ε respectively. Since the membrane acts as an interface to both the interior of the cell and the medium outside, two relaxations appear in the spectrum

The complex permittivity of a 'single-shell' particle is given by [13]

$$\varepsilon^*_{cell} = \varepsilon^*_{mem} \frac{v^3 + 2\dfrac{\varepsilon^*_{\text{int}} - \varepsilon^*_{mem}}{\varepsilon^*_{\text{int}} + 2\varepsilon^*_{mem}}}{v^3 + \dfrac{\varepsilon^*_{\text{int}} - \varepsilon^*_{mem}}{\varepsilon^*_{\text{int}} + 2\varepsilon^*_{mem}}} \tag{1-61}$$

which can be contracted into:

$$\varepsilon^*_{cell} = \varepsilon^*_{mem} \frac{v^3 + 2f_{cm}}{v^3 - f_{cm}} \tag{1-62}$$

where the Clausius-Mossotti factor for the cell is defined as:

$$f_{cm} = \frac{\varepsilon^*_{\text{int}} - \varepsilon^*_{mem}}{\varepsilon^*_{\text{int}} + 2\varepsilon^*_{mem}} \tag{1-63}$$

v is a geometrical factor

$$v = \left(\frac{R_{cell} + d_{mem}}{R_{cell}} \right) \tag{1-64}$$

where R_{cell} is the radius of the cell and d_{mem} is the thickness of the membrane.

Figure 1-13 shows an example of complex permittivity and conductivity of a cell modelled as a single-shelled particles, calculated using the parameters in Table 1-1

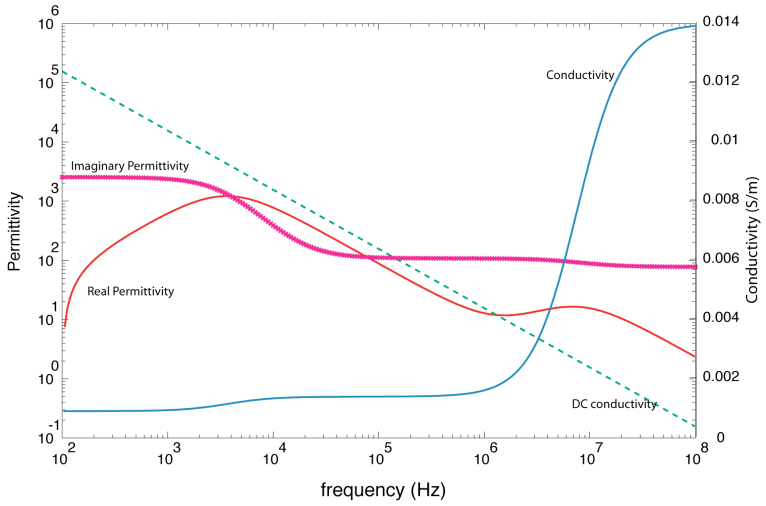

Figure 1-13. Example showing how the dielectric parameters for a single-shelled particle (simulation parameters are in Table 1-1). The DC conductivity term $\sigma_{dc}/\varepsilon\omega_0$ needs to be subtracted from the $\varepsilon''(\omega)$ term to yield the loss term. Conductivity is plotted on the right axis.

Radius of the cell	6μm
Conductivity of the cytoplasm	0.1 S m
Conductivity of the suspending medium	1e-3 S m
Conductivity of the membrane	1e-9 S m
Permittivity of the cytoplasm	50 ε_0
Permittivity of the suspending medium	78 ε_0
Permittivity of the membrane	9 ε_0
Distance between measuring electrodes	20μm
Size of parallel plate electrodes	20μm x 20μm

Table 1-1 Simulation parameters for an example single-shelled cell

The model can be extended to two shells (Figure 1-14) to better fit data acquired from cells that have a nucleus separated from the cytoplasm.

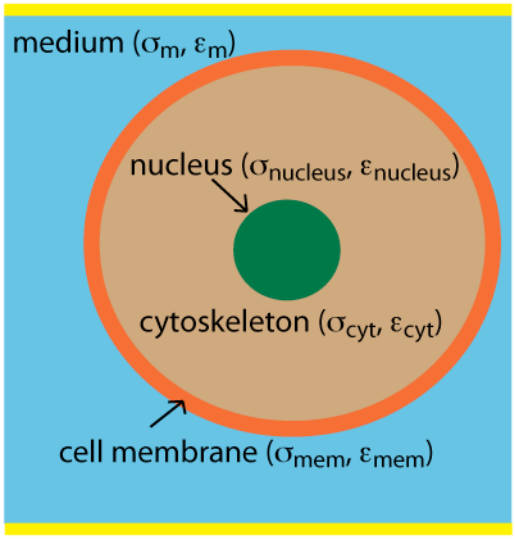

Figure 1-14. Double Shell model of a biological cell. Each element in the model has a conductivity σ and permittivity ε.

$$\varepsilon^*_{cell} = \varepsilon^*_{mem} \frac{v_1^3 + 2\dfrac{\varepsilon^*_{\text{int}} - \varepsilon^*_{mem}}{\varepsilon^*_{\text{int}} + 2\varepsilon^*_{mem}}}{v_1^3 + \dfrac{\varepsilon^*_{\text{int}} - \varepsilon^*_{mem}}{\varepsilon^*_{\text{int}} + 2\varepsilon^*_{mem}}} \tag{1-65}$$

$$\varepsilon^*_{\text{int}} = \varepsilon^*_{cyto} \frac{v_1^3 + 2\dfrac{\varepsilon^*_{nucleus} - \varepsilon^*_{cyto}}{\varepsilon^*_{nucleus} + 2\varepsilon^*_{cyto}}}{v_1^3 + \dfrac{\varepsilon^*_{nucleus} - \varepsilon^*_{cyto}}{\varepsilon^*_{nucleus} + 2\varepsilon^*_{cyto}}} \tag{1-66}$$

$$v_1 = \left(\frac{R_{nucleus} + d_{cyto} + d_{mem}}{d_{mem}} \right) \tag{1-67}$$

$$v_2 = \left(\frac{R_{nucleus} + d_{cyto}}{R_{nucleus}} \right) \tag{1-68}$$

More layers can be modelled by adding further shells to the equation.

1.6.3 Dielectrophoresis (DEP)

The dielectrophoretic force on a particle is the result of the interaction of and imposed electric field and an induced dipole moment. It is possible to characterize the dielectric properties of a particle in a suspending medium from the DEP force.

In an AC field, the time-averaged DEP force $\langle F_{DEP} \rangle$ is given by [1, 5]:

$$\langle F_{DEP} \rangle = \pi \varepsilon_m R^3 \, \mathrm{Re}\left[f_{CM} \right] \nabla \left| \vec{E} \right|^2 \tag{1-69}$$

where R is the particle radius. According to equation (42), the dielectric force is zero if the electric field is uniform, i.e. $\nabla |E|^2 = 0$. The frequency dependence and the direction of the DEP force are governed by the real part of the Clausius-Mossotti factor (equation 1-32). Positive dielectrophoresis or pDEP (the particle is attracted to high intensity electric field regions) occurs when the particle is more polarisable than the medium, (Re[f_{cm}] > 0). Negative dielectrophoresis or nDEP (the particle is attracted to low intensity electric field regions) occurs when the particle is less polarisable than the medium, (Re[f_{cm}] < 0). In practice it is difficult to measure the DEP force directly due to the effects of Brownian motion and electrically induced fluid flow [36].

Often, a parameter termed DEP crossover frequency [23-25] is measured as a function of medium conductivity to determine the dielectric properties of the suspended particles. The DEP crossover frequency is the frequency point where the DEP force switches polarity. According to [1] the crossover frequency is defined to be the frequency point at which the real part of the Clausius-Mossotti factor equals zero;

$$f_{cross} = \frac{1}{2\pi} \sqrt{\frac{(\sigma_m - \sigma_p)(\sigma_p + 2\sigma_m)}{(\varepsilon_p - \varepsilon_m)(\varepsilon_p + 2\varepsilon_m)}} = \frac{1}{\sqrt{2\pi}} \sqrt{\frac{\sigma_m - \sigma_p}{\varepsilon_p - \varepsilon_m} f_{MW}} \tag{1-70}$$

with

$$f_{MW} = \frac{1}{2\pi \tau_{MW}} \tag{1-71}$$

$$\tau_{MW} = \frac{\varepsilon_p + 2\varepsilon_m}{\sigma_p + 2\sigma_m} \tag{1-72}$$

where f_{cross} is the crossover frequency, f_{MW} is the Maxwell-Wagner relaxation frequency and τ_{MW} is the Maxwell-Wagner time constant. Equation (1-70) shows the

relationship between the crossover frequency and the Maxwell-Wagner relaxation frequency. For a biological cell, the interfacial polarization between the plasma membrane and the cytoplasm results in a dispersion typically around 1 MHz. At frequencies well below the dispersion frequency, and assuming a cell diameter of 10 μm, a simplified expression that related the cross over frequency to the membrane capacitance and conductance of the cell can be derived [26, 27]:

$$f_{cross} = \frac{\sqrt{2}}{8\pi RC_{mem}} \sqrt{(4\sigma_m - RG_{mem})^2 - 9R^2G^2_{mem}} \tag{1-73}$$

where C_{mem} and G_{mem} are the specific capacitance and conductance of the membrane, respectively and σ_m the conductivity of the suspending medium.

For the approximation to be valid, the cell interfacial polarization must occur at a frequency much higher than the crossover frequency and the cell internal conductivity must be much higher than that of the plasma membrane.

1.6.4 Electrorotation (ROT)

The interaction of an electric field with a polarized particle creates an induced dipole moment. In a rotating electric field, a torque is exerted on the induced dipole which causes the particle to rotate. The time-averaged torque is given in [1]:

$$\Gamma_{ROT} = -4\pi\varepsilon_m R^3 \,\mathrm{Im}\left[f_{cm}\right]\left|\vec{E}\right|^2 \tag{1-74}$$

Where R is the particle radius; the minus sign indicates that the dipole moment lags the electric field. Two significant differences between the expression for torque as shown in equation (1-74) and dielectrophoretic force in equation (1-69) are notable: while dielectrophoretic force is a function of the gradient of the square of the electric field, the torque is as a function of the square of the electric field. Secondly, the torque depends on the imaginary rather than the real part of the Clausius-Mossotti factor: If f_{cm} is negative the particle will rotate with the field, while it will rotate against the field when the f_{cm} is positive. When viscous drag is accounted for, the rotation rate $R_{ROT}(\omega)$ of the particle is given by [28]:

$$R_{ROT}(\omega) = -\frac{\varepsilon_m \,\mathrm{Im}\left[f_{cm}\right]\left|\vec{E}\right|^2}{2\eta} K \tag{1-75}$$

where K is a scaling factor.

1.6.5 Electro-orientation

The orientation of a particle is caused by an electric field-induced torque acting on a non-spherical particle. As explained in [29] and [30] the torque experienced by an ideal ellipsoidal dielectric particle tends to align the axes of particle with the field, but only alignment along the longest axis is stable.

For the case of a lossy ellipsoidal particle, alignment and stability assume a frequency-dependence: depending on relative conductivity and permittivity values of the medium and the particle all three axial orientations become possible, each in a different frequency range. The general expression for the torque experienced by an ellipsoidal particle is derived by Jones in [31, 32].

1.7 Conclusions and summary

This chapter has outlined the theoretical foundations of dielectric and impedance spectroscopy. It has been shown how the polarization mechanisms affect the dielectric response of cells, which can be explored by a variety of techniques: dielectrophoresis (DEP), electrorotation (ROT), electro-orientation (EOR) and direct impedance measurement.

DEP, ROT, EOR and impedance measurements are closely related, as they are different representations of the same dielectric parameters (for the theoretical relationship between these methods see [33-35]). Figure 1-15 ((a) to (d)) and Figure 1-16 compare the impedance spectrum with DEP and ROT spectra for a single-shell particle whose dielectric parameters are listed in Table 1-2. Dielectrophoresis and electrorotation are attractive techniques for measuring the dielectric properties of single cells, since they are label free, non-invasive method.

However, there are important disadvantages when compared to impedance spectroscopy. The rotation speed and direction of the cell has to be recorded at different frequencies, extensive postprocessing is required (evaluation of video, which can be automated to a certain extent). This makes it impossible to do real-time spectroscopy. Moreover, it is necessary to limit the translational displacement of the cell under study while electrorotation is taking place. This can be done by using dielectrophoretic traps, or optical or hydrodynamic tweezers, but both contribute to increased complexity of the

design. To reduce Joule heating effects it is preferable to use low conductivity solutions, which being non-physiological can alter the normal behaviour of live cells, thus requiring the measurements to take place quickly (within minutes), making it impossible to study the progression of live cells as they are cultured, go through their natural life cycle and/or react to the introduction of chemical compounds of interest.

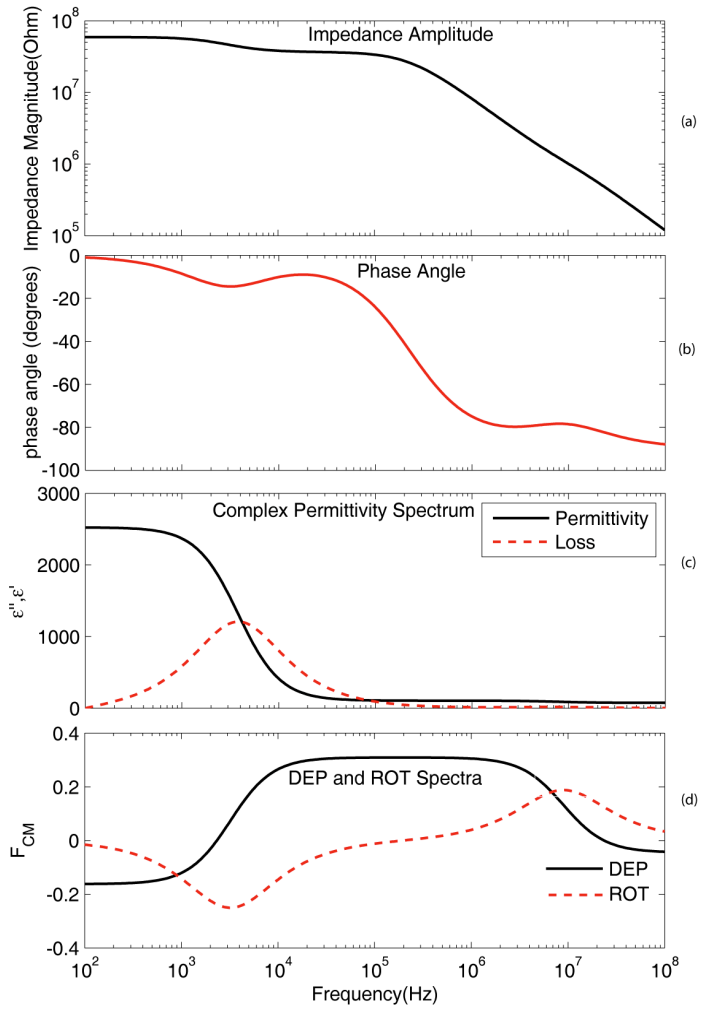

Figure 1-15. Simulation results for a single-shelled cell. Simulation parameters are summarized in Table 1-2. In (a) and (b) the impedance amplitude and phase are plotted. The high-frequency dispersion is barely visible in (a). In (c) the complex permittivity spectrum is plotted. The loss peak for the high frequency dispersion is dwarfed by the low frequency peak. In (d) the real and imaginary part of the CMF are plotted. The regimes of negative and positive DEP are easily identifiable, as well as the ROT.

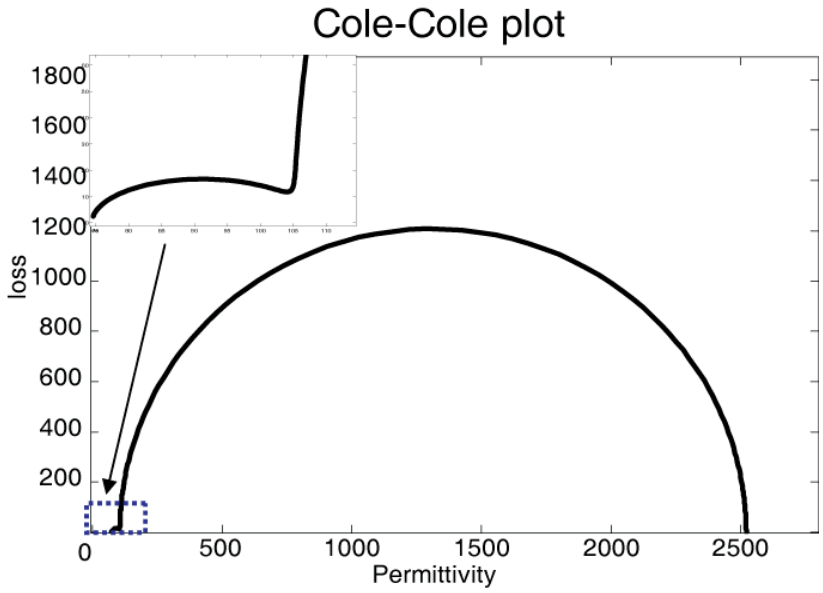

Figure 1-16. Cole-Cole plot for the simulation parameters in Table 1-2. In the inset, the high frequency relaxation, dwarfed by the large low-frequency relaxation.

Radius of the cell	6μm
Conductivity of the cytoplasm	0.1 S/m
Conductivity of the suspending medium	1e-3 S/m
Conductivity of the membrane	1e-9 S/m
Permittivity of the cytoplasm	50 ε_0
Permittivity of the suspending medium	78 ε_0
Permittivity of the membrane	9 ε_0
Distance between measuring electrodes	20μm
Size of parallel plate electrodes	20μm x 20μm

Table 1-2 Simulation parameters used to generate the plots in Figure 1-15 and Figure 1-16 single-shelled cell.

References

[1] H. Morgan, *AC Electrokinetics: colloids and nanoparticles*, Baldock: Research Studies Press, 2002.

[2] R. Pethig, *Dielectric and electronic properties of biological materials*, Chichester: Johm Wiley and Sons, 1979.

[3] R. Feynman, *The Feynman Lectures on Physics*: Addison-Wesley, 1965.

[4] J. C. Maxwell, *A Treatise On Electricity And Magnetism*, Oxford: Clarendon Press, 1881.

[5] T. B. Jones, *Electromechanics of Particles*, Cambridge: Cambridge University Press, 1995.

[6] Debye, *Polar Molecules*, 1929.

[7] Hasted, *Aquous Dielectrics*, London: Chapman and Hall, 1973.

[8] Hasted, *Water A comprehensive treatise*, New York: Plenum Press, 1972.

[9] J. B. R. Buchner, J. Stauber, "The dielectric relaxation of water between 0° C and 35° C," *Chem. Phys. Lett.,* vol. 306, pp. 57-63, 1999.

[10] K. W. Wagner, *Archiv. Elektrotechnik,* vol. 2, pp. 371-389, 1914.

[11] H. P. Schwan, G. Schwarz, J. Maczuk *et al.*, "On Low-Frequency Dielectric Dispersion of Colloidal Particles in Electrolyte Solution," *Journal of Physical Chemistry,* vol. 66, no. 12, pp. 2626-&, 1962.

[12] C. J. F. Bottcher, *Theory of Electric Polarization*, Amsterdam: Elsevier, 1973.

[13] K. R. Foster, and H. P. Schwan, "Dielectric-Properties of Tissues and Biological-Materials - a Critical-Review," *Critical Reviews in Biomedical Engineering,* vol. 17, no. 1, pp. 25-104, 1989.

[14] K. S. Cole, and R. H. Cole, "Dispersion and absorption in dielectrics I. Alternating current characteristics," *Journal of Chemical Physics,* vol. 9, no. 4, pp. 341-351, Apr, 1941.

[15] D. W. Davidson, and R. H. Cole, "Dielectric relaxation in glycerol, propylene glycol, and n-propanol.," *J Chem Phys,* vol. 19, pp. 1484-90, 1951.

[16] S. Havriliak, and S. Negami, "A Complex Plane Representation of Dielectric and Mechanical Relaxation Processes in Some Polymers," *Polymer,* vol. 8, no. 4, pp. 161-&, 1967.

[17] G. Williams, and D. C. Watts, "Non-symmetrical dielectric relaxation behaviour arising from a simple empirical decay function.," *Trans Faraday Soc,* vol. 66, pp. 80-91, 1970.

[18] R. M. Fuoss, and J. G. Kirkwood, "Electrical properties of solids. VIII. Dipole moments in polyvinyl chloride–diphenyl system.," *J Am Chem Soc,* vol. 63, pp. 385–94, 1941.

[19] A. K. Jonscher, "A New Model Of Dielectric Loss In Polymers.," *Colloid Polym Sci,* vol. 253, pp. 231-50, 1975.

[20] K. Asami, "Characterization of biological cells by dielectric spectroscopy," *Journal of Non-Crystalline Solids,* vol. 305, no. 1-3, pp. 268-277, Jul 1, 2002.

[21] T. Hanai, K. Asami, and S. Koizumi, "Dielectric Theory of concentrated suspensions of shell-spheres in particular reference to the analysis of biological cell suspensions," *Bull. Inst. Chem. Res.,* vol. 57, pp. 297-305, 1976.

[22] H. Z. Zhang, K. Sekine, T. Hanai *et al.*, "Dielectric Observations on Polystyrene Microcapsules and the Theoretical-Analysis with Reference to Interfacial Polarization," *Colloid and Polymer Science,* vol. 261, no. 5, pp. 381-389, 1983.

[23] N. G. Green, and H. Morgan, "Dielectrophoresis of submicrometer latex spheres. 1. Experimental results," *Journal of Physical Chemistry B,* vol. 103, no. 1, pp. 41-50, Jan 7, 1999.

[24] I. Ermolina, and H. Morgan, "The electrokinetic properties of latex particles: comparison of electrophoresis and dielectrophoresis," *Journal of Colloid and Interface Science,* vol. 285, no. 1, pp. 419-428, May 1, 2005.

[25] M. P. Hughes, and H. Morgan, "Dielectrophoretic characterization and separation of antibody coated submicrometer latex spheres," *Analytical Chemistry,* vol. 71, no. 16, pp. 3441-3445, Aug 15, 1999.

[26] K. L. Chan, H. Morgan, E. Morgan *et al.*, "Measurements of the dielectric properties of peripheral blood mononuclear cells and trophoblast cells using AC electrokinetic techniques," *Biochimica Et Biophysica Acta-Molecular Basis of Disease,* vol. 1500, no. 3, pp. 313-322, Mar 17, 2000.

[27] P. Gascoyne, R. Pethig, J. Satayavivad *et al.*, "Dielectrophoretic detection of changes in erythrocyte membranes following malarial infection," *Biochimica Et Biophysica Acta-Biomembranes,* vol. 1323, no. 2, pp. 240-252, Jan 31, 1997.

[28] W. M. Arnold, and U. Zimmerman, "Electro-rotation - development of a technique for dielectric measurements on individual cells and particles.," *J. Electrostatics,* vol. 21, pp. 151-191, 1988.

[29] M. Kriegmaier, M. Zimmermann, K. Wolf *et al.*, "Dielectric spectroscopy of Schizosaccharomyces pombe using electrorotation and electroorientation," *Bba-Gen Subjects*, 2001, pp. 135-146.

[30] R. D. Miller, T. B. Jones, "Electro-Orientation Of Ellipsoidal Erythrocytes - Theory And Experiment," *Biophysical Journal*, 1993, pp. 1588-1595.

[31] T. Jones, *Electromechanics of Particles*, New York: Cambridge University Press, 1995.

[32] T. B. Jones, "Basic theory of dielectrophoresis and electrorotation," *Ieee Eng Med Biol*, 2003, pp. 33-42.

[33] H. Ying, R. Holzel, R. Pethig *et al.*, "Differences in the Ac Electrodynamics of Viable and Nonviable Yeast-Cells Determined through Combined Dielectrophoresis and Electrorotation Studies," *Physics in Medicine and Biology,* vol. 37, no. 7, pp. 1499-1517, Jul, 1992.

[34] J. Gimsa, P. Marszalek, U. Loewe *et al.*, "Dielectrophoresis and Electrorotation of Neurospora Slime and Murine Myeloma Cells," *Biophysical Journal,* vol. 60, no. 4, pp. 749-760, Oct, 1991.

[35] X. B. Wang, R. Pethig, and T. B. Jones, "Relationship of Dielectrophoretic and Electrorotational Behavior Exhibited by Polarized Particles," *Journal of Physics D-Applied Physics,* vol. 25, no. 6, pp. 905-912, Jun 14, 1992.

Chapter 2 Literature Review

2.1 Introduction

In this chapter, recent progresses in the field of impedance spectroscopy of cells are reviewed. The advantages of single cell analysis are outlined. Papers on single cell impedance spectroscopy in the context of cytometry are discussed, followed by studies of cell cultures performed with electrode-cell-impedance sensors. Finally, contributions to single cell impedance spectroscopic techniques are reviewed, using both dielectrophoretic based measurements and direct impedance measurements.

2.2 Reviews

A comprehensive review on the topic of dielectric spectroscopy, not only of cells in suspensions, but of biological membranes and emulsions of particles is given by Asami [1]; theoretical analysis and measurement techniques for dielectric spectroscopy of biological cells in the radio frequency range are reviewed by the same author [2]. Kaatze and Feldman, reviewed the basic principles of dielectric spectroscopy and the methods in use to measure the dielectric properties of liquid samples over the frequency range from about 10^{-6} Hz to 10^{12} Hz [3]. The approaches described include frequency domain and time domain techniques, low frequency, high frequency and microwave measurement systems, as well as broadband and spot-frequency modes of operation. Feldman and co-authors presented the principles of time domain dielectric spectroscopy and its application to biological systems including globular and membrane proteins, hydrate water, human erythrocytes, and normal and malignant blood cells of different types [4]. Markx and Davey reviewed techniques and methods for the study of the dielectric properties of cells in the radiofrequencies [5]. Most recently Yi et al. reviewed microfluidics technology for manipulation and analysis of biological cells including impedance spectroscopy and impedance-based flow cytometry [6]. Also of note is the 2008 review by Bao et al where the authors introduce the recent advances in the electric analysis of cells on a microfluidic platform, encompassing both DC (patch clamp) and AC (impedance) methods [7].

2.3 Impedance spectroscopy of cells in suspension

Impedance spectroscopy of cells in bulk has been studied for many years. In principle a simple measurement setup can be used (Figure 2-1): An impedance analyzer is connected to two electrodes immersed in a measurement chamber filled with a suspension of cells.

Data on red blood cells are numerous, as their structure makes the polarization response easy to model – although with some error due their prolate ellipsoidal shape- using the shelled model (as discussed in Chapter 1). Lu et al. measured the dielectric properties of human red blood cells (RBCs) in suspension (volume fraction 50%) correlating dielectric parameters to the age of the patients [8].

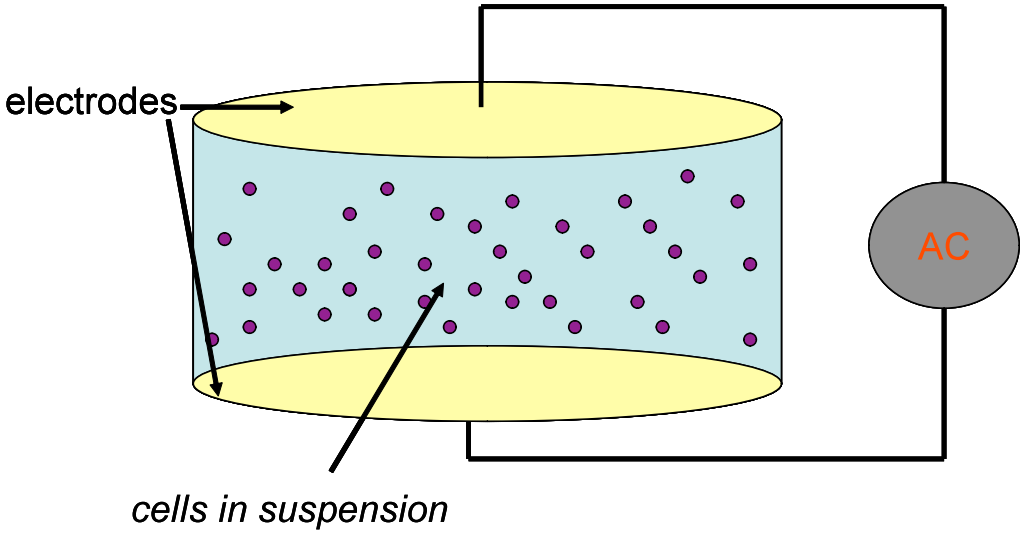

Figure 2-1. Example of system for performing impedance analysis of cells in suspension. Two flat parallel metal electrodes separated by a uniform distance, encompass a known volume of suspending liquid and cells under study. In this example two electrodes are used to measure the response to an AC signal. More sophisticated arrangements involve the use of three or four electrodes to reduce the effects of an ionic double layer on the measuring electrodes.

The dielectric properties of human erythrocytes (red blood cells) suspended in whole blood and in isotonic media at various volume fractions (hematocrit) have been studied in the frequency range 0.2-10 MHz by Beving et al. [9]. Treo et al. presented a method to measure hematocrit in extracorporeal blood systems [10]. They show a high correlation coefficient between measured dielectric decrement and hematocrit level. Di Biasio et al. compare two different models to describe erythrocyte cells: a shelled ellipsoidal particle and a biconcave disk obtained by the revolution of the Cassini oval. They conclude that the use of an ellipsoidal model analysis is essentially accurate [11].

Kaneko compared two dielectric mixture equations, the Pauly-Schwan (P-S) equation and the Hanai-Asami-Koizumi (H-A-K) equation using sheep erythrocyte ghosts whose internal solution is identical with the external solution [12]. It was concluded that the H-A-K equation is applicable to a wider range of volume fraction (up to 0.7) than is the P-S equation (up to 0.3).

There is also a keen interest in studying white blood cells (granulocytes: neutrophils, basophils, and eosinophils; agranulocytes: lymphocytes and monocytes) and their response to drugs. The permittivity and conductivity of mouse lymphocytes and erythrocytes were measured over a frequency range from 0.1 to 250 MHz [13]. Analysis of the lymphocyte dispersion was carried out using a double-shell model while erythrocytes (spherocytes) showed a single dielectric dispersion, which was explained with a single-shell model. Ermolina et al. showed that dielectric permittivity, capacitance and conductivity values of the cell membrane are higher for normal lymphocytes in comparison with malignant ones [14].

Other type of cells have been studied by impedance spectroscopy: A dielectric method for real-time monitoring of yeast cell cycle progression in synchronized cell culture was presented by Asami [15],[16]. The same author measured the relative permittivity and conductivity of the mesophyll protoplasts over a frequency range from 1 kHz to 500 MHz [17]. These protoplasts showed a broad dielectric dispersion, composed of three sub-dispersions assigned to the Maxwell-Wagner process; the plasma membrane, the tonoplast, and the membranes of cytoplasmic organelles (e.g., chloroplasts, granules, etc).

2.4 Single cell analysis

There are important advantages to analyzing the response of single cells instead of a population of millions of cells: these have been outlined in recent reviews by Lindstrom and Meldrum [18] and Di Carlo and Lee [19]. By their very nature, bulk experiments average out the temporal distribution of cell responses, obscuring any individual molecular and cellular behaviour. There are other advantages to single cell measurements: in bulk cultures it can be necessary to concentrate cells, so the results observed could be measurements of the cellular response to the concentration process. In the case of the study of infection of mammalian cells, bulk experiments again reveal the limits of temporal and spatial averaging. Because the infection process does not necessarily affect all cells at once, cells found at different stages of infection will undergo different physiological changes. Such changes might be erroneously measured in an ensemble, as different level of gene expressions will be averaged in a bulk measurement. Additionally, non-standard distribution of events (for example double Gaussian peaks) would be averaged by bulk analyses and not correctly represented.

Impedance spectroscopy at the single cell level has been done using flow cytometers, and in some cases for adherent cell cultures using electrode-cell impedance (or ECIS). ECIS studies focus on changes in the electrode-cell interaction rather than the analysis of the cellular dielectric parameters *per se*. Also dielectrophoretic techniques like DEP and ROT have been used to extrapolate dielectric parameters from cell motion induced by electric forces. A more novel approach, and one that is used in the development of the work described in chapter 3 of this thesis, is direct measurement of the impedance spectrum of single cells.

2.5 Impedance-based cytometry

Cytometers are devices designed for the sequentially analysis of single cells. Impedance-based cytometers do not measure an entire spectrum of frequencies; rather, impedance is measured at one or two frequencies as the cells pass by a sensing element in a microchannel. Already fifty years ago, W.H. Coulter proposed a device that would measure the number and size of particles suspended in an electrolyte by passing them one-by-one through a small orifice, by detecting the change in electrical impedance at low frequency between a pair of electrodes placed at either side of the orifice [20]. Twenty-five years later, Hoffman et al. [21-24] devised a cytometer to detect simultaneously the low and high frequency impedance changes produced by biological cells or particles suspended in saline traversing through a sensing orifice, thus allowing discrimination of the electrical properties of the plasma membrane and intracellular structures. More recently, Cheung, Gawad and colleagues, developed their cytometer using the same concept [25-28]. The authors describe a device that measures differential impedance at two frequencies (602 kHz and 10 MHz) and achieve differentiation of fixed RBCs and RBCs using opacity (ratio of high frequency to low frequency impedance), while RBCs and ghosts were differentiated using phase information (Figure 2-2).

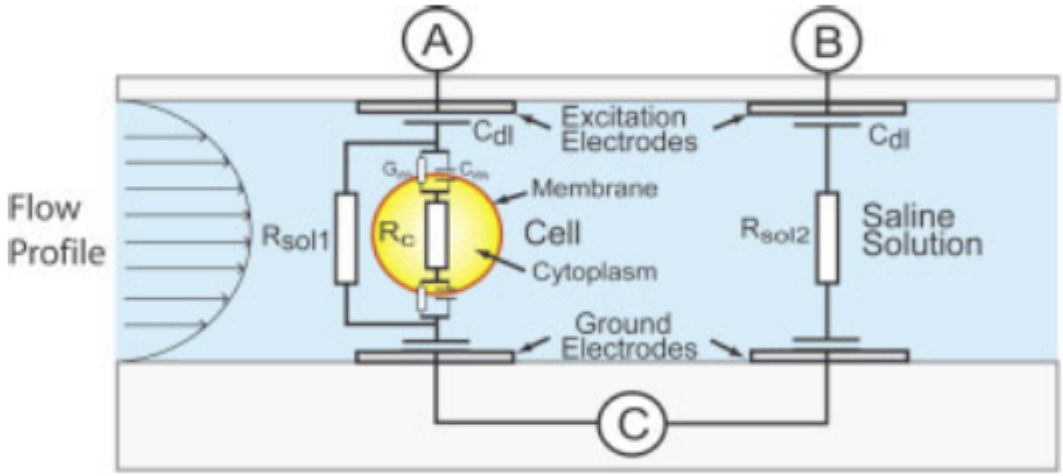

Figure 2-2. Side view of the microfluidic channel showing a cell passing between the measurement and reference electrodes, taken from [25]. Gawad et al. use two pairs of electrodes for measuring differential impedance at two separate frequencies. This cytometer was proven to differentiate different cell sizes, membrane capacitances, and cytoplasm conductivities.

Chun et al. used a microchip device that can size-selectively count microparticles and measure their velocities by using DC-driven electrical detection [29]. The authors demonstrated the ability to discriminate between red and white blood cells, as well as differently sized beads.

Morgan and colleagues designed and fabricated a microflow cytometer to perform differential impedance spectroscopy, similarly to Gawad's device, but also added the capability to simultaneously interrogate the optical properties of the cells, demonstrating that the acquisition of optical and dielectric can be used to uniquely identify rare particles or cells in a larger population [30].

An interesting development has been described by Sun and co-workers [31], whereby the same cytometric platform employed by Cheung and Gawad is used in conjunction with a novel spectroscopic technique that allows 512 evenly distributed frequencies over a range from 976.5625 Hz to 500 kHz to be measured in 1ms. The technique – Maximum Length Sequence (or MLS) processing - quite popular in the digital signal and audio processing environment, is described in detail in [32-34]. Briefly, white noise in the form of a digitally generated pseudo-random electric signal is injected into the measuring chamber (the micro-channel in this case), and the spectral response is recorded. The technique consists of cross-correlating the input sequence to the output response to obtain the transfer function of the system. Although still in its infancy, and thus far limited in the frequency range to 500 kHz, this is a very promising technique which addresses an important limitation of flow-cytometers, i.e. the ability to acquire full spectral information for each streaming cell.

2.6 Electrode-Cell Impedance Spectroscopy

An important limitation of cytometry is that the transient behaviour of cells cannot be studied. This is addressed by a technique known as ECIS (electrode-cell impedance spectrometry), invented by Keese and Giaever [35, 36]. A confluent layer of cells is cultured on sensing metal electrodes (Figure 2-3). A small AC voltage (usually <100 mV) is then applied between the sensing electrode and a larger counter electrode immersed in the cell culture medium, and the electrical impedance is measured. The device can continuously track morphological changes of adherent cells providing quantitative data. The method is capable of detecting vertical motion of cells of the order of 1 nm, much below the resolution of an optical microscope.

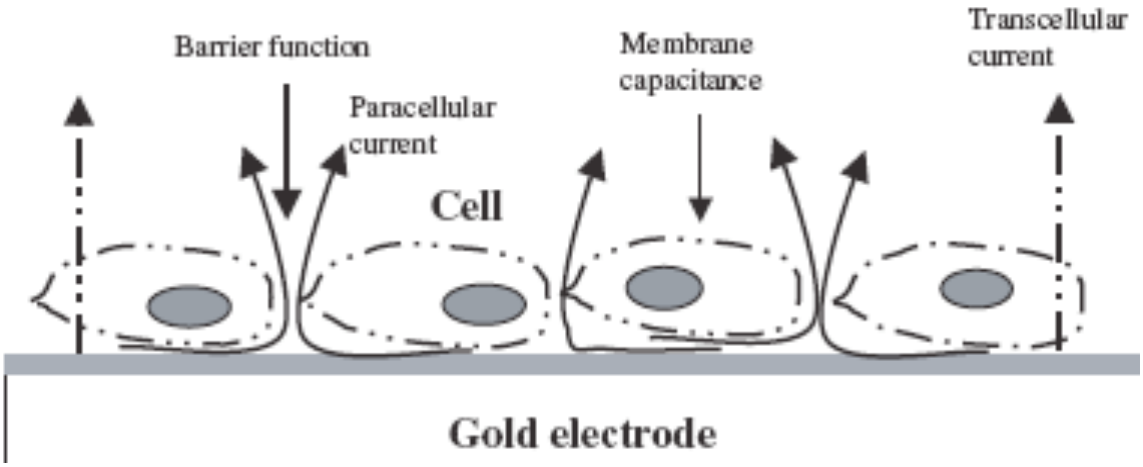

Figure 2-3. The basic operating principle of ECIS is illustrated. Cells adhering to the sensing electrode physically impede the flow of low frequency AC current. As the excitation frequency is increased the cellular membrane is shorted and trans-cellular current starts to flow. Taken from [36].

ECIS has been used to study the kinetics of BALB/3T3 cell adhesion and the cellular responses to a toxic product as a function of time [37]. Concentrations of sodium arsenite, ranging from 10 μM up to 1000 μM were tested in the system, and the results were compared with those obtained with standard protocols used to study basal cytotoxicity induced by chemicals in the BALB/3T3 cell line. The authors concluded that impedance spectroscopy could be successfully used as an alternative method for cytotoxicity assessment of chemicals. Matsue et al. describe recent progress in cell-based electrochemical biosensors [38], especially focusing on the incorporation of micro-fabrication technology and gene-modified engineering. Yeon et al. presented the

use of ECIS to monitor cell growth as a consequence of treatment with potentially cytotoxic agents [39] (Figure 2-4). Human hepatocellular carcinoma cell (HepG2) is adapted to cytotoxicity test using the cell chip. The cells in the stationary phase after plating are used for the cytotoxicity experiment and the impedance is decreased after treatments with several toxicants, such as tamoxifen and menadione, leading to the detachment of dead cells. These results reveal that the microfabricated cell chip system provides an easy real-time monitoring method for cytotoxicity test. Solly et al. have shown that impedance readings of cell proliferation, cytotoxicity, cytoprotection, cell growth inhibition, and apoptosis are well correlated with data determined by the classic methods [40].

De Blasio et al. described an ECIS sensor modified to allow simultaneous microscopic recording of both growth and motility [41], thus enabling cell confluence on the electrodes to be systematically correlated to the impedance in regular time intervals of seconds and for extended periods of time. The authors followed the attachment and spreading behaviour of epithelial Madin-Darby canine kidney strain I (MDCK-I) cell cultures on microelectrodes for up to 40 hr. The studies reveal a high degree of correlation between the measured resistance at 4 kHz and the corresponding cell confluence in 4- to 6-h intervals. Arndt et al. used ECIS to monitor the apoptosis-induced changes with a time resolution in the order of minutes [42].

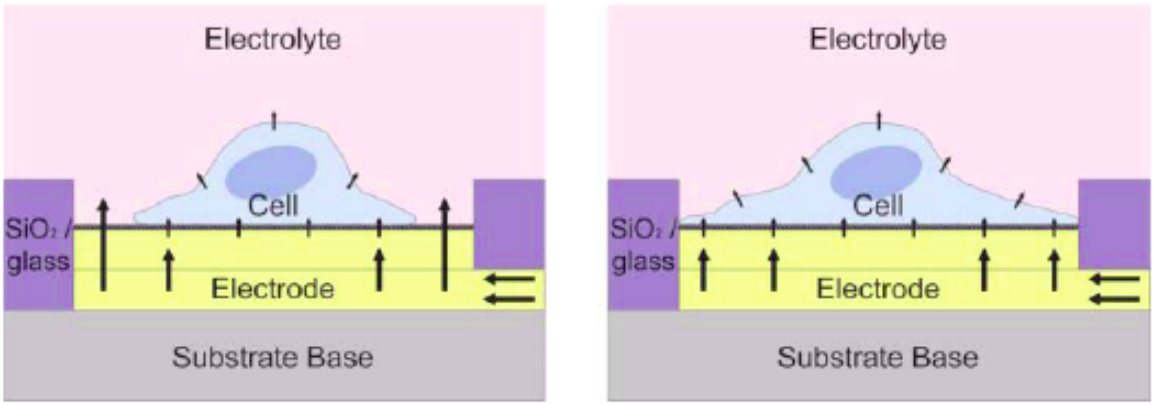

Figure 2-4 Morphological changes in a cell are sensed by measuring changes in cell-electrode impedance: when a cell only partially covers the electrode surface (left), the current passes through the least resistive path between the electrode and electrolyte; once a cell fully spreads across the electrode (right). Taken from [43].

McCoy et al. postulated that since cytopathic effect due to viral infection is typically characterized by a rounded cell morphology and detachment from the surface of the culture dish, ECIS would be useful in quantifying the level of cytopathic effect

due to viral infection [44]. Indeed their experiments confirm that following cell patterning and infection by the influenza virus, the signal impedance from the cell monolayer was reduced in a dose-dependent manner. Furthermore upon pre-treatment with ammonium chloride (NH_4Cl), which inhibits virus entry into the cell the reduction in signal impedance due to influenza infection, was abolished.

Luong has reviewed the uses of ECIS [45-47]. It is notable that even sub-nanometer changes in the distance between the electrode and the ventral surface of the cell significantly affects the measured impedance and can be detected by ECIS thus allowing the detection of cell motion beyond the resolution of an optical microscope. Hug suggests that the initial changes in measured impedance are associated with cell attachment and spreading, whereas after 10 hours, the formation of tight cell-cell contacts is responsible for changes [48]. Furthermore he suggests that the activation of G-protein coupled receptors, which change the level of the second messengers such as cAMP, [Ca21], NO, protein-kinase C, or InsP3, results in cytoskeletal activities (hence cellular motion) that can be detected by ECIS. Rothermel et al., offer an example of impedance measurement of cellular alterations in real-time [49]: a breast carcinoma cell line (MCF-7) was cultured, and cellular alterations were measured by impedance spectroscopy at a frequency ranging from 10 Hz to 1 MHz. Atienza et al. used impedance to quantitatively assess growth factor-induced morphological changes in real time and used this as a measure of RTK activity [50]: COS7 cells treated with epidermal growth factor (EGF) and insulin exhibited a rapid increase in cell impedance. These impedance changes correlated well with an enzyme-linked immunosorbent assay. The same authors showed that cell adhesion on ECM-coated cell sensor arrays is dependent on the concentration of ECM proteins coated and is inhibited by agents that disrupt the interaction of ECM with cell surface receptors [51]. Cell-electrode impedance has been used to measure minute changes in cellular morphology as a result of ligand-dependent GPCR activation (G protein-coupled receptors) by means of pharmacological modulators of GPCR signalling pathways [52]. Keese et al. deliberately disrupted a layer of cultured cells subjecting it to large currents, in a wound-healing assay: the electrode-cell impedance was monitored to chart the migration and ultimate healing of the wound [53].

2.7 Dielectrophoresis and electrorotation to analyze cells

While impedance spectroscopy directly measures the electrical response to an applied field, from the resulting current intensity and phase displacement, dielectrophoresis (DEP) and electrorotation (abbreviated in the literature as ER or ROT) analyze the frequency dependence of motion (translation and rotation) of single particles in an inhomogeneous and rotating external field, respectively (see Figure 2-5 (a) and (b)).

The first example of electrorotation of a single cell is described by Arnold and Zimmermann [54]. Pethig reviews the principles of dielectrophoretic separation of mixtures of bacteria, viable and unviable cells, cancerous and normal cells, and red and white blood cells ([55] and [56]). Broche et al explain how to extract useful data from the dielectrophoretic collection spectrum, in particular for the cytoplasm, and hence determine the properties of multiple populations of cells within a sample [57]. Gimsa et al were able to measure the dielectric properties of human red blood cells in the frequency range from 2 kHz to 200 MHz at physiological ion concentrations [58] and furthermore showed that they could follow changes of dielectric properties on individual red blood cells, after nystatin application [59]. Wang et al. interpreted shifts in the cellular dielectrophoretic crossover frequencies on pro-myelocytic HL-60 cells following treatment with genistein (GEN) to deduce changes in membrane capacitance and conductivity[60].

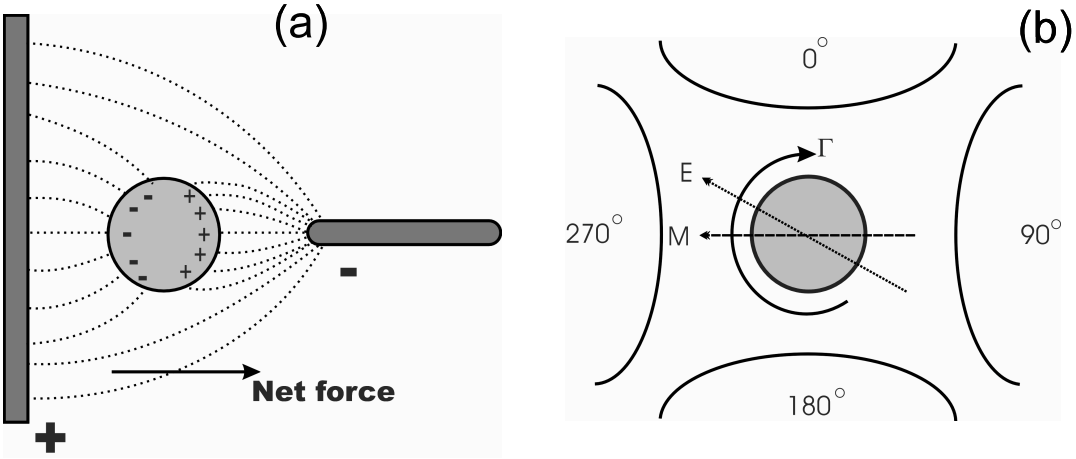

Figure 2-5 (a). Schematic diagram of a polarisable particle suspended in an inhomogeneous electric field: the force is greater in the side facing the point than that on the side facing the

plane, and there is net motion towards the point electrode, where the field is stronger; This effect is called positive dielectrophoresis. If the particle is less polarisable than the surrounding medium, the dipole will align counter to the field and the particle will be repelled from the high field regions; this effect is called negative dielectrophoresis. (b): a schematic of a polarisable particle suspended in a rotating electric field generated by four electrodes with 90° advancing phase. If the field rotates sufficiently quickly, the induced dipole M will lag behind the electric field. The interaction between E and M induces a torque Γ in the particle, causing it to rotate. This effect is known as electrorotation. Taken from [61].

Flanagan et al used DEP to differentiate stem cells and their differentiated progeny. By discriminating NSPCs (neural stem precursor cells) at developmental ages at which they are more likely to generate neurons or astrocytes, the authors were able to show that cellular dielectric properties are effectively markers reflecting their fate bias [62].

Chan et al. measured the dielectric properties of trophoblast cells and mixed peripheral blood mononuclear cells using dielectrophoretic crossover and single cell electrorotation methods [63]. Gascoyne measured the dielectric characteristics of the four main leukocyte subpopulations, namely, B- and T-lymphocytes, monocytes, and granulocytes, by electrorotation over the frequency range 1 kHz to 120 MHz [64]. Mean specific membrane capacitance values were calculated from the electrorotation data adopting a single-shell dielectric model.

Electrorotation has been used successfully to discriminate cancerous cells from populations of healthy cells. Becker et al used electrorotation measurements to demonstrate that the dielectric properties of the metastatic human breast cancer cell line MDA231 were significantly different from those of erythrocytes and T lymphocytes [65]. Cheng et al discriminated metastatic human cervical carcinoma cell line (HeLa cells) from normal human peripheral cells by using inhomogeneous AC fields to create conditions for dielectrophoretic separation of cells [66]. More recently Cristofanilli et al. have reiterated the need for techniques to effectively isolate single cells from a heterogeneous population and have shown that ROT-spectra can be used to find variations in breast cancer cell lines over-expressing p185 transfectants [67].

Archer and colleagues measured the dielectric properties of baby hamster kidney fibroblast (BHK(C-13)) cells before and after infection with herpes simplex virus type 1 (HSV-1) using electrorotation: the membrane capacitance was found to decrease as

the infection progressed, a trend attributed to changes in the cell membrane morphology. [68, 69]

Successful attempts at automating some steps in the electrorotation analysis process have been made. Zhou et al. demonstrated a system to record rotation responses of up to 20 yeast cell at once, using near real-time computer image processing [70]. De Gasperis et al., present an automated system equipped with a computer-controlled quadrature digital synthesizer capable of measuring a ROT spectrum of a single cell with the frequency range 1 kHz-200 MHz in less than 5 min [71]. Laser tweezers are used to facilitate cell selection and positioning in order to maximize the flexibility and accuracy of the system. Gimsa et al. used dynamic light scattering measurements to measure electrorotation spectra combined with electro-orientation, providing information about the dielectric and conductive properties of red blood cells ([72],[73]).

Recently Morgan et al [74] discussed and compared dielectrophoresis, electrorotation and impedance analysis as methods for dielectric spectroscopy of single cells, proposing an impedance-based flow cytometer as a tool for the high speed measurement of dielectric parameters of single cells, a technique discussed in detail in the next section.

2.8 Impedance analysis of trapped single cells

Direct measurement of impedance spectra of cells presents significant challenges in microfabrication of electrodes, design of microfluidic channels and cavities to capture cells, and successful integration with macroscopic components. For these reasons, very few working devices have been proposed yet.

In 1999, Ayliffe et al. produced a microfabricated impedance measurement systems capable of measuring femtoliter volumes of liquids flowing through a channel of 10 μm width and 4μm height. Planar gold strips electroplated on either side of the channel functioned as microelectrodes. The microdevice was connected to a commercially available impedance analyzer to acquire spectra from RBC's obtained from a teleost fish. Impedance spectra were measured over the frequency range from 100 Hz to 2MHz, while each cell, flowing in a bathing the solution was kept stationary in the recording zone via control of the bulk flow with pressure [75]. The system, although novel, has important shortcomings: a high degree of variability in impedance response from different devices required that each device be calibrated prior to use, and the inability to array the electrodes, capture the cells under study and the lack of a reference electrodes to normalize for local conductivity changes in the medium.

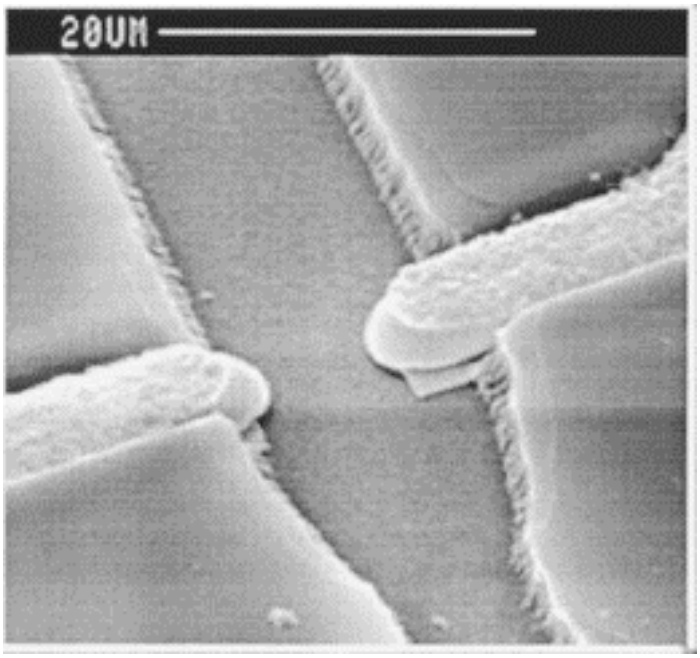

Figure 2-6 SEM of a microchannel with integrated gold electrodes prior to coverslip bonding, from Ayliffe [115].

Cho et al. in 2006 described a silicon-based microdevice for measuring the electrical impedance of a single cell [76]. In this work it was shown that impedance measurements measured (over the range 10 Hz to 100 kHz) on single cells could be used to discriminate normal red blood cells, from red blood cells whose membrane was hardened by alcohol treatment. The device fabrication was complicated (a 7 mask process) by the implementation of micro-cantilever electrodes.

Han et al. used a cell-capturing cavity with integrated opposing electrodes (Figure 2-7) to measure the electrical impedances of human breast cancer cell lines claiming the capability not only to distinguish cancer cells from normal cells, but also to distinguish cancer cells of different pathological stages (MCF-7, MDA-MB-231 and MDA-MB-435) [77]. However, the data presented is rather dubious as the differences between cells are large (one or more order of magnitude differences were found) and most likely cause by heterogeneity of the signal response from cavity to cavity on the device. As in the case of many impedance-based systems, the lack of a differential setup hampers the reliability of the acquired data.

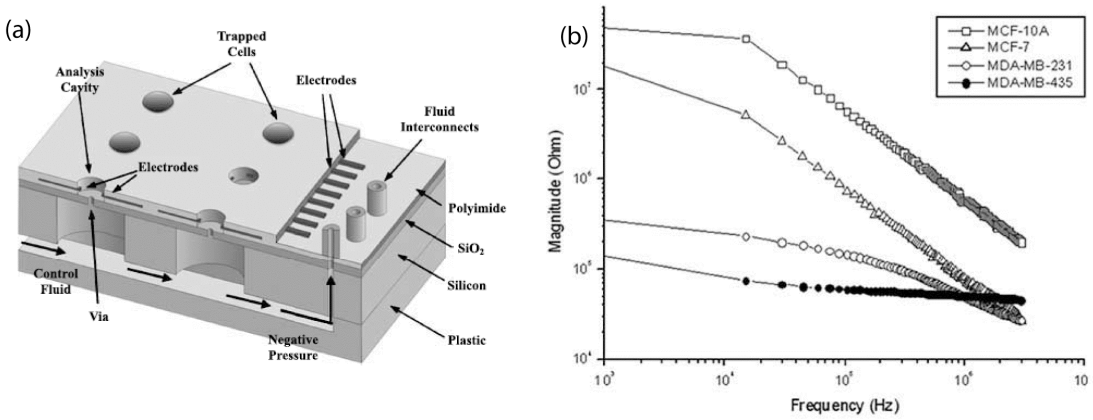

Figure 2-7(a). Example of a device for capture and measurement of the impedance of single cells. The system consists of an eight-element array of analysis cavities, or traps. Cell capture, hold, and release steps are enabled via the application of negative pressure through a backside microchannel. Pairs of opposing electrodes measure the electrical characteristic of the trapped cells. (b) Impedance spectra acquired from cancer cells of different stages. Taken from [72].

The same authors used this platform to trap single cells and measure ion-channel activation: K^+ and Ca_2^+ channels were blocked on some cells and their electrical impedances were measured over a frequency range of 100 Hz to 5.0 MHz and compared to that of unblocked cells [78]. The system was found to be insensitive to ion channel activities, such as how much certain compounds block the ion channels but could still be used to provide positive/negative information of ion channel blockage.

James et al. employed a silicon microdevice, originally engineered for planar patch clamp of cells, to perform long-term impedance spectroscopic monitoring of cells trapped on top of a micropore by the application of negative pressure [79]. They measured changes to macrophages challenged by the introduction of LPS (lipopolysaccharide, an immunostimulant), but the absence of a reference measurement system makes it difficult to prove that the impedance changes were unequivocally attributable to the trapped cells rather than the changes in the bathing medium.

There is no existing device with the ability to capture single cells and perform transient impedance analyses, with differential, parallel plate electrode arrangement, combined with the ability to multiplex the signal from multiple trapping sites. Such a system is introduced in chapter 3 of this thesis.

2.9 Trapping single cells

As mentioned in previous sections, single cell behaviour can be observed using flow cytometry, which traditionally allow the study of single cells that have been previously labelled using fluorescent dyes as these stream serially through a light source, filtering mechanism, and detectors [80]. The technique is a very high throughput serial process, however it is limited in most cases to characterizing fluorescent signals and it does not address time dependent measurements of the same individual cell. As discussed in section 2.5, impedance based flow cytometry devices have been engineered, which trough electrical characterization allow measurement of membrane structure, DNA content, and cell size that may be complementary to optical based analyses.

Cytometers however cannot by their nature address the inability to observe variations in a single cell, which occur over time. Trapping structures need to be incorporated in a device to capture or immobilize every single cell that needs to be observed.

Wheeler et al in 2003 demonstrated a physical structure where a single cell is routed and trapped via hydrostatic pressure while a stream of buffer is focused on it, thus allowing continuous observation while a reagent of interest is perfused [81].

An alternative approach to creating an enclosed chamber surrounding individual cells was proposed by Irimia and coworkers in 2004: using the geometry of fabricated microchannels and the coordinated action of four on-chip thermopneumatic actuators, virtual walls could be formed by liquid-air interfaces which allowed independent isolation of cells and analyte volumes [82].

Ionescu-Zanetti et al [83] have demonstrated a microfluidic platform in which electrophysiological measurements on an array of trapped cells can be performed while optical access is maintained and solutions can be quickly exchanged. The method of single-cell isolation is based on producing microfluidic channels to mimic the glass pipette of traditional patch clamp methods. Similar techniques were also used by Hung et al. to isolate individual cells for electroporation or gap-junctional communication studies [84].

To study large quantities of cells it is often convenient to use arraying techniques, although the ability to perform fast timescale measurements is traded off for the benefit of massive parallelization. Microfabricated or micro-molded wells sized to fit single cells are the simplest and most commonly reported single-cell trapping structures [85-88]: cells are seeded on the pre-filled well array and allowed to settle into wells of comparable size. After settling, the remaining cells, not constrained by the well are flushed away leaving a distribution of single cells remaining in individual wells. These types of structures are quite useful in high throughput fluorescent based analysis of individual cells, as image processing is significantly simplified when compared to cells grown in a Petri dish.

Slight variations of these arraying techniques are based on chemical patterning of surfaces alone with no mechanical confinement. This is usually accomplished by stamping of cell adhesion proteins onto a surface [89-91].

Yet another variation consists in achieving single cell immobilization based on ssDNA recognition: cells are bioengineered to contain a known ssDNA coating on their surface, complementary to strands immobilized at known locations in a microfluidic device so that cells can be localized to the known locations [92].

Dielectrophoretic manipulation techniques of single cells have also been demonstrated for constructing arrays of single cells for high throughput experimentation. Chiou et al. developed an optically controlled electronic substrate that allows on-the-fly reconfiguration of electrodes for dielectrophoretic movement of particles. However the solutions used in their experiments are below physiological levels and may lead to aberrant behaviour in cell studies [93]. Similarly, Voldman and coworkers have demonstrated that arrays of single cells and particles can be assembled and individually addressed. An advantage of this technique is cells of particular interest may be isolated and removed for further analysis. Additionally, by maintaining single cells trapped during microfluidic introduction of reagents, fast timescale responses may be investigated [94-98].

The trapping mechanism presented in this thesis is based on the work performed by Di Carlo and colleagues, who developed a comprehensive technology in which high density regular arrays of single cells are isolated in a purely hydrodynamic fashion in U-shaped weirs within a microfluidic device [99]. In Di Carlo's design single cells are isolated in regular high-density arrays composed of two channel height levels. The larger 40 μm channel height served as the main fluid conduits for cell solutions, while

the 2 μm height regions were used to form elevated trapping regions (Figure 2-8(a)). Having a 2 μm gap allows a fraction of fluid streamlines carrying cells to enter a trap. Once a cell enters a trap and partially occludes the 2 mm gap the fraction of fluid streamlines (and cells) entering the trap region is reduced (Figure 2-8(b)). This leads to a high quantity of single cell isolates (Figure 2-8(c)). In effect the probability of trapping is dependent on the number of cells previously trapped. This is shown statistically, by comparing a Poisson distribution to the experimentally measured distribution: if trapping were independent of the previous trapping events the data should follow a Poisson distribution. Instead single cells are shown in excess of the Poisson distribution while zero, three, and four trapped cells are depressed.

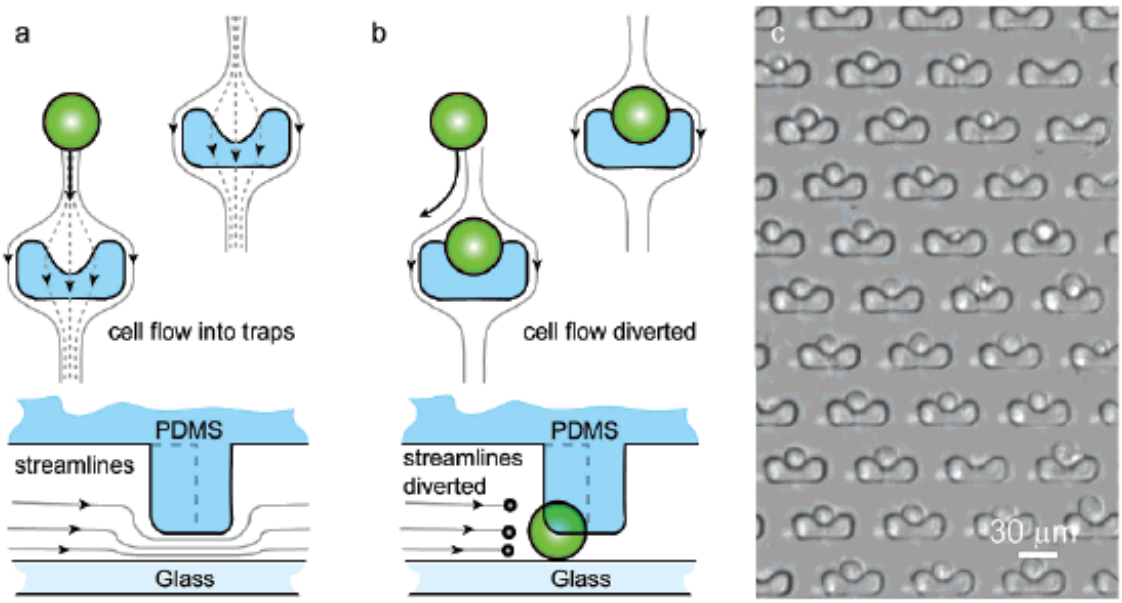

Figure 2-8 Taken from [99]. A schematic diagram is shown to describe the mechanism of cell trapping using flow through arrayed suspended obstacles. Two-layer (40 μm and 2 μm) cup-shaped PDMS trapping sites allow a fraction of fluid streamlines to enter the traps. After a cell is trapped and partially occludes the 2 μm open region, the fraction of streamlines through the barred trap decreases, leading to the self-sealing quality of the traps and a high quantity of single cell isolates. Drawing is not to scale. (c) A phase-contrast image of an array of single trapped cells is shown. The scale bar is 30 μm.

.

2.10 Conclusions

Impedance spectroscopy is a well established method for label free study of cellular and biomolecular structures. It has been successfully employed as a technique to study cellular characteristics since the beginning of the 20th century. Developments in fabrication techniques have provided microfluidic structures through which it has become possible to manipulate and analyse single cells. Consequently there has been a renewed interest in impedance spectroscopy as a method for single analysis.

Techniques such as electrorotation and dielectrophoresis have been employed successfully to measure the dielectric parameters of single cells. However these methods require optical observation of the cell. Impedance spectroscopy of single cells, a truly all-electrical technique, was first demonstrated by Ayliffe in 1999, and similar devices were subsequently engineered by Frazier and others.

Important development were reported by Gawad and coworkers, and Holmes et al. with an impedance based microflow cytometer which for the first time employed a differential setup and a parallel-plate electrodes arrangement. The device cannot perform spectroscopy, as only two frequencies are measured for each cell. This limitation has been addressed by Tao and co-workers in 2007 by employing pseudo-random maximum length sequences as excitation signals to obtain a full spectral response from each cell.

While whole-cell impedance analysis as a technique cannot compete with patch-clamp in terms of sensitivity and selectivity, impedance-based sensors offer important advantages in high throughput potential as well as in the possibilities for multiplexing, scalability and miniaturization. Yet, after decades of research effort and hundreds of publications, no commercial product based on label-free impedance-based biosensors has enjoyed widespread commercial success. Arguably, one of the biggest limitations of (almost all) the existing devices is the lack of a differential setup to normalize the measured response to the changes in temperature, pH and ionic content in the medium. Furthermore, data on reproducibility is seldom presented (ideally coefficient of variance of multiple experiments performed on different days using different sensors), and generally little attention is given to the non-specific response of the sensors.

In the future, impedance spectroscopy could be a technique that, while not displacing or directly competing with more sensitive electrical techniques such as patch-clamp, could gain traction as complementary to imaging methods.

Exploiting key attributes such as low cost, small size, low power, simplified sample preparation, and multiplexing capability, impedance based sensors could be competitive in fields such as point of care diagnostic devices.

References

[1] K. Asami, "Characterization of heterogeneous systems by dielectric spectroscopy," *Progress in Polymer Science,* vol. 27, no. 8, pp. 1617-1659, Oct, 2002.

[2] K. Asami, "Characterization of biological cells by dielectric spectroscopy," *Journal of Non-Crystalline Solids,* vol. 305, no. 1-3, pp. 268-277, Jul 1, 2002.

[3] *Measurement Science & Technology,* Title 17, Public Law No. 2, *Broadband dielectric spectrometry of liquids and biosystems*, 2006, pp. R17-R35.

[4] Y. Feldman, I. Ermolina, and Y. Hayashi, "Time domain dielectric spectroscopy study of biological systems," *Ieee Transactions on Dielectrics and Electrical Insulation,* vol. 10, no. 5, pp. 728-753, Oct, 2003.

[5] G. H. Markx, and C. L. Davey, "The dielectric properties of biological cells at radiofrequencies: Applications in biotechnology," *Enzyme and Microbial Technology,* vol. 25, no. 3-5, pp. 161-171, Aug, 1999.

[6] C. Yi, C.-W. Li, S. Ji *et al.*, "Microfluidics technology for manipulation and analysis of biological cells," *Analytica Chimica Acta,* vol. 560, no. 1-2, pp. 1-23, 2006/2/23, 2006.

[7] N. Bao, J. Wang, and C. Lu, "Recent advances in electric analysis of cells in microfluidic systems," *Anal Bioanal Chem*, Mar 12, 2008.

[8] Y. J. Lu, J. Yu, and Y. H. Ren, "Dielectric-Properties of Human Red-Blood-Cells in Suspension at Radio Frequencies," *Bioelectromagnetics,* vol. 15, no. 6, pp. 589-591, 1994.

[9] H. Beving, L. E. G. Eriksson, C. L. Davey *et al.*, "Dielectric-Properties of Human Blood and Erythrocytes at Radio Frequencies (0.2-10-Mhz) - Dependence on Cell-Volume Fraction and Medium Composition," *European Biophysics Journal with Biophysics Letters,* vol. 23, no. 3, pp. 207-215, Aug, 1994.

[10] E. F. Treo, C. J. Felice, M. C. Tirado *et al.*, "Hematocrit measurement by dielectric spectroscopy," *IEEE Transactions on Biomedical Engineering,* vol. 52, no. 1, pp. 124-127, Jan, 2005.

[11] A. Di Biasio, and C. Cametti, "Effect of the shape of human erythrocytes on the evaluation of the passive electrical properties of the cell membrane," *Bioelectrochemistry,* vol. 65, no. 2, pp. 163-169, Feb, 2005.

[12] H. Kaneko, K. Asami, and T. Hanai, "Dielectric Analysis of Sheep Erythrocyte Ghost - Examination of Applicability of Dielectric Mixture Equations," *Colloid and Polymer Science,* vol. 269, no. 10, pp. 1039-1044, Oct, 1991.

[13] K. Asami, Y. Takahashi, and S. Takashima, "Dielectric properties of mouse lymphocytes and erythrocytes," *Biochimica et Biophysica Acta (BBA) - Molecular Cell Research,* vol. 1010, no. 1, pp. 49-55, 1989/1/17, 1989.

[14] I. Ermolina, Y. Polevaya, and Y. Feldman, "Study of normal and malignant white blood cells by time domain dielectric spectroscopy," *Ieee Transactions on Dielectrics and Electrical Insulation,* vol. 8, no. 2, pp. 253-261, Apr, 2001.

[15] K. Asami, K. Takahashi, and K. Shirahige, "Progression of cell cycle monitored by dielectric spectroscopy and flow-cytometric analysis of DNA content," *Yeast,* vol. 16, no. 15, pp. 1359-1363, Nov, 2000.

[16] K. Asami, E. Gheorghiu, and T. Yonezawa, "Real-time monitoring of yeast cell division by dielectric spectroscopy," *Biophysical Journal,* vol. 76, no. 6, pp. 3345-3348, Jun, 1999.
[17] K. Asami, and T. Yamaguchi, "Dielectric-Spectroscopy of Plant-Protoplasts," *Biophysical Journal,* vol. 63, no. 6, pp. 1493-1499, Dec, 1992.
[18] M. E. Lidstrom, and D. R. Meldrum, "Life-on-a-chip," *Nature Reviews Microbiology,* vol. 1, no. 2, pp. 158-164, Nov, 2003.
[19] D. Di Carlo, and L. P. Lee, "Dynamic Single-Cell Analysis for Quantitative Biology," *Analytical Chemistry,* vol. 78, no. 23, pp. 7918 - 7925, 2006.
[20] W. H. Coulter, "High speed automatic blood cell counter and cell size analyzer," *Proc Natl Electron Conf,* vol. 12, pp. 1034, 1956.
[21] R. A. Hoffman, T. S. Johnson, and W. B. Britt, "Flow Cytometric Electronic Direct-Current Volume and Radiofrequency Impedance Measurements of Single Cells and Particles," *Cytometry,* vol. 1, no. 6, pp. 377-384, 1981.
[22] R. A. Hoffman, and D. E. Swartzendruber, "Electrical-Impedance Analysis of Single Murine Teratocarcinoma Cells," *Experimental Cell Research,* vol. 122, no. 2, pp. 426-429, 1979.
[23] R. A. Hoffman, and W. B. Britt, "Flow-System Measurement of Cell Impedance Properties," *Journal of Histochemistry & Cytochemistry,* vol. 27, no. 1, pp. 234-240, 1979.
[24] R. A. Hoffman, "Classifying Cells Using Rf Impedance," *Biophysical Journal,* vol. 21, no. 3, pp. A130-A130, 1978.
[25] K. Cheung, S. Gawad, and P. Renaud, "Impedance spectroscopy flow cytometry: On-chip label-free cell differentiation," *Cytometry Part A,* vol. 65A, no. 2, pp. 124-132, Jun, 2005.
[26] S. Gawad, K. Cheung, U. Seger *et al.*, "Dielectric spectroscopy in a micromachined flow cytometer: theoretical and practical considerations," *Lab on a Chip,* vol. 4, no. 3, pp. 241-251, 2004.
[27] U. Seger, S. Gawad, R. Johann *et al.*, "Cell immersion and cell dipping in microfluidic devices," *Lab on a Chip,* vol. 4, no. 2, pp. 148-151, 2004.
[28] S. Gawad, L. Schild, and P. Renaud, "Micromachined impedance spectroscopy flow cytometer for cell analysis and particle sizing," *Lab on a Chip,* vol. 1, no. 1, pp. 76-82, 2001.
[29] H. G. Chun, T. D. Chung, and H. C. Kim, "Cytometry and velocimetry on a microfluidic chip using polyelectrolytic salt bridges," *Analytical Chemistry,* vol. 77, no. 8, pp. 2490-2495, Apr 15, 2005.
[30] H. Morgan, D. Holmes, and N. G. Green, "High speed simultaneous single particle impedance and fluorescence analysis on a chip," *Current Applied Physics,* vol. 6, no. 3, pp. 367-370, Jun, 2006.
[31] T. Sun, D. Holmes, S. Gawad *et al.*, "High speed multi-frequency impedance analysis of single particles in a microfluidic cytometer using maximum length sequences," *Lab Chip,* vol. 7, no. 8, pp. 1034, Jan 1, 2007.
[32] T. Sun, N. G. Green, S. Gawad *et al.*, "Analytical electric field and sensitivity analysis for two microfluidic impedance cytometer designs," *IET Nanobiotechnology,* vol. 1, no. 5, pp. 69-79, Oct, 2007.
[33] T. Sun, S. Gawad, C. Bernabini *et al.*, "Broadband single cell impedance spectroscopy using maximum length sequences: theoretical analysis and practical considerations," *Measurement Science & Technology,* vol. 18, no. 9, pp. 2859-2868, Sep, 2007.

[34] T. Sun, D. Holmes, S. Gawad *et al.*, "High speed multi-frequency impedance analysis of single particles in a microfluidic cytometer using maximum length sequences," *Lab on a Chip,* vol. 7, no. 8, pp. 1034-1040, 2007.

[35] I. Giaever, and C. R. Keese, "A Morphological Biosensor for Mammalian-Cells," *Nature,* vol. 366, no. 6455, pp. 591-592, Dec 9, 1993.

[36] C. R. Keese, J. Wegener, and L. Giaever, "Monitoring cell-ECM interactions using ECIS," *Genetic Engineering News,* vol. 25, no. 3, pp. 42-43, Feb 1, 2005.

[37] J. Ponti, L. Ceriotti, B. Munaro *et al.*, "Comparison of impedance-based sensors for cell adhesion monitoring and in vitro methods for detecting cytotoxicity induced by chemicals," *Atla-Alternatives to Laboratory Animals,* vol. 34, no. 5, pp. 515-525, Oct, 2006.

[38] T. Matsue, and H. Shiku, "Electrochemical microbiosensors using living cells," *Electrochemistry,* vol. 74, no. 2, pp. 107-113, Feb, 2006.

[39] J. H. Yeon, and J. K. Park, "Cytotoxicity test based on electrochemical impedance measurement of HepG2 cultured in microfabricated cell chip," *Analytical Biochemistry,* vol. 341, no. 2, pp. 308-315, Jun 15, 2005.

[40] K. Solly, X. B. Wang, X. Xu *et al.*, "Application of real-time cell electronic sensing (RT-CES) technology to cell-based assays," *Assay and Drug Development Technologies,* vol. 2, no. 4, pp. 363-372, Aug, 2004.

[41] B. F. De Blasio, M. Laane, T. Walmann *et al.*, "Combining optical and electrical impedance techniques for quantitative measurement of confluence in MDCK-I cell cultures," *Biotechniques,* vol. 36, no. 4, pp. 650-+, Apr, 2004.

[42] S. Arndt, J. Seebach, K. Psathaki *et al.*, "Bioelectrical impedance assay to monitor changes in cell shape during apoptosis," *Biosensors & Bioelectronics,* vol. 19, no. 6, pp. 583-594, Jan 15, 2004.

[43] F. Asphahani, and M. Zhang, "Cellular impedance biosensors for drug screening and toxin detection," *Analyst*, 2007, pp. 835-841.

[44] M. H. McCoy, and E. Wang, "Use of electric cell-substrate impedance sensing as a tool for quantifying cytopathic effect in influenza A virus infected MDCK cells in real-time," *Journal of Virological Methods,* vol. 130, no. 1-2, pp. 157-161, Dec, 2005.

[45] J. H. T. Luong, "An emerging impedance sensor based on cell-protein interactions: Applications in cell biology and analytical biochemistry," *Analytical Letters,* vol. 36, no. 15, pp. 3147-3164, 2003.

[46] J. H. T. Luong, M. Habibi-Rezaei, J. Meghrous *et al.*, "Monitoring motility, spreading, and mortality of adherent insect cells using an impedance sensor," *Analytical Chemistry,* vol. 73, no. 8, pp. 1844-1848, Apr 15, 2001.

[47] J. H. T. Luong, C. D. Xiao, B. Lachance *et al.*, "Extended applications of electric cell-substrate impedance sensing for assessment of the structure-function of alpha 2 beta 1 integrin," *Analytica Chimica Acta,* vol. 501, no. 1, pp. 61-69, Jan 9, 2004.

[48] T. S. Hug, "Biophysical methods for monitoring cell-substrate interactions in drug discovery," *Assay and Drug Development Technologies,* vol. 1, no. 3, pp. 479-488, Jun, 2003.

[49] A. Rothermel, M. Nieber, J. Muller *et al.*, "Real-time measurement of PMA-induced cellular alterations by microelectrode array-based impedance spectroscopy," *Biotechniques,* vol. 41, no. 4, pp. 445-450, Oct, 2006.

[50] J. M. Atienza, N. C. Yu, X. B. Wang *et al.*, "Label-free and real-time cell-based kinase assay for screening selective and potent receptor tyrosine kinase inhibitors using microelectronic sensor array," *Journal of Biomolecular Screening,* vol. 11, no. 6, pp. 634-643, Sep, 2006.

[51] J. M. Atienza, J. Zhu, X. B. Wang *et al.*, "Dynamic monitoring of cell adhesion and spreading on microelectronic sensor arrays," *Journal of Biomolecular Screening,* vol. 10, no. 8, pp. 795-805, Dec, 2005.

[52] N. C. Yu, J. M. Atienza, J. Bernard *et al.*, "Real-time monitoring of morphological changes in living cells by electronic cell sensor arrays: An approach to study G protein-coupled receptors," *Analytical Chemistry,* vol. 78, no. 1, pp. 35-43, Jan 1, 2006.

[53] C. R. Keese, J. Wegener, S. R. Walker *et al.*, "Electrical wound-healing assay for cells in vitro," *Proceedings of the National Academy of Sciences of the United States of America,* vol. 101, no. 6, pp. 1554-1559, Feb 10, 2004.

[54] W. M. Arnold, and U. Zimmermann, "Rotation of an Isolated Cell in a Rotating Electric-Field," *Naturwissenschaften,* vol. 69, no. 6, pp. 297-298, 1982.

[55] R. Pethig, "Dielectrophoresis: Using inhomogeneous AC electrical fields to separate and manipulate cells," *Critical Reviews in Biotechnology,* vol. 16, no. 4, pp. 331-348, 1996.

[56] R. Pethig, and G. H. Markx, "Applications of dielectrophoresis in biotechnology," *Trends in Biotechnology,* vol. 15, no. 10, pp. 426-432, Oct, 1997.

[57] L. M. Broche, F. H. Labeed, and M. P. Hughes, "Extraction of dielectric properties of multiple populations from dielectrophoretic collection spectrum data," *Physics in Medicine and Biology,* vol. 50, no. 10, pp. 2267-2274, May 21, 2005.

[58] J. Gimsa, T. Muller, T. Schnelle *et al.*, "Dielectric spectroscopy of single human erythrocytes at physiological ionic strength: Dispersion of the cytoplasm," *Biophysical Journal,* vol. 71, no. 1, pp. 495-506, Jul, 1996.

[59] J. Gimsa, T. Schnelle, G. Zechel *et al.*, "Dielectric-Spectroscopy of Human Erythrocytes - Investigations under the Influence of Nystatin," *Biophysical Journal,* vol. 66, no. 4, pp. 1244-1253, Apr, 1994.

[60] X. J. Wang, F. F. Becker, and P. R. C. Gascoyne, "Membrane dielectric changes indicate induced apoptosis in HL-60 cells more sensitively than surface phosphatidylserine expression or DNA fragmentation," *Biochimica Et Biophysica Acta-Biomembranes,* vol. 1564, no. 2, pp. 412-420, Aug 31, 2002.

[61] M. P. Hughes, "AC Electrokinetics: Applications for Nanotechnology."

[62] L. A. Flanagan, and A. P. Lee, "Unique Dielectric Properties Distinguish Stem Cells and Their Differentiated Progeny " *Stem Cells Express*, Dec 19, 2007.

[63] K. L. Chan, H. Morgan, E. Morgan *et al.*, "Measurements of the dielectric properties of peripheral blood mononuclear cells and trophoblast cells using AC electrokinetic techniques," *Biochimica Et Biophysica Acta-Molecular Basis of Disease,* vol. 1500, no. 3, pp. 313-322, Mar 17, 2000.

[64] J. Yang, Y. Huang, X. J. Wang *et al.*, "Dielectric properties of human leukocyte subpopulations determined by electrorotation as a cell separation criterion," *Biophysical Journal,* vol. 76, no. 6, pp. 3307-3314, Jun, 1999.

[65] F. F. Becker, X. B. Wang, Y. Huang *et al.*, "Separation of Human Breast-Cancer Cells from Blood by Differential Dielectric Affinity," *Proceedings of the National Academy of Sciences of the United States of America,* vol. 92, no. 3, pp. 860-864, Jan 31, 1995.

[66] J. Cheng, E. L. Sheldon, L. Wu *et al.*, "Isolation of cultured cervical carcinoma cells mixed with peripheral blood cells on a bioelectronic chip," *Analytical Chemistry,* vol. 70, no. 11, pp. 2321-2326, Jun 1, 1998.

[67] M. Cristofanilli, G. De Gasperis, L. S. Zhang *et al.*, "Automated electrorotation to reveal dielectric variations related to HER-2/neu overexpression in MCF-7 sublines," *Clinical Cancer Research,* vol. 8, no. 2, pp. 615-619, Feb, 2002.

[68] S. Archer, H. Morgan, and F. Rixon, "Electrorotation studies of baby hamster kidney fibroblasts (C-13) following infection with herpes simplex virus, Type I," *Biophysical Journal,* vol. 72, no. 2, pp. TU381-TU381, Feb, 1997.

[69] S. Archer, H. Morgan, and F. J. Rixon, "Electrorotation studies of baby hamster kidney fibroblasts infected with herpes simplex virus type 1," *Biophysical Journal,* vol. 76, no. 5, pp. 2833-2842, May, 1999.

[70] X. F. Zhou, J. P. H. Burt, and R. Pethig, "Automatic cell electrorotation measurements: studies of the biological effects of low-frequency magnetic fields and of heat shock," *Physics in Medicine and Biology,* vol. 43, no. 5, pp. 1075-1090, May, 1998.

[71] G. De Gasperis, X. B. Wang, J. Yang *et al.*, "Automated electrorotation: dielectric characterization of living cells by real-time motion estimation," *Measurement Science & Technology,* vol. 9, no. 3, pp. 518-529, Mar, 1998.

[72] J. Gimsa, B. Pruger, P. Eppmann *et al.*, "Electrorotation of Particles Measured by Dynamic Light-Scattering - a New Dielectric-Spectroscopy Technique," *Colloids and Surfaces a-Physicochemical and Engineering Aspects,* vol. 98, no. 3, pp. 243-249, May 22, 1995.

[73] P. Eppmann, J. Gimsa, B. Pruger *et al.*, "Dynamic light scattering from oriented, rotating particles: A theoretical study and comparison to electrorotation data," *Journal De Physique III,* vol. 6, no. 3, pp. 421-432, Mar, 1996.

[74] H. Morgan, T. Sun, D. Holmes *et al.*, "Single cell dielectric spectroscopy," *Journal of Physics D-Applied Physics,* vol. 40, no. 1, pp. 61-70, Jan, 2007.

[75] H. E. Ayliffe, A. B. Frazier, and R. D. Rabbitt, "Electric impedance spectroscopy using microchannels with integrated metal electrodes," *Journal Of Microelectromechanical Systems,* vol. 8, no. 1, pp. 50-57, 1998.

[76] Y. H. Cho, T. Yamamoto, Y. Sakai *et al.*, "Development of microfluidic device for electrical/physical characterization of single cell," *Journal of Microelectromechanical Systems,* vol. 15, no. 2, pp. 287-295, Apr, 2006.

[77] K. H. Han, A. Han, and A. B. Frazier, "Microsystems for isolation and electrophysiological analysis of breast cancer cells from blood," *Biosensors & Bioelectronics,* vol. 21, no. 10, pp. 1907-1914, Apr 15, 2006.

[78] A. Han, and A. B. Frazier, "Ion channel characterization using single cell impedance spectroscopy," *Lab on a Chip,* vol. 6, no. 11, pp. 1412-1414, 2006.

[79] C. James, N. Reuel, E. Lee *et al.*, "Impedimetric and optical interrogation of single cells in a microfluidic device for real-time viability and chemical response assessment," *Biosensors and Bioelectronics,* vol. 23, no. 6, pp. 845-851, Jan 18, 2008.

[80] P. C. H. Li, L. de Camprieu, J. Cai *et al.*, "Transport, retention and fluorescent measurement of single biological cells studied in microfluidic chips," *Lab On A Chip,* vol. 4, no. 3, pp. 174-180, 2004.

[81] A. R. Wheeler, W. R. Throndset, R. J. Whelan *et al.*, "Microfluidic device for single-cell analysis," *Analytical chemistry,* vol. 75, no. 14, pp. 3581-3586, 2003.

[82] D. Irimia, R. G. Tompkins, and M. Toner, "Single-cell chemical lysis in picoliter-scale closed volumes using a microfabricated device," *Anal Chem,* vol. 76, no. 20, pp. 6137-43, Oct 14, 2004.

[83] C. Ionescu-Zanetti, R. M. Shaw, J. G. Seo *et al.*, "Mammalian electrophysiology on a microfluidic platform," *Proceedings of the National*

Academy of Sciences of the United States of America, vol. 102, no. 26, pp. 9112-9117, 2005.

[84] P. Lee, P. Hung, R. Shaw *et al.*, "Microfluidic application-specific integrated device for monitoring direct cell-cell communication via gap junctions between individual cell pairs," *Applied Physics Letters,* vol. 86, no. 22, pp. 223902, 2005.

[85] J. R. Rettig, and A. Folch, "Large-scale single-cell trapping and imaging using microwell arrays," *Analytical chemistry,* vol. 77, no. 17, pp. 5628-5634, 2005.

[86] V. Chin, P. Taupin, S. Sanga *et al.*, "Microfabricated platform for studying stem cell fates," *Biotechnology and bioengineering,* vol. 88, no. 3, pp. 399-415, 2004.

[87] A. Revzin, K. Sekine, A. Sin *et al.*, "Development of a microfabricated cytometry platform for characterization and sorting of individual leukocytes," *Lab on a chip,* vol. 5, no. 1, pp. 30-7, Dec 31, 2005.

[88] E. Ostuni, C. S. Chen, D. E. Ingber *et al.*, "Selective deposition of proteins and cells in arrays of microwells," *Langmuir,* vol. 17, no. 9, pp. 2828-2834, 2001.

[89] C. S. Chen, X. Y. Jiang, and G. M. Whitesides, "Microengineering the environment of mammalian cells in culture," *MRS Bulletin,* vol. 30, no. 3, pp. 194-201, 2005.

[90] C. S. Chen, M. Mrksich, S. Huang *et al.*, "Geometric control of cell life and death," *Science,* vol. 276, no. 5317, pp. 1425-1428, 1997.

[91] G. M. Whitesides, "The 'right' size in nanobiotechnology," *Nature Biotechnology,* vol. 21, pp. 1161-1165, 2003.

[92] R. Chandra, E. Douglas, R. Mathies *et al.*, "Programmable Cell Adhesion Encoded by DNA Hybridization," *Angewandte Chemie International Edition,* vol. 45, no. 6, pp. 896-901, 2006.

[93] P. Chiou, and M. C. Wu, "Light-actuated AC electroosmosis for optical manipulation of nanoscale particles," *Proc. Solid-State Sens., Actuators, Microsyst. Workshop*, Mar 23, 2006.

[94] J. Voldman, "A microfabricated dielectrophoretic trapping array for cell-based biological assays," ,*PhD Thesis*, May 15, 2001.

[95] J. Voldman, "Electrical forces for microscale cell manipulation," *Annual Review of Biomedical Engineering,* vol. 8, pp. 425-454, 2006.

[96] J. Voldman, "Engineered systems for the physical manipulation of single cells," *Current Opinion in Biotechnology,* vol. 17, no. 5, pp. 532-537, 2006.

[97] J. Voldman, "nDEP microwells for single-cell patterning in physiological media," *Lab on a chip*, Jul 29, 2007.

[98] J. Voldman, M. L. Gray, M. Toner *et al.*, "A microfabrication-based dynamic array cytometer," *Analytical chemistry,* vol. 74, no. 16, pp. 3984-3990, 2002.

[99] D. Di Carlo, N. Aghdam, and L. P. Lee, "Single-cell enzyme concentrations, kinetics, and inhibition analysis using high-density hydrodynamic cell isolation arrays," *Anal Chem*, 2006, pp. 4925-4930.

Chapter 3 Hydrodynamic cell trapping array for impedance analysis of single cells

3.1 Introduction

Single cells are ideal sensors for detecting chemical and biological toxins or mutagens and are also widely used for screening pharmacologically active compounds. Cell analysis systems have applications in drug discovery, bio-threat detection, and environmental pollutant identification [1]. Most biosensors require analysis of a label attached to a molecule. The amount of label is measured and correlated to the number of bound targets. Labels can be fluorophores, magnetic beads, radioactive tags, enzymes that produce an easily detectable product (optical or electrochemical), or nanoparticles.

Impedance spectroscopy is a non-invasive, label-free analytical method that probes the response of cells to their environment. This all-electrical technique is used in many areas including the analysis of fluids [2], polymers [3], ion cells [4], batteries [5], corrosion phenomena [6], electrochemical kinetics/mechanisms, and biological systems at the tissue [7] and whole-organism level [8]. Impedance spectroscopy has been used to measure the passive electrical properties of biological cells for many years, both in bulk suspensions [9-15] and on substrates [16-24]. Traditionally, impedance measurements have been performed on suspensions of cells [25, 26], but this method is insensitive to rare events. Bulk measurements also lead to temporal averaging: fast, time-dependent transitions occurring at the single-cell level may spread slowly through the population and could be interpreted as a gradual change [27]. Experimental platforms that analyse large number of individual cells overcome this problem, whereby any heterogeneity within a cell population is measured [28].

Microfabrication technologies now enable the development of microdevices with single cell analysis capabilities. A number of methods have been published [29-33] that describe single cell capture coupled with impedance analysis, but no existing device features a differential electrode arrangement that measures multiple signals from multiple trapping sites.

The device presented here, enables for the first time the measurement of toxin activity at the single cell level in a non-invasive and label-free manner. The continuous impedance response of captured single cells perfused with solutions of Streptolysin-O

is measured (Figure 3-1), enabling the quantification of electrical conductivity changes in the cell membrane occurring as a consequence of pore formation.

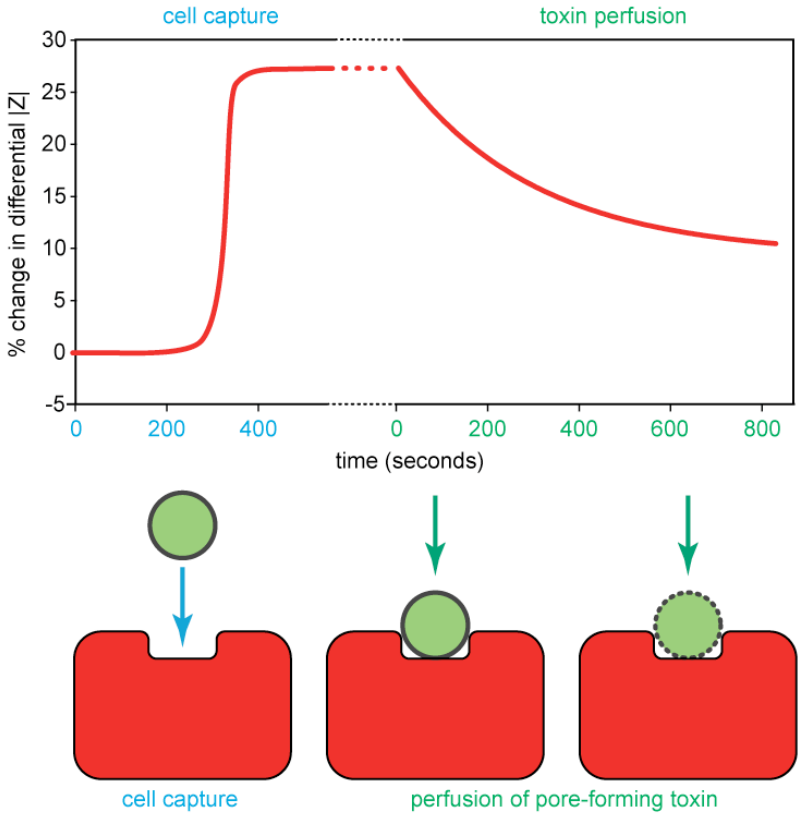

Figure 3-1 Schematic representation of single cell capture event and subsequent poration due to perfusion of a pore-forming toxin. Upon cell capture the electrical impedance, sampled in a range between 100 kHz to 1 MHz, is expected to suddenly increase. Slight motion of the trapped cell is shown not to cause significant variation in the sampled impedance. Upon perfusion of a pore-forming toxin, as the cellular membrane becomes permeable, the overall cell complex conductivity of the cell increases resulting in a measurable decrease of the measured impedance. The rate of impedance decrease can be correlated to the potency or quantity of toxin perfused. This schematic is representative of values obtained experimentally.

The device described in this chapter is fabricated using SU-8 microfluidic and trapping structures, patterned on a glass substrate on which platinum electrodes are evaporated. A second glass substrate on which a conductive layer of Indium Tin Oxide has been sputtered is bonded to the top of the SU-8 structures to close the channel as well and provide a common ground electrode.

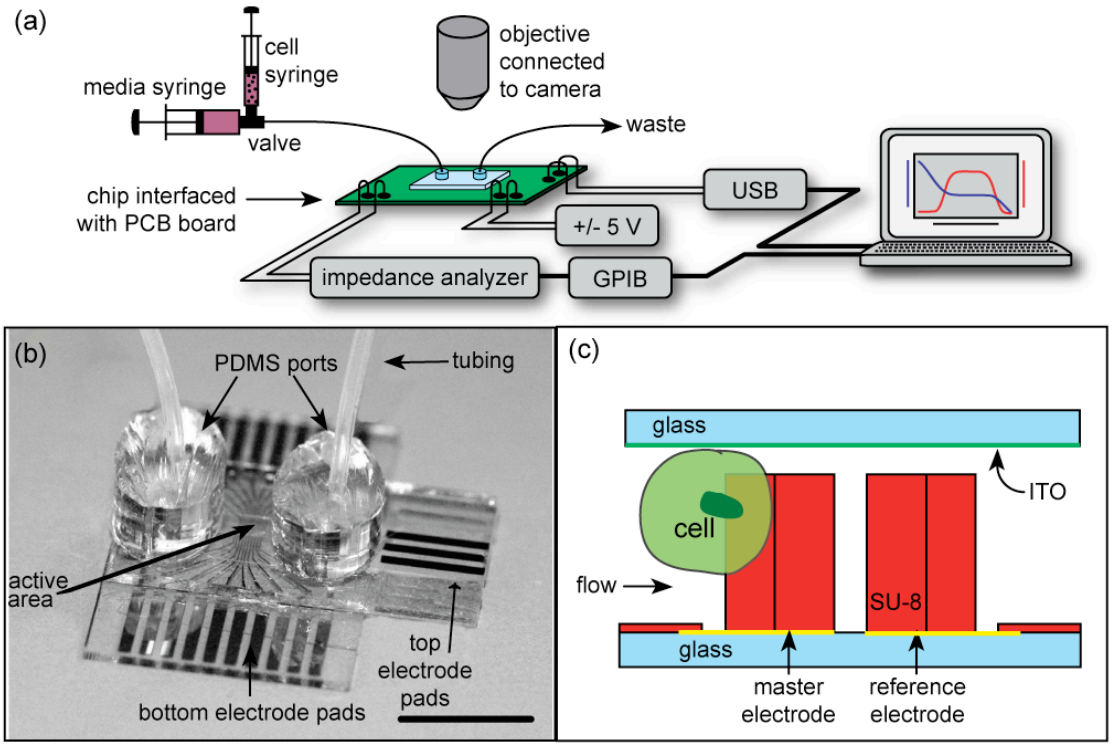

Figure 3-2 Overview of the experimental setup. (a) The microfluidic device is mounted on a PCB board that makes electrical connections to the chip and interfaces to a computer and the impedance analyzer. A microscope is used to image the device, and a syringe pump to flow cells and media. (b) Image of a device with tubing attached via PDMS ports, scale bar = 1 cm. (c) Schematic cross section of the trapping region showing the two electrodes used for differential measurements.

To eliminate changes in impedance due to temperature, pH, and conductivity, a differential measurement system is used: two impedance spectra are acquired, one from a trap containing a cell and a second reference spectrum from an empty trap located nearby. The design of the trapping structures ensures that the reference trap remains empty because it faces downstream, as represented schematically in Figure 3-2 and imaged from top in Figure 3-3(a). The latter figure shows the microfluidic channel with 6 sets of traps, and the pairs of electrodes, one sample and one reference. Also shown in Figure 3-3(b) is an example of a trapped HeLa cell labeled with Celltracker™ dye.

The proximity of the two parts of the trapping site ensures that experimental conditions (pH, temperature, ionic content) are similar. The cell signal is obtained by normalizing the two spectra:

$$\left|Z_{diff}\right| = \frac{\left|Z_{cell}\right|}{\left|Z_{reference}\right|} \qquad (3\text{-}1)$$

$$\phi_{diff} = \frac{\phi_{cell}}{\phi_{reference}} \qquad (3\text{-}2)$$

As shown in Figure 3-2 the device sits on a microscope stage for optical monitoring, and is connected to a dielectric analyzer to record the impedance spectra. Syringe pumps are employed to inject the suspended cells as well as to perfuse medium and/or drugs into the chip. Individually addressable electrodes and micrometer-sized traps are integrated in a microfluidic platform to provide a non-invasive, label-free tool for single cell analysis. Measurements are performed on the cells that are hydro-dynamically trapped by normalizing the spectrum of a trap containing a single cell to a neighbouring empty trap. Long-term studies are therefore not influenced by local changes in temperature, pH, or conductivity. The spectrum is analysed to determine changes membrane electric parameters.

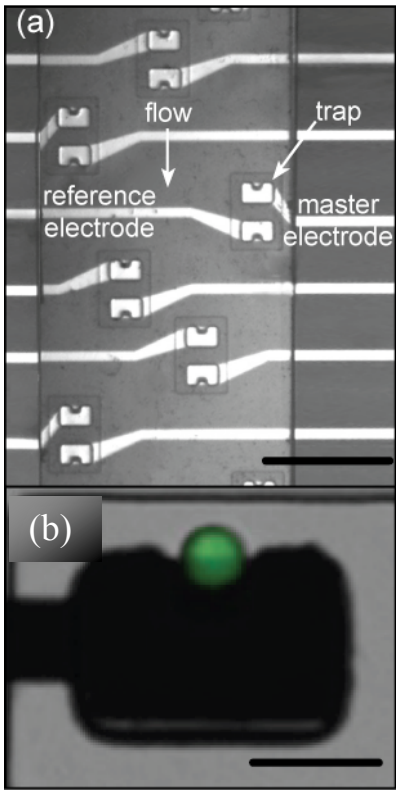

Figure 3-3 (a) Photograph of the micro-channel containing multiple trapping sites, each of which has a pair of electrodes/traps, scale bar = 250 μm. (b) Image of a trapped single HeLa cell, labelled with Celltracker ™ scale bar = 20 μm.

Individual HeLa (Human Negroid cervix epitheloid carcinoma) cells were trapped and continuously monitored over an extended time period during exposure to

Tween and Streptolysin-O (SLO). Tween 20 is a surfactant that is often used to lyse mammalian cells by compromising the cellular membrane. SLO is a pore-forming toxin produced by the Gram-positive bacterium Streptococcus pyogenes, responsible for a variety of diseases such as streptococcal toxic shock syndrome, streptococcal skin infection, and scarlet fever. This bacterial toxin is classified as a member of the cholesterol-dependent cytolysin (CDC) family, a large group of proteins that attack cholesterol containing membranes to form ring-shaped pores that mediate cell death [34-37]. These toxins form 30 nm pores that allow molecules (such as small proteins) to permeate out of the cellular envelope. As such, they are employed by cell biologists as tools for controlled poration of cell membranes: these agents are easy to handle, they are stable and can be stored over long periods. Transmembrane pores formed by bacterial toxins are well defined in size and they do not pass the plasma membrane to attack intracellular membranes. Additionally, since they are devoid of enzymatic (proteolytic) activity, they cause no alteration of cell constituents [38, 39].

3.2 Mechanism of hydrodynamic trapping of single cells

The hydrodynamic trapping mechanism employed by this device is identical to the one exploited by Dino Di Carlo for the development of his hydrodynamic cell trapping arrays for fluorescence assays [40, 41].

Briefly, single cells are captured in arrays of trapping structures patterned in the middle micro-channel is relatively wide (in this device it has a width of 500 μm) and with a height higher than the diameter size of the target cell (in this device it has a height of 25 μm). The patterned traps however are not quite as tall as the channel walls, so as to leave a gap of 3μm that allows a fraction of fluid streamlines to carry cells to enter a trap. Once a cell enters a trap and partially occludes the 3 μm gap, the fraction of fluid streamlines (and cells) entering the trap region is reduced. This leads to a high quantity of single cell isolates. This mechanism is illustrated schematically in Figure 3-4.

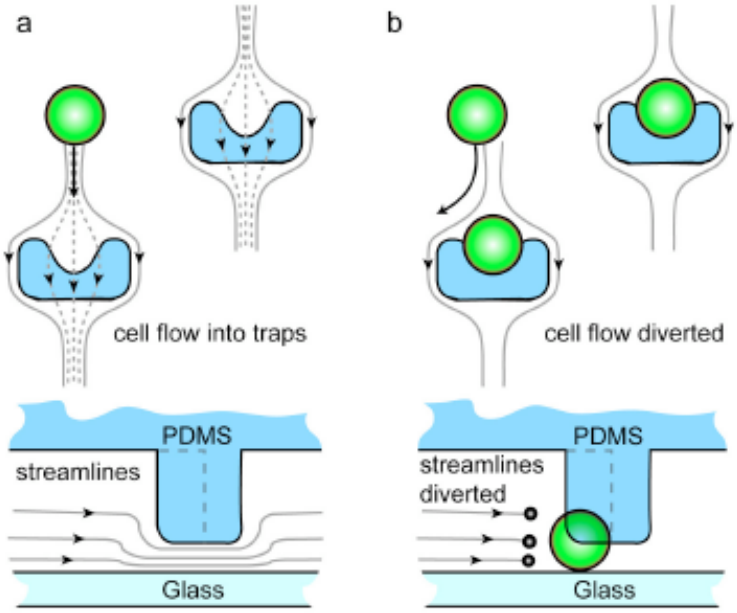

Figure 3-4 A schematic diagram is shown to describe the mechanism of cell trapping using flow through arrayed suspended obstacles. Two-layer cup-shaped trapping sites allow a fraction of fluid streamlines to enter the traps. After a cell is trapped and partially occludes the narrow open region, the fraction of streamlines through the barred trap decreases, leading to the self-sealing quality of the traps and a high quantity of single cell isolates. Drawing is not to scale. Taken from [42].Reproduced by permission from the author.

Di Carlo has shown in [42] that this capture design results in a high number of single cell captures; by comparing a Poisson distribution to the experimentally measured distribution of captured cells it is shown that the probability of trapping is dependent on the number of cells already captured. Therefore single cells are shown in excess of the Poisson distribution while zero, three, and four trapped cells are depressed.

3.3 Fabrication

To simplify fabrication, a large area ground optically transparent electrode is used for the lid of the device. Each cell trap is bounded by an SU8 structure that almost completely encloses the driven small electrode. The device was made by bonding two microfabricated substrates, aligning the cell traps to the measurement electrodes. The general scheme for fabrication is shown in Figure 3-5. A lift off process was used to pattern metal electrodes (70 nm Pt with a Ti 25 nm adhesion layer using an Edwards EB3 electron beam evaporator) onto a 4" Pyrex wafer for the bottom substrate and onto an ITO-coated Pyrex wafer for the top substrate. The metal on the bottom substrate serves as working electrodes for the impedance measurements. The metal on the top substrate serves to make low-resistance connections between the ITO surface and electronics. The bottom substrate was patterned with a 1 μm thick layer of SU8 (SU8 2001, Microchem) which insulated the connections to the sensing electrodes. A second 25 μm SU8 layer (SU8 2025) was patterned on top of this insulation layer forming both the walls of the fluidic channels and the U-shaped cell traps. The top (ITO) substrate was patterned with a 3 μm layer of SU8 (SU8 2005), to create a 3 μm separation between the top of the traps and the top substrate in addition to insulating much of the upper electrode outside of the sensing areas (lithography masks for the device are included in the appendix). This gap is integral to the hydrodynamic trapping process. Similar traps have been fabricated using PDMS [28], however the flexible nature of PDMS makes if impossible to reliably align the traps with the metal electrodes on the base. Each pair of wafers had twelve devices. Wafers were diced with a MP500 free shape cutting machine (MDI Schott, Germany). After drilling access ports, the substrates were bonded as follows. The were attached to an x-y stage with double-side adhesive tape and a drop of isopropyl alcohol (IPA) was used to wet the bottom substrate and provide temporary adhesion to the top substrate for alignment by hand.

Once aligned, the two substrates were clamped and put in an oven for 5 minutes at 50°C to evaporate the IPA. A UV-curable glue (Norland Optical Adhesive 74), was applied to the edges using a 25G hypodermic needle and allowed to wick in for a few seconds, then set by exposure to UV light for 30 minutes.

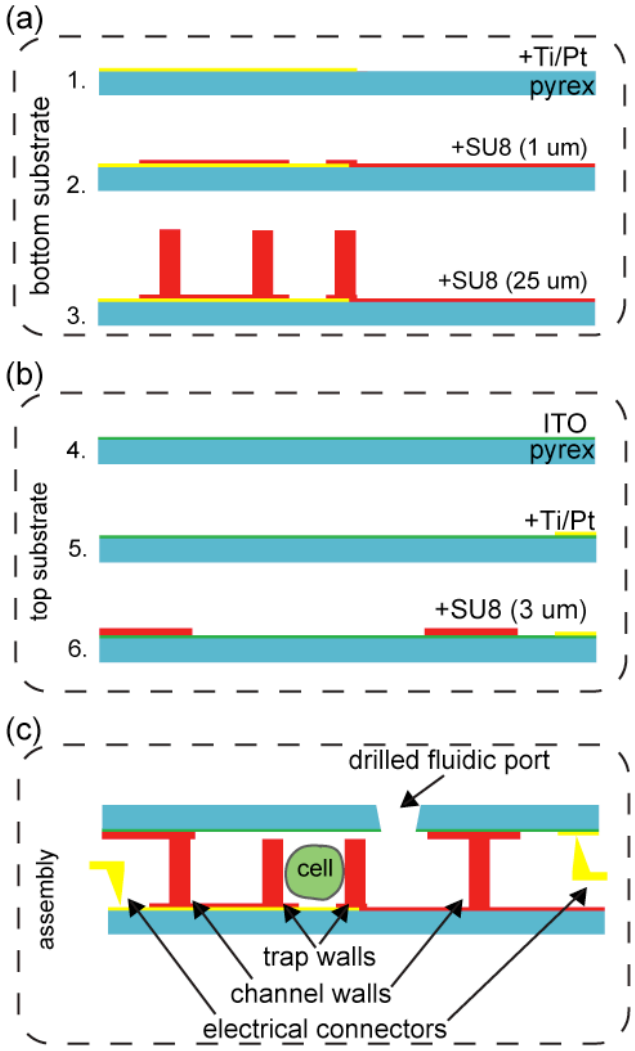

Figure 3-5 Schematic diagram showing fabrication steps. The device was made by assembling two microfabricated substrates.(a) The bottom substrate (glass) has Ti/Pt electrodes. A 1-µm layer of SU8 is used to insulate the electrodes ensuring that only the active electrode is exposed to the solution. A second SU8 layer (25 µm thick) is patterned on top of this layer to form the walls of the fluidic channels and the U-shaped cell traps. (b) On the top substrate (ITO-coated glass) Ti/Pt metal pads were evaporated to make contacts, and a 3 µm layer of SU8 was patterned as a spacer, creating a gap separating the top of the traps from the top ITO substrate when assembled. (c) The device was assembled by aligning the two substrates, clamping them and bonding them with UV-curable glue. Alignment was performed using stereo-microscope.

3.4 FEM Simulations

Finite element analysis simulations were performed in COMSOL Multiphysics v3.4 (COMSOL, Burlington, MA) and MATLAB v7.5 (Mathworks, Natick, MA). A summary of the geometry and boundary conditions is given in Figure 3-6. To improve accuracy when integrating the total current over the boundaries, *weak constraints* were used. The cell sits in PBS (ε=78, σ=1.6 S/m); the electrical properties of the SU8 trap are ε=5, σ=0 S/m and the cell was modelled as a sphere with a complex permittivity calculated at each frequency point using the single shell model (Equation 1-61) and the following values: ε_{cyto}=70, σ_{cyto}=1.6 S/m, $\varepsilon_{membrane}$=9, $\sigma_{membrane}$=1x10^{-8} S/m, with a membrane thickness = 5 nm.

The ionic double layer, which has a thickness of 1 nm and a relative permittivity of 20, was modelled as a dielectric slab with thickness of 1 μm to obviate the difficulty of meshing a nanometer-thick layer. Of course, the relative permittivity of the slab employed in the model was also increased a thousand fold to ε=37000, to obtain the correct value of double layer capacitance – validated by experimental findings.

Simulations were performed using both 3-D and 2-D (quasi) axisymmetric models, as shown in Figure 3-6. The system is not exactly axi-symmetric (the electrode is square and not round, and the trapping structure does not fully encircle the electrode). However the 2-D approximation for simple model geometries gave results in good agreement with analytical calculations (not shown). Changes in impedance spectra due to variations in cell membrane conductance, cell size and position in the trap were simulated.

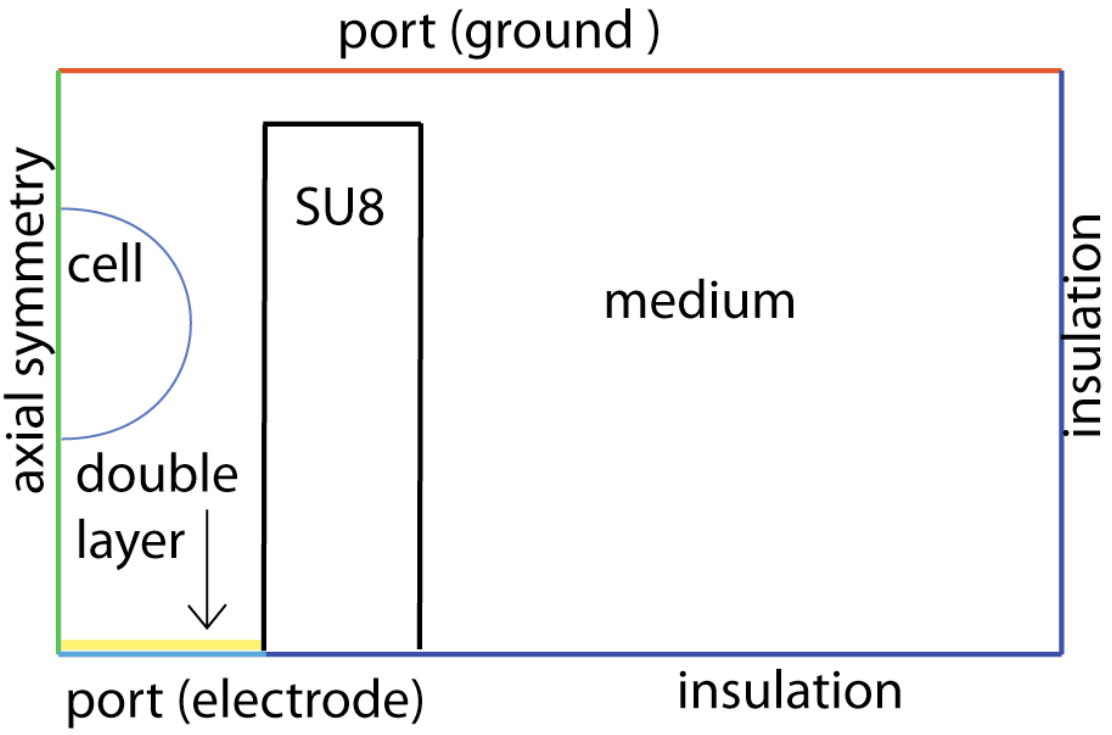

Figure 3-6 Outline of the Finite Element Model (FEM) of a single cell in a trap site: (a) A 2-D model, which exploits the axial symmetry of the system, is meshed with 60,000 elements. The mesh and boundary conditions are indicated in the diagram.

Figure 3-7 shows the electric field lines and electrical potential for traps with and without the SU-8 boundary as a function of frequency. In this simulation a cell is placed on the centre line of the trap, midway between the top and bottom electrode. The field simulations clearly demonstrate that this design of SU-8 structure confines the electric field to the region where the cell is trapped, increasing the effective volume fraction, increasing the sensitivity of the measurement defined as the change of measured impedance divided by the change in the cell dielectric parameters. This design is relatively insensitive to the position of the trapped cell. Variations in the position of the cell within the channel by up to ±12μm, for a channel height of 25μm result in a maximum change in the magnitude of the impedance of 3% at 100 kHz (as shown in Figure 3-13).

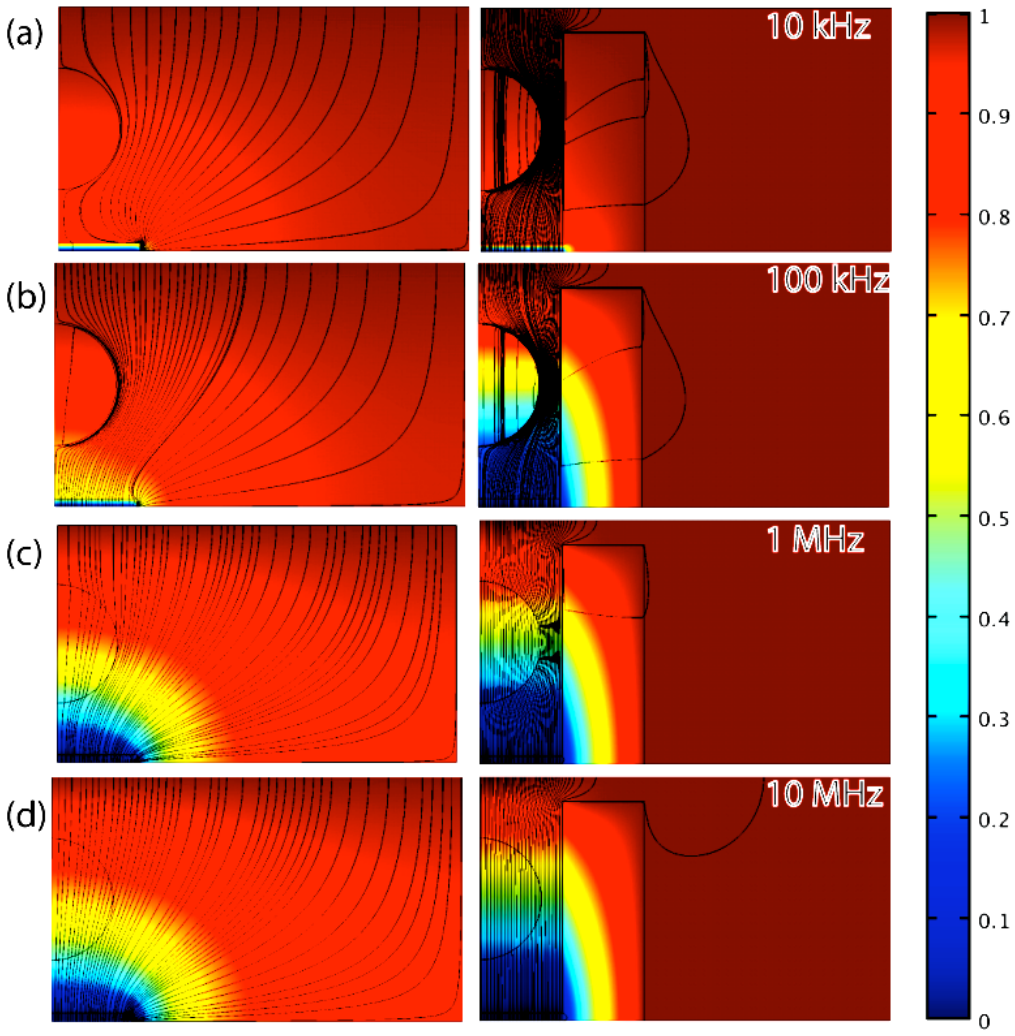

Figure 3-7 Electrical potential and current density (streamlines) as for 2-D axi-symmetrical models of a cell immobilized between an electrode on the bottom and a large electrode on the top, with and without the SU8 structure. The medium surrounding the cell is ε=78, σ=1.6 S/m;, the SU8 trap is ε=5, σ=0 S/m). The cytoplasm has permittivity ε=70, and conductivity σ=1.6 S/m , with membrane ε=9, σ =1x10^{-8} S/m and thickness = 5 nm. With the SU8 the current flux is well confined to the cell, therefore improving the sensitivity. (a) At frequencies below 10 kHz the electric potential drops across the ionic double layer. (b) Up to 100 kHz, the cell membrane effectively shields the cell from the electric field, so that the behaviour is dominated by cell size and membrane properties. (c-d) Above 1 MHz the cell membrane is shunted and the impedance is dominated by the cell cytoplasm.

In order to estimate the sensitivity of the system to changes in cell parameters, simulations were performed for difference values of cell membrane conductivity and cell dimensions, keeping the cell membrane capacitance constant at 1.6 μF/cm^2, a value consistent with experimental measurements of mammalian cell membranes [43]. Figure

3-8 and Figure 3-9 show how changes in cell size or membrane conductivity (over the range of 10^{-7} to 10^{-4} S/m) affect the impedance spectrum in the same range of frequencies. At frequencies lower than 50 kHz, any changes are masked by the double layer. In Figure 3-10, the magnitude of the impedance and the phase response are plotted against the logarithm of membrane conductivity change at five sample frequencies. In Figure 3-11, the magnitude of the impedance and the phase response are plotted against changes in cell radius at five sample frequencies.

In Figure 3-12, these simulations results are combined in contour plots to show that variations in cell size and changes in membrane conductivity affect the impedance spectrum of a cell in the same frequency range: for |Z| this is between 10^5 and 10^6 Hz, whereas for phase it's between 10^6 and 10^7 Hz. From these plots it is evident that the interpretation of spectroscopic results can be extremely difficult when *both* size and their membrane permeability change in the cells under study. This finding suggests that microscopy data should be recorded and correlated to the electrical data to de-couple the effects of volumetric changes in the cell from any changes occurring to the membrane permeability.

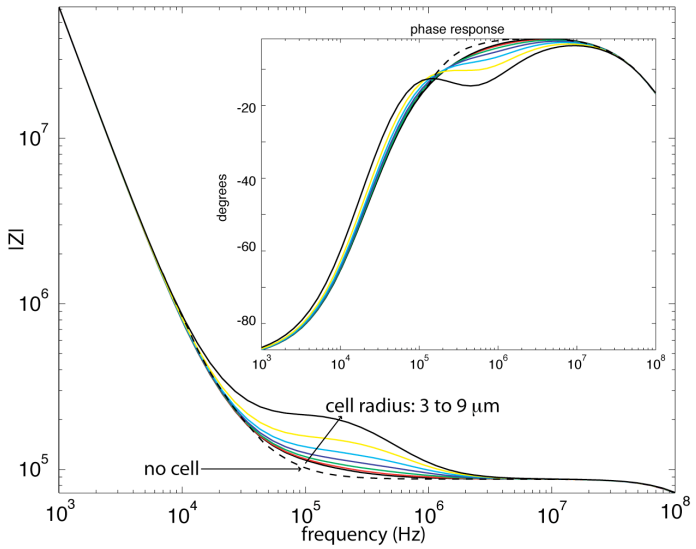

Figure 3-8 Effect of cell radius on impedance spectrum (on the phase response in the inset). Maximum changes in |Z| occur in the frequency 10^5 – 10^6 Hz and 10^5- 10^7 in phase.

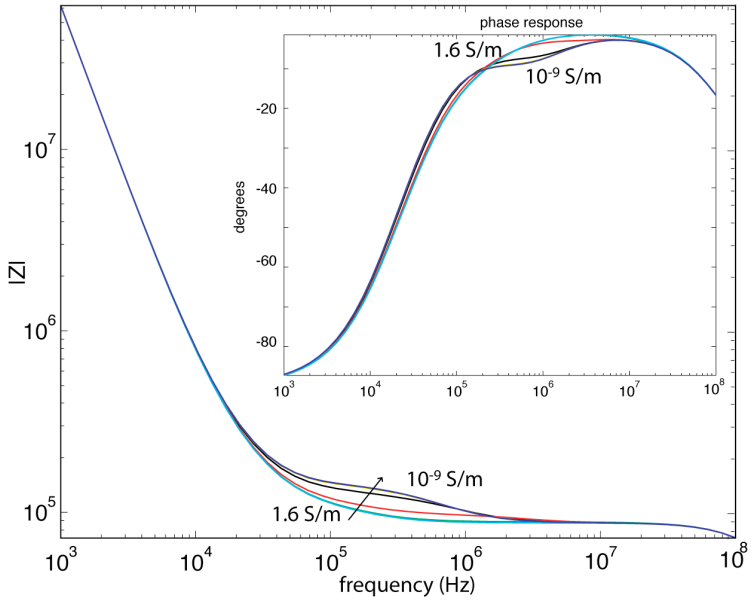

Figure 3-9 Effect of membrane conductance on impedance spectrum (phase response in inset).

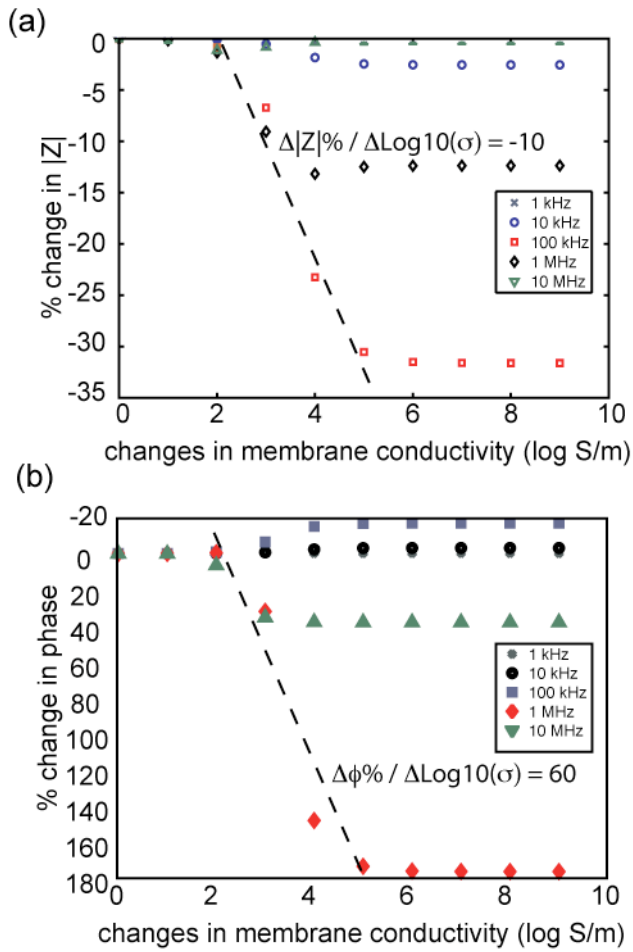

Figure 3-10 Percent changes in the (a) impedance and (b) phase at 5 sample frequencies (1 kHz, 10 kHz, 100 kHz, 1MHz, 10 MHz) due to changes in the conductance of the cellular membrane. Reference conductance value (i.e. the value with respect to which the change is

indicated on the x-axes) is that of an intact membrane, 10^{-9} S/m. The membrane conductivity has to rise by 2 to 3 order of magnitudes to cause measurable changes in the impedance spectrum; conductivities changes in the range of 10^{-7} to 10^{-5} cause drops in |Z| (sampled at f = 100 kHz and 1 MHz) of approximately 10% per order of magnitude change. Note that whereas the |Z| spectrum is more sensitive to changes in membrane conductivity at f = 100 kHz, the phase response is more sensitive at f = 1MHz.

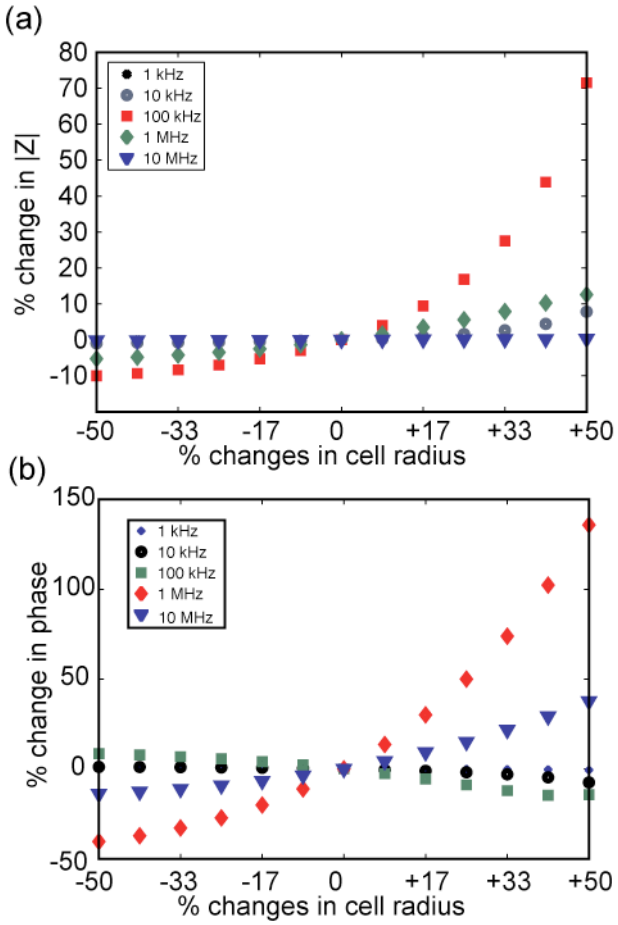

Figure 3-11 Changes in the impedance magnitude (a) and phase (b) at 5 sampled frequencies (1 kHz, 10 kHz, 100 kHz, 1MHz, 10 MHz) due to changes in cell radius, reference cell radius: 6 μm. For this geometry the relationship between changes in |Z| and changes in cell size is non-linear: the device is significantly more sensitive to increases than decreases in radius, particularly at f=100 kHz. This behaviour is to be expected as increases in cell radius cause a cubic increase in the volume fraction (i.e. the ratio of volume enclosed by the measuring electrodes to the volume of the cell being measured).

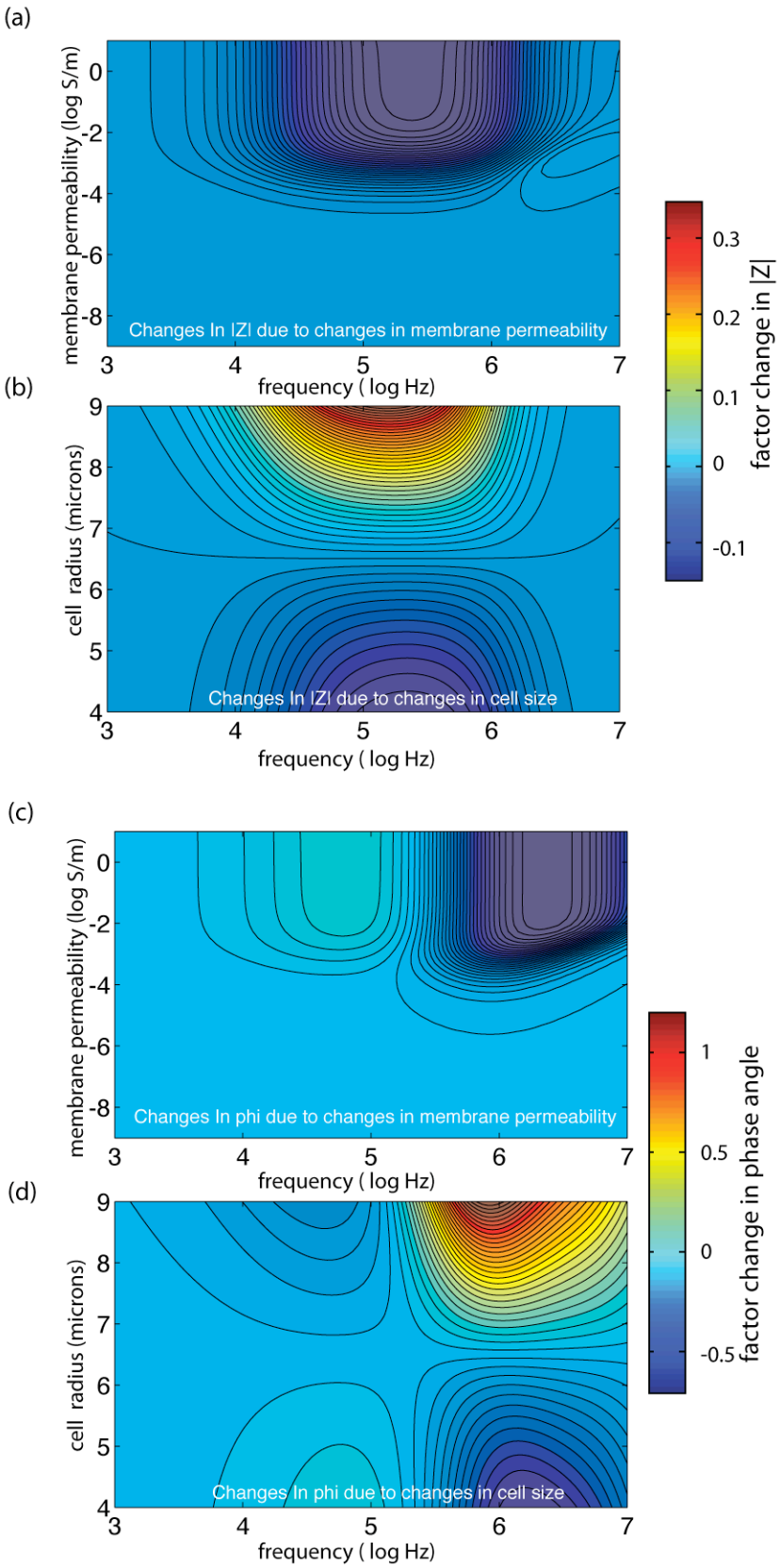

Figure 3-12 Contour plots of changes in impedance response (magnitude and phase) due to changes in cell size or membrane permeability. (a) Changes in |Z| at frequencies ranging from 10^3 to 10^7 Hz, for membrane conductivity values ranging from 1 S/m to 10^{-9} S/m. (b) Changes in |Z| at frequencies ranging from 10^3 to 10^7 Hz, for cell radius values ranging from 4 to 9 μm.

Comparing (a) and (b) it is evident that both types of changes affect the impedance magnitude maximally at f = 300 kHz. (c) Changes in phase response at frequencies ranging from 10^3 to 10^7 Hz, for membrane conductivity values ranging from 1 S/m to 10^{-9} S/m. (d) Changes in phase response at frequencies ranging from 10^3 to 10^7 Hz, for cell radius values ranging from 4 to 9 μm. Comparison of the plots in (c) and (d) suggests that the phase response is mostly affected at frequencies higher than 1MHz, and while the membrane conductivity has a peak effect at f = 5 MHz, the cell radius has a maximum effect at f = 1MHz. This would indicate that deconvolution of the two competing effects could be more feasible by looking at phase data in the 10^6 to 10^7 frequency range.

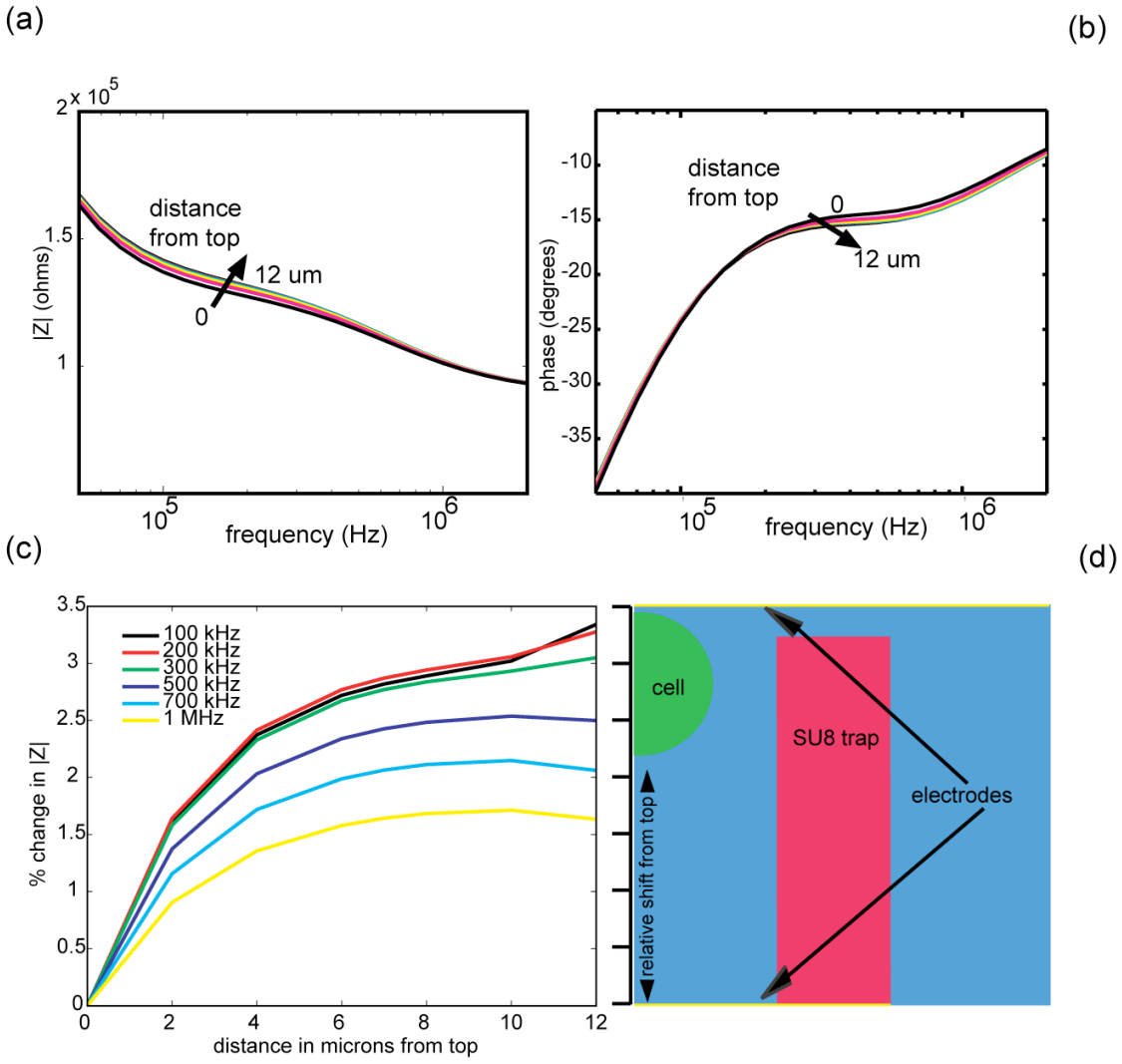

Figure 3-13 (a) Effect of cell vertical shift between two electrodes on impedance spectrum and on the phase response in (b): spectral changes are most pronounced in the 10^5 – 10^6 range in the |Z| response as was the case for changes in cell size and membrane conductivity. (c) Effect of vertical shift of the trapped cell on impedance spectrum (sampled at individual frequencies between 100 kHz and 1 MHz): The % changes with respect to a cell lodged on the topmost position tail off as soon as the cell become 'shielded' by the SU-8 structure. (d) Graphical

representation of the simulation scenario: the simulated space has axial symmetry. The cell, modelled as a sphere of 15 μm diameters is shifted along the y-axis, between two electrodes spaced 30 μm apart.

Calculations are carried out to estimate the effect that pore forming toxins such as Streptolysin-O (SLO) have on the measured impedance response of a single cell:
Assuming that SLO has a single pore-conductance similar to that of Perfringolysin-O (PFO), which belongs to the same family of cholesterol-dependent cytolysin (CDC) toxins, and has a single pore conductance (*G*) of 4.5 nS (as measured by patch clamp in [44]) the conductivity of the cell membrane porated by a single SLO toxin pore can be estimated to have a conductivity of 32 nS/m, assuming in the calculation a cell diameter of 15 μm, a cellular membrane 5 nm thick:

$$G = \sigma \frac{A}{l} \tag{3-3}$$

$$\sigma = G \frac{l}{A} \tag{3-4}$$

$$\sigma = 4.5 \cdot 10^{-9} \frac{5 \cdot 10^{-9}}{\pi \cdot \left(\frac{15 \cdot 10^{-6}}{2} \right)^2} = 4.5 \cdot 10^{-9} \times 7.0736 = 3.18 \cdot 10^{-8} \left[S/m \right] \tag{3-5}$$

Clearly the insertion of single pores cannot be detected by impedance spectroscopic analysis: as shown by simulation results (Figure 3-10,Figure 3-11,Figure 3-12), even in the frequency range where changes in |Z| are most pronounced in response to changes in membrane conductivity (100kHz to 1MHz), for changes in the impedance spectrum to be detectable (i.e. higher than 1%), the membrane conductivity needs to be as high as 1 x 10^{-5} S/m.

The effect of multiple pores on the overall impedance response of the cell is not linear, so FEM simulations combined with analytical calculations are needed to predict their effect on the overall cellular impedance response, and vice versa, to establish the number of open pores on the cellular membrane from the measured impedance response. The simulation results shown in Figure 3-14 demonstrate that the impedance response is quite insensitive to the insertion of a small number of pores, but can be used to quantify the effect of many thousands of pores, with some confidence, assuming that other cellular parameters (such as cell shape and size) don't change.

Hence it can be calculated that it takes the insertion of $1x10^3$ pores for the overall impedance magnitude to change by 2%, and of a $2\ x10^4$ pores to elicit changes in |Z| at 300 kHz of the order of 10% - in turn corresponding to a packing density of the pores of 1 and 30 per μm^2, respectively.

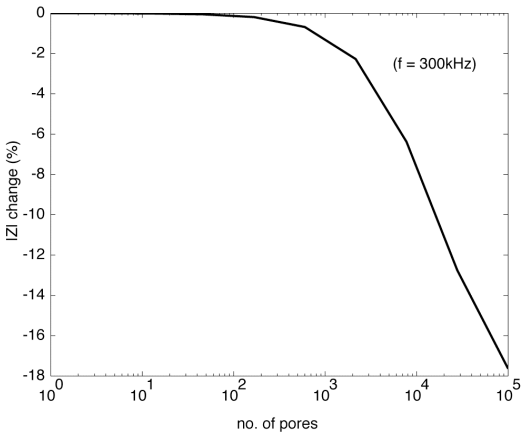

Figure 3-14 Modelled change in magnitude of impedance of a trapped single cell, sampled at 300 kHz, induced by the introduction of SLO pores in the membrane. The magnitude of the impedance is not sensitive enough to detect the insertion of 100 pores or less in the membrane.

3.5 Experimental setup

3.5.1 Microfluidic assembly

The chip was held in a PCB with spring-loaded connectors (SAMTEC SEI series) to contact the electrode pads and connected to a pump and impedance analyzer as shown in Figure 3-2(a). Cells were observed with a microscope. Impedance signals were acquired using two 8-way integrated multiplexers (ADG608, Analog Devices), controlled by MATLAB via a USB interface. The impedance of each trap was measured using an impedance analyzer (Novocontrol Alpha-N) controlled by MATLAB via a GPIB interface. Microfluidic ports were made by punching 27G holes in small casts of PDMS. These ports were aligned and bonded to drilled holes in the upper glass surface.

3.5.2 Data acquisition and multiplexing procedure

In a typical experiment, the impedance spectrum was continuously recorded (in time) over the frequency range 100 Hz to 2 MHz, in 50 steps logarithmically spaced. The signal was multiplexed from 8 active trapping electrodes and their respective 8 reference electrodes. The corresponding active (or 'master') and reference spectra acquired for each pair and at each point in time were stored in individual files to be later post-processed: the 'active' spectrum was normalized by the 'reference' spectrum to eliminate the influence of electrolyte contributions which result from temperature, ionic composition and pH changes.

To analyze transient changes occurring to specific cellular components - such as the conductivity of the cell membrane- in response to a give chemical stimulus, it is useful to isolate a frequency or range of frequencies of interest and analyze their changes over time. Based on the FEM simulations reported in section 3.4, the normalized magnitude of the impedance sampled at f = 300 kHz was used to assess dielectric changes to the shell of captured polyelectrolyte microcapsules (as shown in section 3.8) responding to abrupt changes in pH and conductivity of the perfused solution, as well as to the membrane of captured single cells (as shown in section 3.6) responding to the perfusion of pore-forming toxins.

Figure 3-15 illustrates the functional role of the pair of electrodes patterned on each trap, as well as the way the data was subsequently stored and analyzed.

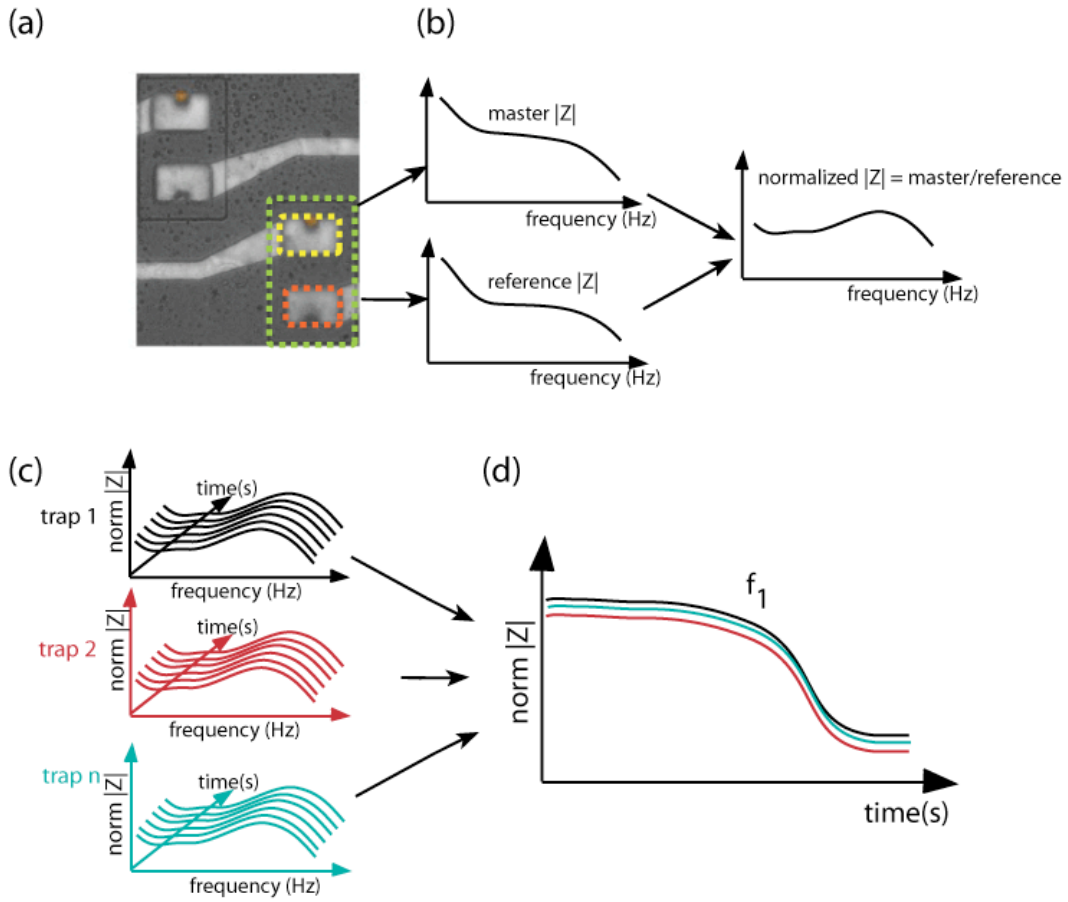

Figure 3-15 Multiplexing and data acquisition steps: (a) each trapping site consists of a pair of traps, one open in the direction of the flow ("master", marked in yellow), the other open in the opposite direction ("reference", marked in red). As the cells flow from top to bottom, only the "master" traps can capture them, while the "reference" traps always stay empty. (b) Full impedance spectra are continuously acquired from both electrodes and saved in individual files, unique to each point in time and acquisition electrode. Master and reference spectra are subsequently used to produce a normalized spectrum to eliminate spurious electrolyte contributions. (c) data from multiple trapping site (up to 8) is acquired by multiplexing the signal from 16 electrodes to the dielectric analyzer. From each trap location impedance spectra are recorded continuously in time, for as long as the experiment is running. (d) A single frequency or a narrower range of frequencies can be selectively plotted against time, to study changes occurring to specific cellular parameters, as cells undergo changes brought on by specific chemical stimuli.

3.5.3 Cell culture, medium and toxin preparation

HeLa cells (Human Negroid cervix epitheloid carcinoma) were cultured in DMEM culture medium (4mM L-glutamine, Hepes buffer, no Pyruvate (Sigma)) with 5% foetal calf serum (Gibco) and 100 μg/ml Penicillin/Streptomycin (Gibco). The cells were grown in 75cm^2 flasks with 50 ml of culture medium. These were incubated at 37 °C and 5% CO_2. To maintain good cell growth, the cells were split every 3rd or 4th day. The cells were detached from the culture flask by trypsinisation: the culture medium is removed and ~7 ml of Trypsin-EDTA (Gibco, 0.25% Trypsin, 1mM EDTA) added to the flask; this is then be incubated for about 5 minutes at 37ºC and the cells are periodically checked with a microscope. Finally, 10 ml of culture medium are added to the flask to neutralize the Trypsin. To suspend the cells in Phosphate Buffer Saline (PBS) solution, the trypsinized cells in the medium were aspirated from the flask and pipetted into Falcon™ Conical Centrifuge Tubes (BD Biosciences). They were centrifuged for 5 minutes at 1000 RPMs. The supernatant aspirated and disposed of. The pellet was then resuspended in PBS.

Streptolysin-O toxin (Sigma) was prepared by mixing to concentrations of 100 kU/ml, 10kU/ml and 100 U/ml in PBS and mixed with 100 mM DTT (dithiothreitol). DTT was necessary to activate the toxin, by creating a reducing environment for cysteine residues.

3.6 Experiments on HeLa cells.

HeLa cells (suspended in PBS) were injected at a volumetric flow rate of 10 μl/min through the device and when captured by the traps said rate was set to 1 μl/min to keep each cell lodged into a trap while maintaining a slow constant perfusion flow of fresh medium; an impedance change was measured as shown in Figure 3-16, which shows the average response measured for 7 different single cells at a frequency of 300 kHz. Typical increases in |Z| ranged from 20% to 30%, consistent with simulation results (data not shown). Error bars show one standard deviation, which can be attributed to cell-to-cell variability, and to a lesser extent to variations in the position of the cell within the trap.

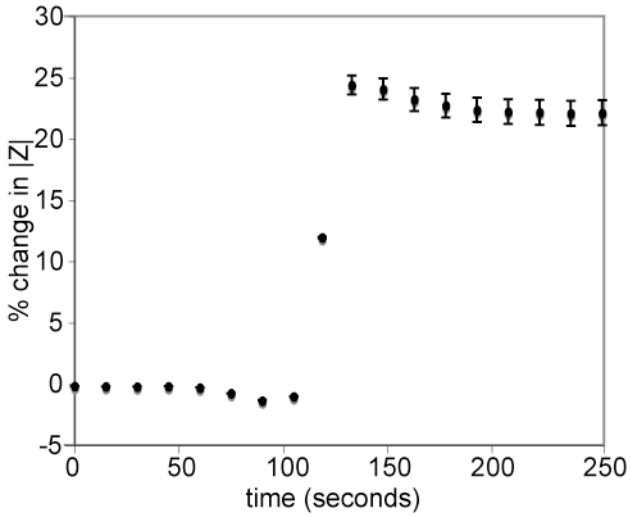

Figure 3-16 Change in the magnitude of the impedance (f = 300 kHz) when cells are captured. Error bars are one standard deviation for 7 cells

In order to demonstrate cell poration, HeLa cells were captured in the traps and perfused with PBS containing different concentrations of Tween 20, a nonionic surfactant that porates and eventually disrupt cell membranes [45, 46]. The effect of different concentrations of Tween on the magnitude of the impedance (measured at 300 kHz) is shown in Figure 3-17. A solution of 1% w/w causes complete cell lysis resulting in a large sudden decrease in impedance magnitude (25% over 10 seconds), Figure 3-17 (a). Prior to lysis, there is a short increase in the impedance, which is attributed to swelling of the cell, as confirmed optically. Presumably, water enters the cell through the disrupted membrane, and then the cell bursts. A lower concentration of Tween 20 (0.01% w/w) causes a gradual decrease in the impedance (4% over 100 seconds), as shown in Figure 3-17 (b).

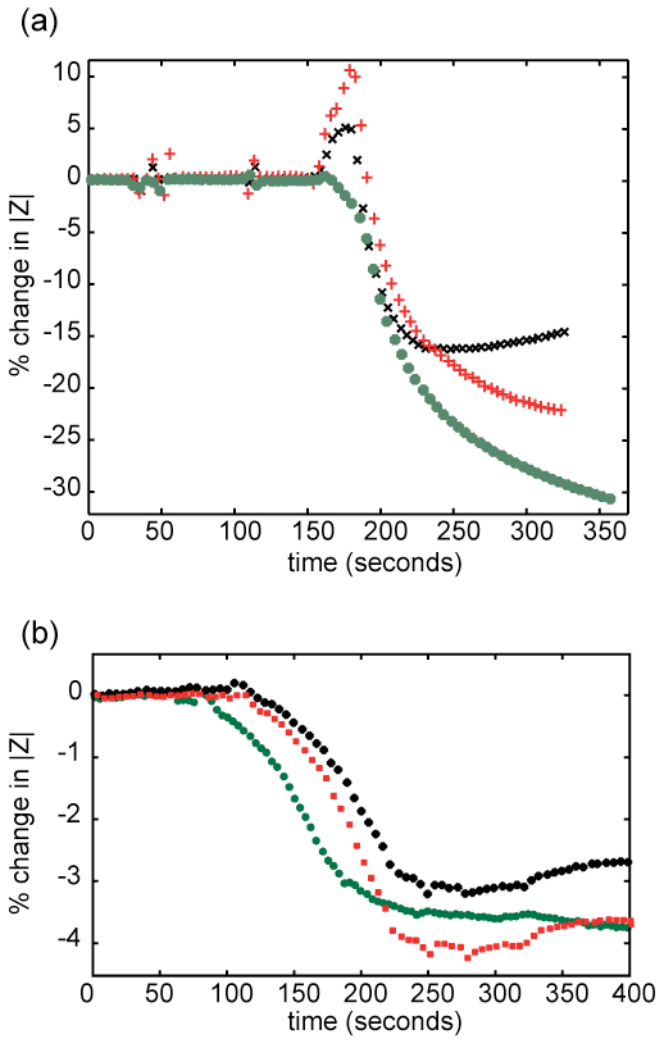

Figure 3-17 Change in the magnitude of the normalized impedance (at *f*=300 kHz) of three individual cells plotted against time showing the typical change in impedance when single HeLa cells are perfused with Tween 20. (a) 1% w/w Tween20 causes a differential |Z| change (at 300 kHz) of 20% - 30 % in 20-50 seconds. This decrease in measured impedance is consistent with the impedance increase registered for the cell capture event, shown in Figure 3-16: effectively, a cell lysed with 1% Tween20 becomes electrically transparent after 300 seconds. A transient increase in |Z| of the order of 5%-10% occurs before poration probably due to transient osmotic swelling. From simulation data, a 10% increase in impedance magnitude can be ascribed to an increase of less than 1μm in cell radius. Such a minute change would be difficult to detect optically unless observing the cell understudy through a high magnification objective (i.e. > 50x). (b) 0.01% Tween 20 causes a differential |Z| change (at 300 kHz) of 3-5 % in 150 seconds

When cells were perfused with DTT-activated SLO (in PBS) in quantities ranging from 100 U/ml to 10 kU/ml a similar change in impedance magnitude was

recorded as shown in Figure 3-18. The definition of one *unit* is that quantity which will cause 50% lysis of 50 μl of a 2% red blood cell suspension in phosphate buffered saline, pH 7.4 after incubation at 37 degrees for 30 minutes. DTT was necessary to activate the toxin, by creating a reducing environment for cysteine residues.

A solution of 100 U/ml causes an initial increase in impedance (cell swelling) followed by a gradual decrease; 1 kU/ml had a similar but more pronounced effect. The decreases could be fitted by a single exponential decay with characteristic times in Table 1. In general, higher concentrations of toxin cause faster decays, and the final value of impedance is the same for each case as the cell is porated and becomes electrically opaque.

SLO concentration	Time constant		statistics	
	value	error	Chi-Sqr	R-square
10 kU/ml	29.83106	3.03921	1.81E-04	0.8792
1 kU/ml	151.5457	5.27479	2.92E-05	0.9804
100 U/ml	482.4297	75.87931	1.30E-04	0.59458

Table 3-1 Exponential decay time constants are fitted to the data for the impedance response of single cells to SLO toxin. The decay time constants span from 30 seconds to 480 seconds

This data indicates that the final value of the impedance magnitude is independent of the toxin concentration in the solution. Unlike the data for the Tween, where the cells are completely lysed, the change in impedance is not as great. The rate of change in impedance and therefore the rate of pore insertion were significantly faster for the higher concentration solution (10 kU/ml in 20 seconds). From simulation, the magnitude of the change in impedance can be correlated with a change in membrane conductance (assuming no other parameters change). The recorded value of 10% change in impedance magnitude at 300 kHz is equivalent to the insertion of ~10000 pores. The time constants extracted from the impedance data are consistent with experimental data obtained by fluorescence assay [47], where 10k U/ml and 100 U/ml were found to cause fluorescent intensity loss with time constants of 25s and 150s respectively.

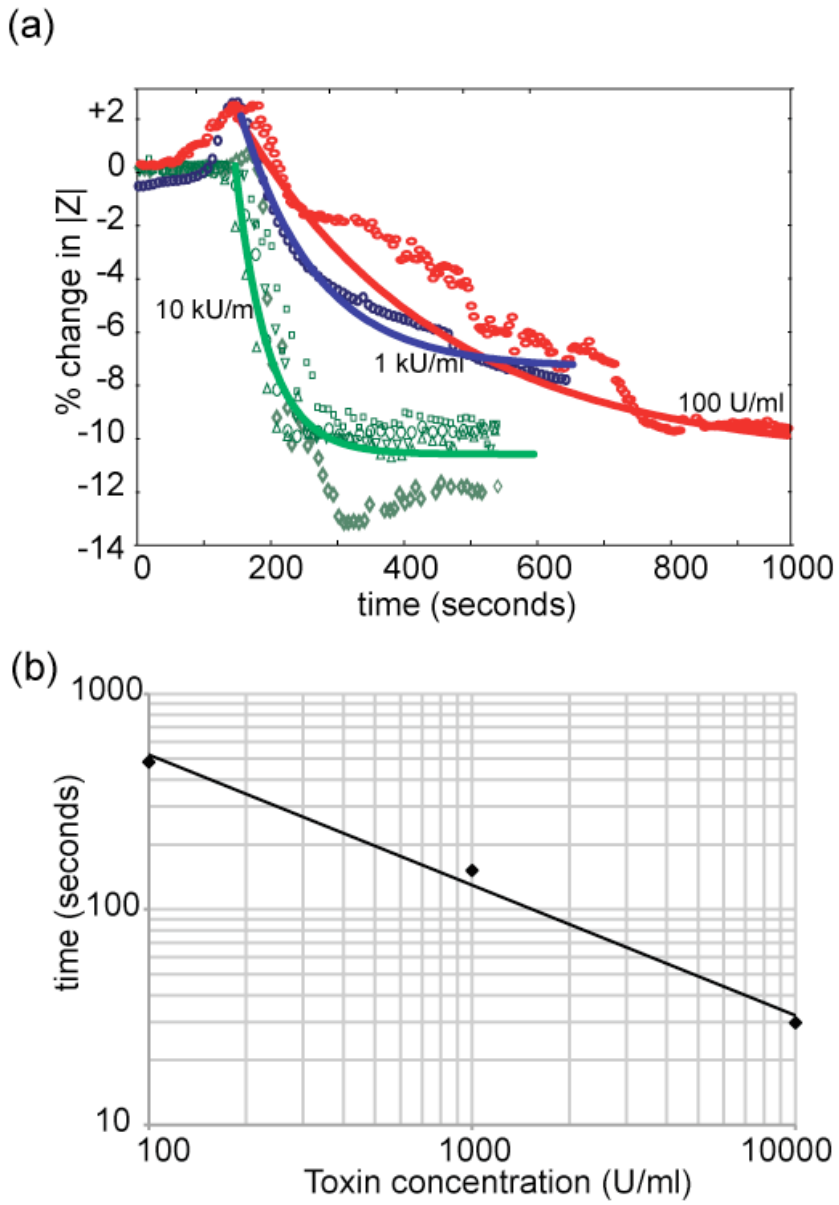

Figure 3-18 Change in the magnitude of the normalized impedance (at *f*=300 kHz) of individual cells plotted against time showing the typical change in impedance when single HeLa cells are perfused with SLO toxin suspended in solution Three different concentrations were assayed and differential impedance spectra were acquired over time at a fixed frequency of 300 kHz. The exponential curves (solid lines) are the average responses for 10 kU/ mL, 1kU/ mL, 100 U/ mL. (b)Time constant of the fitted exponential decay in impedance spectrum at 300 kHz plotted against the toxin concentration. The straight line in the loglog plot shows that the behaviour is characterized by a power law.

3.7 Polyelectrolyte capsules

Polyelectrolyte microcapsules were synthesized using the Layer-by-Layer (LbL) technique pioneered by Decher 10 years ago [48]. The method entails the self assembly of charged polymers onto an oppositely charged sacrificial colloidal substrate followed by final dissolution of the substrate. LBL assembly performed on flat substrates results in multilayer films. LBL can also be performed on beads to obtain hollow microcapsules. Upon adsorption of a polyelectrolyte layer, the surface charge is reversed, promoting the adsorption of a next, oppositely charged, polyelectrolyte, a process illustrated schematically in Figure 3-19

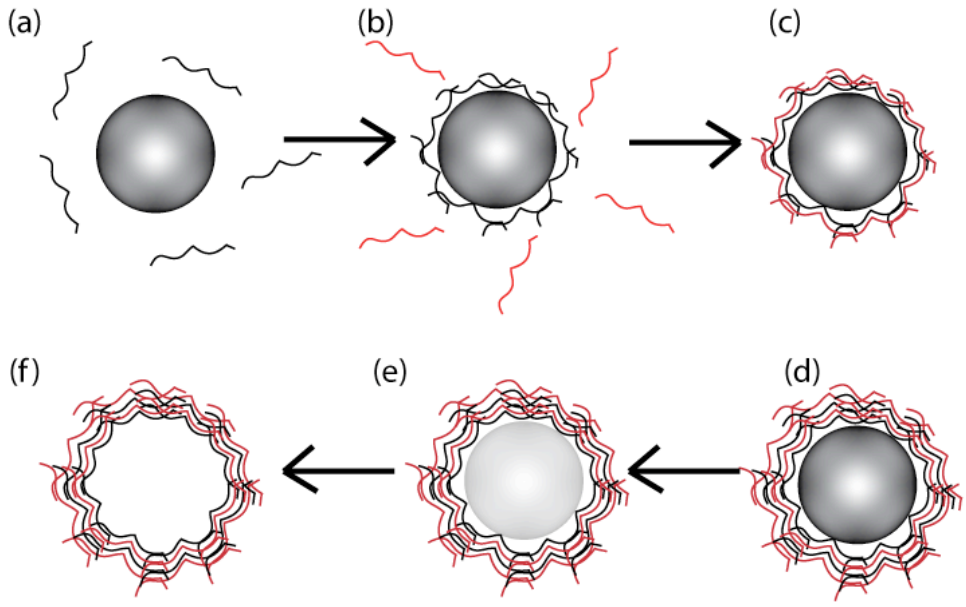

Figure 3-19 Processing steps for the preparation of polyelectrolyte microcapsules. (a) The sacrificial colloids are immersed in a solution with a polyelectrolyte of charge opposite to that of their surface charges. (b) After self assembly of a first film, the medium is replaced with a polyelectrolyte of opposite charge (c)-(d) multiple steps are performed to form as many polyelectrolyte layers as desired (e) once the desired number of films has self-assembled, the coated colloids are immersed in a solvent to dissolve the core. (f) suspended hollow polyelectrolyte microcapsules remain after decomposition of the colloidal core.

By employing different types of polyelectrolyte species at the self assembly stage, it has been shown that it is possible to obtain microcapsules with shells that respond to specific stimuli (such as pH, salt concentration, magnetic field, temperature) that then triggers the capsules to release their contents at a desired site and time. LBL polyelectrolyte shells can also be synthesized to be responsive to the presence of

specific compounds such as glucose or biotin [49, 50]. One of the most attractive uses for such stimuli-responsive polyelectrolyte capsules is their use as bio-compatible vectors for localized and time-controlled drug-delivery. A hollow capsule shell that can change its permeability in response to an external stimulus could deliver microcapsules loaded with a 'cargo' of drug molecules to be released upon exposure to an environment with altered pH, or ionic content, or temperature.

In view of these applications, a technique for characterizing the state of the permeability of the microcapsule shell would be an advantage for perfecting microcapsule preparation protocols. Such a method should allow measurement over an extended period of time, while an external stimulus is provided. Current characterization techniques include the use of X-rays to investigate the internal structure of the polyelectrolyte films [51] and AFM to analyze their surface morphology [52].Neither technique however provides a mean to continuously monitor the permeability of the shell in the presence of an external stimulus. Confocal fluorescence microscopy has been successfully employed to monitor the release of pre-loaded FITC-dextrans [53] varying molecular weights revealing important information, such as the molecular weight of the molecules that can be loaded/released for a given alteration in the provided stimulus. However, the method does not allow monitoring of transient or reversible behaviour, which would undoubtedly be exploited for the remote loading and unloading of cargo into the capsules. An example of such an experiment is represented in Figure 3-20. Empty capsules flow into a small volume, become transiently permeable to allow uptake of a sample, then flow out loaded with a cargo to be re-released later in a different environment.

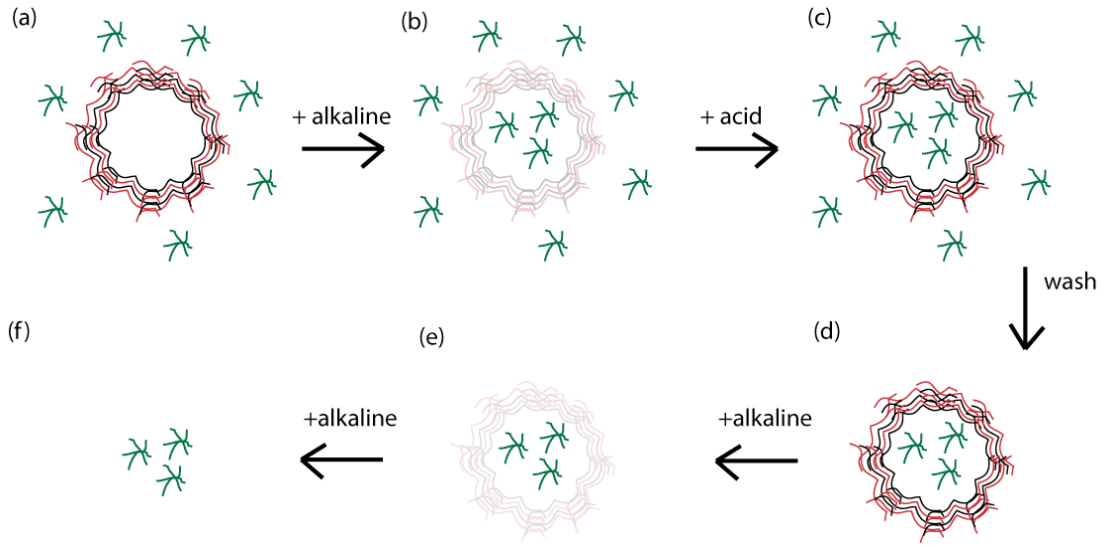

Figure 3-20 Possible mechanism for loading and unloading of a molecular cargo into the pH responsive hollow microcapsules. (a) the formed hollow microcapsules are incubated in a pH neutral with the molecules to be loaded (b) as the neutral solution is replaced with an alkaline solution (11 < pH < 12), the microcapsule shell becomes permeable, while still maintaining the integrity of the whole capsule. The molecules can flow in and out of the porated shell. (c) as a lower pH solution is introduced, the capsule shell becomes impermeable trapping the molecules inside. (LOADING). (d) the suspension of loaded microcapsules is washed in a pH neutral solution. (e)-(f) to release the loaded molecular cargo, the capsules can be suspended in a highly alkaline bath (pH > 12) which will dissolve the shell .

Antipov. and Dejugnat studied the pH-dependent behaviour of PSS/PAH-based polyelectrolyte capsules extensively [54, 55]. They showed that the physico-chemical mechanism underlying the change in shell permeability of the microcapsules. When the environmental pH becomes higher, for the case of a poly-base polymer coating, or lower, than the pKa for the case of a poly-acid, the polyelectrolytes become uncharged, forming pores in the membrane, which when uncontrolled, disassemble the capsules. It is possible to reverse, or fine-tune, the poration process by carefully controlling the environmental pH. Exploiting this property, Sukhorukov et al. filled PSS/PAH capsules with FITC-dextrans while the capsules were in a 'permeable' state, at low pH. By successively increasing the pH of the solution dextrans were entrapped in the capsules [53].

Interestingly, the pH dependent change in permeability of capsules containing weak polyelectrolytes is accompanied by swelling of the capsules when the pH is shifted towards the pK_a of one of the polyelectrolytes. In experiments performed in bulk solution, PSS/PAH capsules started to swell when the pH was above 11 and disassembled when the pH was above 12 [56].Similarly, the same capsules, when exposed to pH levels lower than 11 rapidly shrink and become impermeable to high molecular weight compounds.

In summary size change of the capsules correlates with shell permeability: at pH > 11 the capsules swell and their shell become permeable, when exposed to pH <11, they shrink and become impermeable. Such extreme levels of pH do not occur naturally in mammalian cells, where pH levels are much closer to a neutral level of 7. It is therefore a challenge for chemists to design polyelectrolyte capsules with shells capable of altering their shell permeability following much less drastic changes in pH.

Microcapsules were used as surrogates for biological cells, to test the microfluidic device. They can be synthesized in the right size for the trap (around 10μm diameter). Their porosity can be changed as alkaline buffer disassembles the polyelectrolyte matrix.

The ultimate purpose of the device is to trap cells and measure changes in impedance induced by the application of external stimuli. Therefore pH responsive microcapsules are a good model for to monitoring transient changes after injection of solution at high pH, leading to changes in shell permeability.

3.8 Measurement on polyelectrolyte capsules in bulk

3.8.1 Experimental observations with bright field microscopy

An initial experiment was carried out in bulk to confirm that the predicted behaviour of the microcapsules was measured experimentally.

Polyelectrolyte microcapsules were synthesized using the Layer-by-Layer (LbL) technique [48] following the protocol provided by of Sukhorukov [57], employing a poly(styrene sulfonate)/poly(allylamine hydrochloride) polyelectrolyte pair (PSS/PAH) and 10 μm diameter Polystyrene beads as substrates.

The experiment was carried out as follows: the capsules were synthesized in neutral acidity buffer (pH = 7), and while kept in a Petri dish imaged under bright field microscopy (Figure 3-21).

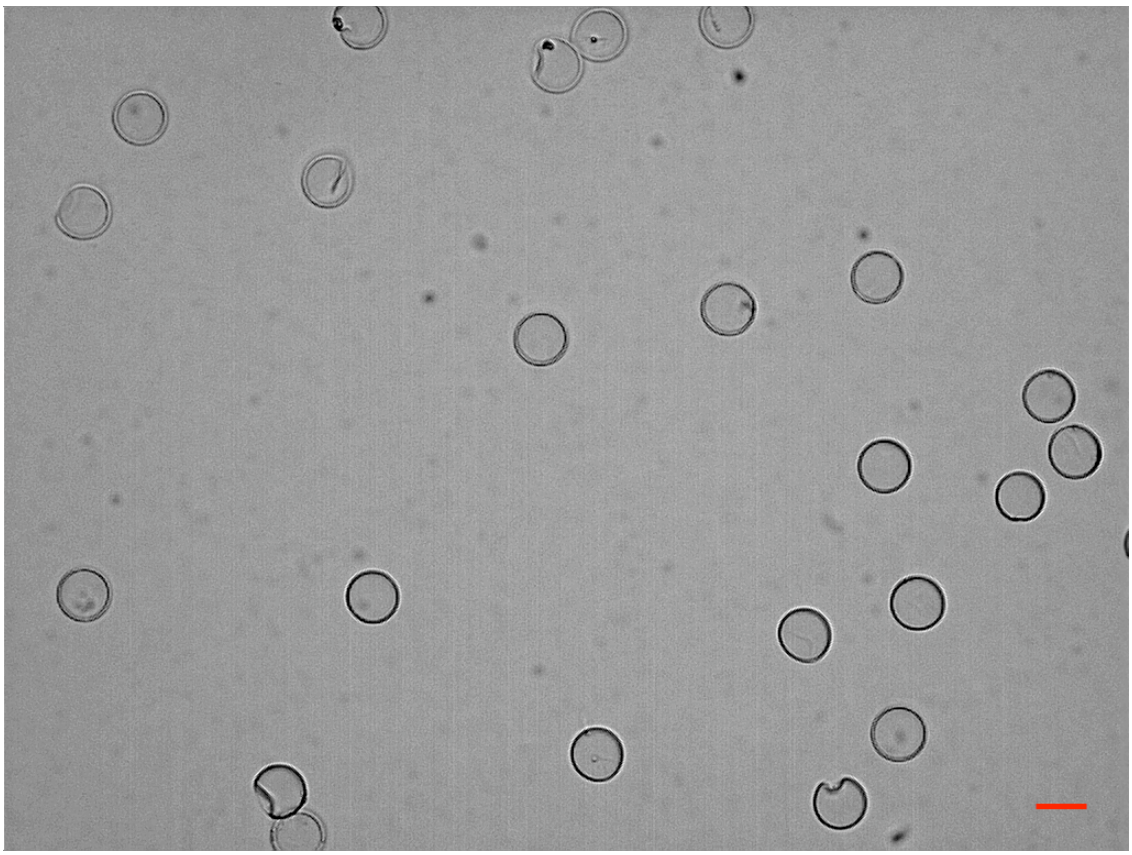

Figure 3-21 PEL microcapsules suspended in PBS at pH = 7, imaged in bright field microscopy. Scale bar = 10 μm.

Several field of view images were acquired, stitched together and the images processed with ImageJ image processing software package to measure the mean diameter of the synthetized capsules. The capsules were found to have a mean diameter of 10.05 μm (standard deviation = 0.48 μm, n =100).

Subsequently, and while continuously acquiring imaging data, the phosphate buffer saline acidity was adjusted to pH= 11 with the addition of NaOH in the dish. The capsules mean diameter increased on average by 20%, to 12.07 μm (standard deviation = 0.58 μm, n =100) and their shell appeared thinner within 1 second after the initial perfusion. At t =7 seconds, the capsules were reperfused with HCl to bring the overall pH of the suspension solution below pH = 11. The capsules were found to shrink for about 20 seconds until a steady state was reached. At t = 30 s, the mean diameter of the capsules was 8.08 μm (standard deviation = 0.5 μm, n =100). This behaviour is consistent with that previously reported in the literature [56]. Sample time-stamped images from this experiment are shown in Figure 3-22

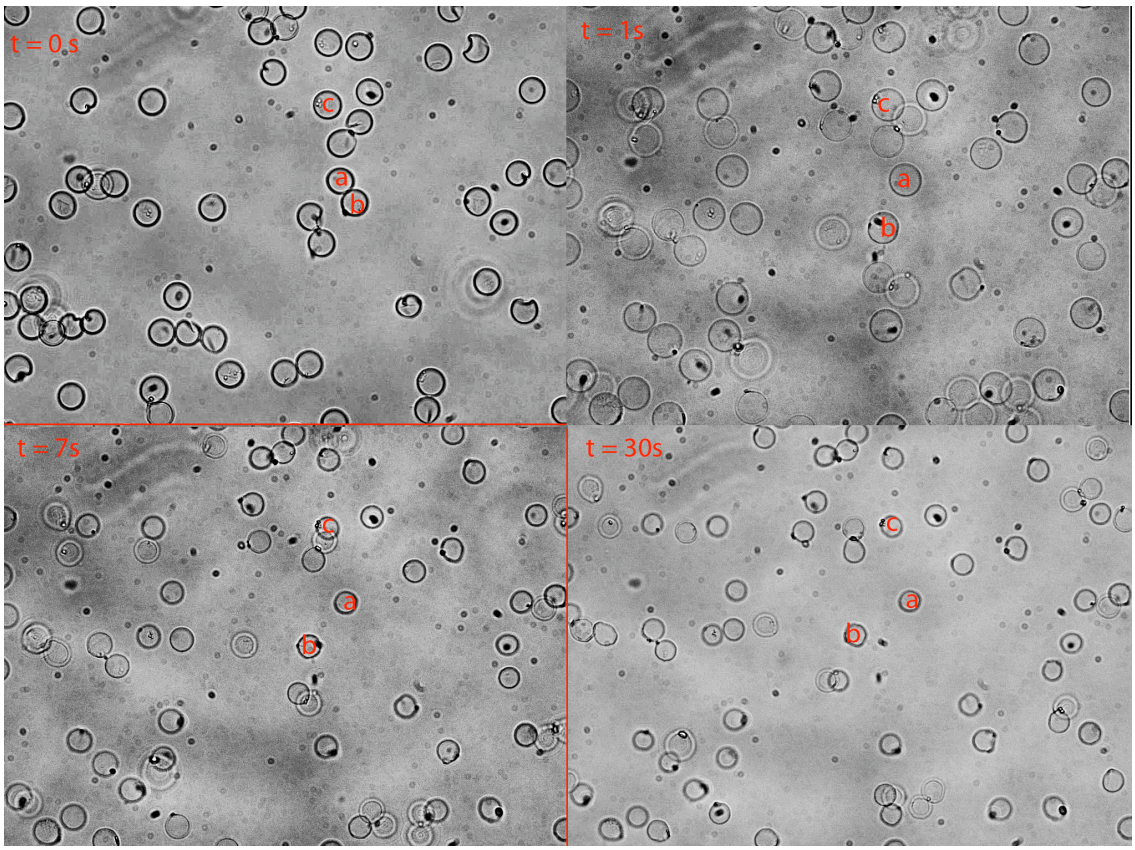

Figure 3-22. Evolution of PEL capsules synthesized in PBS, at pH = 7 and exposed to PBS at pH = 11 at t = 0s. After just one second, the capsules swell to 5-6 times their initial volume, as the integrity of their shells is compromised. At t = 7 s, acid solution was introduced to bring the pH of the suspension solution back to pH = 7. The capsules began to shrink back to dimensions measurably smaller than their original ones, and their shells appeared to have regained the original integrity.

3.8.2 Experimental observations using fluorescence microscopy

As in the experiment reported in the previous section, polyelectrolyte microcapsules were synthesized using the Layer-by-Layer (LbL) technique [48] following the protocol provided by of Sukhorukov [57], employing a poly(styrene sulfonate)/poly(allylamine hydrochloride) polyelectrolyte pair (PSS/PAH) and 10 μm diameter polystyrene beads as substrates. Before the polystyrene substrates was dissolved however they were suspended in a solution with Rhodamine 6G (Invitrogen), so that upon core dissolution they would encapsulate the dye. Rhodamine is a water soluble fluorescent dye commonly employed for biological staining studies due to its stability in a wide range of acidity (for example Rhodamine is reported to be insensitive

to pH changes from 2 to 12 in [58]). The emission and excitation spectra of Rhodamine are shown in Figure 3-23.

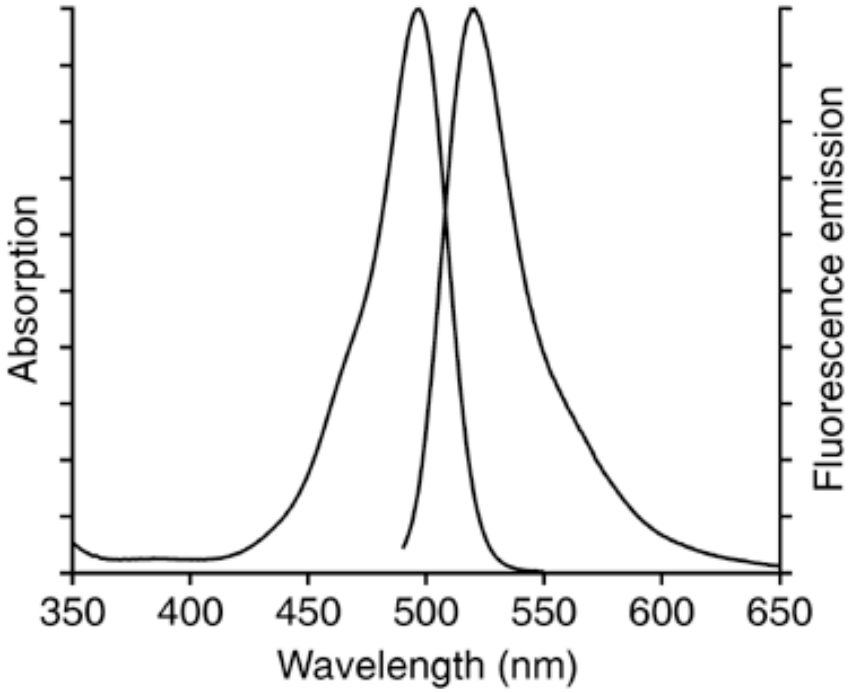

Figure 3-23. Absorption and fluorescence emission spectra of rhodamine in pH 7.0 buffer. Taken from Invitrogen.com

The dye-encapsulating polyelectrolyte capsules were released in a Petri dish suspended in PBS buffer at pH = 7. As in the previous experiment, NaOH was introduced to increase the pH of the solution to 11, while continuously recording the optical microscopy data. Immediately after the introduction of the NaOH the capsules were observed to swell and brighten up (Figure 3-24). Within a second, the capsules were swollen and bright enough to saturate the CCD sensor, and within three seconds their fluorescence had returned to the original level. Of note, the background fluorescence was noticeably increased, most likely due to the fact that dye previously encapsulated in the capsule membrane matrix had been released in the bulk solution.

The sudden increase in fluorescence can be correlated to the porated state of the capsule shell, as it's been shown [59] that PSS, one of the constituent polyelectrolytes in the shells, combines with and quenches the rhodamine dye molecules. Presumably, during the membrane poration, the dye dissociates from the PSS giving origin to a brief burst of fluorescence, before it being dispersed in the bulk solution surrounding the capsules.

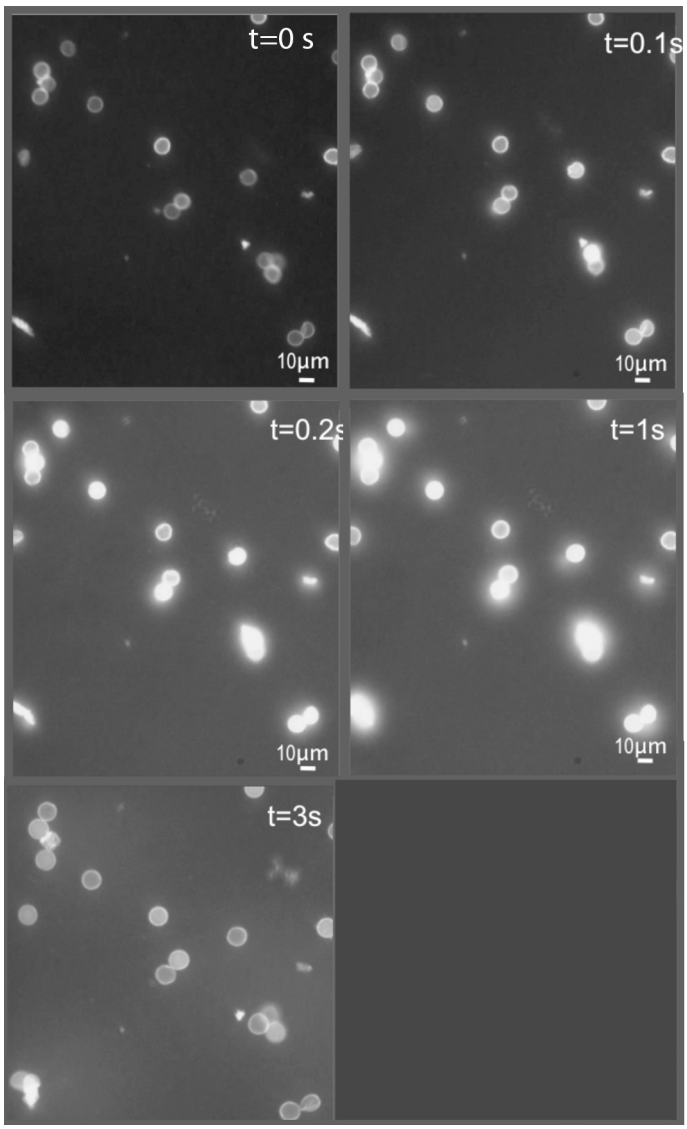

Figure 3-24 Polyelectrolyte capsules encapsulating fluorescent dye (Rhodamine 6G). The permeability of the shell can be assessed from the fluorescence intensity of the capsules as well as from the dielectric response. The capsules, observed in bulk, exhibit a sharp increase in fluorescence intensity within the first second of exposure to alkaline buffer, which causes the capsules shell matrix to enlarge, presumably due to the release of dye from the capsule shell and consequent unquenching of the dye. The background intensity also increases following the dispensing of the alkaline buffer, as the dye previously encapsulated is released in the bulk solution.

3.9 Measurements of polyelectrolyte capsules in the microfluidic device

The cell traps were used to analyze the transient behaviour of the microcapsules as a function of the pH of the medium. The microcapsules, suspended in different dilutions of PBS were introduced into the device at a flow rate of 10 μl/min; upon capture the flow rate was diminished to 1 μl/min; complete impedance spectra were acquired from reference and master trap locations; temporal data was recorded and plotted at a frequency of f = 300 kHz. Figure 3-25 shows collated micrographs of captured rhodamine stained capsule captured in the trapping structured of the microfluidic device.

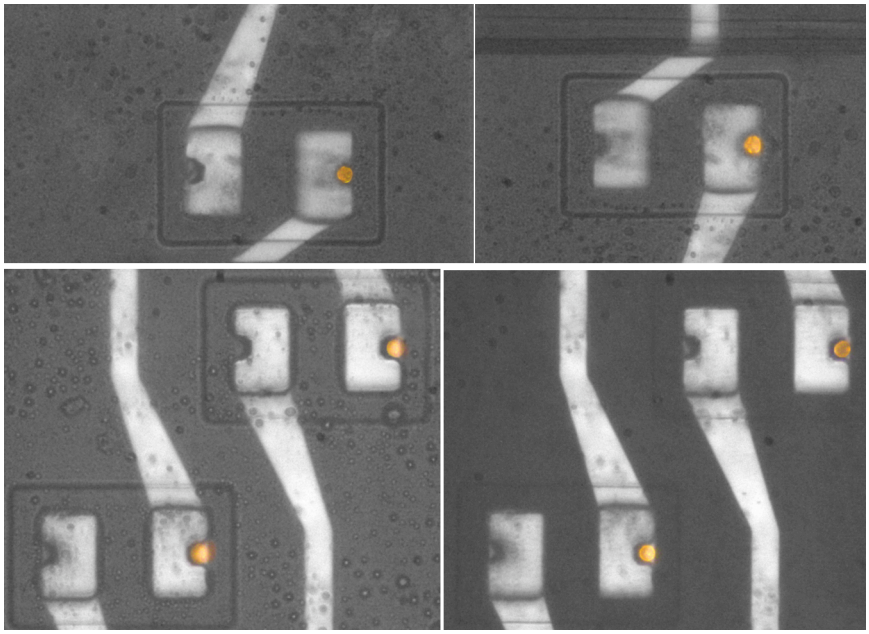

Figure 3-25 Rhodamine-stained polyelectrolyte capsules captured in traps.

Figure 3-26(a) shows four spectra for captured capsules suspended in 1:100 PBS:water solution (conductivity = 12 mS/m). The normalized impedance data sampled at 300 kHz (Figure 3-26) show an average step increase of 12% upon capture of the capsules into the trap. Individual traces show variability that can be attributed only to some extent to variability in the position of the capsules in the traps: it's been previously shown by numerical simulation (Figure 3-13) that changes in position within the trap should yield changes in the measured impedance response no greater than 3%. An outlier trace is visible in Figure 3-26; its elevated value of impedance increase upon

capture (30% above average) could easily be justified by the capsules diameter being 12 μm, instead of the predicted 10 μm. When the experiment was repeated in 100% PBS (conductivity = 1.6 S/m) the measured impedance increases (with respect to values of impedance with no capsule in the trap) were more moderate (4 to 6 %), as shown in Figure 3-26(b). In both cases, once capture had occurred, the impedance was relatively stable and did not change over the course of ten minutes or more, while the capsules were held in the traps by the medium being continuously perfused at a flow rate of 1 μl/min.

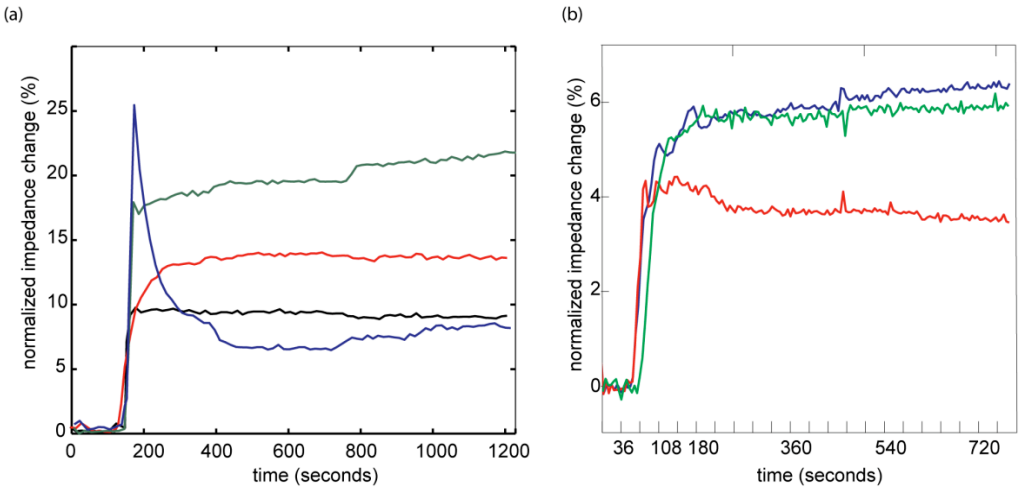

Figure 3-26 Normalized impedance changes (sampled at f = 300 kHz) as a function of time. The step changes are caused by the capture of polyelectrolyte microcapsules. Different colour traces indicate different capture events occurred in the course of the same experiment. (a) Capture of microcapsules suspended in diluted PBS (sigma = 12mS/m). (b) Capture of microcapsules suspended in PBS (sigma = 1.6 S/m)

After capturing the microcapsules (in PBS, pH 7.2), a solution of the same conductivity but with a pH value adjusted to 11.2 by the addition of NaOH was flowed into the device. Figure 3-27 shows the normalized impedance change (at 300kHz) as a function of time for the response of the captured microcapsules to the perfusion of alkaline medium: a decrease in normalized impedance, which ranges from -3% to -7% is induced. Observation of the capsules showed that they had swollen at the same time, confirming the observation of capsules behaviour in bulk. As the impedance at 300 kHz would be expected to increase in response to an increase in capsule radius, and decrease in response to an increase in permeability (caused by the perfusion of the alkaline solution), the two effects are antagonist.

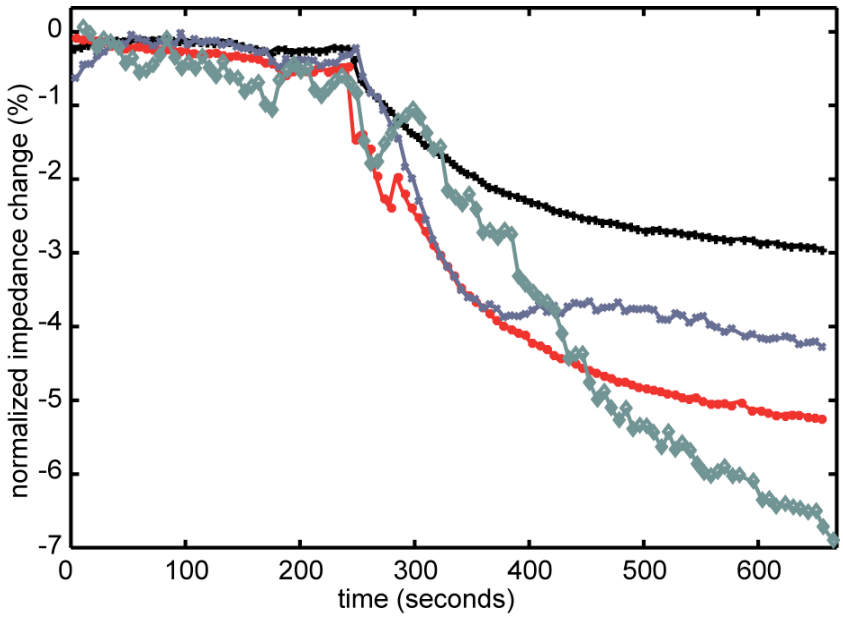

Figure 3-27 Normalized impedance changes (sampled at f = 300 kHz) as a function of time, for polyelectrolyte capsules suspended in diluted PBS (sigma = 12mS/m). Different color traces indicate different capsules monitored in the course of the same experiment. The sharp decrease in impedance suggest that the capsules are porated in response to perfusion of pH 11 solution,

From the optical observations in the bulk experiment, where capsules increases in diameter of the order of 20% was observed, it is possible to extrapolate a related increase in impedance of 15% (referring to the numerical simulations discussed in section 3.4). The fact that an average net decrease in impedance of 4.75% was recorded indicates that the poration of the shell would have caused, on its own, a decrease in impedance of almost 20%. This would indicate an increase in shell permeability of two orders of magnitudes, yielding the membrane conductance change to change from a modelled value of 1 μS/m to 100 μS/m.

Rhodamine-fluorescent capsules were also introduced in the microdevice to establish whether the change in measured impedance could be correlated to the sudden change in fluorescence observed in the experiment in bulk described in the previous section. As shown in Figure 3-28, following the introduction of an alkaline solution the level of fluorescence increases suddenly, followed by an exponential decrease. The sudden increase is due to unquenching of the dye, which results when it is released from the lattice of the PSS shell of the capsule; the consequent decrease is due to slow release of dye, which diffuses away into the bulk solution. Perfusion of a solution of pH 12 leads to much more abrupt membrane poration and a sharper decrease in fluorescence. The capsules therefore show transient responses that correlate to the

degree of alkalinity of the solution perfused, although it was found that perfusion of a solution with pH > 12 caused irreversible capsule destruction.

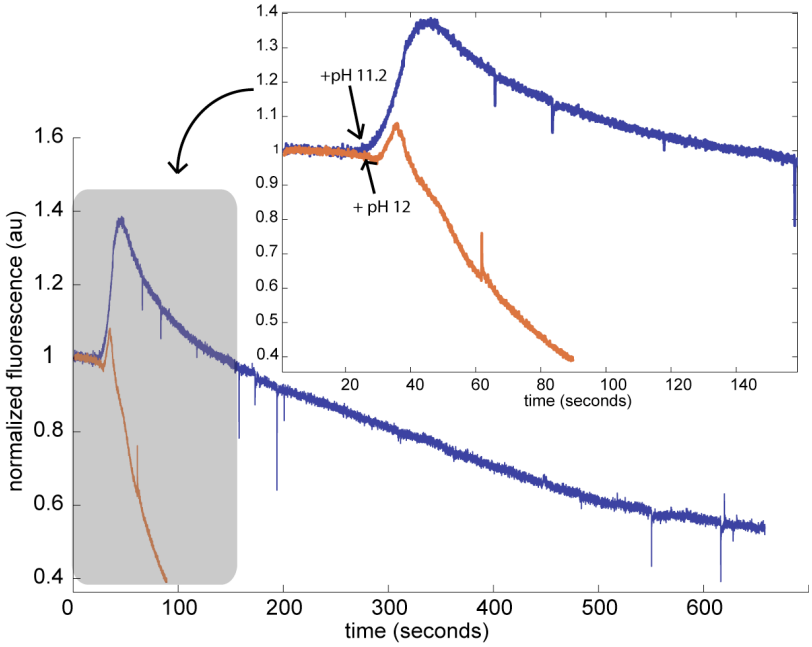

Figure 3-28 Fluorescence levels of Rhodamine-stained microcapsules, as a function of time: in response to perfusion of solutions of pH 11.2 and 12 a sudden burst of fluorescent intensity is followed by a steady decrease, at a rate dependant on the alkalinity of the solution perfused. In the inset, details of the main plot are represented. The perfusion of pH 12 buffer causes the capsule's shell to deteriorate at a much faster rate. The level of fluorescence was quantified by sampling the luminosity level in the red channel of the capsule and normalized to a reference sample to take into account photo-bleaching of the dye.

When the fluorescence and impedance data was recorded simultaneously, a degree of correlation was observed. The transient increase in impedance occurs when the capsules quickly swell giving a fluorescence "burst". The gradual decrease in impedance that follows is due to the increase in the permeability of the membrane. The decrease in fluorescence measures diffusion of the dye. (Figure 3-29). It's difficult to confirm this data unequivocally by means of impedance spectroscopy because, as previously mentioned, the swelling causes an increase in impedance, whereas poration of the shell causes a decrease, two contrasting effects that mask each other.

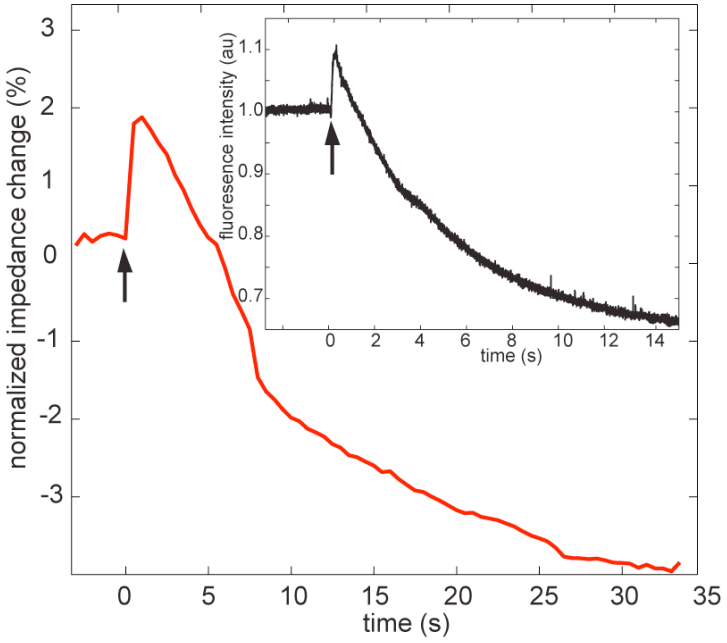

Figure 3-29 Changes in impedance (main plot), in response to perfusion of solutions of pH 11.2 correlate well with changes in fluorescence (inset plot) . A transient swelling can explain the temporary increase in impedance, while the poration of the shell would explain the subsequent impedance decrease.

3.10 Localized generation of pH gradients

One use for the device is the capability of addressing/measuring each single trap independently. The electrodes can be used for measuring impedance, but also to provide an external stimulus through an applied potential. When a DC potential is applied between an electrode lying underneath a captured group of capsules and the common ITO ground electrode the voltage generates a pH gradient leading to changes in permeability of the capsules, mimicking the electrochemically induced lysis that occurs when mammalian cells are subjected to pH gradients: The dominant mechanism for electrochemical cell lysis is the cleaving of fatty acid groups of cell membrane phospholipids by hydroxide ions that are electrochemically generated at the cathode [60]. Capsules captured in neighbouring traps were monitored and their fluorescence level used as control. The fluorescence traces and corresponding images are shown in Figure 3-31. The fluorescence level of the control capsules only decreases slightly (by 5%, probably by photo-bleaching of the dye), the fluorescence of the exposed to the increase in pH dropped sharply when a DC potential of 1.7 V was applied. The

fluorescence continued to drop, (although at a slower rate) after the DC potential was removed.

The change in fluorescence after the application of high voltages (2 V) at DC and at AC (10 kHz and 100 kHz) was also measured. Fluorescence traces are shown in Figure 3-32. The sharpest decrease in fluorescence occurred when the potential was DC. However, capsules were also found to lose their fluorescence upon application of AC voltages, indicating successful poration at a rate inversely proportional to the applied frequency. This experimental finding empirically confirms the experimental results presented by Menachery et al. [61] (Figure 3-30) who used DEP force to burst the membrane of mammalian cells and reported that the magnitude of the electric field dropped across the cellular membrane is inversely proportional to the frequency of the voltage applied at the electrodes.

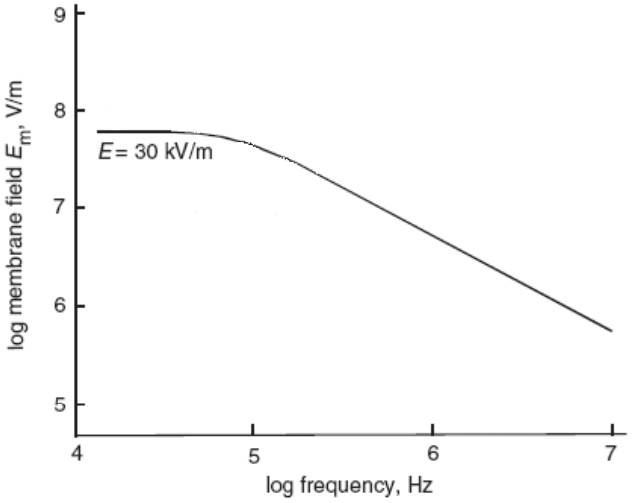

Figure 3-30 Induced field membrane variation vs. frequency of applied field at the electrodes. Taken from Menachery et al. [61]

Because the application of DC voltage tends to damage the patterned electrodes, it would be preferable to use AC potentials for the localized poration and lysis of cells. Indeed and Gascoyne and Vykoukal [62], have also demonstrated that it is feasible to lyse cells by applying large AC potentials.

This device could be used as a platform for the continuous impedance spectroscopic monitoring of cells responding not only to chemical stimuli, but also to the generation of local electric field for the controlled membrane poration and/or lysis.

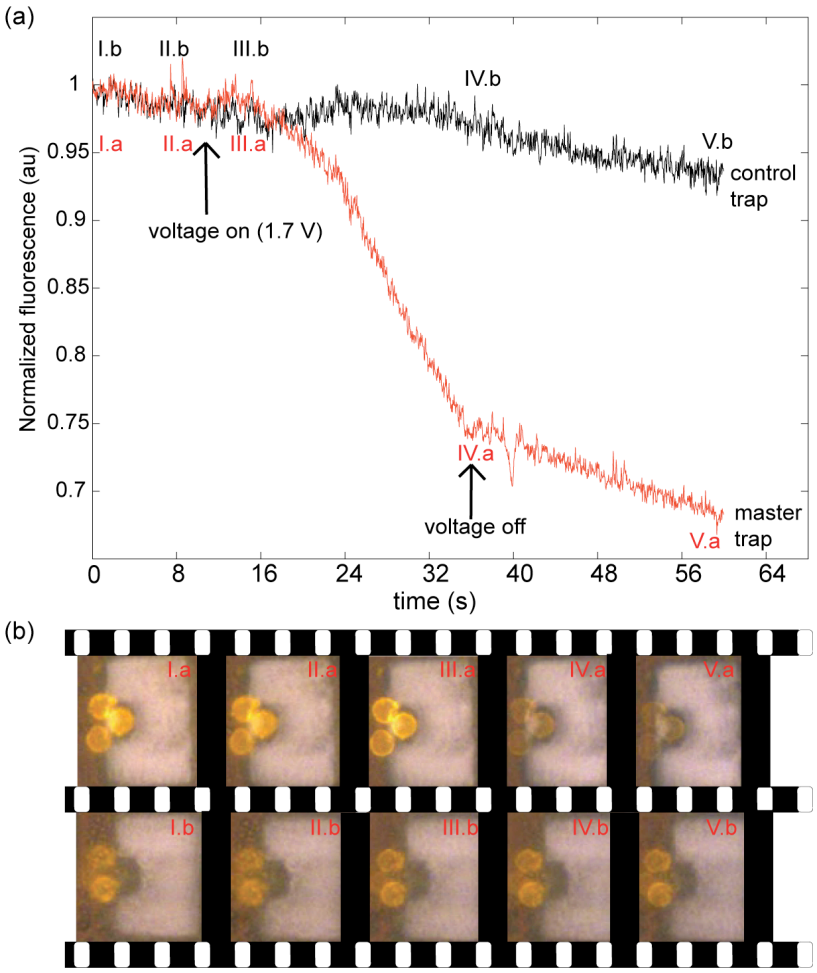

Figure 3-31 Effect of DC potential on polyelectrolyte capsules. In (a) fluorescence traces are shown for a trap filled with capsules (red) and neighbouring inactivated trap, also filled with capsules. As a DC potential is applied, electrolysis occurs and an electrochemically OH gradient forms between the electrode address and the large common ground electrode. In a few seconds the localized altered pH environment causes the addressed capsules membrane to porate and release the encapsulated dye. In (b) screenshots of a captured video are shown for the addressed trap (top) and the control trap (bottom).

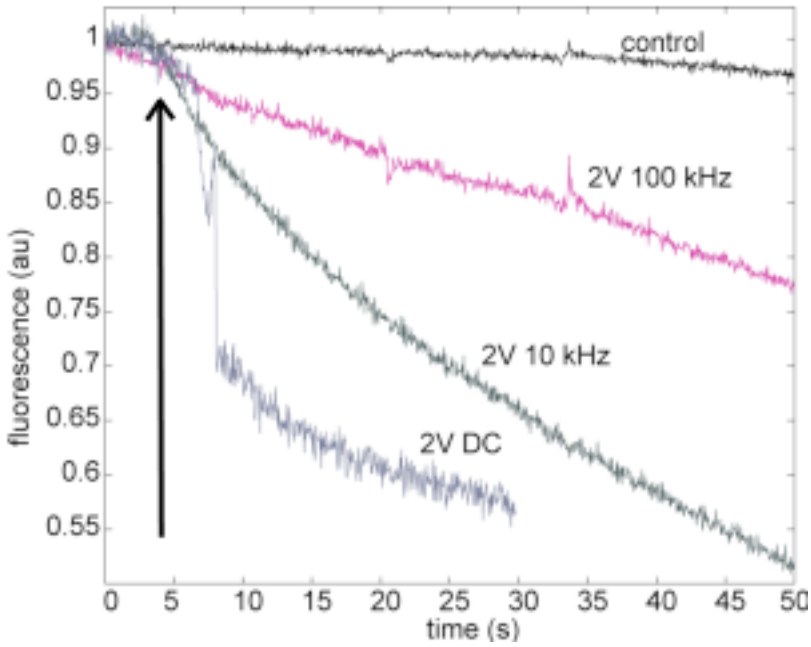

Figure 3-32 Effect of DC and AC potential on captured polyelectrolyte microcapsules. A 2V DC potential cause a visible reaction to occur and a quick poration of the capsule captured within the addressed trap. AC voltages at 10 kHz and 100 kHz also cause poration of the addressed capsules, without a visible electrolysis reaction. The arrow indicates the point in time when at which field was applied.

3.11 Discussion

Label-free analysis of single cells is unquestionably a challenging task. Although impedance spectroscopy offers potential for highly automatable, scalable, label-free measurements of single cells, important limitations constrain its usefulness and warrant considerations. In this section, after a brief overview of well-established methods for characterizing the effect of toxins on mammalian cells, impedance spectroscopy is compared to two other methods for performing dielectric spectroscopy (electrorotation and dielectrophoresis) in the context of studying toxins. Although widely used to measure steady-state values of membrane capacitance and conductance of cells [63-72], neither ROT or DEP can be used to measure the transient changes that occur to the dielectric spectrum of biological single cells challenged with drugs or toxins.

The *de facto* gold standard method for the study of cell membrane properties is patch clamp. In its classical incarnation it is difficult to operate and has low throughput. However it has extremely high resolution and sensitivity (single channel currents can be measured). In the context of the work presented in this chapter, voltage patch-clamp of whole cells or excised membrane patches has been used to quantify the effect on membrane permeability of Leukotoxin LTX toxin [73], the effect of scorpion toxin-induced pores on cardiac myocytes [74] and the mechanism of membrane damage by bacterial hemolysin [75-77].

Fluorescence confocal microscopy has been used with some success by measuring the efflux of dyed species from the cells under study. This method can be used on an arrayed population of single cells,[47] where HeLa cells were dyed with Calcein AM then flowed into an array of hydrodynamic traps. SLO monomers were quickly introduced and the fluorescent intensity of the cells was monitored over time. Toxin was introduced at concentrations of 100U/mL (.091 μg/mL) and 10kU/mL (9.1 μg/mL), and it was observed that higher concentrations of toxin resulted in a faster efflux of dye from the cell.

Toxin activity can also be assayed using supported or suspended bilayer membranes, either by monitoring the DC resistance of the membrane of using AC impedance spectroscopy. For example Wilkop et al. formed a solid supported

membrane by deposition of liposomes and measured the charge transfer resistance before and after the insertion of SLO monomers. It was found that lower charge transfer resistance values were measured as the number of SLO monomers introduced in the bathing solution increased [78].

Similarly, Misakian et al. measured single ion currents through alpha-hemolysin channels on a suspended bilayers [79]. Of course, experimenting on suspended lipid bilayers simplifies the experimental protocol, as no live cells are required to insert pores in a cellular membrane. However the cellular response *in vivo* is always the result of a cascade of events that cannot be reproduced in an artificial, simplified, setup. For example, studying the Anthrax Toxin by means of whole voltage patch clamp, Wolfe et al. demonstrated that pore formation depended on specific cellular receptors and exhibited voltage-dependent inactivation at large potentials [80].

Compared to other methods of analysis that measure the dielectric properties of cells (dielectrophoretic cross-over frequency measurements and electrorotation), impedance spectroscopy is the only method that, at least in principle, does not require visual observation of the cells during measurement. Cross-over frequency and electrorotation measurements require quantitative analysis of captured video sequences: in the former case to quantify velocity of translational motion of the cells, in the latter to quantify rotational velocity. Impedance spectroscopy directly measures the passive electrical response of the cells, facilitating real time measurements of cell response, with savings in post-processing time. Moreover, dielectric spectroscopy allows measurement of the kinetic response of cells to drugs or toxins with a temporal resolution unmatched by either DEP or ROT spectroscopy. Finally, as DEP and ROT rely on the measurement of cell movement in response to the application of an electric field, it's not feasible to immobilize cells and challenge them with a chemical stimulus *while* measuring their response.

Perhaps the most important limitation of impedance spectroscopy is that it measures the properties of the entire sample volume, i.e. the cell under study as well as the volume of fluid around it. It is also difficult to decouple the effect that multiple cell parameters have on the overall dielectric response: most notably changes in cell size and membrane conductivity both affect the measured spectrum at frequencies lower than 10 MHz. At frequencies lower than 10 kHz, the ionic double layer modifies the

measured signal. In a recent review on impedance sensors for toxin detection [1], Asphahani and Zhang point out that for the specific case of ECIS sensors (i.e., electrode cell-substrate impedance sensing), which are used for the characterization of adherent cells, the effect of toxic and harmful agents has been quantitatively characterized. However all the studies measured differences in cell attachment and spreading caused by different toxin concentrations, and/or exposure time to the toxic agent, not the actual effect of the different compounds on the cell membrane parameters.

Electrorotation and DEP experiments are not immune to the synergistic effect that cell membrane conductivity and cell radius have on the overall response. There are also additional limitations that need to be addressed: for electrorotation experiments, the solution conductivity has to be much lower than the internal conductivity of the cell [63], effectively preventing the study of cells in their native environment. For both DEP and ROT, experiments on the same cell population need to be performed in a range of solution conductivities, to obtain values of cell membrane conductance and capacitance.

In the case of ROT, the peak frequency is related to the membrane capacitance (C_m) and conductance (G_m) by the following expression [66]:

$$f_{pk} = \frac{K_{ms}}{\pi r^2 C_m} + \frac{G_m}{2\pi r C_m} + \frac{\sigma_s}{\pi r C_m} \tag{3-6}$$

When measured across a range of solution conductivities the plot of $f_{pk} \cdot r$ against conductivity of the solution σ_s gives a graph with slope

$$m = \frac{1}{\pi C_m} \tag{3-7}$$

and an intercept

$$c = \frac{1}{\pi C_m}\left(\frac{K_{ms}}{r} + \frac{rG_m}{2}\right) = \frac{r}{2\pi C_m}\left(\frac{2K_{ms}}{r^2} + G_m\right) \tag{3-8}$$

Where C_m is the membrane capacitance, r is the cell radius, G_m is the membrane conductance (ie the conductance across the cellular membrane, mainly a function of the ion flux through the mebrane pores and ion channels), K_{ms} is the membrane surface

conductance (ie the conductance parallel to the membrane surface, mainly associated with the ionic double layer induced by the net charges on the cell membrane).

By defining

$$G^*_m = \frac{2K_{ms}}{r^2} + G_m \tag{3-9}$$

the total effective membrane conductance, equation (3-8) can be re-written as:

$$c = \frac{rG^*_m}{2\pi C_m} \tag{3-10}$$

Analogously, from the expression that relates the DEP cross-over frequencies

$$f_{xo} = \frac{\sqrt{2}}{2\pi C_m r}\sigma_s - \frac{\sqrt{2}G^*_m}{8\pi C_m} \tag{3-11}$$

When measuring across a range of solution conductivities the plot of $f_{xo} \cdot r$ against conductivity of the solution σ_s gives a graph with slope

$$m = \frac{\sqrt{2}}{2\pi C_m} \tag{3-12}$$

$$c = -\frac{\sqrt{2}G^*_m r}{8\pi C_m} \tag{3-13}$$

In both DEP and ROT measurements, when cells have to be re-suspended in a range of different solution conductivities, it becomes impossible to measure transient responses to drugs or toxins. ROT is difficult to automate and extensive post-processing is required, so that only the results of a few dozen cells are usually recorded. DEP experiments on the other hand, are somewhat easier to automate and therefore more data points per experiment are usually acquired. Notably, Pethig et al. developed a cell profiler, capable of acquiring hundreds of data points per experiment [81]. However for the simplifying assumptions made by Pethig to hold, it is necessary that the membrane conductivity be much smaller than the medium conductivity, a condition certainly satisfied by healthy cells, but not by cells whose membrane is porated by toxins or large ion channels.

Clearly, the cell radius influences the DEP cross-over frequency, and ROT-spectroscopy measurements, as much as the membrane capacitance. Therefore accurate measurements of cell radius are required for high quality membrane capacitance measurements.

Quantifying the effect of membrane pores and ion channels on the membrane conductance is particularly challenging with DEP and ROT, as the *effective* membrane conductance is the sum of trans-membrane conductance and surface conductance (as formalized in eqn. (3-9)): Gascoyne et al. measured the changes in erythrocyte membranes following malarial infection by means of ROT and DEP [64]. In the study the authors recognize that the trans-membrane conductance cannot be derived unambiguously from the dielectrophoretic data and have to rely on data patch-clamping techniques to derive values of membrane conductivity for cells infected by malaria.

The cell trapping and recording device proposed in this chapter provides a capability for capturing single cells in an array of traps and continuously monitoring changes in impedance change induced by chemical agents or external stimulus. The trap and reference electrode allows a differential signal to be recorded, thus reducing the effect that local changes in solution temperature, conductivity or pH. However, there are aspects of the device that could be improved. For example, the electrodes should be modified to increase their capacitance and reduce the double layer effect, e.g. by coating coated with a layer of conductive polymer or IrOx. The trap design could be modified to maximize trapping efficiency: traps should be arrayed in a symmetric fashion, as shown by Skelley et al.[82]

Other aspects remain problematic:

The devices are difficult to fabricate, and many steps in the fabrication process, especially the alignment /bonding of the top and bottom substrate, depend on the dexterity of the operator for a successful outcome.

The trapping mechanism is specific to a particular cell size, making it necessary to design a different device for a specific cell line.

It is difficult to accurately measure or control cell size – a sophisticated imaging system would be necessary to record the size of the cell at each trap continuously over time. This would defeat the point of developing a highly scalable, highly automatable, inexpensive label-free system.

Finally, the need for an all-electrical measurement systems is fading, because imaging technology has progressed and cheap multi-megapixel CCD and CMOS sensors are now available. Even consumer-grade digital cameras and cellular phones feature imaging sensors that are adaptable to desktop scientific instruments and even

point of care devices. In a recent review the use of cellphone cameras in conjunction with cheap plastic optic elements is considered a promising avenue for the development of novel imaging system (both bright field and fluorescence-based) for the diagnosis of Malaria and TB in third world countries [83].

3.12 Conclusions

It's been shown that this device is suited to non-invasively quantify the effect of surfactants and pore-forming toxins on captured cells without the aid of labels, fluorescent or otherwise. This platform allows for multiplexed recording of continuous differential impedance spectra from individual cells held in an array of hydrodynamic traps. Finite element analysis shows high sensitivity to pore formation. The system was demonstrated by assaying the transient response of HeLa cells to the lysing effects of the surfactant Tween and the kinetic pore-forming effect of the bacterial toxin, streptolysin-O. Tween is found to elicit changes in the differential impedance response of the trapped cells with direct correlation to its concentration. Perfusion of the toxin elicited exponential decays in the differential impedance response with time constants inversely proportional to toxin concentration. The combination of single hydrodynamic cell trapping with single cell impedance analysis provides a simple scalable label-free cell analysis system.

Additional uses of this platform include the capability to electroporate or lyse single cells by applying a dc potential to a single electrode thus generating a localized OH gradient which disrupts the cellular membrane as demonstrated by Nevill et al. [60] The reaction occurring at the electrode prevents real-time impedance measurements, although quantitative studies can still be conducted by using optical means or by delayed measurements.

Acknowledgements

J. Tanner Nevill contributed to the design and fabrication stages of the project. Thanks to Dino Di Carlo for helpful discussions during the designing stages and devising the toxin experiments. Catia Bernabini prepared the PEL capsules.

References

[1] F. Asphahani, and M. Zhang, "Cellular impedance biosensors for drug screening and toxin detection," *Analyst*, 2007, pp. 835-841.

[2] E. Nwankwo, and C. J. Durning, "Fluid property investigation by impedance characterization of quartz crystal resonators - Part I: Methodology, crystal screening, and Newtonian fluids," *Sensor Actuat A-Phys*, 1999, pp. 99-109.

[3] C. Fernandez-Sanchez, C. J. McNeil, and K. Rawson, "Electrochemical impedance spectroscopy studies of polymer degradation: application to biosensor development," *Trac-Trend Anal Chem*, 2005, pp. 37-48.

[4] B. Y. Liaw, G. Nagasubramanian, R. G. Jungst *et al.*, "Modeling of lithium ion cells - A simple equivalent-circuit model approach," *Solid State Ionics*, 2004, pp. 835-839.

[5] Y. Y. Xia, Y. H. Zhou, and M. Yoshio, "Capacity fading on cycling of 4 V Li/LiMn2O4 cells," *J Electrochem Soc*, 1997, pp. 2593-2600.

[6] G. W. Walter, "A Review Of Impedance Plot Methods Used For Corrosion Performance Analysis Of Painted Metals," *Corros Sci*, 1986, pp. 681-703.

[7] R. P. Kedar, T. H. Bourne, T. J. Powles *et al.*, "Effects Of Tamoxifen On Uterus And Ovaries Of Postmenopausal Women In A Randomized Breast-Cancer Prevention Trial," *Lancet*, 1994, pp. 1318-1321.

[8] R. F. Kushner, and D. A. Schoeller, "Estimation Of Total-Body Water By Bioelectrical Impedance Analysis," *Am J Clin Nutr*, 1986, pp. 417-424.

[9] F. Bordi, C. Cametti, and T. Gili, "Dielectric spectroscopy of erythrocyte cell suspensions. A comparison between Looyenga and Maxwell– …," *Journal of Non-Crystalline Solids*, Dec 31, 2002.

[10] G. H. Markx, H. J. G. Tenhopen, J. J. Meijer *et al.*, "Dielectric-Spectroscopy As A Novel And Convenient Tool For The Study Of The Shear Sensitivity Of Plant-Cells In Suspension-Culture," *J Biotechnol*, 1991, pp. 145-157.

[11] C. L. Davey, and D. B. Kell, "The influence of electrode polarisation on dielectric spectra, with special reference to capacitive biomass measurements - I. Quantifying the effects on electrode polarisation of factors likely to occur during fermentations," *Bioelectroch Bioener*, 1998, pp. 91-103.

[12] H. P. Schwan, "Mechanisms Responsible For Electrical-Properties Of Tissues And Cell-Suspensions," *Med Prog Technol*, 1993, pp. 163-165.

[13] C. Merla, and G. D'inzeo, "Dielectric Spectroscopy of Blood Cells Suspensions: Study on Geometrical Structure of Biological Cells," *Proceedings of the 28th IEEE EMBS Annual International Conference*, Jul 13, 2006.

[14] G. Fuhr, H. Glasser, T. Muller *et al.*, "Cell Manipulation And Cultivation Under Ac Electric-Field Influence In Highly Conductive Culture Media," *Bba-Gen Subjects*, 1994, pp. 353-360.

[15] R. Lisin, B. Z. Ginzburg, M. Schlesinger *et al.*, "Time domain dielectric spectroscopy study of human cells .1. Erythrocytes and ghosts," *Bba-Biomembranes*, 1996, pp. 34-40.

[16] J. H. T. Luong, C. Xiao, B. Lachance *et al.*, “Extended applications of electric cell-substrate impedance sensing for assessment of the structure– …,” *Analytica Chimica Acta*, Dec 31, 2004.
[17] C. Xiao, and J. H. Luong, “Assessment of cytotoxicity by emerging impedance spectroscopy,” *Toxicol Appl Pharmacol,* vol. 206, no. 2, pp. 102-12, Aug 6, 2005.
[18] C. Xiao, B. Lachance, G. Sunahara *et al.*, "An in-depth analysis of electric cell-substrate impedance sensing to study the attachment and spreading mammalian cells," *Anal Chem*, 2002, pp. 1333-1339.
[19] L. Ceriotti, J. Ponti, P. Colpo *et al.*, “Assessment of cytotoxicity by impedance spectroscopy,” *Biosensors & bioelectronics,* vol. 22, no. 12, pp. 3057-63, 2007.
[20] L. Ceriotti, J. Ponti, F. Broggi *et al.*, “Real-time assessment of cytotoxicity by impedance measurement on a 96-well plate,” *Sensors & Actuators: B. Chemical*, Dec 31, 2007.
[21] G. Ciambrone, “Cellular Dielectric Spectroscopy: A Powerful New Approach to Label-Free Cellular Analysis,” *Journal of Biomolecular Screening,* vol. 9, no. 6, pp. 467-480, Sep 1, 2004.
[22] P. Linderholm, T. Braschler, J. Vannod *et al.*, “Two-dimensional impedance imaging of cell migration and epithelial stratification,” *Lab Chip,* vol. 6, no. 9, pp. 1155, Jan 1, 2006.
[23] J. Wegener, C. R. Keese, and I. Giaever, “Recovery of adherent cells after in situ electroporation monitored electrically,” *Biotechniques,* vol. 33, no. 2, pp. 348, 350, 352 passim, 2002.
[24] J. Wegener, S. Zink, P. Rösen *et al.*, “Use of electrochemical impedance measurements to monitor beta-adrenergic stimulation of bovine aortic endothelial cells,” *Pflugers Arch,* vol. 437, no. 6, pp. 925-34, May 1, 1999.
[25] K. Asami, "Dielectric spectroscopy of biological cells," *Bioelectrochemistry and Bioenergetics*, 1996, pp. 141-145.
[26] E. Gheorghiu, and K. Asami, “Monitoring cell cycle by impedance spectroscopy: experimental and theoretical aspects,” *Bioelectrochemistry and Bioenergetics*, Dec 31, 1998.
[27] M. E. Lidstrom, and D. R. Meldrum, “Life-on-a-chip,” *Nat Rev Microbiol,* vol. 1, no. 2, pp. 158-64, Nov 1, 2003.
[28] D. Di Carlo, and L. P. Lee, “Dynamic single-cell analysis for quantitative biology,” *Anal Chem,* vol. 78, no. 23, pp. 7918-25, Dec 1, 2006.
[29] S. Cho, and H. Thielecke, "Micro hole-based cell chip with impedance spectroscopy," *Biosens Bioelectron*, 2007, pp. 1764-1768.
[30] A. Han, and A. B. Frazier, “Ion channel characterization using single cell impedance spectroscopy,” *Lab on a chip,* vol. 6, no. 11, pp. 1412-4, Oct 31, 2006.
[31] C. James, N. Reuel, E. Lee *et al.*, “Impedimetric and optical interrogation of single cells in a microfluidic device for real-time viability and chemical response assessment,” *Biosensors and Bioelectronics,* vol. 23, no. 6, pp. 845-851, Jan 18, 2008.
[32] A. Han, L. Yang, and A. Frazier, “Quantification of the Heterogeneity in Breast Cancer Cell Lines Using Whole-Cell Impedance Spectroscopy,” *Clinical Cancer Research,* vol. 13, no. 1, pp. 139-143, Jan 1, 2007.
[33] L. S. Jang, and M. H. Wang, “Microfluidic device for cell capture and impedance measurement,” *Biomed Microdevices*, May 16, 2007.
[34] I. Walev, M. Palmer, A. Valeva *et al.*, "Binding, Oligomerization, And Pore Formation By Streptolysin-O In Erythrocytes And Fibroblast Membranes -

Detection Of Nonlytic Polymers," *Infection and Immunity*, 1995, pp. 1188-1194.
[35] S. Bhakdi, M. Roth, A. Sziegoleit *et al.*, "Isolation and identification of two hemolytic forms of streptolysin-O.," *Infection and Immunity*, Dec 31, 1984.
[36] S. Bhakdi, J. Tranum-Jensen, and A. Sziegoleit, "Mechanism of membrane damage by streptolysin-O," *Infection and Immunity,* vol. 47, no. 1, pp. 52-60, 1984.
[37] J. E. Alouf, and C. Geoffroy, "Production, Purification, And Assay Of Streptolysin O," *Method Enzymol*, 1988, pp. 52-59.
[38] I. Walev, S. C. Bhakdi, F. Hofmann *et al.*, "Delivery of proteins into living cells by reversible membrane permeabilization with streptolysin-O," *Proceedings of the National Academy of Sciences of the United States of America*, 2001, pp. 3185-3190.
[39] S. Bhakdi, U. Weller, I. Walev *et al.*, "A guide to the use of pore-forming toxins for controlled permeabilization of cell membranes," *Medical microbiology and immunology,* vol. 182, no. 4, pp. 167-75, 1993.
[40] D. Di Carlo, L. Y. Wu, and L. P. Lee, "Dynamic single cell culture array," *Lab Chip*, 2006, pp. 1445-1449.
[41] D. Di Carlo, N. Aghdam, and L. P. Lee, "Single-cell enzyme concentrations, kinetics, and inhibition analysis using high-density hydrodynamic cell isolation arrays," *Anal Chem*, 2006, pp. 4925-4930.
[42] D. Di Carlo, "Microfluidic Technologies for Single Cell Analysis," Bioengineering, University of California, Berkeley, 2005.
[43] Y. Feldman, I. Ermolina, and Y. Hayashi, "Time domain dielectric spectroscopy study of biological systems," *Dielectrics and Electrical Insulation, IEEE Transactions on,* vol. 10, no. 5, pp. 728- 753, 2003.
[44] L. A. Shepard, O. Shatursky, A. E. Johnson *et al.*, "The mechanism of pore assembly for a cholesterol-dependent cytolysin: formation of a large prepore complex precedes the insertion of the transmembrane beta-hairpins," *Biochemistry,* vol. 39, no. 33, pp. 10284-93, 2000.
[45] N. Borghi, S. Kremer, V. Askovic *et al.*, "Tube extrusion from permeabilized giant vesicles," *Europhys. Lett.,* vol. 75, no. 4, pp. 666-672, Jan 2, 2007.
[46] J. J. Biesele, and P. Goldhaber, "A study of cytoplasmic lipid granularity in tissue culture cells," *Cancer Research,* vol. 15, no. 11, pp. 767-73, 1955.
[47] D. Di Carlo, J. Shaw, and L. P. Lee, "Dynamic Studies Of Pore Forming Toxins Using A Microfluidic Cell Array."
[48] G. Decher, "Fuzzy nanoassemblies: Toward layered polymeric multicomposites," *Science,* vol. 277, no. 5330, pp. 1232-1237, 1997.
[49] H. Inoue, "Disintegration of layer-by-layer assemblies composed of 2-iminobiotin-labeled poly(ethyleneimine) and avidin," *Biomacromolecules,* vol. 6, no. 1, pp. 27-29, 2005.
[50] K. Sato, "Sugar-induced disintegration of layer-by-layer assemblies composed of concanavalin a and glycogen," *Langmuir,* vol. 21, no. 2, pp. 797-799, 2005.
[51] X. Arys, "Ordered polyelectrolyte "multilayers". 1. Mechanisms of growth and structure formation: A comparison with classical fuzzy "multilayers"," *Macromolecules,* vol. 34, no. 10, pp. 3318-3330, 2001.
[52] S. T. Dubas, "Swelling and smoothing of polyelectrolyte multilayers by salt," *Langmuir,* vol. 17, no. 25, pp. 7725-7727, 2001.
[53] G. B. Sukhorukov, A. A. Antipov, A. Voigt *et al.*, "pH-controlled macromolecule encapsulation in and release from polyelectrolyte multilayer nanocapsules," *Macromol Rapid Comm*, 2001, pp. 44-46.

[54] A. A. Antipov, “Polyelectrolyte multilayer capsules as vehicles with tunable permeability,” *Advances in Colloid and Interface Science,* vol. 111, no. 1-2, pp. 49-61, 2004.
[55] C. Dejugnat, “PH-responsive properties of hollow polyelectrolyte microcapsules templated on various cores,” *Langmuir,* vol. 20, no. 17, pp. 7265-7269, 2004.
[56] T. Mauser, “Reversible pH-dependent properties of multilayer microcapsules made of weak polyelectrolytes,” *Macromolecular Rapid Communications,* vol. 25, no. 20, pp. 1781-1785, 2004.
[57] G. B. Sukhorukov, C. Bernabini, ed., 2008.
[58] M. Adamczyk, and J. Grote, “Efficient synthesis of rhodamine conjugates through the 2'-position,” *Bioorganic & Medicinal Chemistry Letters,* vol. 10, no. 14, pp. 1539-1541, 2000.
[59] I. Moreno-Villoslada, M. Jofre, V. Miranda *et al.*, “pH Dependence of the Interaction between Rhodamine B and the Water-Soluble Poly(sodium 4-styrenesulfonate),” *The Journal of Physical Chemistry B,* vol. 110, no. 24, pp. 11809-11812, 2006.
[60] J. T. Nevill, R. Cooper, M. Dueck *et al.*, "Integrated microfluidic cell culture and lysis on a chip," *Lab Chip*, 2007, pp. 1689-1695.
[61] A. Menachery, and R. Pethig, "Controlling cell destruction using dielectrophoretic forces," *IEE P-Nanobiotechnol*, 2005, pp. 145-149.
[62] P. R. C. Gascoyne, and J. V. Vykoukal, "Dielectrophoresis-based sample handling in general-purpose programmable diagnostic instruments," *Proceedings of the IEEE*, 2004, pp. 22-42.
[63] R. Pethig, and M. Talary, “Dielectrophoretic detection of membrane morphology changes in Jurkat T-cells undergoing etoposide-induced apoptosis,” *IET Nanobiotechnology,* vol. 1, no. 1, pp. 2, 2007.
[64] P. R. C. Gascoyne, R. Pethig, J. Satayavivad *et al.*, “Dielectrophoretic detection of changes in erythrocyte membranes following malarial infection,” *Biochimica Et Biophysica Acta-Biomembranes,* vol. 1323, no. 2, pp. 240-252, 1997.
[65] M. S. Talary, K. I. Mills, T. Hoy *et al.*, “Dielectrophoretic separation and enrichment of CD34+ cell subpopulation from bone marrow and peripheral blood stem cells,” *Medical & biological engineering & computing,* vol. 33, no. 2, pp. 235-7, 1995.
[66] R. Pethig, L. Jakubek, R. Sanger *et al.*, “Electrokinetic measurements of membrane capacitance and conductance for pancreatic -cells,” *IEE Proceedings - Nanobiotechnology,* vol. 152, no. 6, pp. 189, 2005.
[67] R. Pethig, and D. B. Kell, “The passive electrical properties of biological systems: their significance in physiology, biophysics and biotechnology,” *Physics in medicine and biology,* vol. 32, no. 8, pp. 933-70, Aug 1, 1987.
[68] F. F. Becker, X. B. Wang, Y. Huang *et al.*, “Separation of human breast cancer cells from blood by differential dielectric affinity,” *Proc Natl Acad Sci USA,* vol. 92, no. 3, pp. 860-4, Jan 30, 1995.
[69] F. F. Becker, X. B. Wang, Y. Huang *et al.*, “The removal of human leukaemia cells from blood using interdigitated microelectrodes,” *Journal of Physics D: Applied Physics*, Dec 31, 1994.
[70] M. Cristofanilli, G. De Gasperis, L. Zhang *et al.*, “Automated electrorotation to reveal dielectric variations related to HER-2/neu overexpression in MCF-7 sublines,” *Clin Cancer Res,* vol. 8, no. 2, pp. 615-9, Jan 31, 2002.
[71] P. R. C. Gascoyne, X. B. Wang, Y. Huang *et al.*, “Dielectrophoretic separation of cancer cells from blood,” *Industry Applications*, Dec 31, 1997.

[72] J. Gimsa, T. Müller, T. Schnelle *et al.*, "Dielectric spectroscopy of single human erythrocytes at physiological ionic strength: dispersion of the cytoplasm," *Biophys J,* vol. 71, no. 1, pp. 495-506, Jun 30, 1996.

[73] D. Karakelian, J. D. Lear, E. T. Lally *et al.*, "Characterization of Actinobacillus actinomycetemcomitans leukotoxin pore formation in HL60 cells," *Biochimica Et Biophysica Acta-Molecular Basis Of Disease,* vol. 1406, no. 2, pp. 175-187, 1998.

[74] D. Elgar, F. Verdonck, A. Grobler *et al.*, "Ion selectivity of scorpion toxin-induced pores in cardiac myocytes," *Peptides,* vol. 27, no. 1, pp. 55-61, 2006.

[75] G. Menestrina, M. Dalla Serra, M. Comai *et al.*, "Ion channels and bacterial infection: the case of beta-barrel pore-forming protein toxins of Staphylococcus aureus," *FEBS Lett,* vol. 552, no. 1, pp. 54-60, Sep 17, 2003.

[76] G. Menestrina, C. Pederzolli, M. DallaSerra *et al.*, "Permeability increase induced by Escherichia coli hemolysin A in human macrophages is due to the formation of ionic pores: A patch clamp characterization," *Journal Of Membrane Biology,* vol. 149, no. 2, pp. 113-121, 1996.

[77] G. Menestrina, M. D. Serra, C. Pederzolli *et al.*, "Bacterial hemolysins and leukotoxins affect target cells by forming large exogenous pores into their plasma membrane. Escherichia coli hemolysin A as a case example," *Bioscience Reports,* vol. 15, no. 6, pp. 543-551, 1995.

[78] T. Wilkop, D. K. Xu, and Q. Cheng, "Characterization of pore formation by streptolysin o on supported lipid membranes by impedance spectroscopy and surface plasmon resonance spectroscopy," *Langmuir,* vol. 23, no. 3, pp. 1403-1409, 2007.

[79] M. Misakian, J. J. Kasianowicz, B. Robertson *et al.*, "Frequency response of alternating currents through the Staphylococcus aureus alpha-hemolysin ion channel," *Bioelectromagnetics,* vol. 22, no. 7, pp. 487-493, 2001.

[80] J. Wolfe, "Whole-cell Voltage Clamp Measurements of Anthrax Toxin Pore Current," *Journal of Biological Chemistry,* vol. 280, no. 47, pp. 39417-39422, 2005.

[81] R. Pethig, V. Bressler, C. Carswell-Crumpton *et al.*, "Dielectrophoretic studies of the activation of human T lymphocytes using a newly developed cell profiling system," *Electrophoresis,* vol. 23, no. 13, pp. 2057-63, Jun 30, 2002.

[82] A. M. Skelley, O. Kirak, R. Jaenisch *et al.*, "Studying Reprogramming Of Somatic Cells Via Fusion With Embryonic Stem Cells: A Massively Parallel Device For Cell Fusion.", *Proceedings of MicroTAS*, Paris, 2007

[83] P. Yager, D. Gonzalo, and J. Gerdes, "Point-of-Care Diagnostics for Global Health," *Annu. Rev. Biomed. Eng.,* vol. 10, 2008.

Chapter 4 Electrode polarization and the double layer

4.1 Introduction

The topic of electrical double layers is broad and its ramifications span multiple applications, such as electrokinetics, colloid science, filtration membranes, polyelectrolytes, emulsions, percolation, corrosion phenomena. In this chapter, the classical theoretical model of the double layer (Gouy – Chapman – Stern model) is explained. Then, an explanation of the constant phase element, a distributed circuit element commonly employed to fit double layer impedance data acquired to equivalent circuit models, is given. Finally experimental results are presented: low-frequency impedance spectroscopy is used to characterize the ionic double layer for the specific case of flat metal electrode/ liquid electrolyte interface, with monovalent electrolytes at neutral pH. The dependency of the ionic double layer on the electrolyte concentration as well as on the applied AC potential is explored. Observations are made with regard to discrepancies found between experimental results and classical theoretical predictions, and hypotheses are discussed to explain said discrepancies.

4.2 Classical theory of the double layer

When a polarisable electrode (that is, an electrode operated at a regime where no charge transfer reaction occurs at the surface) comes into contact with an electrolyte, charges from the electrolyte opposite in sign to the charges present on the surface of the electrode, move to the electrode/electrolyte interface and provide a localized condition of electro-neutrality and a layer of charge termed the double layer. This term has historical significance and von Helmholtz [1] initially postulated that a sheet of counter-charges in a solution would accumulate at the surface of a polarized electrode, separated by a distance of molecular order, effectively forming a parallel plate capacitor.

Gouy [2] and Chapman [3] independently extended von Helmholtz's theory, proposing that the charge layers are not equally thick. Whereas charge carriers on the electrode could occupy a molecularly thin layer, the layer of charges in the solution would need to be significantly thicker. Therefore most counterions would be adjacent to the electrode where electrostatic forces overcome thermal processes, while progressively

lesser concentrations would be found at greater distances (i.e. the layer would *diffuse* into the bulk). The average distance *d* could be taken as the inter-electrode distance of an equivalent parallel plate capacitor and would be dependent on the electrolyte concentration and the potential applied to the polarized electrode: the higher the voltage and the more concentrated the electrolyte, the more compact the diffuse layer.

This simple model provided qualitative but not quantitative agreement with experimental observations and was further modified by Stern in 1924 [4] who split the solution side of the "double layer" into the inner layer or *Stern* layer and the outer layer or *diffuse* layer, separating the two parts by an imaginary plane .

In some cases, the separation of the EDL into a charge-free Stern layer and a diffuse layer is not sufficient to interpret experiments. The inner layer could be further divided in two regions: between the surface and the inner Helmholtz plane (IHP) a layer of ions is adsorbed to the surface; Between the IHP and the outer Helmholtz plane (OHP) bound hydrated ions are present. This is schematically illustrated in Figure 4-1

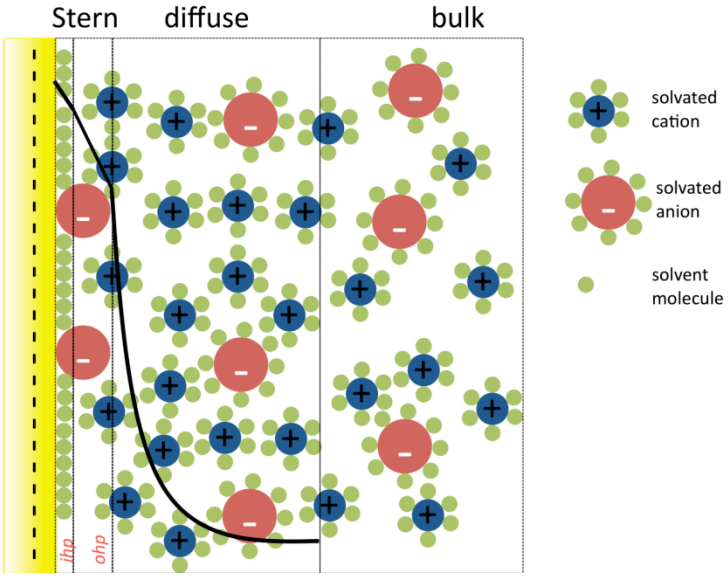

Figure 4-1 Schematic diagram of the ionic double layer. At the solid surface, counterions are adsorbed. Further out, dehydrated ions, hindered in their mobility are found. Together with the adsorbed ions this forms the Stern layer. Further out a diffuse layer of counterions is found. This is equivalent to a concentration-dependent capacitance. The bulk of the solution is made of hydrated ions and counterions. The thick black line represents the electrical potential across the solution from the electrode surface to the bulk. The linear decrease across the Stern layer is followed by an exponential drop across the diffuse layer. The slope of the potential across the bulk electrolyte is constant.

Lyklema [5] suggests that such rigid subdivisions are certainly artificial, but are nonetheless valuable: the characteristics of the *diffuse layer* can be described with relatively simple analytical equations which are valid for relatively low potentials (< *kT/q* or 25 mV). The *Stern layer* on the other hand, is in close contact with the electrode surface and reflects surface heterogeneities, which even the most involved models, cannot account for completely. Manciu points out that these simple theories have received widespread criticism for almost a century and yet survived [6]. One reason is that some of the parameters (the surface charge and surface potential) are not accurately known and can in most cases be fitted to account for the experimental data.

Many corrections have been introduced into the traditional approach to account for the changes in the dielectric constant of water due to the presence of ions [7], high electric field strengths [8], finite size of the hydrated ions [9], image forces [10], ion-dispersion [11] and ion-hydration forces [12, 13], and so on. In the context of this thesis the most involved models are not relevant, since the experimental resolution of impedance spectroscopic methods is limited.

The next section presents analytical equations that model the potential distribution in the diffuse layer. Also the solution to the Poisson-Boltzmann (PB) equation is used to derive approximate values of diffuse layer thickness for different solution concentrations.

4.3 Potential distribution across the diffuse layer

The potential distribution in the diffuse layer satisfies the Poisson-Boltzmann equation

$$\nabla^2\phi = -\frac{\rho_d(x)}{\varepsilon\varepsilon_0} \tag{4-1}$$

Where ρ_d is the charge density in the diffuse layer, and ϕ is the potential. The distance x is from the outer Helmholtz plane. The local charge density is the sum of all ion species *I,* and is related to the local concentration of the electrolyte

$$\rho_d(x) = \sum_i n_i^o z_i q \exp\left(\frac{-z_i q\phi(x)}{k_B T}\right) \tag{4-2}$$

Where n^o is the bulk concentration of ions, z is the valence of the ions, T is the temperature, k_B is the Boltzmann constant and q is the magnitude of the electronic charge.

This simplification assumes that the electrolyte is symmetric.

Combining (4-1) and (4-2) yields

$$\nabla^2\phi(x) = -\frac{\sum_i n_i^o z_i q \exp\left(\frac{-z_i q\phi(x)}{k_B T}\right)}{\varepsilon\varepsilon_0} \tag{4-3}$$

$$\nabla^2\phi(x) = -\frac{q}{\varepsilon\varepsilon_0}\sum_i n_i^o z_i \exp\left(\frac{-z_i q\phi(x)}{k_B T}\right) \tag{4-4}$$

The solution to (4-4) is the potential distribution as a function of the distance x from the polarized surface. Debye and Huckel provided an approximate analytical solution for the case of spherical geometries and low surface potentials [14]:

$$\phi = \phi_0 \exp(-\kappa r) \tag{4-5}$$

Where r is the radial distance from the surface and

$$\kappa^2 = \frac{q^2}{\varepsilon\varepsilon_0}\sum_i \frac{n_i^o z_i^{\,2}}{k_B T} \tag{4-6}$$

If the electrolyte is symmetrical, κ^{-1}, the characteristic potential decay length, referred to as the Debye length is:

$$\kappa^{-1} = \sqrt{\frac{\varepsilon\varepsilon_0 k_B T}{2n^0 z^2 q^2}} \tag{4-7}$$

For the case of KCl solution (1-1) at room temperature (300^o K), an expression for the Debye length as a function of molarity is:

$$\kappa^{-1} = \frac{3.05}{\sqrt{c}} \tag{4-8}$$

Table 4-1 contains numerical values for the Debye length in nm, for a given concentration, in the case of typical electrolyte solutions at 25^oC.

Debye length (nm)			
Conc (M)	Electrolyte type: 1-1	Electrolyte type: 2-1	Electrolyte type: 2-2
1.00E-04	30.4	17.55	12.41
1.00E-03	9.61	5.55	3.92
1.00E-02	3.04	1.76	1.24
1.00E-01	0.96	0.56	0.39
1.00E+00	0.30	0.17	0.12

Table 4-1. Debye length vs. solution concentration, for the case of 1-1, 2-1 and 2-2 electrolytes. As an example, Dulbecco's Phosphate Buffer Saline (or DPBS), a medium most commonly used to suspend mammalian cells, contains 137 mM NaCl, 10 mM Phosphate, 2.7 mM KCl, so the Debye length is smaller than 1nm.

Introducing a normalized dimensionless potential

$$\psi = \frac{q}{k_B T}\phi \tag{4-9}$$

then for flat surfaces, (4-4) can be re-written as:

$$\frac{kT}{q}\frac{d^2\psi(x)}{dx^2} = -\frac{q}{\varepsilon\varepsilon_0} z n_0 \left(e^{-z\psi} + e^{z\psi}\right) \tag{4-10}$$

Introducing the Debye length (4-7) is rewritten as:

$$\frac{d^2 z\psi(x)}{dx^2} = \kappa^2 \sinh\left[z\psi\left(x\right)\right] \tag{4-11}$$

This differential equation can be integrated after multiplying both sides by $2\frac{d\psi}{dx}$

$$2\frac{d\psi}{dx}\frac{d^2 z\psi(x)}{dx^2} = 2\frac{d\psi}{dx}\kappa^2 \sinh\left[z\psi\left(x\right)\right] \tag{4-12}$$

$$2\frac{d\left(d\psi/dx\right)^2}{dx} = 2\frac{d\psi}{dx}\kappa^2 \sinh\left[z\psi\right] \tag{4-13}$$

$$2\frac{d\left(d\psi/dx\right)^2}{dx} = \frac{2}{z}\kappa^2 \frac{d\left(\sinh(z\psi)\right)}{dx} \tag{4-14}$$

Integrating gives:

$$\left(d\psi/dx\right)^2 = \frac{2}{z^2}\kappa^2 \cosh(z\psi) + const. \tag{4-15}$$

The integration constant is obtained from the boundary condition that at large distance from the surface, $\frac{d\psi}{dx} \to 0$ and $x \to 0$. The constant is then equal to -1.

$$\frac{d\psi}{dx} = \pm\frac{\kappa\sqrt{2}}{z}\sqrt{\cosh(z\psi) - 1} \tag{4-16}$$

Using the relation

$$\cosh x = 1 + 2\sinh^2\left(\frac{x}{2}\right) \tag{4-17}$$

(4-16) can be rewritten as

$$\frac{d\psi}{dx} = \pm 2\frac{\kappa}{z}\sinh\left(\frac{z\psi}{2}\right) \tag{4-18}$$

Inserting the expression for κ:

$$\frac{d\psi}{dx} = \pm\sqrt{\frac{8n^0 zq^2}{\varepsilon\varepsilon_0 k_B T}}\sinh\left(\frac{z\psi}{2}\right) \tag{4-19}$$

Substituting for ψ:

$$\frac{d\phi}{dx}\frac{q}{k_B T} = \pm\sqrt{\frac{8n^0 zq^2}{\varepsilon\varepsilon_0 k_B T}}\sinh\left(\frac{zq\phi}{2k_B T}\right) \tag{4-20}$$

$$\frac{d\phi}{dx} = \pm\sqrt{\frac{8n^0 zq}{\varepsilon\varepsilon_0}}\sinh\left(\frac{zq\phi}{2k_B T}\right) \tag{4-21}$$

The electric field in the diffuse double layer is then:

$$E = -\frac{d\phi}{dx} = \sqrt{\frac{8n^0 zq}{\varepsilon\varepsilon_0}}\sinh\left(\frac{zq\phi}{2k_B T}\right) \tag{4-22}$$

This solution for the potential distribution in the diffuse layer is widely used. If the diffuse layer is treated as a parallel plate capacitor, the Debye length (κ^{-1}) can be considered the thickness of the dielectric. It follows that the addition of a *Stern* layer introduces another capacitor (of sub-nanometer thickness), in series with the *diffuse layer*. The total double layer capacitance consists of two capacitances in series

$$C_{DL} = \left(C_{diffuse}^{-1} + C_{stern}^{-1}\right)^{-1} \tag{4-23}$$

Bard and Faulkner provide the following general expression for the overall double layer capacitance:

$$C_{DL} = \left(\frac{d_{stern}}{\varepsilon_{stern}\varepsilon_0} + \frac{1}{\sqrt{\left(2\varepsilon_{dif}\varepsilon_0 z^2 e^2 n^0 / kT\right)\cosh\left(ze\phi_{stern}/2kT\right)}} \right)^{-1} \quad (4\text{-}24)$$

Where d_{stern}, ε_{stern},ϕ_{stern}, are the thickness, relative permittivity and potential of the Stern (or outer Helmholtz layer). Using this expression is somewhat problematic as the above mentioned parameters are hard to extract. Nonetheless, the expression suggests that while the capacitance of the diffuse layer has a voltage dependence, the Stern capacitance does not. A third capacitor could be added in series to model a layer of specifically adsorbed ions.

It remains debatable what value of permittivity should be assigned to a dielectric slab that is only one or two molecular diameters thick. Lyklema suggests that the quotient ε/d be left unresolved for these molecular capacitors. To de-couple the two or three capacitance values, measurements should be performed at high salt concentration where the diffuse layer vanishes and the effect of the *Stern* layer dominates.

The electrokinetic behaviour of some colloidal particles cannot be fully characterized by the classical model and discrepancies can be found in values of zeta potentials obtained from different electrokinetics measurements [15]. For example Zukoski and Saville [16] presented extensive experimental results for the electrophoretic mobility and electrical conductivity of two polystyrene latex systems and showed that the zeta potentials inferred from the suspension conductivity were larger than those derived from electrophoresis. Mangelsdorf and White in the introduction to their papers on a dynamic model of the double layer [17, 18], review several authors' attempts to bring completeness to the standard electrokinetic theory by postulating that anomalous surface conduction phenomena can be ascribed to a Stern layer of elusive nature.

Ennis and White warn that even though much better agreement in the zeta potentials obtained with mobility measurements and deduced from conductivity measurements can be achieved with a dynamic Stern layer, the introduction of further model complexity raises the danger that the additional parameters will absorb various theoretical and experimental errors, without any additional insight being gained into the nature of the system [19]. The main difficulty in reaching a consensus as to the nature of the Stern layer, and the double layer stems from the fact that few experimental techniques can probe ion distributions in solutions near interfaces. Few double layer parameters can be measured directly without making assumption [5]. Other than

surface double layer capacitance and dielectric relaxations which can be measured by impedance spectroscopy, AFM can measure directly the magnitude and potential dependence of diffuse double-layer forces at electrode surfaces as shown by Bard et al. [20, 21] and Barten et al [22].

4.4 Impedance spectroscopy and the double layer

In the context of bio-sensors and lab-on-a-chip devices, AC electrical measurements are widely used and examples include sensing of self-assembled monolayers (SAM) [23-26], on-line monitoring of cell cultures [27, 28] healing tissue cultures [29] , impedance based micro flow-cytometry [30] impedance spectroscopy of cells [31] (both in bulk and a at a single-cell level). In all cases the double layer at the surface of the measurement electrodes cannot be ignored, and needs to be characterized for its effects to be understood and compensated. For AC-electrokinetic based electrohydrodynamic systems, where the ionic double layer is involved in the transport of fluid along an electrode surface, it is beneficial to have an effective way to quantitatively characterize the EDL.

As discussed previously, the ionic double layer can be modelled as a non-ideal capacitor (in series with the measuring electrode), whose dielectric parameters change as a function of surface characteristics (fractal index and dimensions), electrolyte species and concentration, temperature, applied AC voltage and DC bias.

Impedance spectroscopy (IS) is an ideal measurement tool for characterizing the DL, as it allows direct measurements of the double layer capacitance.

However:

1. Impedance spectroscopy is limited in its *power of resolution*. An impedance spectrum is by definition the response of the system and does not easily allow the de-convolution of several contributing effects. Educated guesses and control experiments must be performed to uniquely identify each circuit component contribution.

2. Some prior knowledge of the system under study is needed to develop a meaningful equivalent circuit fitting procedure: any number of equivalent circuit models could be adopted to fit the acquired data. Macdonald [34] warns against the fallacies and the arbitrariness of equivalent circuit modelling. The

analytical tools presented in the previous section are used to estimate the contribution of the diffusion and Stern layer to the total impedance response.

4.5 Equivalent Circuit models

As impedance spectroscopy is a technique that has its genesis in electrical engineering, it should not be surprising that many efforts have been made to model the measured impedance responses by means of equivalent circuits.

The advantage of using electrical circuit components to model the physical phenomena that make up a certain measured impedance response lies in the immediate recognisability of the elements and their frequency response, and consequently in the inherent potential for standardized analysis. The disadvantage however is that electrode polarization and surface chemical reaction phenomena are seldom correctly represented by ideal circuit elements; furthermore it is quite possible to model (or rather, approximate) a given impedance response using different circuit elements arranged in various configurations, yielding ambiguity to the interpretation. Therefore extreme care must be taken when relating the physical phenomena to be modelled to the parameters of any chosen equivalent circuit model.

For the impedance response of an electrolyte contained in a measuring cell of known geometrical shape and dimensions, many equivalent circuit models have been proposed over the years; it ought to be pointed out that no one circuit is universally appropriate since different levels of description might be required depending on the finality of the measurement data being modelled. Figure 4-2 to Figure 4-4 illustrate equivalent circuit models of increasing complexity that have found widespread use for the interpretation of impedance spectroscopy data.

One of the simplest models to represent electrode polarization, where the bulk properties of the electrolyte are not taken into consideration, is a parallel RC circuit (Figure 4-2(a)). The double layer building on the polarized electrode is represented by a single capacitive element C_{DL} and a parallel resistor R_{ct}. This resistive element is sometimes termed “polarization resistance” or “charge-transfer resistance” to indicate that a reaction is occurring at the surface of the electrode and a conductive path is present between the electrode surface and the bulk electrolyte. The model can be reduced to a simple capacitance (Figure 4-2(b)) for ideally polarizable electrodes such

as mercury electrodes and near-ideally polarisable electrodes operated at linear regimes (V < 25 mV) and with no DC voltages giving origin to electrochemical reactions.

Conversely, when impedance measurements are performed to study specific components of the ionic double layer, it is useful to model the Stern layer and the diffuse layer as discrete elements, by assigning capacitive values that depend on their thickness and their respective dielectric constant as well as on the surface area of the electrode. The parallel $R_{ct}//C_{DL}$ model can therefore be expanded to two parallel RC combinations to model the Stern and diffuse layer behaviours separately (Figure 4-2(c)). This model too can be simplified to a simple series combination of capacitors when the phenomena that cause resistive leakage (such as surface reactions) don't occur (Figure 4-2(d)).

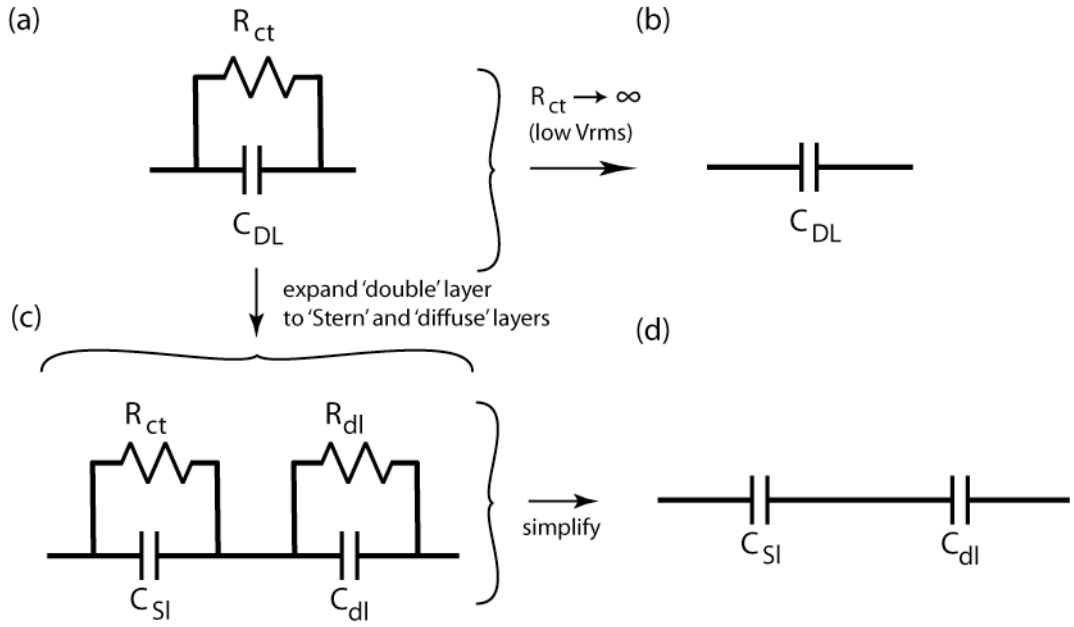

Figure 4-2 Equivalent circuit models to represent electrode polarization. (a) A simple electrical circuit representation of the electrode polarization phenomena employs a single capacitor with a parallel resistor to model the 'leaky' nature of the electrode polarization capacitance. (b) If the measurements are operated at low voltages and no reactions occur on the surface of the electrode under study, or if the electrode under study is ideally polarisable (as in the case of mercury electrode) the resistor element becomes superfluous and can be eliminated from the model. (c-d) Conversely, if modelling individual components of the double layer (diffuse and Stern layer) is of interest, it is useful to employ multiple parallel RC combinations or simply multiple capacitances in series.

In cases where it is desirable to model the bulk properties of the electrolyte – for example when measuring the impedance response of a system across a range of frequencies extending to higher regimes, the electrolyte properties are modelled by a capacitance C_{sol} and resistance R_{sol} (Figure 4-3). If the electrodes in the measuring cell are of equal size and shape and in a parallel plate arrangement, the solution resistance is directly proportional the distance divided by the electrode area. The constant of proportionality is the electrolyte conductivity. Similarly, the solution capacitance is directly proportional to the electrode area and inversely proportional to their distance. The constant of proportionality is the dielectric constant of the electrolyte. Depending on whether the electrolyte is solid and approximating a perfect dielectric, or liquid approximating a perfect conductor, the resistor or capacitor elements respectively, can be considered superfluous and eliminated to simplify the model.

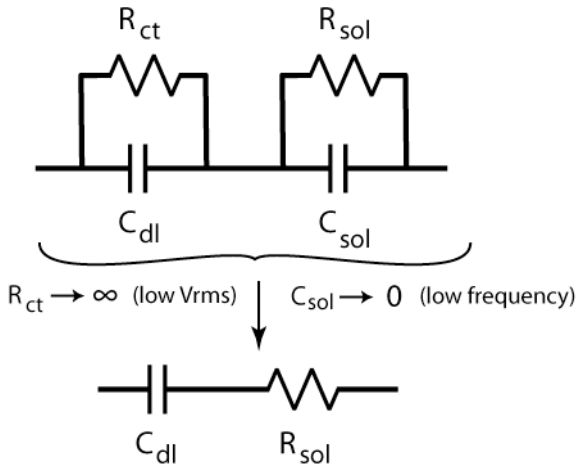

Figure 4-3 Equivalent circuit models to represent electrode polarization and bulk solution. When measuring the impedance spectrum of a system, it can be necessary to model properties of the electrolyte between the measuring electrodes (bulk). The solution resistance and capacitance can be modelled easily if the electrodes are equal in size and shape. The equivalent circuit model can be suitably simplified if either the solution capacitance or resistance are not apparent in the frequency range being measured.

In most cases, a capacitor or combination of capacitors will not adequately model the measured frequency response exhibited by a polarized electrode. In such cases a quasi-capacitive empirical element termed “Constant Phase Element” (or CPE) is employed

in place of the capacitor (Figure 4-4). Such element has been so designated because its phase angle response is independent of frequency and it has been found to be extremely valuable to the interpretation of experimental data on solid and liquid electrolyte.

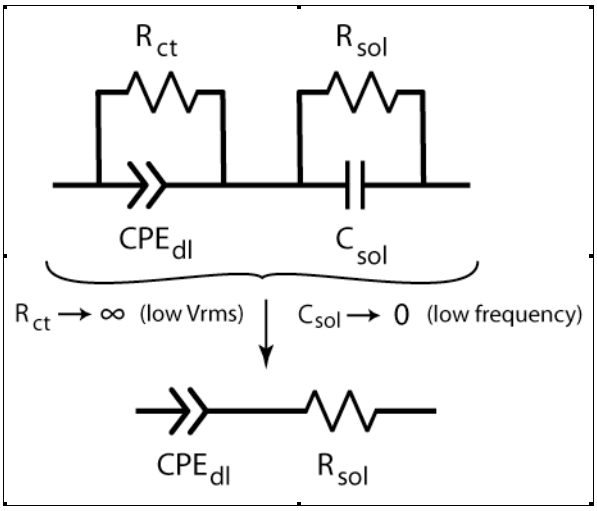

Figure 4-4 Equivalent circuit models to represent electrode polarization by means of a constant phase element and bulk solution. As in Figure 4-3, the model can be simplified when measuring at frequencies where the solution capacitance might not have a measurable effect.

The following section is wholly dedicated to the CPE.

4.6 The constant phase element

The presence of a quasi-capacitive behaviour at an electrochemical interface is attributed to charging an ionic layer as a result of the polarization processes in the electrolyte. There is still no single explanation for the origin of the non-ideality in the capacitance: some authors have attributed it to discontinuities and in-homogeneities in the charge layer [32-34], others to the fractal nature of the surface [35-38], or to geometrical discontinuities in the surface (not of fractal origin) [39-42]. Regardless of the root cause of this behaviour, it is now commonplace to use a Constant Phase Angle Element (CPA or CPE) to model the DL. The origin and use of CPEs has been extensively discussed in the literature [43-48].

The impedance of a CPE element is defined as:

$$Z_{CPE} = \frac{1}{(j\omega)^P T} \tag{4-25}$$

The exponent P determines the constant phase angle which is:

$$\phi = P\frac{\pi}{2}, -1 \le P \le 1 \tag{4-26}$$

The CPE acts like a capacitor where $T = \mathrm{C}$, when $P = 1$. The CPE can also yield an inductive impedance when $P = -1$, and a purely resistive one for $P = 0$. This is schematically illustrated in Figure 4-5

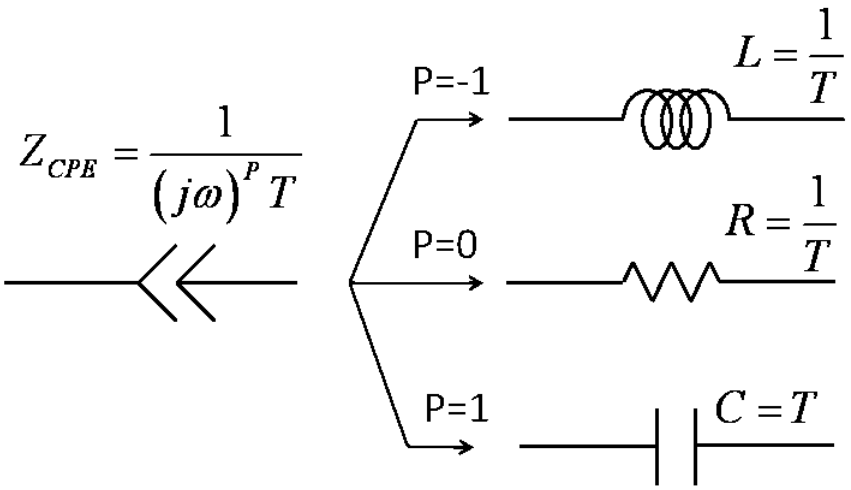

Figure 4-5 The distributed element "CPE" reduces to the lump circuit elements L,R,C when the exponent P assumes integer values of -1,0,1 respectively. For metal electrode surfaces P is confined to values between 0.5 and 1, which correlate well with the fractal dimension of the surface.

For electrode surfaces, Liu [49] established a relationship between the fractal dimension of the interface and the exponent of the CPE element, *P*. This ranges from 0.5 (for an ideally rough surface) to 1 (for an ideally smooth surface). The relationship can be defined as:

$$P = \frac{1}{D-1} \tag{4-27}$$

For a surface, the fractal dimension (D) can be measured optically (i.e. independently), hence a verifiable link is found between the surface roughness and the CPA element: for a smooth surface, the fractal dimension, D = 2 results in P = 1, whereas a highly porous/rough surface has D = 3 for which obtains P = 0.5.

Halsey [36, 37] presents a perturbative approach to the calculation of the impedance. This approach is qualitatively in agreement with the fractal hypothesis, yielding CPA-type corrections to the impedance only for very, or "'fractally" rough surfaces. van Heuveln [50] postulates that to describe the charging process at a material interface

with only a single capacitor is a large simplification of the real situation and that electrode polarization must result in a discontinuous and non-homogeneous double layer with different charging (or discharging) behaviour with respect to pure capacitance behaviour. When describing the energy storage properties of a CPE compared to a capacitor, it can be reasoned that whereas a capacitor has frequency independent energy efficiency because of a constant ratio between the energy lost per cycle (real part of the impedance) and the energy stored per cycle (imaginary part of the impedance), a CPE is an imperfect energy storage element, with the exponent P a measure of the imperfection.

In the time domain, van Heuveln numerically evaluates the relaxation curves of CPE elements for *P* ranging from 0.5 to 1. For decreasing values of *P*, the decay is faster at small values of *t*, whereas at larger values of *t* the decay is considerably slowed down. This is illustrated in Figure 4-6

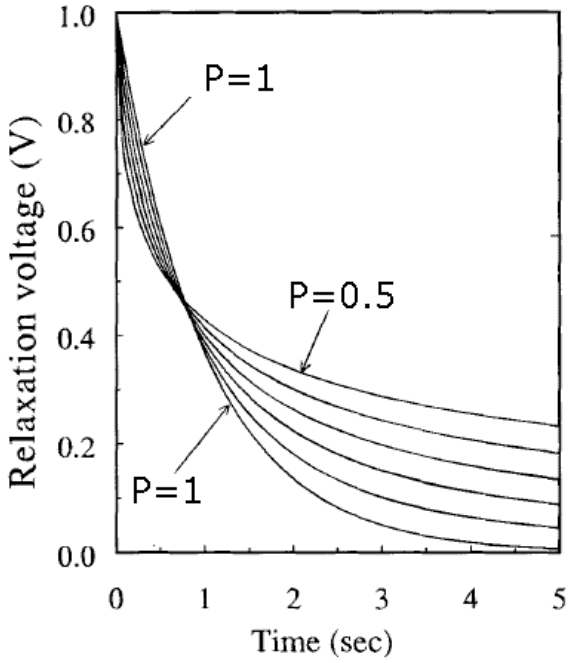

Figure 4-6 Taken from [50]: Relaxation curves for CPE with different powers. When *P*=1, the CPE behaves as an ideal capacitor. As *P* assumes decreasing values, the voltage decay gets progressively faster (initially) and slower (finally)

Already in 1941 Cole and Cole [51] proposed that the deviation from ideal behaviour of some dielectric materials is caused by a distribution of relaxation times and the parameter P should be related to the width of the distribution. MacDonald [52] defines a distribution of relaxation times related to the CPE as:

$$G(\tau) = \frac{\sin(n\pi)}{\pi} T\tau^{-P} \tag{4-28}$$

Where $G(\tau)$ is the distribution of relaxation times, τ is the relaxation time, T is the base of the CPE element.

The examples of CPE behaviour in various fields of research are numerous, not all explanations are based on the assumption that a certain distribution of relaxation times or activation energies causes CPE behaviour or non-ideal dielectric behaviour for that specific dielectric. Brug [53] points out that the CPE might be just an intrinsic property of the electrical double-layer (the atoms, molecules and ions subject to extremely high electric field strengths and fluctuations therein). The atomic movements in the interfacial structure, that occur on application of the AC potential, would be accompanied by a dissipation of energy during the cycle of the AC perturbation as a consequence of mechanical coupling to neighbouring atoms.

4.7 Conversion of constant phase element to ideal capacitance

It is sometimes necessary to convert or 'map' CPE data to capacitance values, so as to determine the thickness or dielectric constant of the material under study and to compare parameters for surfaces that exhibit different values of CPE exponent. From the definition of impedance

$$Z_{CPE} = \frac{1}{(j\omega)^P T} \tag{4-29}$$

and

$$Z_C = \frac{1}{j\omega C} \tag{4-30}$$

Despite this difference, T is often used as if it were the capacitance, ignoring the influence of the parameter P. This is dimensionally incorrect and it leads to a systematic overestimation of the dielectric constant or the underestimation of the material thickness.

A step-by-step derivation of the relationship between C and CPE is presented here:

Given

$$Z_{CPE} = \frac{1}{(j\omega)^P T} \tag{4-31}$$

and knowing that

$$(j\omega)^n = \omega^n \left[\cos\left(\frac{\pi}{2} n\right) + j \sin\left(\frac{\pi}{2} n\right) \right] \tag{4-32}$$

$$Z_{CPE} = \frac{\omega^{-P}}{T} e^{-j\frac{\pi}{2}P} \tag{4-33}$$

Since

$$Z_C = \frac{1}{j\omega C} \tag{4-34}$$

Setting

$$Z_C = Z_{CPE} \tag{4-35}$$

and solving for C, results in

$$C = -\frac{j\,T}{\omega^{-P} e^{-\frac{1}{2} j P\pi} \omega} \tag{4-36}$$

$$C = -j\,T\omega^{P-1} e^{-\frac{1}{2} j P\pi} \tag{4-37}$$

$$C = T\omega^{P-1} \left[\sin\left(\frac{\pi}{2} P\right) - j \cos\left(\frac{\pi}{2} P\right) \right] \tag{4-38}$$

According to van Westing [54]

$$C = \frac{T\omega^{P-1}}{\sin\left(\frac{\pi}{2} P\right)} \tag{4-39}$$

Proposing that the radial frequency be considered to be in the centre of the logarithmic frequency range of the applied signal. It is apparent however that van Westing's solution is mathematically incorrect.

Jovic [55] suggests

$$C = T\omega^{P-1} \sin\left(\frac{\pi}{2} P\right) \tag{4-40}$$

Taking the real part of the right-hand side of (4-40), he suggested that the frequency to be used should be the frequency at which the phase angle has a maximum.

While Hsu and Mansfeld [56] propose that

$$C = T\omega^{P-1} \tag{4-41}$$

by taking the magnitude of the right-hand side of (4-41), and choosing the frequency ω to be that at which the imaginary part of the impedance has a local maximum. This is however impractical as such a local maximum only occurs if a small resistive element

exists in parallel to the CPA element (this instance is quite common in reaction/corrosion studies, but not in dielectric spectroscopy).

Brug [53] proposes a frequency-independent method, referring to Cole, who equates the impedance expression for an R-CPE network (i.e. a solution resistance in series to a double layer CPE) to its time response and finds the equivalent capacitance value.

Letting

$$\alpha = 1 - P \tag{4-42}$$

$$Z_{R-CPE} = R + \frac{1}{(j\omega)^P T} = R + (j\omega)^{-(1-\alpha)} T^{-1} \tag{4-43}$$

$$Z_{R-C} = R + \frac{1}{j\omega C} = R + (j\omega C)^{-1} \tag{4-44}$$

According to Cole [51] the impedance can also be expressed as a function of a time constant so that:

$$Z_{R-CPE} = R\left(1 + (j\omega\tau)^{-(1-\alpha)}\right) \tag{4-45}$$

$$R \cdot \left[1 + (j\omega\tau)^{-(1-\alpha)}\right] = R + (j\omega)^{-(1-\alpha)} T^{-1} \tag{4-46}$$

$$T = R^{-1}\tau^{1-\alpha} = R^{-P}C^{1-\alpha} \tag{4-47}$$

$$C^{1-\alpha} = \frac{T}{R^{-\alpha}} \tag{4-48}$$

$$C = \left(TR^{-\alpha}\right)^{-\frac{1}{\alpha-1}} = \left(TR^{-\alpha}\right)^{\frac{1}{1-\alpha}} \tag{4-49}$$

$$C = \left(TR^{1-P}\right)^{\frac{1}{P}} \tag{4-50}$$

In the more general case (illustrated in Figure 4-7) the impedance response can be modelled with a solution resistance in series with a parallel combination of double layer CPE in parallel with a charge transfer resistance, R_{ct}:

$$C = \left(TR^{-\alpha}\right)^{-\frac{1}{\alpha-1}} = \left(\frac{T}{\left(\frac{1}{R_s} + \frac{1}{R_{ct}}\right)^{\alpha}}\right)^{\frac{1}{1-\alpha}} = \left(\frac{T}{\left(\frac{1}{R_s} + \frac{1}{R_{ct}}\right)^{1-P}}\right)^{\frac{1}{P}} \tag{4-51}$$

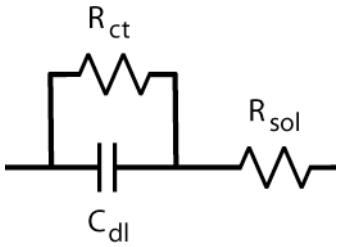

Figure 4-7. Equivalent circuit diagram for a polarisable electrode. The diffuse layer is modelled by the capacitor Cdl. Charge transfer is modelled by the resistor Rct. Bulk solution is modelled by the resistor Rsol. When the electrode is ideally polarisable, no charge transfer occurs at the interface and Rct has an infinite value, effectively disappearing.

In conclusion, when dealing with physical phenomena that can only be modelled accurately by circuits featuring constant phase elements, it is incorrect to compare values of CPE-T directly, without taking into account the CPE-P factors. Also incorrect is the all too common approximation CPE-T = C, unless it is explicitly specified at which frequency the CPE elements has the chosen capacitance value (so that referring to (4-29) and (4-30), it is possible to obtain both CPE-T and CPE-P).

Alternatively, if an approximation is sufficient, Brug's method appears to be the least arbitrary, as it is frequency independent and also the one which is supported by a convincing physical explanation. An alternative, frequency independent, method for obtaining an equivalent value of C is proposed as follows: The original CPE element is replaced by a capacitor, such that the cut-off frequency of the original R-CPE circuit is matched by that of a new circuit R-C (in other words, a value is fitted to a capacitor 'C' so as to obtain phase response curves that cross at φ=45°). This results in an equivalent circuit model, which preserves the 'average' time constant. To summarize and compare the methods described in this section, equivalent capacitance values are presented in the plot below (Figure 4-8), for values of *P* varying between 0.5 and 1.

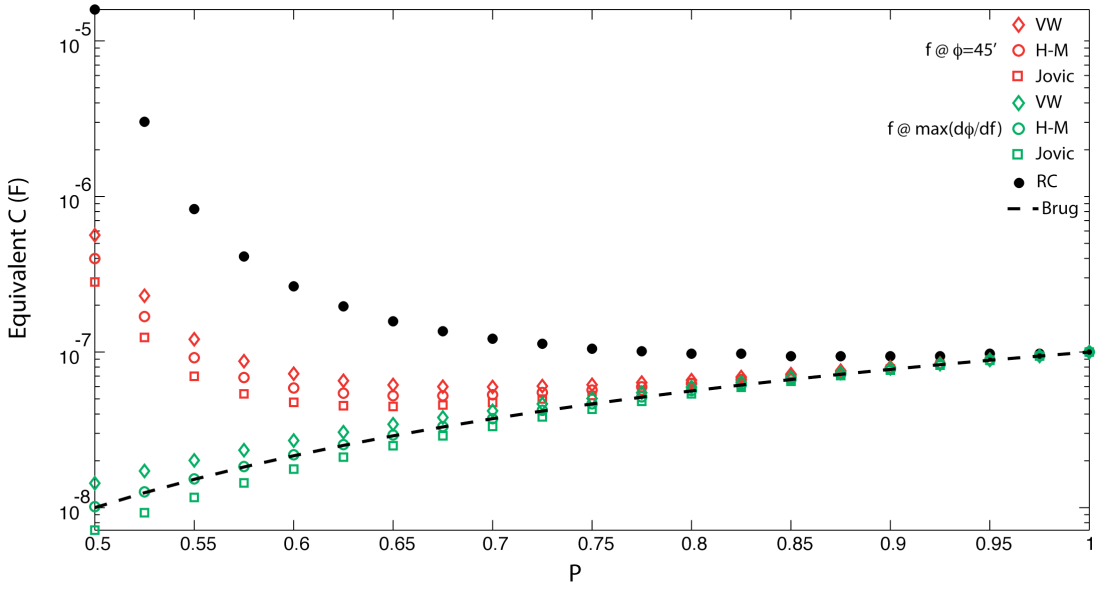

Figure 4-8. A summary of equivalent capacitance values resulting from the conversion from CPE (T = 1e-7) according to the different methods described in this chapter. Van Westing's (VW), Hsu-Mansfeld's (HM), and Jovic's methods are all dependent on the arbitrary choice of a frequency parameter: in red, the operating frequency chosen is that at which the phase of the R-CPE spectral response is equal to 45°. In green, the operating frequency chosen is that at which the phase of the R-CPE spectral response has its maximum slope. Black dots are used for the RC method, which results in equivalent capacitance values that tend to increase asymptotically as P approaches 0.5. This behaviour can be explained by referring to the decay times associated with the CPE element as illustrated in Figure 4-6: when P is 0.5, the decay time is infinite, so it can be approximated by an infinitely large capacitance. Brug's method, also frequency independent, results in values that slowly tend to decrease instead.

Figure 4-9 shows the impedance responses of the R-CPE circuit for power values of 0.9 to 0.6 (typical of electrode-electrolyte interface), compared to the 'equivalent circuits' obtained with the methods just described.

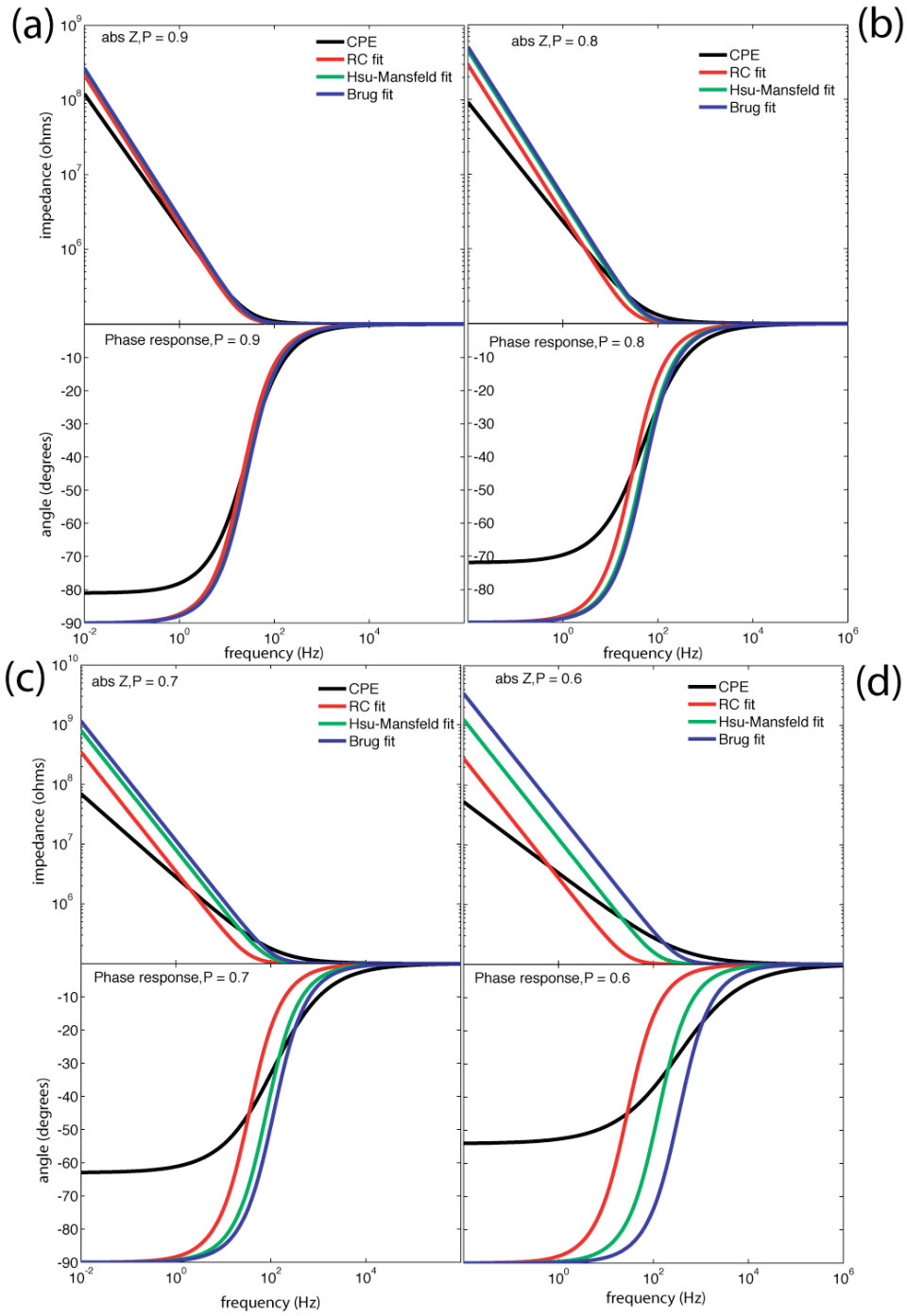

Figure 4-9 Complex impedance spectra in their magnitude and phase representation (|Z| and ϕ) for series R-CPE circuits and 'equivalent' RC circuits obtained using three different fitting methods are compared: RC, Hsu-Mansfeld, Brug. In (a) to (d) P is varied from 0.9 to 0.6. Clear differences between the three methods emerge for values of P < 0.8. Most notably: the RC-fit phase curve always crosses the R-CPE phase at ϕ=45; the Brug RC curves have their inflection points occurring at the same frequencies as the R-CPE curves regardless of the value of P.

4.8 Experimental

In this section, the behaviour of the ionic double layer is examined using impedance spectroscopy.

The dependence of the measured response on electrolyte concentration and applied voltage is examined using Au and Pt electrodes. For all measurements KCl solutions concentrations ranging from 100μM to 1 M are used, at excitation voltages ranging from 25mV to 1V AC RMS (0 DC bias).

The Au and Pt electrodes were deposited by J. Tanner Nevill, at the UC Berkeley Sensors and Actuators Center.

For the Au electrodes, a 200 nm Au layer was e-beam evaporated at a chamber pressure of 2 x 10^{-7} Torr, at room temperature and a deposition rate around 2 Å/ s, over a 20nm adhesion layer of Cr evaporated using the same parameters.

For the Pt electrodes, a 200 nm Ti layer was e-beam evaporated at a chamber pressure of 2 x 10^{-7} Torr, at room temperature and a deposition rate around 20 Å/ s, over a 20nm adhesion layer of Ti evaporated using the same parameters.

The surface roughness of the electrodes was empirically assumed to increase with faster evaporation rates used during the deposition process (as reported in the literature and determined by AFM measurements in [57] and [58]). Although this assumption was qualitatively proven by impedance measurement results, the actual roughness values for the electrode surfaces were not independently quantified using other measurements.

In the later sections, measurements on doped silicon and polysilicon electrodes, used to model the nanogap capacitor device (described in Chapter 6) are reported.

The silicon electrode was fabricated by K. H. Jeong at the UC Berkeley Sensors and Actuators Center, as follows: starting with a four inch silicon wafer, a 1 μm thick layer of phosphosilicate glass (PSG) was deposited by low pressure chemical vapor deposition (LPCVD). The wafer was then brought to a high temperature to allow diffusion of phosphorus from the PSG into the silicon wafer, which resulted in a heavily doped silicon wafer. The PSG was then removed in an HF bath, and the remaining wafer was electrically conductive enough to act as the bottom electrode.

The doped polysilicon electrode was fabricated as follows: The surface of a silicon wafer was thermally oxidized under tightly controlled conditions to create a 300nm thin

and uniform SiO_2 layer. Heavily doped poly-silicon at a thickness of 300 nm was then deposited onto the SiO_2 using LPCVD.

For both the silicon and polysilicon electrodes, contact to the measuring probes was provided via a gold pad evaporated and patterned using a standard lift off procedure.

All electrodes, metal and semiconductor, were cleaned before and after each measurement with acetone, ethanol, isopropyl alcohol and finally DI water. They were then dried under a gentle stream of nitrogen.

The effect of a native layer of oxide on the overall impedance response of the semiconductor electrodes is discussed.

Complex impedance measurements were performed over a wide range of frequencies (from 0.1 Hz to 1 MHz). The measured spectra for all electrodes, electrolyte concentrations and excitation voltage are presented as impedance magnitude and phase response plots. From each complex spectrum a fitting routine was employed to fit values to equivalent circuits which model the double layer as a constant phase element and resistor in series with a resistor for the solution in bulk (Figure 4-10). In most cases the parallel or charge transfer resistor had such high values that it could be ignored. Discrepancies between the experimental data and the theoretical predictions for the double layer capacitance are discussed.

In all cases, although the full impedance spectrum is plotted, only values acquired over a narrower range of frequencies (from 0.1 Hz to 10 kHz) were used for the fitting procedure. This is because the higher frequency components are not influenced by the double layer constituents (diffuse layer and Stern layer), rather by the bulk properties of the electrolyte which are not of interest in this study. The models therefore fail to correctly predict the impedance response of the systems under study at frequencies higher than 10 kHz, but this should cause no concern as long as the model is only intended to predict the behaviour of the double layer.

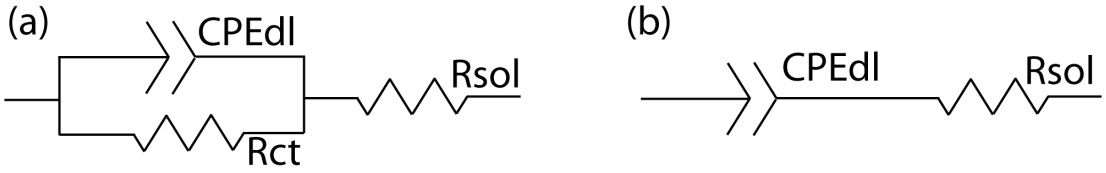

Figure 4-10 Equivalent circuits used to model the impedance response of the ionic double layer building at the electrode/electrolyte interface of flat metal electrodes.(a) The resistor R_{sol} models the solution resistance, while Rct models charge transfer reactions. The constant phase

element CPE_{dl} models the quasi-capacitive response of the double layer (lumping together the effects of the Stern and Diffuse layer). (b) When no charge transfer reaction occurs, R_{ct} assumes very high values and can be effectively ignored.

4.9 Dependence on electrolyte concentration

4.9.1 Gold electrode

Protocol

A smooth gold electrode of 3mm x 3mm sides, was immersed in serial dilutions of KCl (ranging from 0.1 mM to 1M) and excited by a 25 mV RMS AC signal to measure the low frequency impedance.

Results and discussion

The measured spectra are presented as impedance magnitude and phase response plots in Figure 4-11. From each complex spectrum a fitting routine was employed to fit values to an equivalent circuit model consisting of a solution resistance in series with a double layer constant phase element (the equivalent circuit diagram is drawn in Figure 4-10(b)).

The fitted circuit element values are presented in Table 4-2 and plotted in Figure 4-12. In Figure 4-12(a) it can be seen that CPE-P increases monotonically from 0.83 to 0.9 with solution concentration. This is unexpected as the power of a CPE is classically attributed to the roughness of the electrode surface, as discussed in the previous section, and should be independent of the ionic concentration of the electrolyte. The same behaviour was observed repeatedly, and with different electrode materials (both semiconductors and metals).

CPE-T also increases monotonically (Figure 4-12(b)) from 1.3×10^{-6} to 2.2×10^{-6}. This is expected, as the diffuse layer thickness is inversely proportional to the solution concentration (see Table 4-1). The values of equivalent capacitance derived using equation (38) remains fairly constant across the range of solution concentrations.

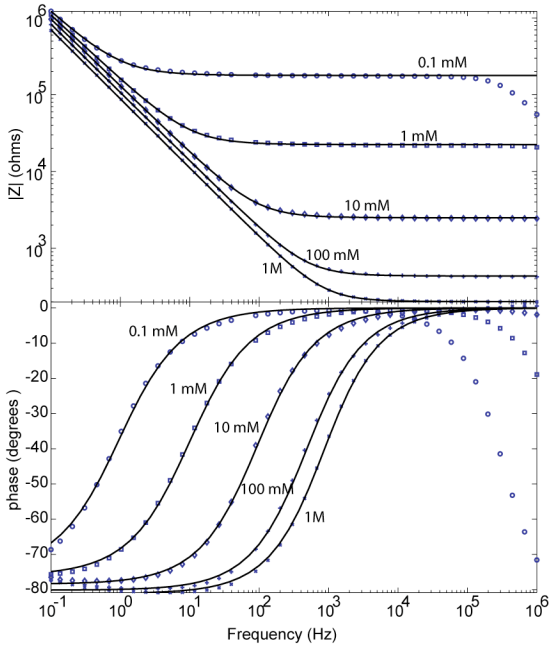

Figure 4-11. Impedance spectra (top: impedance magnitude, bottom: phase) for Cr/Au electrode immersed in KCl solutions of concentration ranging from 1 M to 0.1 mM; the AC excitation voltage is 25 mV RMS. Data points are plotted as symbols. Electrical circuit model responses are plotted as solid lines. The values for the circuit elements in the models are reported in Table 4-2

Conc. [M]	Rs [Ω]	CPE-T F^N]	CPE-P	C [F]	CPE/m^2 [F^N/m^2]	C/m^2 [F^N/m^2]
1	201.5	2.16E-06	0.9013	9.24E-07	2.40E-01	1.03E-01
1.00E-01	434.2	1.82E-06	0.89056	7.59E-07	2.03E-01	8.43E-02
1.00E-02	2494	1.55E-06	0.87158	6.83E-07	1.72E-01	7.59E-02
1.00E-03	22372	1.36E-06	0.84471	7.17E-07	1.51E-01	7.97E-02
1.00E-04	178710	1.26E-06	0.8313	9.35E-07	1.40E-01	1.04E-01

Table 4-2 Equivalent circuit model parameter values fitted to impedance spectra acquired from a gold electrode immersed in serially diluted concentrations of KCl. The fitted circuit parameters are R_s, R_p, CPE (solution resistance, charge transfer resistance and double layer constant phase element respectively). CPE-T and CPE-P refer to the base and exponent of the constant phase element, respectively. The equivalent capacitance value, C, is calculated according to Equation (4-51)

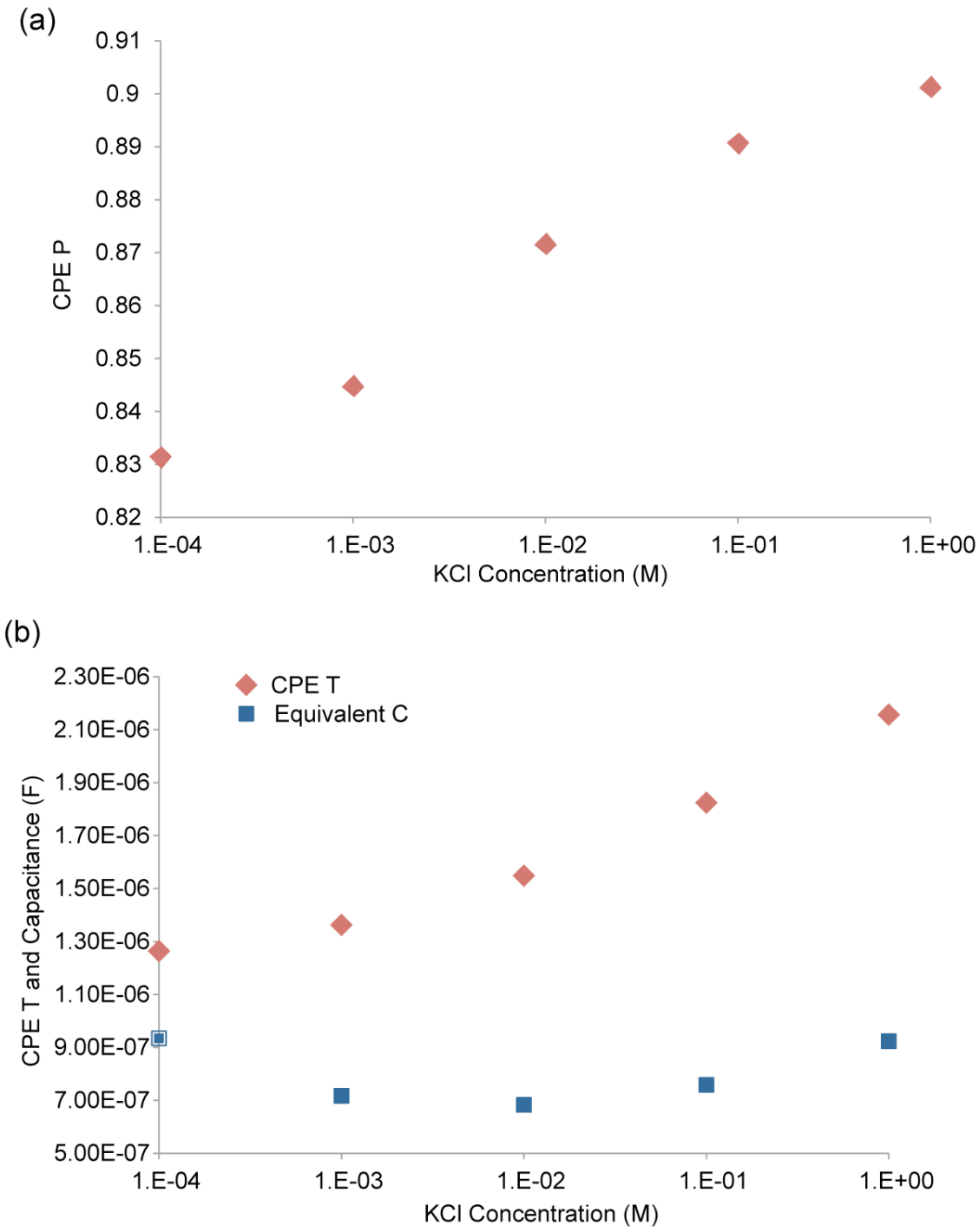

Figure 4-12. Double layer equivalent circuit model values extracted from impedance measurements on a gold electrode, applying an AC excitation voltage of 25 mV in serially diluted concentrations of KCl, ranging from 0.1mM to 1M. (Corresponding impedance plots are shown in Figure 4-11).

4.9.2 Platinum electrode

Protocol

A platinum electrode was immersed in serially dilutions of KCl (ranging from 0.1 mM to 1M concentration) and excited by a 25 mV AC RMS signal.

Results and discussion

The measured impedance spectra are shown in Figure 4-13. Fitting was performed using the equivalent circuit diagram is drawn in Figure 4-10(b) and the values are shown in Table 4-3 and plotted in Figure 4-14. In Figure 4-14(a) it can be seen that the values of CPE-P are generally much lower than the ones measured on the smooth gold electrode, confirming the empirical relationship between surface roughness and CPE power factor. However, it is also evident that CPE-P increases monotonically with solution concentration (from 0.45 to 0.75), as for the gold electrode.

CPE-T also increases monotonically (Figure 4-14 (b)). This is expected, as the diffuse layer thickness is inversely proportional to the solution concentration (see Table 4-1). Except for the 100μM electrolyte, the values of equivalent capacitance, derived using equation (38) remains fairly constant across the range of solution concentrations

Conc. [M]	Rs [Ω]	CPE-T F^N]	CPE-P	C [F]	CPE/m^2 [F^N/m^2]	C/m^2 [F^N/m^2]
1	1652	1.68E-05	0.74217	4.82E-06	0.4653	0.1338
1.00E-01	2048	1.25E-05	0.73094	3.25E-06	0.3475	0.0902
1.00E-02	3451	1.06E-05	0.69116	2.43E-06	0.2955	0.0675
1.00E-03	17100	1.02E-05	0.58965	3E-06	0.2821	0.0834
1.00E-04	130550	9.71E-06	0.475	1.26E-05	0.2698	0.3506

Table 4-3 Equivalent circuit model parameter values fitted to impedance spectra acquired from a platinum electrode immersed in serially diluted concentrations of KCl. The fitted circuit parameters are Rs, CPE (solution resistance, and double layer constant phase element respectively). CPE-T and CPE-P refer to the base and exponent of the constant phase element, respectively. The equivalent capacitance value, C_{eq}, is derived according to Equation (4-51)

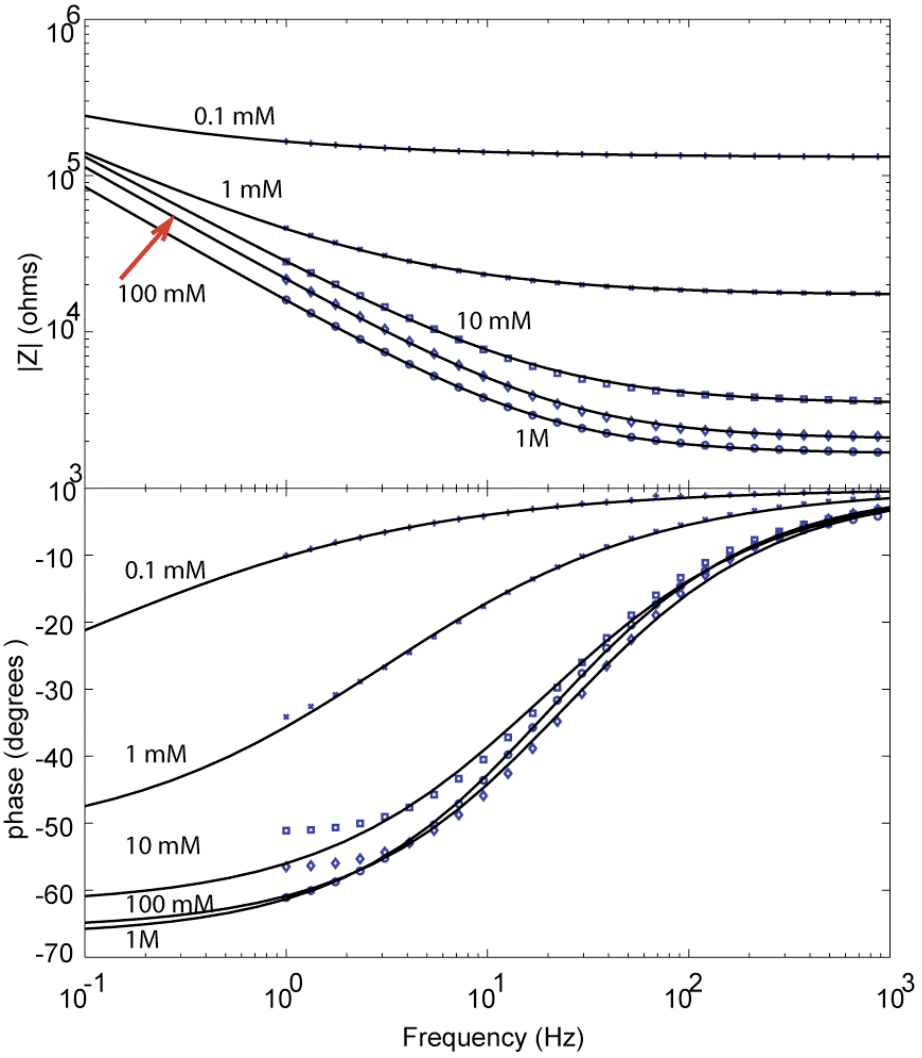

Figure 4-13. Impedance (top: impedance magnitude, bottom: phase) measurements on a rough Ti/Pt electrode immersed in KCl solutions of concentration ranging from 1 M to 0.1 mM; the AC excitation voltage is 25 mV RMS. Data points are plotted as symbols. Electrical circuit model responses are plotted as solid lines. The values for the circuit elements in the models are reported in Table 4-3.

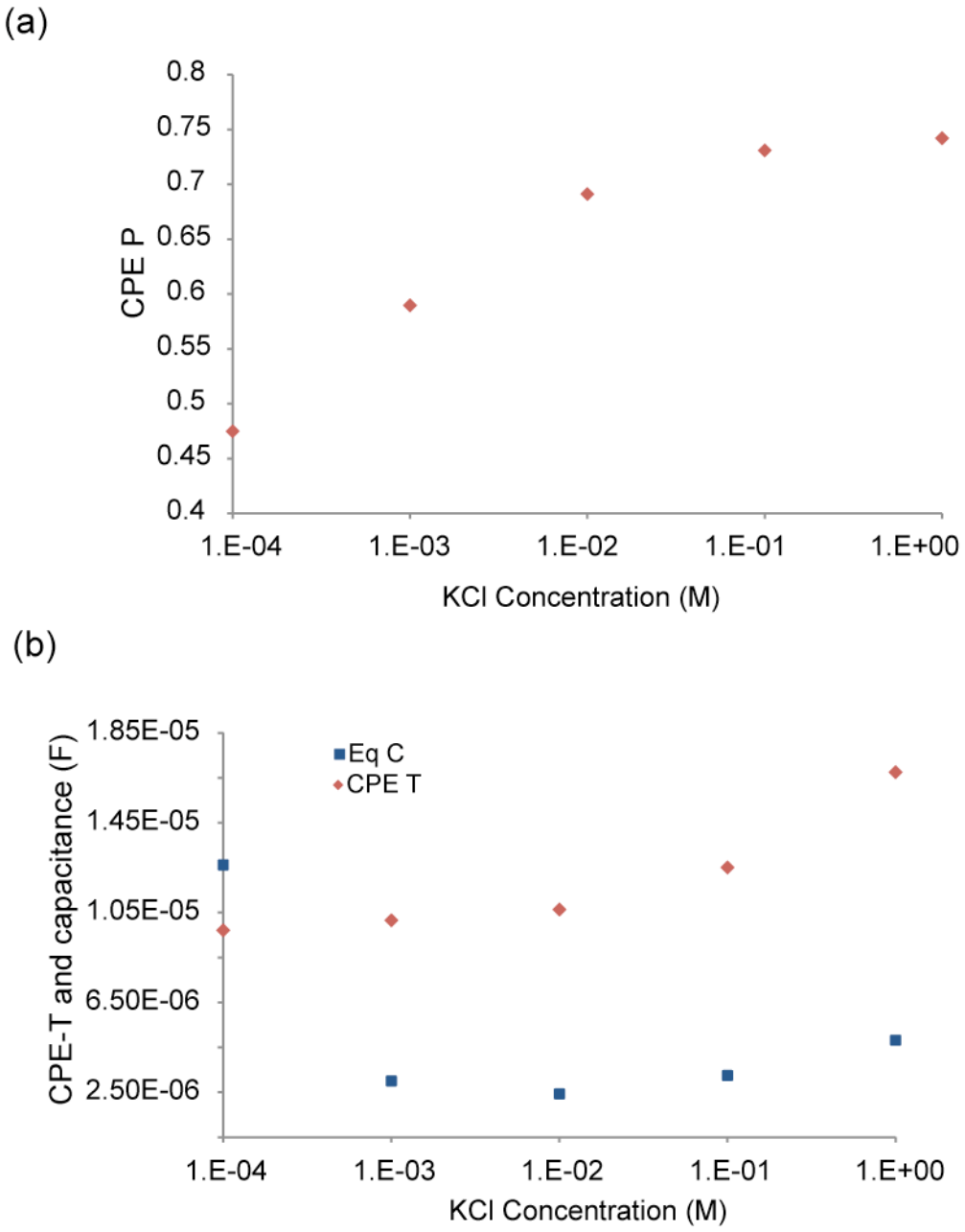

Figure 4-14. Double layer equivalent circuit model values extracted from impedance measurements on a platinum electrode, applying an AC excitation voltage of 25 mV in serially diluted concentrations of KCl, ranging from 0.1mM to 1M. (Corresponding impedance plots are shown in Figure 4-13).

4.10 Dependence on applied voltage

4.10.1 Gold electrode

Protocol

A gold electrode was immersed in a KCl solution (10mM and 100mM concentration) and excited by an AC signal ranging from 50 mV to 250 mV RMS.

Results and discussion

The impedance spectra are presented together with the modelled responses in Figure 4-15 and Figure 4-16. From each complex spectrum a fitting routine was employed to fit values to an equivalent circuit model shown in Figure 4-10(b). The fitted values are presented in Table 4-4 and Table 4-5, and plotted in Figure 4-17. In Figure 4-17(a) it can be seen that CPE-P decreases monotonically with applied voltage for both 10 mM and 100 mM KCl solutions. Again, this is an unexpected but interesting trend that the classical theory doesn't explain. It could be hypothesized that the higher applied voltages increase the level of disorder on the surface resulting in a less ordered distribution of the double layer charges.

CPE-T increases monotonically with applied voltage (Figure 4-17(b)). GCS theory predicts that a higher potential on the charged electrode will result in a sharper drop of potential across the double layer, and consequently, a thinner diffuse layer and higher measured capacitance. The trend is preserved in plot of equivalent capacitance.

As for the case of low-voltage excitation, CPE-P is consistently higher when the solution is more concentrated.

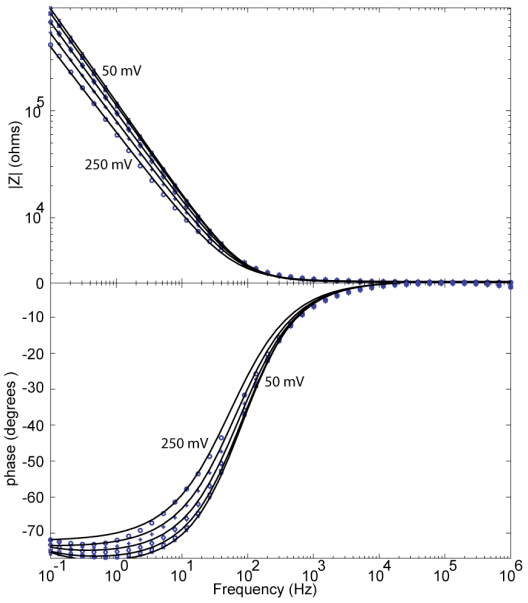

Figure 4-15. Impedance spectrum (top: impedance magnitude, bottom: phase) measurements on Cr/Au electrode immersed in a 10mM KCl solution; the AC excitation voltage varies from 50 mV to 250 mV RMS. Data points are plotted as symbols. Electrical circuit model responses are plotted as solid lines. The values for the circuit elements in the models are reported in Table 4-4.

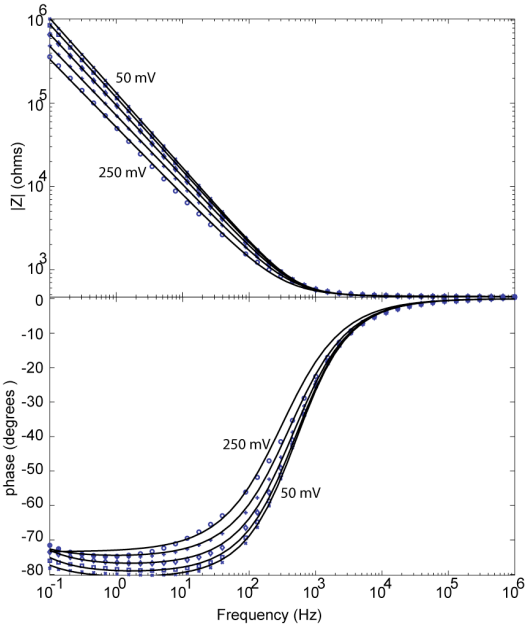

Figure 4-16. Impedance spectrum (top: impedance magnitude, bottom: phase) measurements on Cr/Au electrode immersed in a 100mM KCl solution; the AC excitation voltage varies from 50 mV to 250 mV RMS. Data points are plotted as symbols. Electrical circuit model responses are plotted as solid lines. The values for the circuit elements in the models are reported in Table 4-5.

ACV [mV]	Rs [Ω]	CPE-T [F^N]	CPE-P	Rp [Ω]	C [F]	CPE/m^2 [F^N/m^2]	C/m^2 [F^N/m^2]
50	2512	1.65E-06	0.87747	1.47E+07	7.6687E-07	0.1833	0.0852
1.00E+02	2515	1.82E-06	0.86371	1.83E+07	7.76896E-07	0.2020	0.0863
1.50E+02	2520	2.19E-06	0.84468	2.00E+07	8.39606E-07	0.2428	0.0933
2.00E+02	2526	2.77E-06	0.823	8.40E+07	9.54695E-07	0.3083	0.1061
2.50E+02	2537	3.67E-06	0.80194	7.12E+14	1.157E-06	0.4080	0.1286

Table 4-4. Equivalent circuit model parameter values fitted to impedance spectra acquired from a gold electrode immersed in a solution of 10mM KCl at excitation voltage ranging from 50mV to 250 mV RMS. The fitted circuit parameters are Rs and CPE (solution resistance and double layer constant phase element respectively). CPE-T and CPE-P refer to the base and exponent of the constant phase element, respectively. The equivalent capacitance value, Ceq, is derived according to Equation (4-51)

ACV [mV]	Rs [Ω]	CPE-T [F^N]	CPE-P	Rp [Ω]	C [F]	CPE/m^2 [F^N/m^2]	C/m^2 [F^N/m^2]
50	475.1	1.43E-06	0.90157	1.58E+07	6.43128E-07	0.1585	0.0715
1.00E+02	474.1	1.67E-06	0.88589	1.10E+07	6.66835E-07	0.1859	0.0741
1.50E+02	473.1	2.16E-06	0.86223	8.34E+06	7.17016E-07	0.2395	0.0797
2.00E+02	472.9	3.01E-06	0.83564	1.07E+07	8.27783E-07	0.3340	0.0920
2.50E+02	475.7	4.33E-06	0.81628	2.99E+13	1.07731E-06	0.4815	0.1197

Table 4-5 Equivalent circuit model parameter values fitted to impedance spectra acquired from a gold electrode immersed in a solution of 100mM KCl at excitation voltage ranging from 50mV to 250 mV RMS. The fitted circuit parameters are Rs, Rp, CPE (solution resistance, charge transfer resistance and double layer constant phase element respectively). CPE-T and CPE-P refer to the base and exponent of the constant phase element, respectively. The equivalent capacitance value, Ceq, is derived according to Equation (4-51)

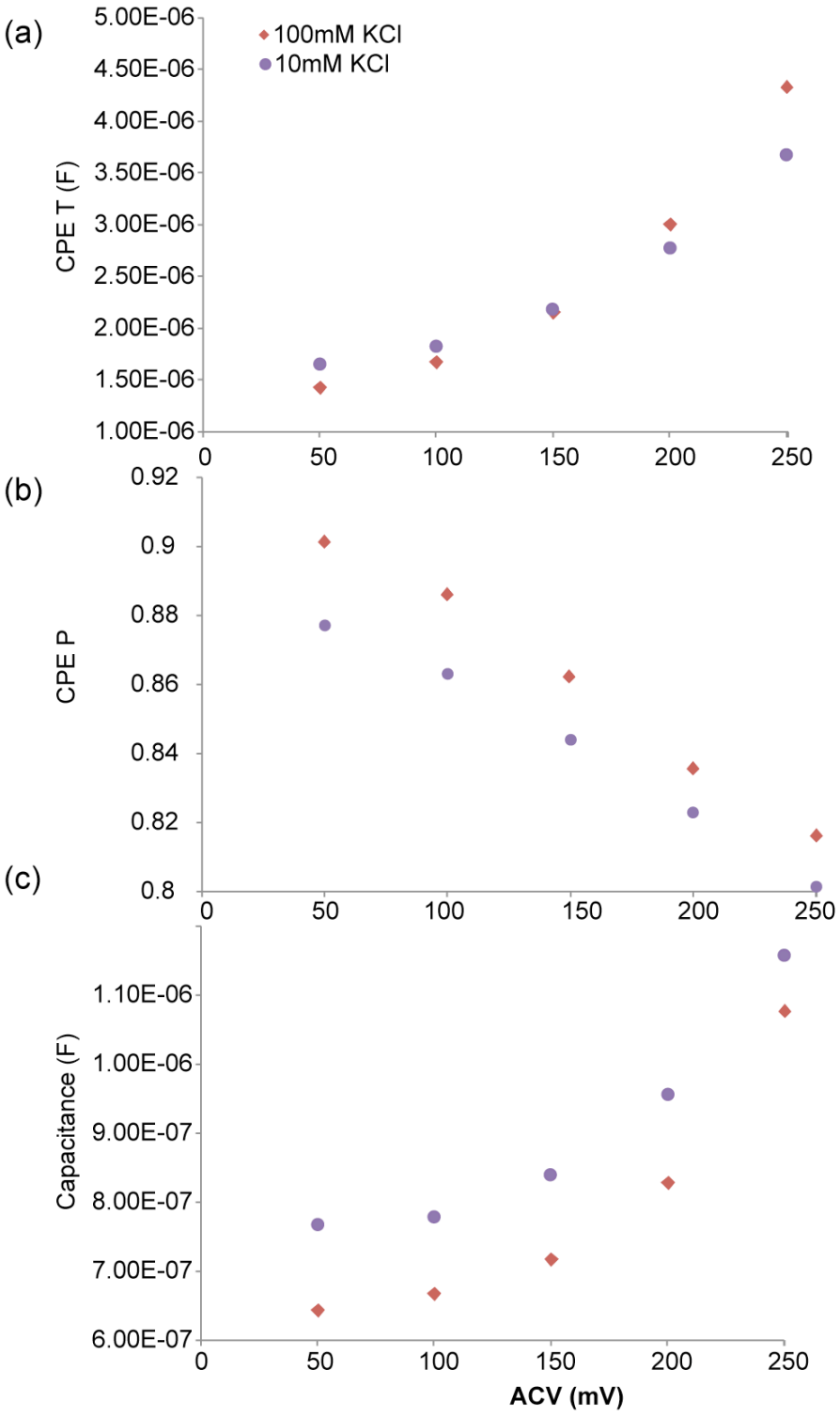

Figure 4-17 Double layer capacitance equivalent circuit model values extracted from impedance measurements on a Cr/Au electrode applying AC excitation voltages ranging from 50 mV to 250 mV in 10mM and 100 mM KCl solutions (impedance plots are shown in Figure 4-15 and Figure 4-16).

4.10.2 Platinum electrode

Protocol

A platinum electrode was immersed in a KCl solution (100mM and 1M concentration) and excited by an AC signal ranging from 25mV to 1 V RMS.

Results and discussion

The impedance spectra are shown in Figure 4-18 and Figure 4-19, fitted to the equivalent circuit model of Figure 4-10. The fitted values are presented in Table 4-6 and plotted in Figure 4-20.

As for gold electrodes, CPE-P decreases monotonically with applied voltage for both 100 mM and 1 M KCl solutions. It should be noted that power factor for gold decreases roughly from 0.9 to 0.8 when varying the applied voltage from 50mV to 250mV; the same decrease occurs in platinum over a much wider range of 25 mV to 1000 mV. In fact, in the 50-250 mV range, CPE-P for Pt stays essentially constant suggesting that the power factor is a parameter dependent on a complex interaction between the electrolyte and the electrode that goes beyond just the surface characteristics of the metal electrode.

CPE-T increases monotonically for both 100 mM and 1M KCl, although for 100 mM KCl, CPE-T increases at a faster rate and at 0.8 V RMS, the capacitance is the same for 100 mM and 1M KCl. Examination of the data in Table 4-6 shows that the ratio of solution resistances (for 100mM and 1M KCl) stays the same as the excitation voltage increases. This indicates that no significant changes occur in the bulk solution; however, the ratio of double layer capacitances does increase significantly indicating, (as evident from the plots in Figure 4-20 (a) and (b)) that the increasing voltage affects the lower concentration solution more. This in turn could suggest that the diffuse layer is most affected by the applied voltage, as the Stern layer has a less important effect at lower concentrations.

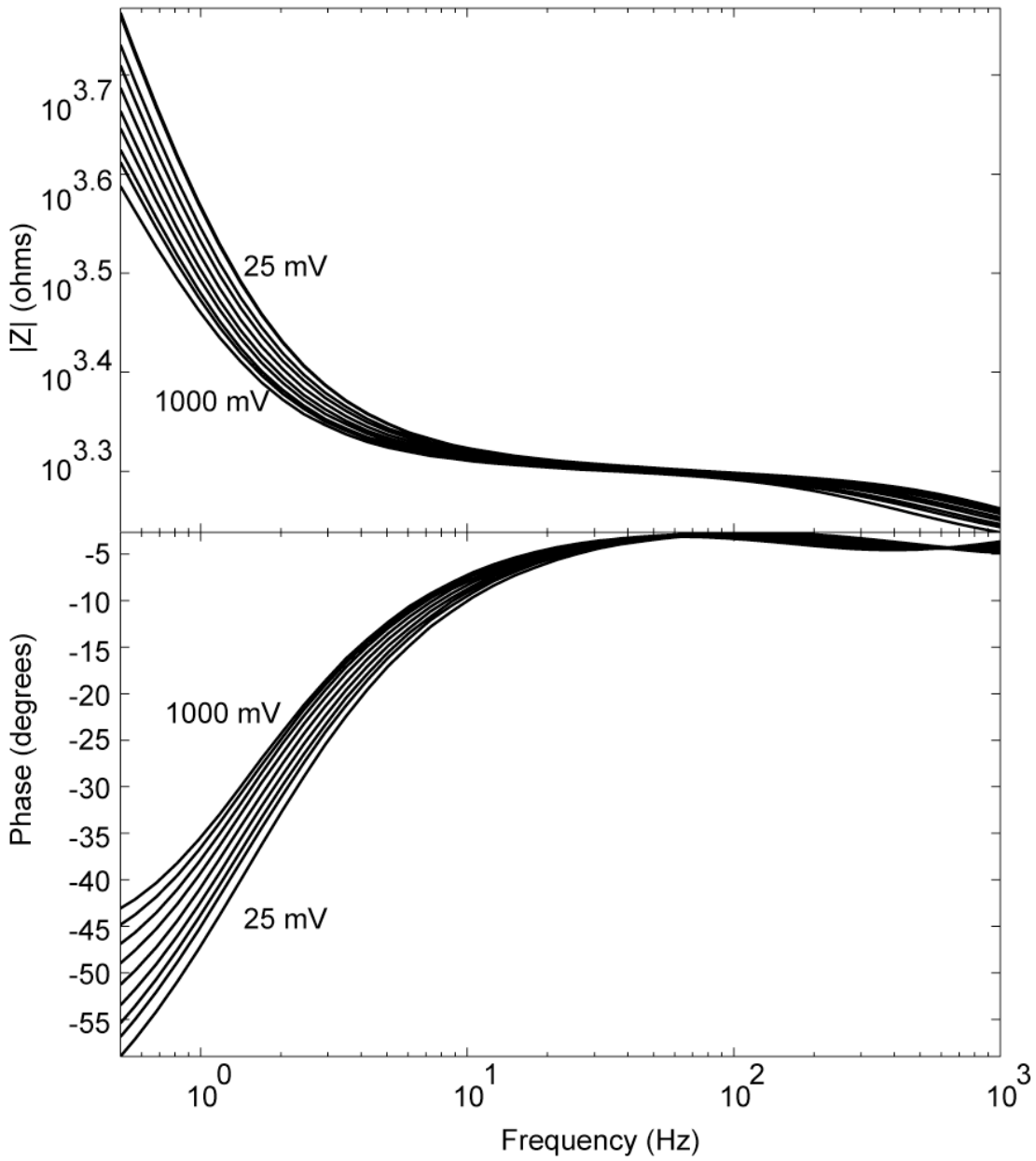

Figure 4-18. Impedance (top: magnitude, bottom: phase) measurements on Ti/Pt electrode immersed in a 100mM KCl solution; the AC excitation voltage varies from 25 mV to 1 V RMS. The corresponding values for the circuit elements in the equivalent circuit model are reported in Table 4-6 and plotted in Figure 4-20.

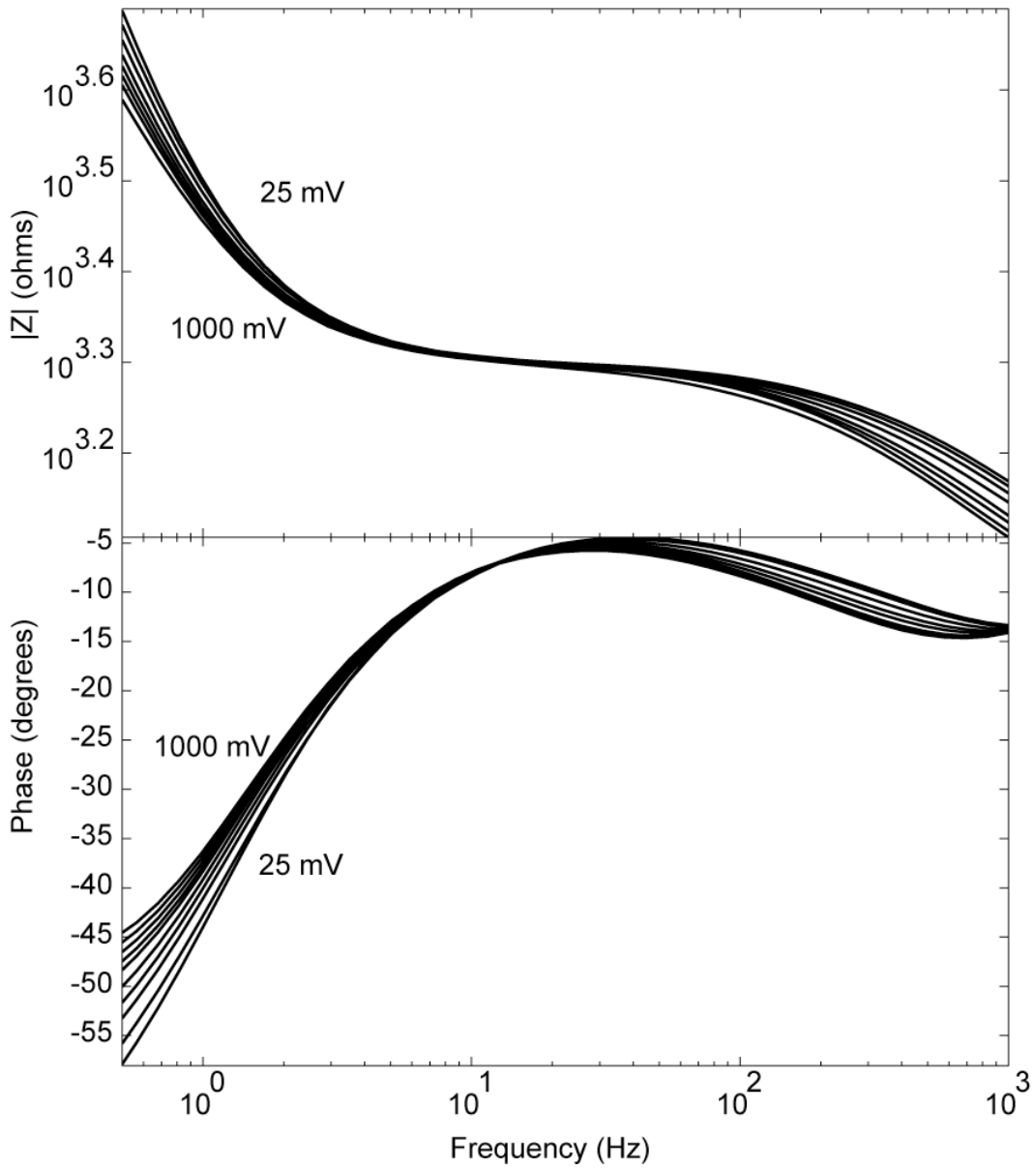

Figure 4-19. Impedance (top: magnitude, bottom: phase) measurements on Ti/Pt electrode immersed in a 1M KCl solution; the AC excitation voltage varies from 25 mV to 1 V RMS. The corresponding values for the circuit elements in the equivalent circuit model are reported in Table 4-6 and plotted in Figure 4-20.

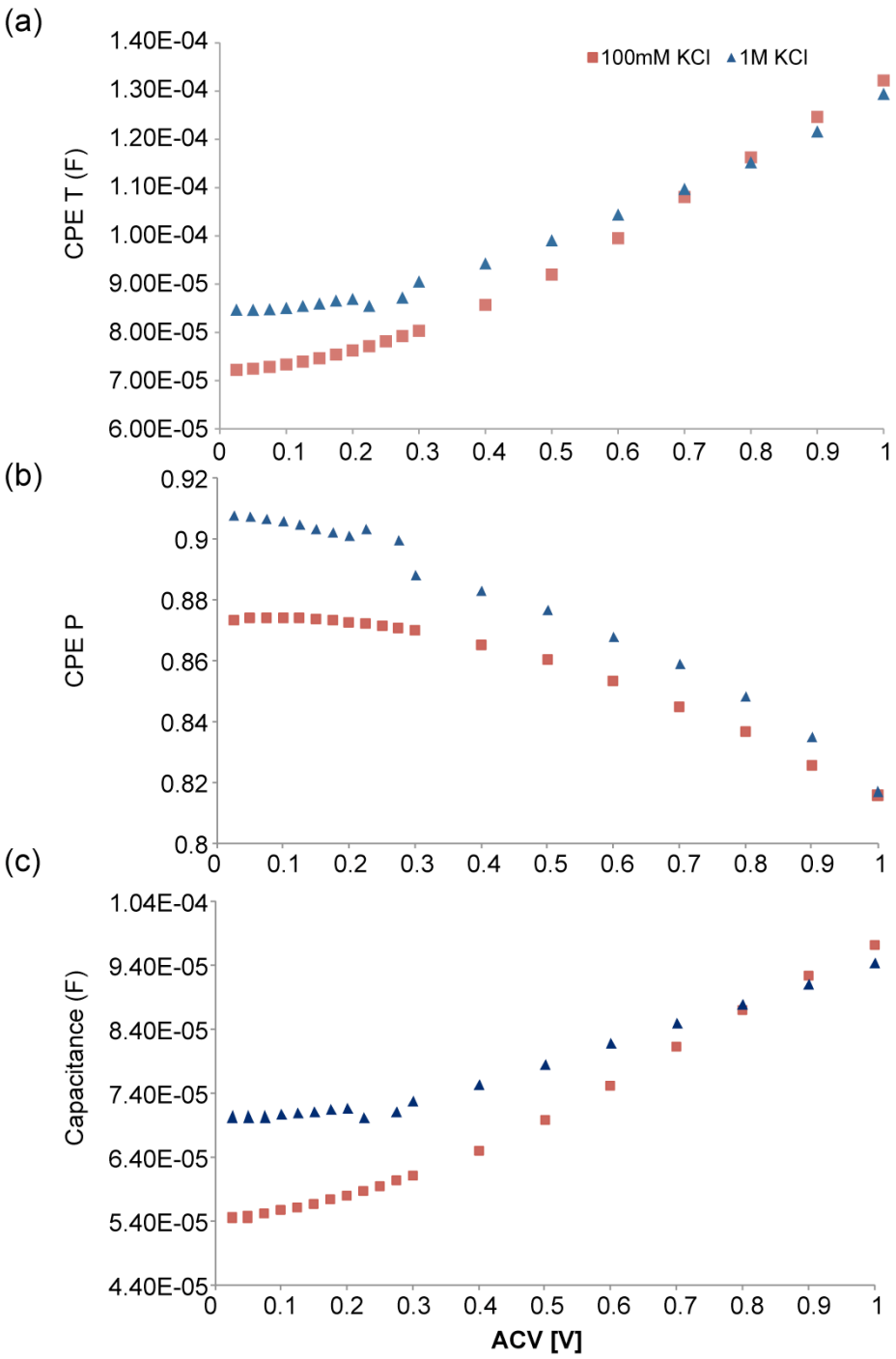

Figure 4-20. Double layer capacitance equivalent circuit model values extracted from impedance measurements on a Ti/Pt electrode applying AC excitation voltages ranging from 25mV to 1V in 100mM and 1M KCl solutions (impedance plots are shown in Figure 4-18 and Figure 4-19).

Voltage	Rsol	Rsol	ratio	CPE-T	CPE-T	ratio	CPE-P	CPE-P	ratio
0.025	1993	1964	1.01	7.22E-05	8.47E-05	0.85	0.8730	0.9076	0.96
0.05	1994	1963	1.02	7.25E-05	8.47E-05	0.86	0.8738	0.9071	0.96
0.075	1993	1962	1.02	7.29E-05	8.48E-05	0.86	0.8740	0.9065	0.96
0.1	1992	1962	1.02	7.33E-05	8.51E-05	0.86	0.8741	0.9056	0.97
0.125	1992	1960	1.02	7.39E-05	8.55E-05	0.87	0.8739	0.9045	0.97
0.15	1991	1959	1.02	7.46E-05	8.60E-05	0.87	0.8736	0.9034	0.97
0.175	1990	1958	1.02	7.54E-05	8.66E-05	0.87	0.8730	0.9019	0.97
0.2	1989	1955	1.02	7.62E-05	8.69E-05	0.88	0.8725	0.9010	0.97
0.225	1989	1852	1.07	7.71E-05	8.55E-05	0.90	0.8720	0.9033	0.97
0.25	1988			7.82E-05			0.8714		
0.275	1987	1848	1.08	7.92E-05	8.72E-05	0.91	0.8707	0.8993	0.97
0.3	1986	1946	1.02	8.03E-05	9.05E-05	0.89	0.8700	0.8880	0.98
0.4	1977	1939	1.02	8.57E-05	9.43E-05	0.91	0.8649	0.8827	0.98
0.5	1971	1933	1.02	9.20E-05	9.91E-05	0.93	0.8600	0.8765	0.98
0.6	1963	1926	1.02	9.95E-05	1.04E-04	0.95	0.8532	0.8676	0.98
0.7	1955	1919	1.02	1.08E-04	1.10E-04	0.98	0.8446	0.8588	0.98
0.8	1948	1912	1.02	1.16E-04	1.15E-04	1.01	0.8364	0.8479	0.99
0.9	1941	1902	1.02	1.25E-04	1.22E-04	1.02	0.8253	0.8346	0.99
1	1936	1885	1.03	1.32E-04	1.29E-04	1.02	0.8157	0.8169	1.00
legend:		100mM KCl		1M KCl					

Table 4-6 Equivalent circuit model parameter values fitted to impedance spectra acquired from a Titanium electrode immersed in a solution of 100mM KCl at excitation voltage ranging from 25mV to 1 V RMS. The fitted circuit parameters are Rs, and CPE (solution resistance and double layer constant phase element respectively).

Voltage	C/m^2	C/ m^2	CPE/ m^2	CPE/ m^2
0.025	0.3782	0.4900	0.5015	0.5881
0.05	0.3806	0.4892	0.5032	0.5879
0.075	0.3831	0.4894	0.5059	0.5888
0.1	0.3861	0.4902	0.5093	0.5907
0.125	0.3896	0.4916	0.5135	0.5936
0.15	0.3933	0.4934	0.5182	0.5970
0.175	0.3974	0.4958	0.5236	0.6013
0.2	0.4019	0.4968	0.5295	0.6036
0.225	0.4069	0.4873	0.5358	0.5936
0.25	0.4123		0.5427	
0.275	0.4182	0.4937	0.5503	0.6056
0.3	0.4241	0.5050	0.5580	0.6286
0.4	0.4510	0.5223	0.5951	0.6547
0.5	0.4838	0.5451	0.6388	0.6880
0.6	0.5217	0.5676	0.6910	0.7251
0.7	0.5638	0.5897	0.7505	0.7619
0.8	0.6039	0.6100	0.8074	0.8002
0.9	0.6411	0.6320	0.8658	0.8447
1	0.6748	0.6552	0.9182	0.8989
legend:	100mM KCl		1M KCl	

Table 4-7 The equivalent capacitance value, Ceq, is derived according to Equation (4-51) and normalized by the area of the electrode to yield specific capacitance values of F/m^2. Specific values of CPE/m^2 are also presented in the table.

4.11 Semiconductor electrodes

4.11.1 Silicon electrode

Protocol

A doped silicon electrode was immersed in dilute KCl solutions (ranging from 0.1 mM to 1M concentration) and excited by a 25 mV AC RMS signal to measure its low frequency impedance response. The experiment was repeated after exposure of the silicon surface for 1 minute to O_2 plasma using a Tegal Plasmod (power: 100 W, operating pressure: 100mTorr).

Results and discussion

The measured impedance spectra are presented in Figure 4-23 and Figure 4-24. Fitting was done using the equivalent circuit diagram of Figure 4-10(a)). The fitted circuit element values are presented in Table 4-8 and Table 4-9, and plotted in Figure 4-21.

O_2 plasma causes the double layer CPE-T to significantly increase (double) and the power factor (CPE-P) to decrease, particularly at low concentrations. The increase in CPE-T and decrease in CPE-P, would suggest an effective roughening and increase in the electrode surface area.

As in the case of metal electrodes, CPE-P was found to increase with increased solution concentration, although the trend is more pronounced after exposing the electrode to O_2 plasma. Similarly, CPE-T was found to increases monotonically, as expected, as the diffuse layer thickness is inversely proportional to the solution concentration.

Whereas theory predicts that the diffuse layer should change 100-fold (from 30nm to 0.3nm) for a concentration range of 0.1mM to 1M, the change in measured capacitance is only 2-fold. Such discrepancy can be explained by the presence of a thicker dielectric slab in series to the measured double layer. It is postulated that a 1-nm native oxide layer dominates here the overall capacitive response.

Conc. [M]	Rs [Ω]	CPE-T [F^N]	CPE-P	Rp [Ω]	Ceq [F]
1	32.87	2.75E-06	0.86928	657970	6.76601E-07
1.00E-01	171.8	2.46E-06	0.83628	998050	5.375E-07
1.00E-02	1442	1.93E-06	0.83557	1.26E+06	6.06064E-07
1.00E-03	12804	1.79E-06	0.80943	1.58E+06	7.34191E-07
1.00E-04	102580	1.06E-06	0.87926	2.37E+06	7.79135E-07

Table 4-8 Equivalent circuit model parameter values fitted to impedance spectra acquired from a silicon electrode immersed in serially diluted concentrations of KCl. The fitted circuit parameters are Rs, Rp, CPE (solution resistance, charge transfer resistance and double layer constant phase element respectively). CPE-T and CPE-P refer to the base and exponent of the constant phase element, respectively. The equivalent capacitance value, Ceq, is derived according to Equation (4-51)

Conc. [M]	Rs [Ω]	CPE-T [F^N]	CPE-P	Rp [Ω]	Ceq [F]
1	34.48	5.66E-06	0.85455	393080	1.32279E-06
1.00E-01	171.7	5.21E-06	0.80044	626020	9.06389E-07
1.00E-02	1401	4.93E-06	0.75348	6.39E+05	9.67394E-07
1.00E-03	12278	4.99E-06	0.66569	3.73E+05	1.20716E-06
1.00E-04	100340	3.63E-06	0.73910	3.35E+05	2.31944E-06

Table 4-9 Equivalent circuit model parameter values fitted to impedance spectra acquired from a silicon electrode, after O_2 plasma cleaning, immersed in serially diluted concentrations of KCl.. The fitted circuit parameters are Rs, Rp, CPE (solution resistance, charge transfer resistance and double layer constant phase element respectively). CPE-T and CPE-P refer to the base and exponent of the constant phase element, respectively. The equivalent capacitance value , Ceq, is derived according to Equation (4-51)

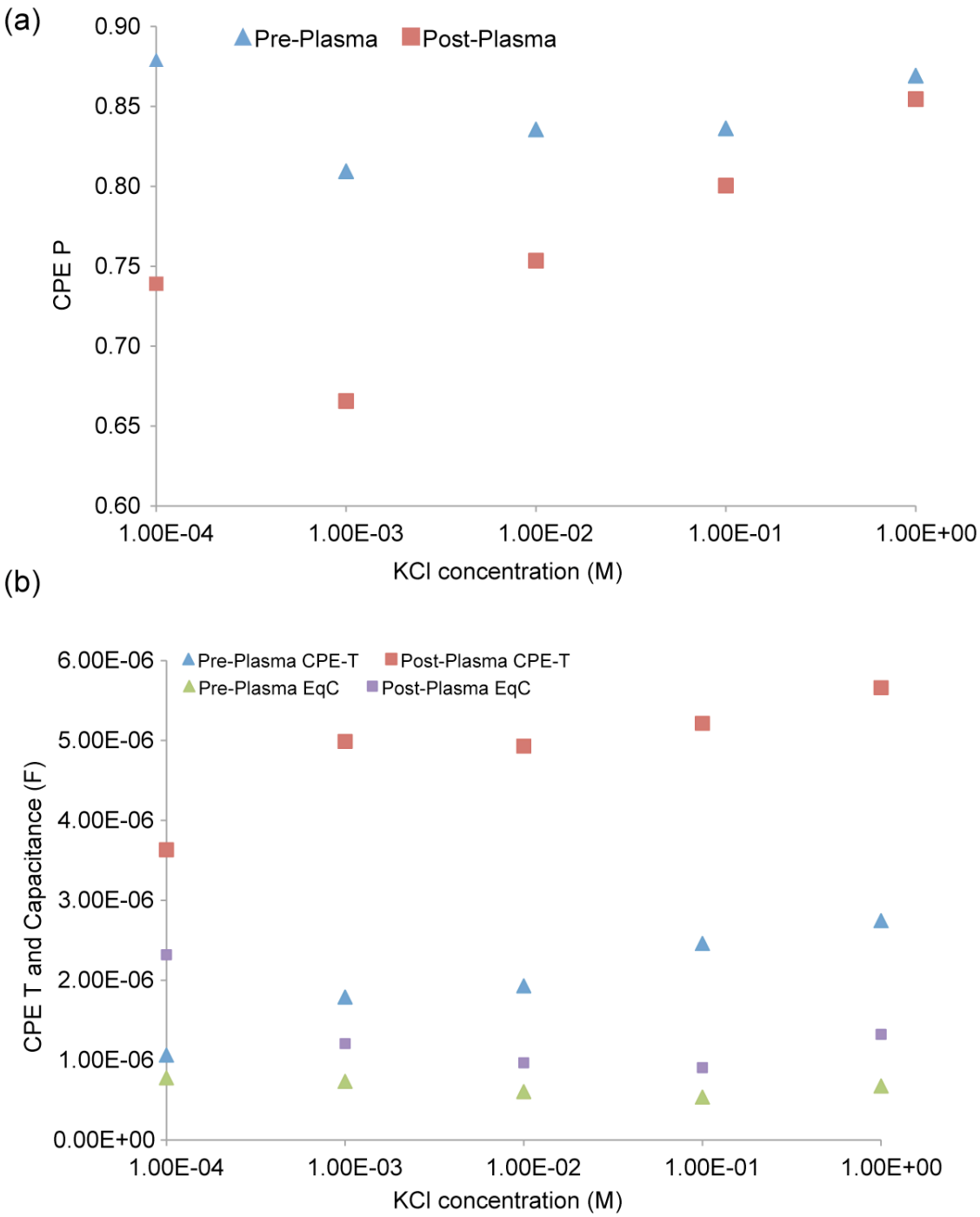

Figure 4-21. Double layer capacitance equivalent circuit model values extracted from impedance measurements on a silicon electrode, before and after O_2 plasma treatment, applying an AC excitation voltage of 25 mV in serially diluted concentrations of KCl, ranging from 0.1mM to 1M. (Corresponding impedance plots are shown in Figure 4-23 and Figure 4-24).

4.11.2 Polysilicon electrode.

Protocol

A doped polysilicon electrode was immersed in diluted KCl (ranging from 0.1 mM to 1M concentration) and excited by a 25 mV AC RMS signal to measure its low frequency impedance response. The experiment was repeated after O_2 plasma cleaning the silicon surface using a Tegal Plasmod (power: 100 W, operating pressure: 100mTorr).

Results and discussion

The impedance spectra are plotted Figure 4-25 and Figure 4-26 and fitted to the equivalent circuit diagram of Figure 4-10(a). The values are presented in Table 4-10 and

1.00E-04	83675	7.17E-06	0.66059	4.28E+05	5.03518E-06

Table 4-11, and plotted in Figure 4-22.

O_2 plasma causes the double layer CPE-T to increase (roughly 3-fold) and the power factor (CPE-P) to decrease by about 20%, across the concentration spectrum. The increase in CPE-T and decrease in CPE-P, would suggest an effective roughening and increase in the electrode surface area.

Contrary to the case of metal and silicon electrodes, CPE-P was found to decrease with increased solution concentration, although the trend was reversed after exposing the electrode to O_2 plasma. CPE-T was found to be roughly constant before plasma treatment; after plasma treatment it was found to increase 4-fold with concentration. As in the case of the silicon electrode, it is concluded that a 1-nm native oxide layer would dominate the overall capacitive response.

Conc. [M]	Rs [Ω]	CPE-T [F^N]	CPE-P	Rp [Ω]	Ceq [F]
1	32.4	5.72E-06	0.84643	466880	1.20342E-06
1.00E-01	173.4	3.58E-06	0.85996	558560	1.0757E-06
1.00E-02	1399	2.98E-06	0.87146	9.25E+05	1.32998E-06
1.00E-03	12751	2.34E-06	0.91131	1.37E+06	1.66278E-06
1.00E-04	83515	1.76E-06	0.89963	4.87E+06	1.4154E-06

Table 4-10 Equivalent circuit model parameter values fitted to impedance spectra acquired from a polysilicon electrode immersed in serially diluted concentrations of KCl. The fitted circuit parameters are Rs, Rp, CPE (solution resistance, charge transfer resistance and double layer constant phase element respectively). CPE-T and CPE-P refer to the base and exponent of

the constant phase element, respectively. The equivalent capacitance value, Ceq, is derived according to Equation (4-51).

Conc. [M]	Rs [Ω]	CPE-T [F^N]	CPE-P	Rp [Ω]	Ceq [F]
1	31.98	1.71E-05	0.75311	377030	1.4585E-06
1.00E-01	172.6	1.43E-05	0.71583	405630	1.31299E-06
1.00E-02	1432	8.25E-06	0.70790	2.75E+05	1.31809E-06
1.00E-03	13476	5.46E-06	0.73168	2.72E+05	2.06202E-06
1.00E-04	83675	7.17E-06	0.66059	4.28E+05	5.03518E-06

Table 4-11 Equivalent circuit model parameter values fitted to impedance spectra acquired from a polysilicon electrode, after O_2 plasma cleaning, immersed in serially diluted concentrations of KCl.. The fitted circuit parameters are Rs, Rp, CPE (solution resistance, charge transfer resistance and double layer constant phase element respectively). CPE-T and CPE-P refer to the base and exponent of the constant phase element, respectively. The equivalent capacitance value , Ceq, is derived according to Equation (4-51)

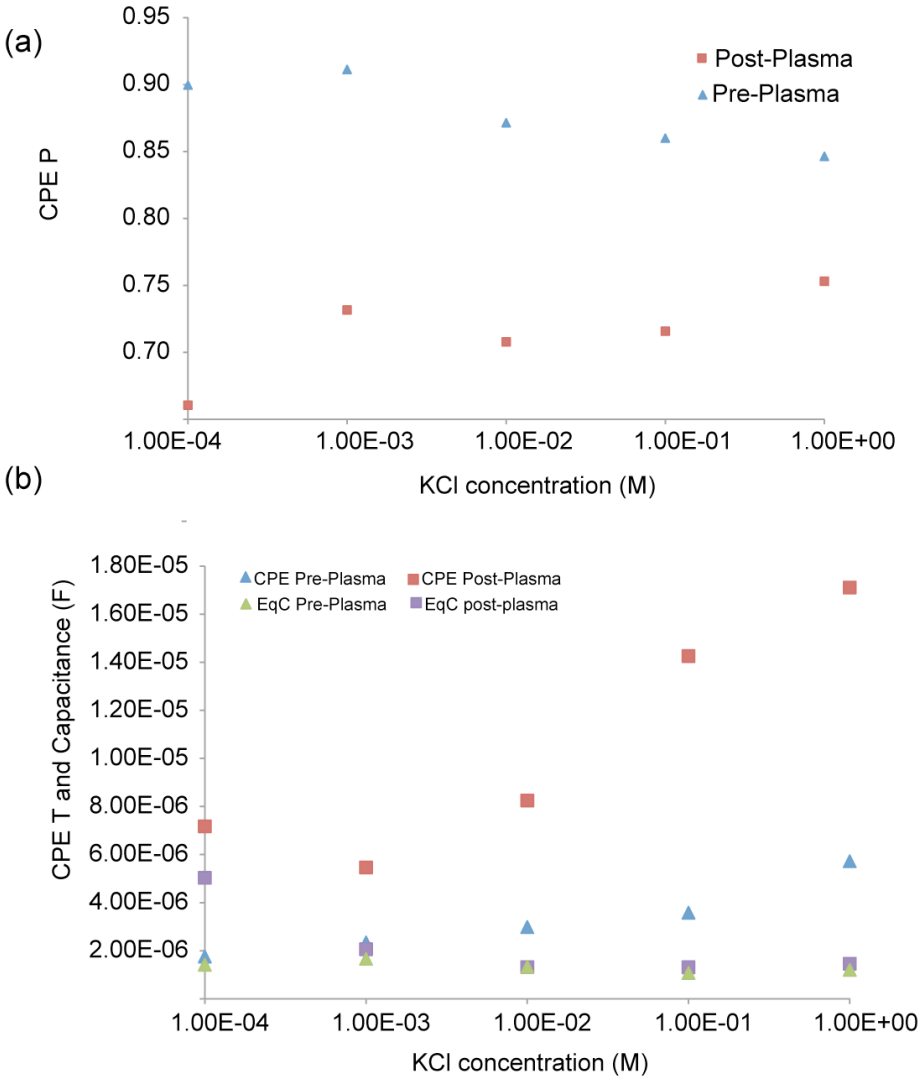

Figure 4-22 Double layer capacitance equivalent circuit model values extracted from impedance measurements on a polysilicon electrode, before and after O_2 plasma treatment, applying an AC excitation voltage of 25 mV in serially diluted concentrations of KCl, ranging from 0.1mM to 1M. (Corresponding impedance plots are shown in Figure 4-25 and Figure 4-26).

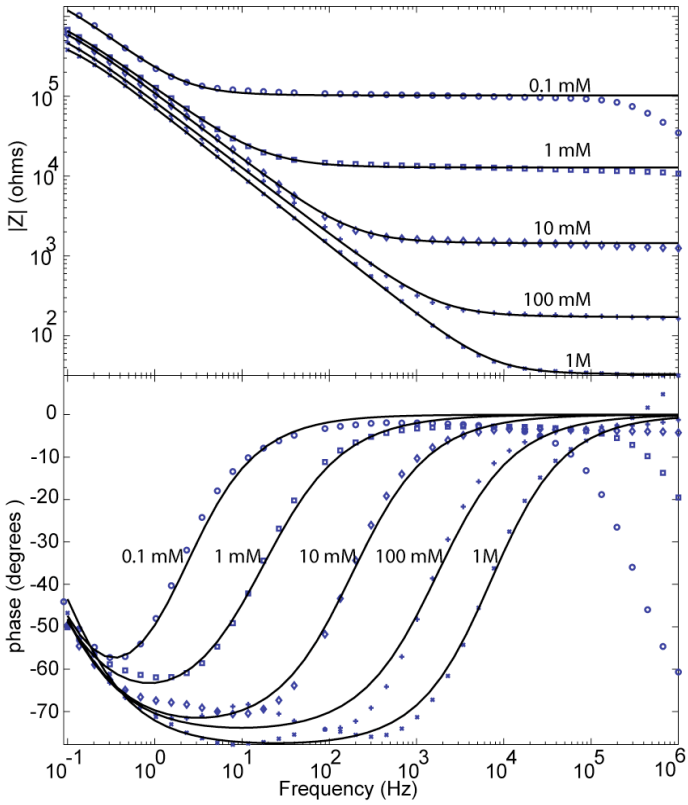

Figure 4-23 Impedance measurements of silicon electrode immersed in KCl solutions of concentration ranging from 1 M to 0.1 mM; the AC excitation voltage is 25 mV RMS. Data points are plotted as symbols. Electrical circuit model responses are plotted as solid lines. The values for the circuit elements in the models are reported in Table 4-8.

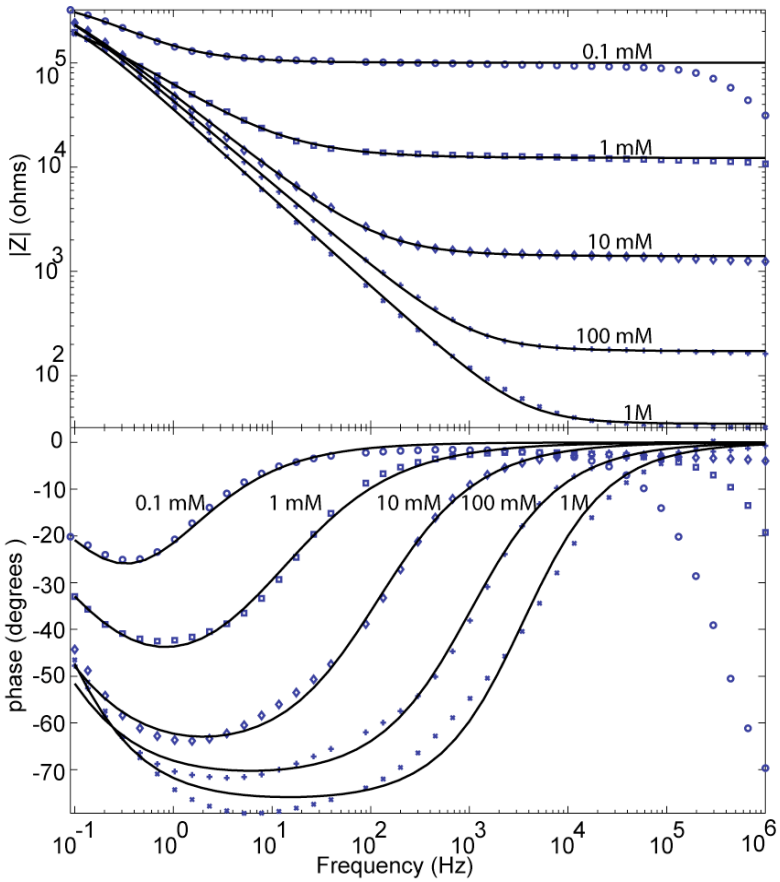

Figure 4-24 Impedance spectrum for silicon electrode exposed to O_2 plasma, immersed in KCl solutions of concentration ranging from 1 M to 0.1 mM; the AC excitation voltage is 25 mV RMS. Data points are plotted as symbols. Electrical circuit model responses are plotted as solid lines. The values for the circuit elements in the models are reported in Table 4-9

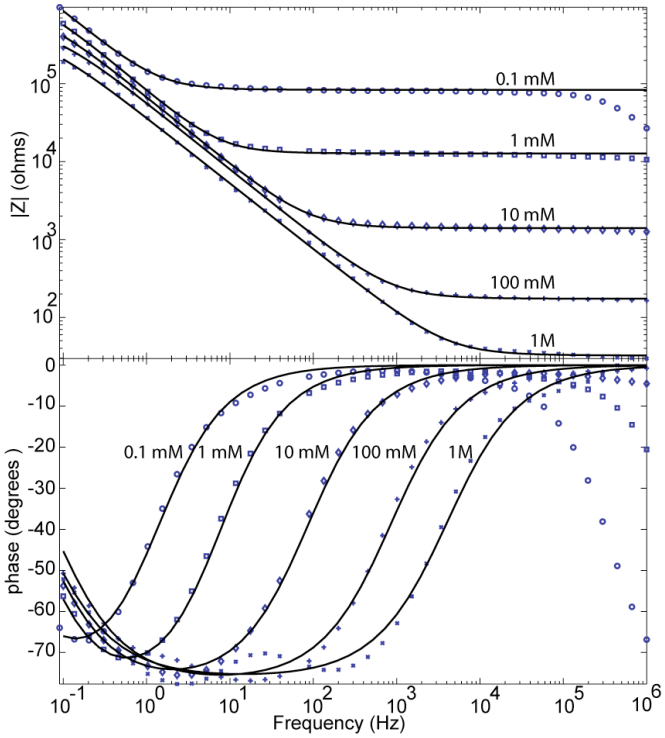

Figure 4-25 Impedance spectrum (top: impedance magnitude, bottom: phase response) measurements on polysilicon electrode immersed in KCl solutions of concentration ranging from 1 M to 0.1 mM; the AC excitation voltage is 25 mV RMS. Data points are plotted as symbols. Electrical circuit model responses are plotted as solid lines. The values for the circuit elements in the models are reported in Table 4-10.

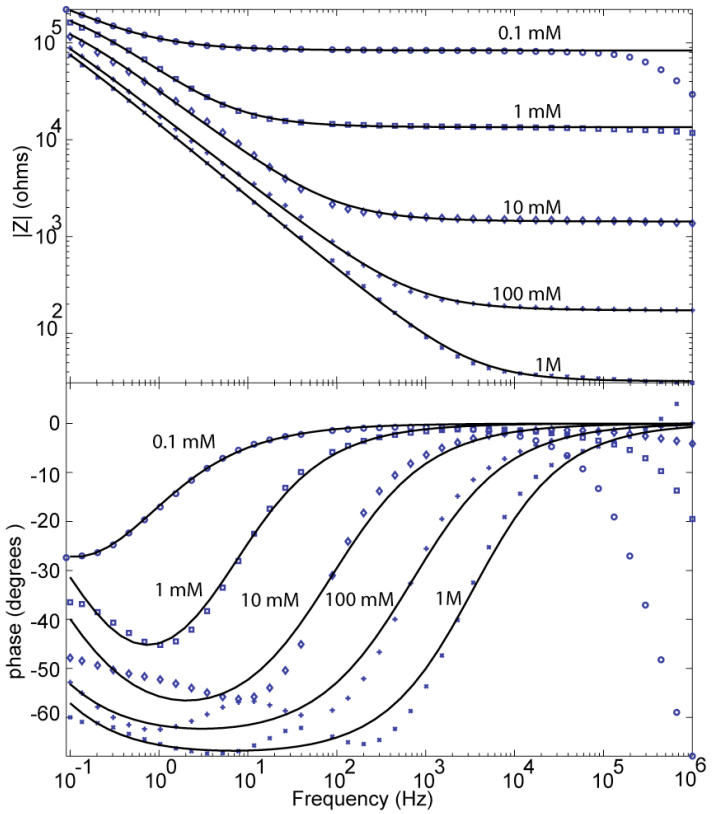

Figure 4-26 Impedance spectrum for polysilicon electrode exposed to O_2 plasma, immersed in KCl solutions of concentration ranging from 1 M to 0.1 mM; the AC excitation voltage is 25 mV RMS. Data points are plotted as symbols. Electrical circuit model responses are plotted as solid lines. The values for the circuit elements in the models are reported in

1.00E-04	83675	7.17E-06	0.66059	4.28E+05	5.03518E-06

Table 4-11 .

4.12 Discussion and Conclusions

Close scrutiny of the literature indicates that there is a wide range of parameters that characterise the electrical double layer. Therefore, the results presented in this chapter were aimed at obtaining values for the modelling and characterization of the double layer capacitance of the materials for the electrodes used in chapters 3,5 and 6 while clarifying some of the inconsistencies found in data available from existing literature.

The results can be summarised as follows:

1. Measurements on smooth gold electrodes resulted in a higher value for the CPE-P than on rough Ti surfaces, confirming the well-documented hypothesis that the power factor is related to surface roughness.
2. The base of the constant phase element (CPE-T) *increases* with solution concentration and with applied voltage, as predicted by GCS theory.
3. The power of the constant phase element (CPE-P) was found to *increase* with the solution concentration and *decrease* with the applied voltage. These trends are not predicted nor explained by the classical double layer theory.
4. For Pt electrodes, at voltages higher than 0.7 V RMS, the double layer capacitance for 100 mM was the same as for 1 M
5. The voltage dependence of CPE-P and CPE-T was more pronounced for gold electrodes than for platinum electrodes
6. Measurable changes in the double layer capacitance on semiconductor electrodes for different electrolyte concentrations are smaller than predicted, presumably due to the native oxide layer which acts as a series capacitor that can dominate the equivalent circuit.

Points (1) and (2), warrant no further discussion: experimental results were in agreement with theoretical predictions of increasing double layer capacitance with more concentrated electrolytes as well as with higher applied voltages. Also qualitative confirmation of the dependence of the CPE power factor on electrode surface roughness was obtained. Point (3) is an interesting finding because traditionally the CPE power factor has been considered a measure of surface roughness (of fractal nature or otherwise), yet measurements performed with the same electrodes, in the

same measuring cell and under the same measuring conditions (excitation voltage amplitude, frequency range, dc bias, and temperature) resulted in CPE-P values that depended on electrolyte concentration. These results demonstrate that impedance data cannot be used to unambiguously define surface characteristics through the fractal index. This behaviour has not been previously reported in the literature.

It is hypothesized here that the CPE power factor correlates not just to the mechanical roughness of the electrode surface but also to the non-uniformity of the ionic layer that is attracted to the electrode-electrolyte interface and constitutes the double layer.

Qualitatively it can be appreciated that as the electrolyte concentration increases, more ions are present on the interface, hence constituting a layer progressively more uniform. Grahame's equation, which relates the surface charge density to the applied potential, can be used to quantify this assertion.

For a flat surface

$$\sigma = -\sqrt{8\varepsilon\varepsilon_0 n_0 k_B T}\sinh\left(\frac{z\psi_0}{2k_B T}\right) \tag{4-52}$$

Which, at T = 25'C, for KCl, simplifies to

$$\sigma = 0.1174\sqrt{c}\sinh\left(19.5\psi_0\right) \tag{4-53}$$

Where the charge density s is in Cm^{-2}, c is the ionic concentration in mol/L. From the charge density value, dividing by the value of fundamental charge, the number of ions/m^2 can be readily calculated. To calculate a fraction of occupied surface area the ions are assumed to have a radius of .150 nm [57].

By assuming a voltage of 25 mV, the values in the following table can be calculated:

V=25mV	c (mol/l)	sinh term	(Charge/m2)	ions/m2	% occ. area
	1.00E-04	4.88E-01	5.72E-04	3.58E+15	0.36
	1.00E-03	4.88E-01	1.81E-03	1.13E+16	1.13
	1.00E-02	4.88E-01	5.72E-03	3.58E+16	3.58
	1.00E-01	4.88E-01	1.81E-02	1.13E+17	11.31
	1.00E+00	4.88E-01	5.72E-02	3.58E+17	35.77

Table 4-13 Ion density on the electrode surface as a function of bulk ionic concentration at V = 25mV

When operating at low potentials, at the lower concentrations in the range, there are very few ions in the solution and the electrode surface uniformly can only be populated sparsely.

Interestingly, however, at higher voltages the CPE power factor decreases. In fact at higher voltages the surface ion density increases and should form a more uniform layer (see table below), which would result in an increased power factor.

50mV	c (mol/l)	sinh term	(Charge/m2)	ions/m2	% occ. area
	1.00E-04	9.75E-01	1.14E-03	7.15E+15	0.72
	1.00E-03	9.75E-01	3.62E-03	2.26E+16	2.26
	1.00E-02	9.75E-01	1.14E-02	7.15E+16	7.15
	1.00E-01	9.75E-01	3.62E-02	2.26E+17	22.62
	1.00E+00	9.75E-01	1.14E-01	7.15E+17	71.54
100mV	c (mol/l)	sinh term	(Charge/m2)	ions/m2	% occ. area
	1.00E-04	1.95E+00	2.29E-03	1.43E+16	1.43
	1.00E-03	1.95E+00	7.24E-03	4.52E+16	4.52
	1.00E-02	1.95E+00	2.29E-02	1.43E+17	14.31
	1.00E-01	1.95E+00	7.24E-02	4.52E+17	45.25
	1.00E+00	1.95E+00	2.29E-01	1.43E+18	143.08
250mV	c (mol/l)	sinh term	(Charge/m2)	ions/m2	% occ. area
	1.00E-04	4.88E+00	5.72E-03	3.58E+16	3.58
	1.00E-03	4.88E+00	1.81E-02	1.13E+17	11.31
	1.00E-02	4.88E+00	5.72E-02	3.58E+17	35.77
	1.00E-01	4.88E+00	1.81E-01	1.13E+18	113.12
	1.00E+00	4.88E+00	5.72E-01	3.58E+18	357.70
700mV	c (mol/l)	sinh term	(Charge/m2)	ions/m2	% occ. area
	1.00E-04	1.37E+01	1.60E-02	1.00E+17	10.02
	1.00E-03	1.37E+01	5.07E-02	3.17E+17	31.67
	1.00E-02	1.37E+01	1.60E-01	1.00E+18	100.16
	1.00E-01	1.37E+01	5.07E-01	3.17E+18	316.72
	1.00E+00	1.37E+01	1.60E+00	1.00E+19	1001.57
1V	c (mol/l)	sinh term	(Charge/m2)	ions/m2	% occ. area
	1.00E-04	1.95E+01	2.29E-02	1.43E+17	14.31
	1.00E-03	1.95E+01	7.24E-02	4.52E+17	45.25
	1.00E-02	1.95E+01	2.29E-01	1.43E+18	143.08
	1.00E-01	1.95E+01	7.24E-01	4.52E+18	452.46
	1.00E+00	1.95E+01	2.29E+00	1.43E+19	1430.81

Table 4-14 Ion density on the electrode surface as a function of bulk ionic concentration at voltages ranging from 50mV to 1V.

The decrease of power factor with increasing voltage must be explained by the onset of faradaic processes which occur once threshold voltages for oxidation and reduction reactions on the electrode surface are reached.

Altough gold and platinum electrodes, when operated at low voltages (~50 mV) or so, in physiological solutions (e.g. KCl, NaCl, PBS) can be considered good approximations for ideal polarizable electrodes, at sufficiently high potentials the water at the negatively charged electrode will be reduced to hydrogen gas:

Reduction reaction: $2H^+(aq) + 2e^- \rightarrow H_2(g)$ (4-54)

Whilst at the negatively charged electrode, an oxidation reaction will occur generating oxygen gas

Oxidation reaction: $2H_2O \rightarrow O_2(g) + 4H^+(aq) + 4e^-$ (4-55)

The reaction that occurs can be modelled in the equivalent circuit model of the double layer as a resistor in parallel to the double layer capacitance: when no reaction occurs, no path exists for charges to cross the electrode/electrolyte interface therefore the electrode behaves as ideally polarizable and the resistance in the model is infinitely high. When reactions start to occur so does charge transfer, lowering the resistance in the equivalent model. When the resistance has a value comparable or smaller than the low frequency impedance of the double layer capacitance, it begins to dominate the impedance response of the system, thus lowering the relevance of the contribution of the double layer capacitance.

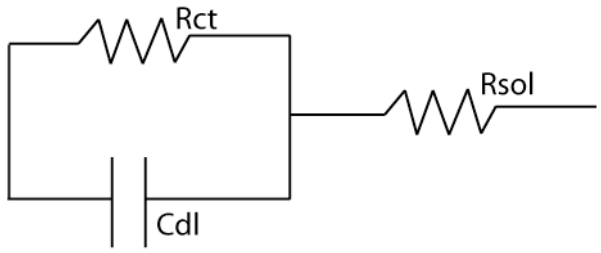

Figure 4-27 Equivalent circuit model for a non-ideal polarisable electrode: Rct models any charge transfer reactions, Cdl models double layer capacitance, Rsol models the solution resistance.

For example, for the platinum electrodes, and at voltages above 0.7 V, the measured double layer capacitance for 100mM and 1M KCl solutions was the same (point (4)). Arguably, even if the double layer capacitances were different (since the debye length of the diffuse layer in 1M KCl should be $\sqrt{10}$ smaller that in 100mM), the difference couldn't be measured as the charge transfer resistance would mask the capacitive changes.

Finally, measurements for doped silicon and polysilicon electrodes show that semiconductors are poor materials for impedance-based sensors because even though

they can be made to be sufficiently conductive, a native oxide layer spontaneously forms on cotact with the atmosphere which significantly diminishes their sensitivity (sensitivity being defined here as the relative percent change in impedance with respect to a given percent change in the double layer capacitance) . This finding is consistent with experimental results obtained with the nanogap capacitive sensor described in Chapter 6 and the deleterious effects of parasitic silicon oxide on impedance based biosensors are further discussed in section 7 of Chapter 6.

References

[1] V. Helmholtz, "Uber die Erhaltung der Kraft," *Ann. Physik,* vol. 89, pp. 568-579, 1853.

[2] G. Gouy, "Sur la constitution de la charge electrique a la surface d'un electrolyte," *Compt. Rend.,* vol. 149, pp. 654-657, 1909.

[3] D. L. Chapman, "A contribution to the theory of electrocapillarity," *Philos Mag,* vol. 25, no. 475, 1913.

[4] E. Stern, *Z. Elektrochem.,* vol. 30, 1924.

[5] J. Lyklema, *Fundamentals of interface and colloid science* London: Academic Press, 1991.

[6] M. Manciu, and E. Ruckenstein, "The polarization model for hydration/double layer interactions: the role of the electrolyte ions," *Advances in Colloid and Interface Science,* vol. 112, no. 1-3, pp. 109-128, Dec, 2004.

[7] M. Spaarnay, *Rec Trav Chem BA,* vol. 77, pp. 872, 1958.

[8] Y. Gur, I. Ravina, and A. J. Babchin, "Electrical Double-Layer Theory .2. Poisson-Boltzmann Equation Including Hydration Forces," *Journal of Colloid and Interface Science,* vol. 64, no. 2, pp. 333-341, 1978.

[9] S. Levine, and G. M. Bell, "Modified Poisson-Boltzmann Equation and Free Energy of Electrical Double Layers in Hydrophobic Colloids," *Discussions of the Faraday Society*, no. 42, pp. 69-&, 1966.

[10] B. Jonsson, and H. Wennerstrom, "Image-Charge Forces in Phospholipid-Bilayer Systems," *Journal of the Chemical Society-Faraday Transactions Ii,* vol. 79, pp. 19-35, 1983.

[11] M. Bostrom, D. R. M. Williams, and B. W. Ninham, "Surface tension of electrolytes: Specific ion effects explained by dispersion forces," *Langmuir,* vol. 17, no. 15, pp. 4475-4478, Jul, 2001.

[12] E. Ruckenstein, and M. Manciu, "Specific ion effects via ion hydration: II. Double layer interaction," *Advances in Colloid and Interface Science,* vol. 105, pp. 177-200, Sep, 2003.

[13] M. Manciu, and E. Ruckenstein, "Specific ion effects via ion hydration: I. Surface tension," *Advances in Colloid and Interface Science,* vol. 105, pp. 63-101, Sep, 2003.

[14] P. Debye, *Phys. Z.,* vol. 24, 1923.

[15] I. Ermolina, and H. Morgan, "The electrokinetic properties of latex particles: comparison of electrophoresis and dielectrophoresis," *Journal of Colloid and Interface Science,* vol. 285, no. 1, pp. 419-428, 2005.

[16] C. F. Zukoski, and D. A. Saville, "An Experimental Test of Electrokinetic Theory Using Measurements of Electrophoretic Mobility and Electrical-Conductivity," *Journal of Colloid and Interface Science,* vol. 107, no. 2, pp. 322-333, 1985.

[17] C. S. Mangelsdorf, and L. R. White, "The dynamic double layer - Part 1 - Theory of a mobile Stern layer," *Journal Of The Chemical Society-Faraday Transactions,* vol. 94, pp. 2441-2452, 1998.

[18] C. S. Mangelsdorf, and L. R. White, "The dynamic double layer - Part 2 - Effects of Stern-layer conduction on the high-frequency electrokinetic transport properties," *Journal Of The Chemical Society-Faraday Transactions,* vol. 94, pp. 2583-2593, 1998.

[19] J. Ennis, and L. R. White, "Dynamic Stern layer contribution to the frequency-dependent mobility of a spherical colloid particle: A low-zeta-potential analytic solution," *Journal of Colloid and Interface Science*, 2, 1996, pp. 446-459.

[20] J. Wang, S. W. Feldberg, and A. J. Bard, "Measurement of double-layer forces at the polymer film/electrolyte interfaces using atomic force microscopy: Concentration and potential-dependent interactions," *J Phys Chem B*, 2002, pp. 10440-10446.

[21] J. Wang, and A. J. Bard, "Direct atomic force microscopic determination of surface charge at the gold/electrolyte interface - The inadequacy of classical GCS theory in describing the double-layer charge distribution," *J Phys Chem B*, 2001, pp. 5217-5222.

[22] D. Barten, J. M. Kleijn, J. Duval *et al.*, "Double layer of a gold electrode probed by AFM force measurements," *Langmuir*, 2003, pp. 1133-1139.

[23] L. Yang, and R. Bashir, "Electrical/electrochemical impedance for rapid detection of foodborne pathogenic bacteria," *Biotechnology Advances,* vol. 26, pp. 135-150, 2008.

[24] T. H. Degefa, and J. Kwak, "Electrochemical impedance sensing of DNA at PNA self assembled monolayer," *Journal of Electroanalytical Chemistry,* vol. 612, pp. 37-41, 2008.

[25] R. K. Shervedani, and A. Hatefi-Mehrjardi, "Electrochemical characterization of directly immobilized glucose oxidase on gold mercaptosuccinic anhydride self-assembled monolayer," *Sensors and Actuators B-Chemical,* vol. 126, pp. 415-423, 2007.

[26] F. Bjorefors, R. M. Petoral, and K. Uvdal, "Electrochemical impedance Spectroscopy for investigations on ion permeation in omega-functionalized self-assembled monolayers," *Analytical Chemistry,* vol. 79, pp. 8391-8398, 2007.

[27] L. Ceriotti, J. Ponti, F. Broggi *et al.*, "Real-time assessment of cytotoxicity by impedance measurement on a 96-well plate," *Sensors & Actuators: B. Chemical*, Dec 31, 2007.

[28] L. Ceriotti, J. Ponti, P. Colpo *et al.*, "Assessment of cytotoxicity by impedance spectroscopy," *Biosensors & bioelectronics,* vol. 22, no. 12, pp. 3057-63, Jun 14, 2007.

[29] D. R. Merrill, and P. A. Tresco, "Impedance characterization of microarray recording electrodes in vitro," *Proceedings of the 26th Annual International Conference of the Ieee Engineering in Medicine and Biology Society, Vols 1-7*, Proceedings of Annual International Conference of the Ieee Engineering in Medicine and Biology Society, pp. 4349-4352, 2004.

[30] T. Sun, D. Holmes, S. Gawad *et al.*, "High speed multi-frequency impedance analysis of single particles in a microfluidic cytometer using maximum length sequences," *Lab Chip,* vol. 7, no. 8, pp. 1034, Jan 1, 2007.

[31] Y. Feldman, E. Polygalov, I. Ermolina *et al.*, "Electrode polarization correction in time domain dielectric spectroscopy," *Meas Sci Technol*, 2001, pp. 1355-1364.

[32] A. E. Ukshe, "Nature of the Relaxation of a Constant Phase Element," *Soviet Electrochemistry,* vol. 29, no. 1, pp. 167-172, 1993.

[33] A. Sadkowski, "On the ideal polarisability of electrodes displaying cpe-type capacitance dispersion," *Journal of Electroanalytical Chemistry,* vol. 481, no. 2, pp. 222-226, 2000.

[34] G. Lang, and K. E. Heusler, "Comments on the ideal polarisability of electrodes displaying cpe-type capacitance dispersion," *Journal of Electroanalytical Chemistry,* vol. 481, no. 2, pp. 227-229, 2000.

[35] T. Kaplan, and L. J. Gray, “Effect of disorder on a fractal model for the ac response of a rough interface,” *Physical Review B*, Jan 1, 1985.
[36] T. C. Halsey, "Double-Layer Impedance At A Rough-Surface - A Perturbative Approach," *Phys Rev A*, 1987, Pp. 5877-5880.
[37] T. C. Halsey, "Frequency-Dependence Of The Double-Layer Impedance At A Rough-Surface," *Phys Rev A*, 1987, Pp. 3512-3521.
[38] T. Pajkossy, and L. Nyikos, “Scaling-Law Analysis to Describe the Impedance Behavior of Fractal Electrodes,” *Physical Review B,* vol. 42, no. 1, pp. 709-719, 1990.
[39] E. P. M. Vanwesting, G. M. Ferrari, and J. H. W. Dewit, “The Determination of Coating Performance Using Electrochemical Impedance Spectroscopy,” *Electrochimica Acta,* vol. 39, no. 7, pp. 899-910, 1994.
[40] E. P. M. Vanwesting, G. M. Ferrari, and J. H. W. Dewit, “The Determination of Coating Performance with Impedance Measurements .2. Water-Uptake of Coatings,” *Corrosion Science,* vol. 36, no. 6, pp. 957-977, 1994.
[41] E. P. M. Vanwesting, G. M. Ferrari, and J. H. W. Dewit, “The Determination of Coating Performance with Impedance Measurements .3. in-Situ Determination of Loss of Adhesion,” *Corrosion Science,* vol. 36, no. 6, pp. 979-994, 1994.
[42] Z. Kerner, and T. Pajkossy, “Impedance of rough capacitive electrodes: the role of surface disorder,” *Journal of Electroanalytical Chemistry,* vol. 448, no. 1, pp. 139-142, 1998.
[43] L. Nyikos, and T. Pajkossy, “Fractal Dimension and Fractional Power Frequency-Dependent Impedance of Blocking Electrodes,” *Electrochimica Acta,* vol. 30, no. 11, pp. 1533-1540, 1985.
[44] T. Pajkossy, and L. Nyikos, “Impedance of Planar Electrodes with Scale-Invariant Capacitance Distribution,” *Journal of Electroanalytical Chemistry,* vol. 332, no. 1-2, pp. 55-61, Aug 14, 1992.
[45] H. P. Schwan, “Electrode Polarization Impedance and Measurements in Biological Materials,” *Annals of the New York Academy of Sciences,* vol. 148, no. A1, pp. 191-&, 1968.
[46] H. P. Schwan, and C. D. Ferris, “4-Electrode Null Techniques for Impedance Measurement with High Resolution,” *Review of Scientific Instruments,* vol. 39, no. 4, pp. 481-&, 1968.
[47] J. C. Wang, “Impedance of a Fractal Electrolyte-Electrode Interface,” *Electrochimica Acta,* vol. 33, no. 5, pp. 707-711, May, 1988.
[48] P. Zoltowski, “On the electrical capacitance of interfaces exhibiting constant phase element behaviour,” *Journal of Electroanalytical Chemistry,* vol. 443, no. 1, pp. 149-154, Feb 10, 1998.
[49] S. H. Liu, “Fractal Model for the Ac Response of a Rough Interface,” *Physical Review Letters,* vol. 55, no. 5, pp. 529-532, 1985.
[50] F. H. van Heuveln, “Analysis of Nonexponential Transient Response Due to a Constant-Phase Element,” *J Electrochem Soc*, Jan 1, 1994.
[51] K. S. Cole, and R. H. Cole, "Dispersion and absorption in dielectrics I. Alternating current characteristics," *Journal of Chemical Physics*, 1941, pp. 341-351.
[52] J. R. Macdonald, “Impedance spectroscopy,” *Ann Biomed Eng*, Jan 1, 1992.
[53] G. J. Brug, A. L. G. Vandeneeden, M. Sluytersrehbach *Et Al.*, "The Analysis Of Electrode Impedances Complicated By The Presence Of A Constant Phase Element," *Journal Of Electroanalytical Chemistry*, 1984, pp. 275-295.

[54] E. P. M. Vanwesting, G. M. Ferrari, And J. H. W. Dewit, "The Determination Of Coating Performance With Impedance Measurements .2. Water-Uptake Of Coatings," *Corros Sci*, 1994, Pp. 957-977.
[55] V. D. Jovic, "Determination of the correct value of C," *consultrsr.com*.
[56] C. H. Hsu, and F. Mansfeld, "Technical note: Concerning the conversion of the constant phase element parameter Y-0 into a capacitance," *Corrosion*, 2001, pp. 747-748.
[57] M. Khaneghie, A. Zendehnam, and M. Mirzaei, "Statistical characteristics of fluctuation of heights, surface roughness and fractal properties of Cu thin films," *Journal of Physics: Conference Series,* vol. 61, pp. 529-533, 2007.
[58] Petrovic, Strbac, Bundaleski *et al.*, "Surface roughness minimum: Ag thin layer deposited on a glass," *Serbian Chemical Society,* 2001.

Chapter 5 Novel electrode materials

5.1 Introduction

A direct comparison of the impedance of three electrode materials, platinum black, iridium oxide, and PPy/PSS (polypyrrole/poly(styrenesulphonate)) is presented. These materials are compared to pure platinum electrodes of identical dimensions, by fitting data to equivalent circuit models. Electron microscopy is also used to image the surfaces. The relative increase in electrode/electrolyte interface area is estimated and the practical use of these materials for biological applications discussed. Platinum black is a well-characterized and often used electrode, and serves as a benchmark for comparing iridium oxide and PPy/PSS electrodes. The results suggest that iridium oxide and PPy/PSS are good alternative materials and could be used in place of platinum black electrodes.

The use of electrode materials that reduce the parasitic effect of the double layer on the low frequency impedance would be beneficial for many different systems. For example, when studying counterion polarization phenomena, Schwan et al. [1] pointed out that the low-frequency dielectric properties of polystyrene suspensions are directly proportional to the diffusion constant of the counterion cloud and inversely proportional to the particle radius squared, resulting in relaxation frequencies as low as 9 Hz for a 10μm diameter particle, and as high as 14.5 kHz for a 100 nm particle. This low-frequency dielectric relaxation, termed "α dispersion" is also particularly relevant to the dielectric study of DNA in solution [2-5], charged macromolecules [6] and viruses [7]. Therefore, it is obvious that any electrode polarization effect occurring at frequencies below 10 kHz will impinge and possibly irrecoverably mask any counterion polarization effects.

To minimize the effect of electrode polarization it is necessary to minimize its contribution to the overall sensor impedance; maximizing the electrode capacitance. This can be achieved by operating the electrode in dilute solutions, but this is not always feasible for bio-medical applications. Alternatively the geometry of the sensor can be altered to maximize the exposed surface area. This can also be difficult as it is usually desirable to miniaturize measuring volumes to minimize the quantity of the solution under study.

A more feasible alternative for biological applications is to maximize the *electrode-electrolyte interface* area. This can be achieved either by mechanically roughening the electrode surface to obtain an electrode-electrolyte interface area that is

effectively larger than the actual electrode surface, or to use an *ad-hoc* electrode material or treatment that leads to a high electrode-electrolyte interface area.

To this extent much effort has gone into developing electrode surfaces that are alternative to noble metals like platinum and gold, which while attractive because of their wide availability, inertness and biocompatibility, have a comparatively smooth surface. A traditional alternative is platinum black electrodes, where a fine platinum powder is electrodeposited on the surface of a smooth platinum electrode to yield a porous and fractal surface with a much higher effective area [8]. The fragility of the electrodeposited black film, the toxicity of the platinizing solution, (water: hexachloroplatinic acid: lead acetate), the poor reproducibility of the deposition protocols have restricted the adoption of platinum black for lab-on-a-chip devices, notwithstanding its desirable electrical properties.

Titanium nitride is an alternative material, and has been used for biomedical purposes by Norlin et al. [9] and Franks et al. [10]. Both groups found that TiN offered similar improvements, in terms of high electrode surface area, as platinum black, without incurring in the fragility and biotoxicity issues of the latter.

In this chapter two emerging electrode materials are examined: iridium oxide and PPy/PSS polyelectrolyte electrodes. Sputtered iridium oxide is a novel material for low-frequency impedance spectroscopy, although it has been used extensively as a material for electrode and probe for neural recordings [11-20], as well as to measure local changes in pH induced by metabolic cellular activity [18, 21, 22]. Here a full impedance characterization is reported and it is demonstrated that it is possible to increase the effective surface area producing values that are equivalent to platinum black, but without the durability and toxicity issues. Comparison focuses on four key parameters; (1) increase in electrode/electrolyte interface area relative to a plain platinum surface, (2) ease of fabrication, (3) potential toxicity for biological applications, and (4) durability and lifetime of the surface.

5.2 Methods

5.2.1 Electrode preparation

All electrodes (8 mm x 8 mm) were patterned onto 4” Pyrex wafers and diced into 25mm x 75 mm rectangles. Each electrode was connected by a 0.5 mm electrode

line to a 15mm x 10mm metal contact pad at the opposite end of the slide. All metal films were sputtered (Nordiko NS 2550 DC) with either a Pt or Ir targets of 99.9% purity at 10^{-5} mbar using a Ti adhesion layer. The electrodes were made using a lift-off process.

5.2.2 Platinum Black treatment

The platinum black treatment was achieved using well-documented techniques [23]. Briefly, the electrode was connected to the negative terminal of a dc power supply and immersed in a solution of 1.4% v/v hexachloroplatinic acid diluted in DI water. To this solution, 0.02% w/v lead acetate was added. A platinum foil counter-electrode was also immersed in the solution and connected to the positive terminal of the power supply. A potential of 1.6 V was applied, resulting in a current density of 8 mA/cm^2, for 120 seconds. The plated electrodes, appearing a matt-black, were then thoroughly rinsed and stored in saline solution until use.

5.2.3 Iridium Oxide sputtering and activation

Iridium oxide sputtering was performed by Andre Van Ooyen at the University of Aachen, Germany. All iridium oxide films were reactively sputtered in Ar/O_2 plasma onto a Ti adhesion layer and platinum sub-layer. Film thickness was determined with a *Tencor PA-10* profilometer. DC voltage was applied to the target with a power of 180 W and the argon flow in the plasma was kept at 100 sccm (standard cubic centimetre per minute). A sputtered film thickness of approximately 300 nm was reached.

The electrode was activated using a CHI 750 electrochemical workstation, operating in 'cyclic voltammetry' mode with a platinum foil counter electrode and an Ag/AgCl reference electrode in a saline solution (154 mM NaCl). Activation parameters: V_{min} = -1.1, V_{max} = 1.2, V_{rate} = 0.1 V/m. Figure 5-1 shows the resultant CV curves. Figure 5-2 shows the injection charge capacity (obtained by integrating the voltage along the CV curve obtained for each cycle) compared to the double layer capacitance, as measured after 0, 10, 20 and 50 activation cycles. It is immediately apparent that when used for impedance spectroscopy purposes, iridium oxide electrodes show a remarkable increase in double layer capacitance after only 10 activation cycles. Additional voltammetry leads to only marginal improvements.

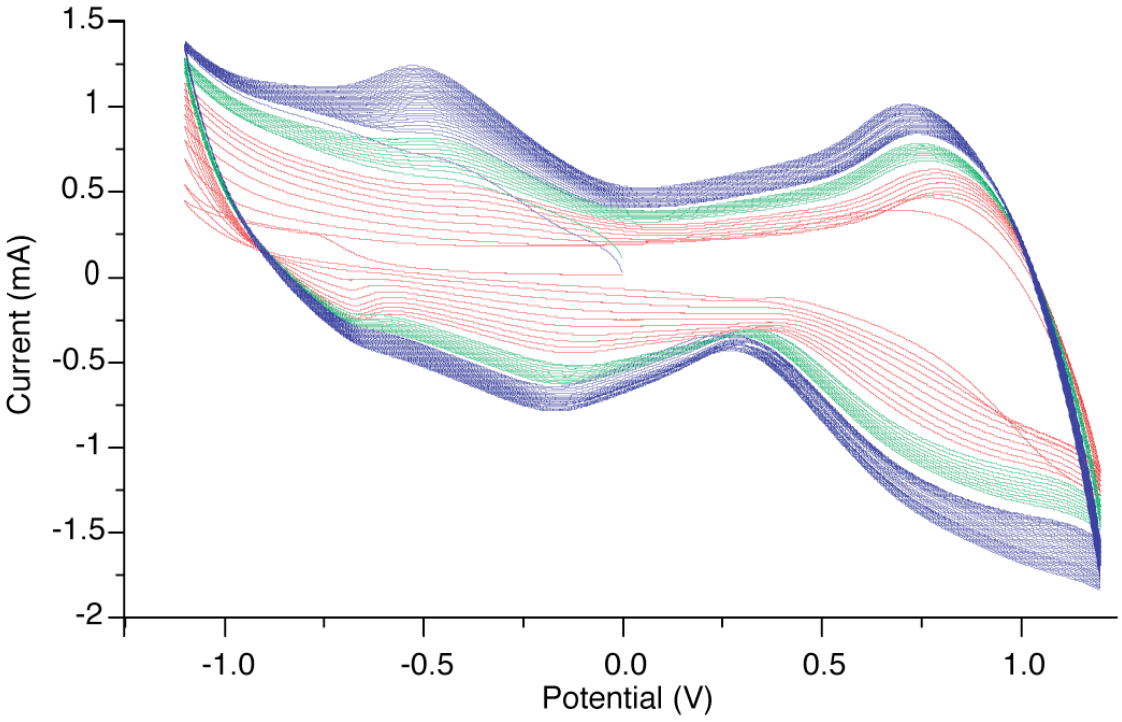

Figure 5-1 Current vs voltage curves, scanned at 0.1 V/s. The colour refers to three successive activation steps (red, green and blue), each of which consisted of 10 complete cycles. The increased charge injection capacity is evident from the larger and larger area that is enclosed by the CV curves. The main feature of the CV curves is their symmetry along the potential axis, resulting in transfer of equal integral anodic and cathodic charges through the phase boundary electrode/electrolyte. Iridium changes its oxidation state repeatedly during the potential cycling, and from this aspect it can be stated that the activated iridium oxide show a reversible electrochemical behaviour. The shape of the curves is complicated; the existing current peaks are broad and not very well depicted, which suggests the existence of various active surface sites with different formal potentials participating in the redox processes

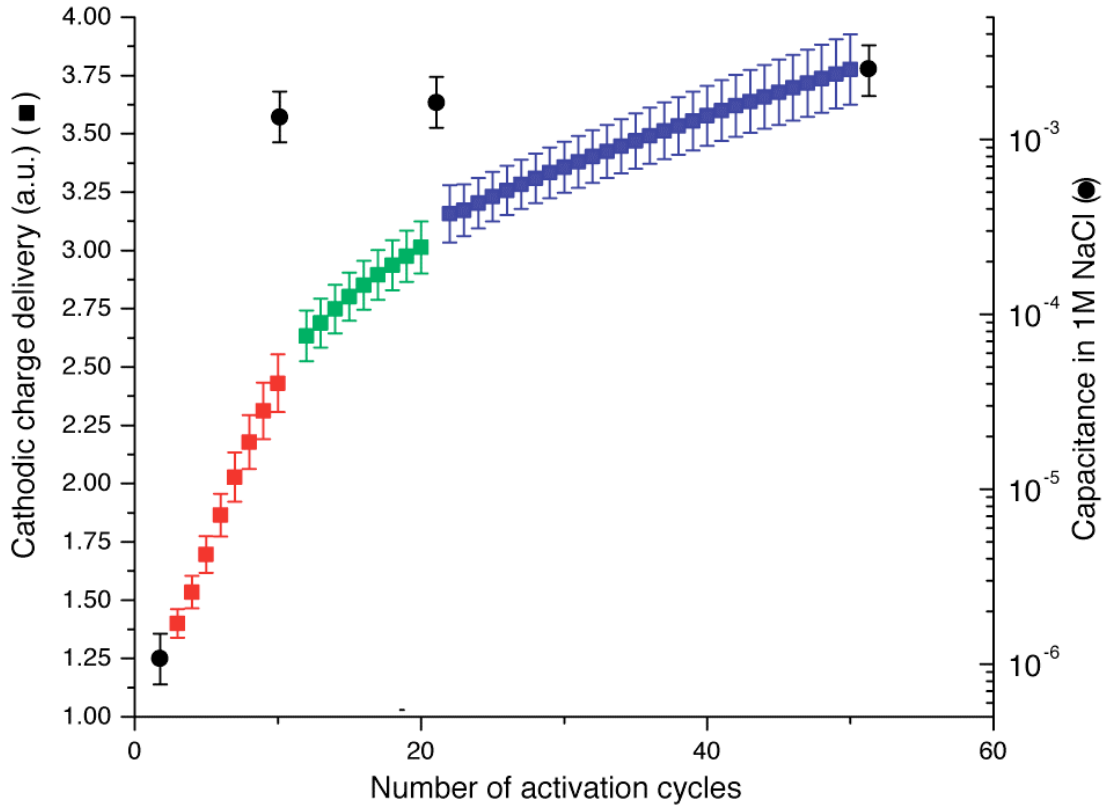

Figure 5-2 (left axis, coloured) Charge injection capacity evolution plotted against number of activation cycles. (right axis, black) Capacitance measured in 1M NaCl.

5.2.4 PPy/PSS galvanostatic deposition

The activation solution was prepared following the protocol of George et al [24]. Briefly, 0.2 M Pyrrole reagent (98% Sigma) and 0.2 M of Poly(4-styrenesulfonic acid) solution (Sigma), were mixed and stirred for 15 minutes at room temperature. The electrodes were immersed in the polymer solution and connected to the positive terminal of a DC power supply. A platinum foil counter-electrode was also immersed in the solution and connected to the negative terminal of the power supply. A voltage of 1.24 V was applied resulting in a current density of 1.5 mA/cm^2. The deposition was carried out for 180 seconds.

5.3 Measurement setup

5.3.1 Dielectric Analyzer Setup

A high-resolution dielectric analyzer (Novocontrol Alpha-N) was used to acquire the impedance spectra. The instrument was set to output 0V DC bias, and an excitation signal of 25 mV RMS amplitude was swept in frequencies ranging from 1 MHz to 1 Hz in 50 steps, logarithmically spaced. Occasionally, frequencies as low as 0.01 Hz were sampled when good capacitive fits were difficult to achieve because of extremely high capacitance values.

5.3.2 Measuring Cell

The electrodes were positioned in a custom-made plastic measuring cell filled with 5 ml of solution, such that they were completely submerged. The cell was designed to hold the electrodes at a fixed distance of 5.8 mm. Wires were bonded to contact pads with conductive epoxy, connecting the electrodes to the dielectric analyzer via coaxial lines. All measurements were taken using two of the same type and size of electrode in order to maintain a uniform electric field.

5.3.3 Electrolyte Solutions

Serial dilutions of NaCl electrolyte were prepared in concentrations ranging from 1 M to 0.1 mM. 0.9% w/v physiological saline (i.e. 154 mM NaCl) was also used for the time-lapse measurements. Dulbecco's phosphate buffer saline modified solution (without calcium chloride and magnesium chloride) was bought from Sigma-Aldrich.

5.3.4 Equivalent Circuit Analysis

Fitting to equivalent circuit models was performed using a linear least-squares fitting algorithm in Zview (Scribner Associates). Both the fits and the percentage error are reported below.

5.3.5 Imaging Setup

Scanning Electron Microscope images were taken with a Hitachi S-5000 SEM at the UC Berkeley Electron Microscopy Laboratory facility. The samples were diced with a diamond scribe, and placed directly into the SEM without any additional treatment, with the exception of the iridium oxide sample. In this case the iridium oxide sample was coated with an additional layer of platinum and gold mixture that was less than 2nm thick (Tousimis Sputter Coater).

5.4 Results

5.4.1 Measurements in Serial Concentrations of NaCl

To characterize the impedance response of the double layer, spectra were acquired after submerging the electrodes in NaCl, measuring the response of double layers of thickness from ~30 nm (for 0.1 mM NaCl) to ~1nm (for 1 M NaCl). The response from three pairs of electrodes for each material tested were recorded and their mean |Z| and phase plotted in Figure 5-3 to Figure 5-6.

Examining the impedance plots for platinum electrodes (Figure 5-3 (a) and (b)), it can be seen that the lower capacitive slope onset is at 10 kHz for the most concentrated solution (1 M), moving at progressively lower frequencies for the more diluted solutions (down to 10 Hz for 0.1 mM). These changes are reflected in the phase curves: the phase tend to capacitive values (-70^{o}) at higher frequencies for the more concentrated solutions, gradually shifting to lower frequencies for the more diluted ones. A higher frequency capacitive slope is also visible for the 0.1mM curve, corresponding to the capacitance of the bulk solution.

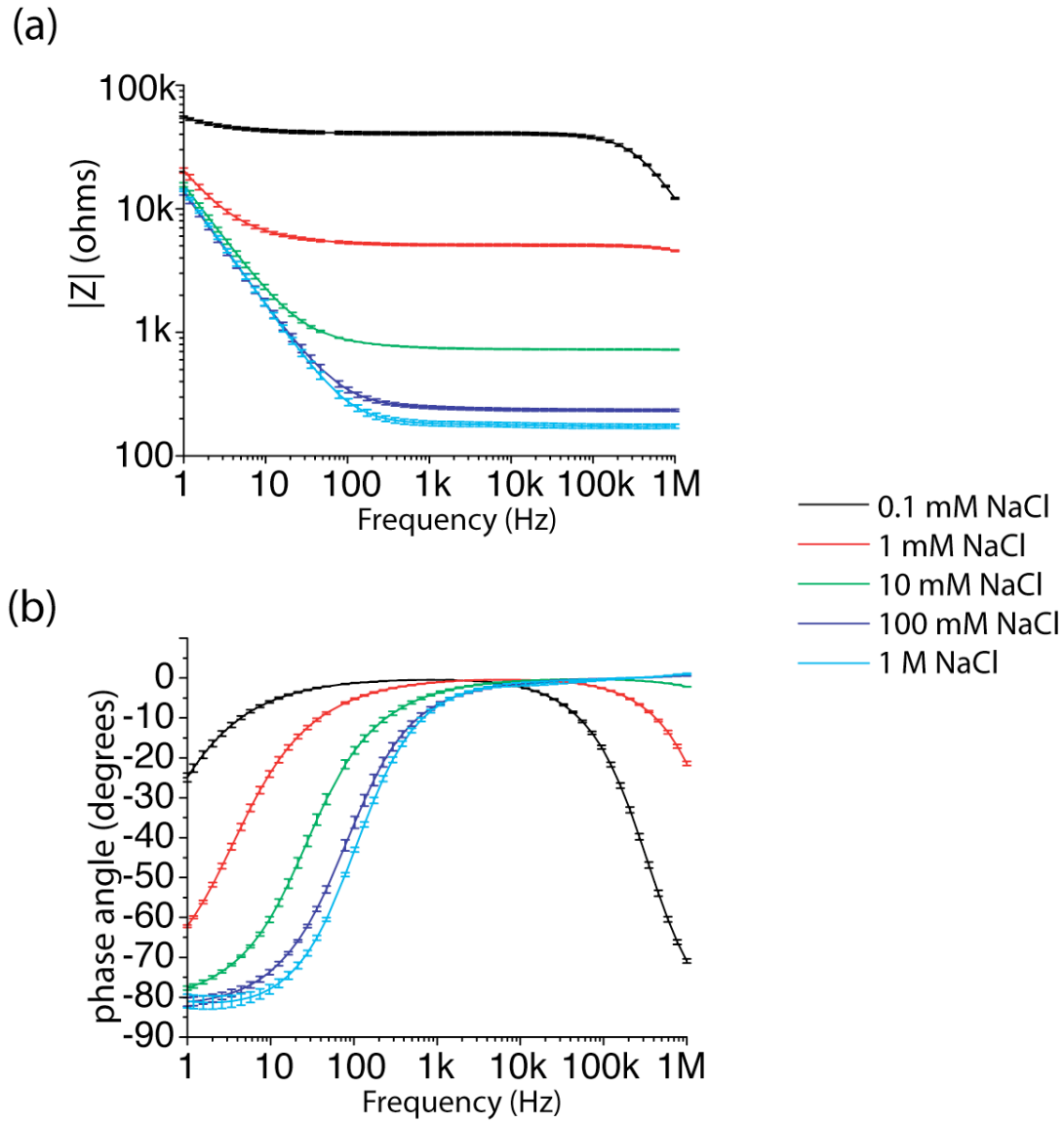

Figure 5-3 Impedance spectra acquired for plain platinum in serially diluted solutions of NaCl. Error bars represent one standard deviation. (a) magnitude of impedance (b) phase.

Iridium oxide electrodes, activated with 50 CV cycles exhibit spectra (Figure 5-4 (a) and (b)) where the |Z| capacitive slope onsets is 'pushed' down three decades in the frequency range, to 10 Hz for 1M NaCl, 1 Hz for 1mM, and out of the measured spectrum for 0.1mM. The phase curves are mostly resistive and tend to capacitive values at lower frequencies. The phase values at the lower end of the spectrum (1Hz) range from -35° to 0°.

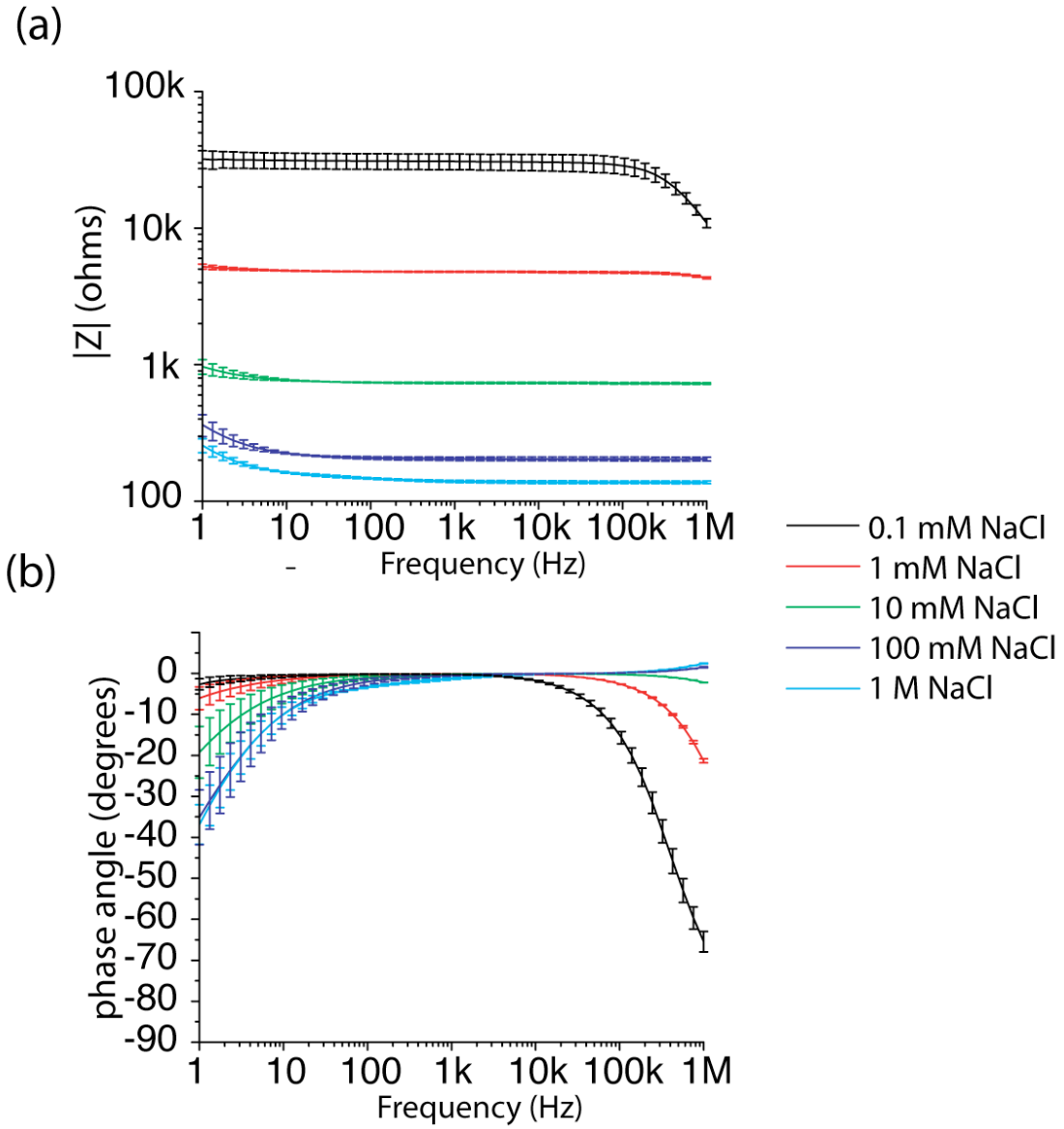

Figure 5-4 Impedance spectra acquired for iridium oxide, activated by 50 CV cycles, in serially diluted solutions of NaCl. Error bars represent one standard deviation. (a) magnitude of impedance (b) phase

The platinum black impedance spectra (Figure 5-5 (a) and (b)) show the capacitive slope breakpoint decreases in frequency to 2 Hz for 1M NaCl, and out of the measured range for the more dilute solutions. The phase curves are mostly resistive (0°) and tend to capacitive values at lower frequencies. The phase values at the lower end of the spectrum (1Hz) range from -20° to 0°, indicating a slight improvement over the iridium oxide electrode response.

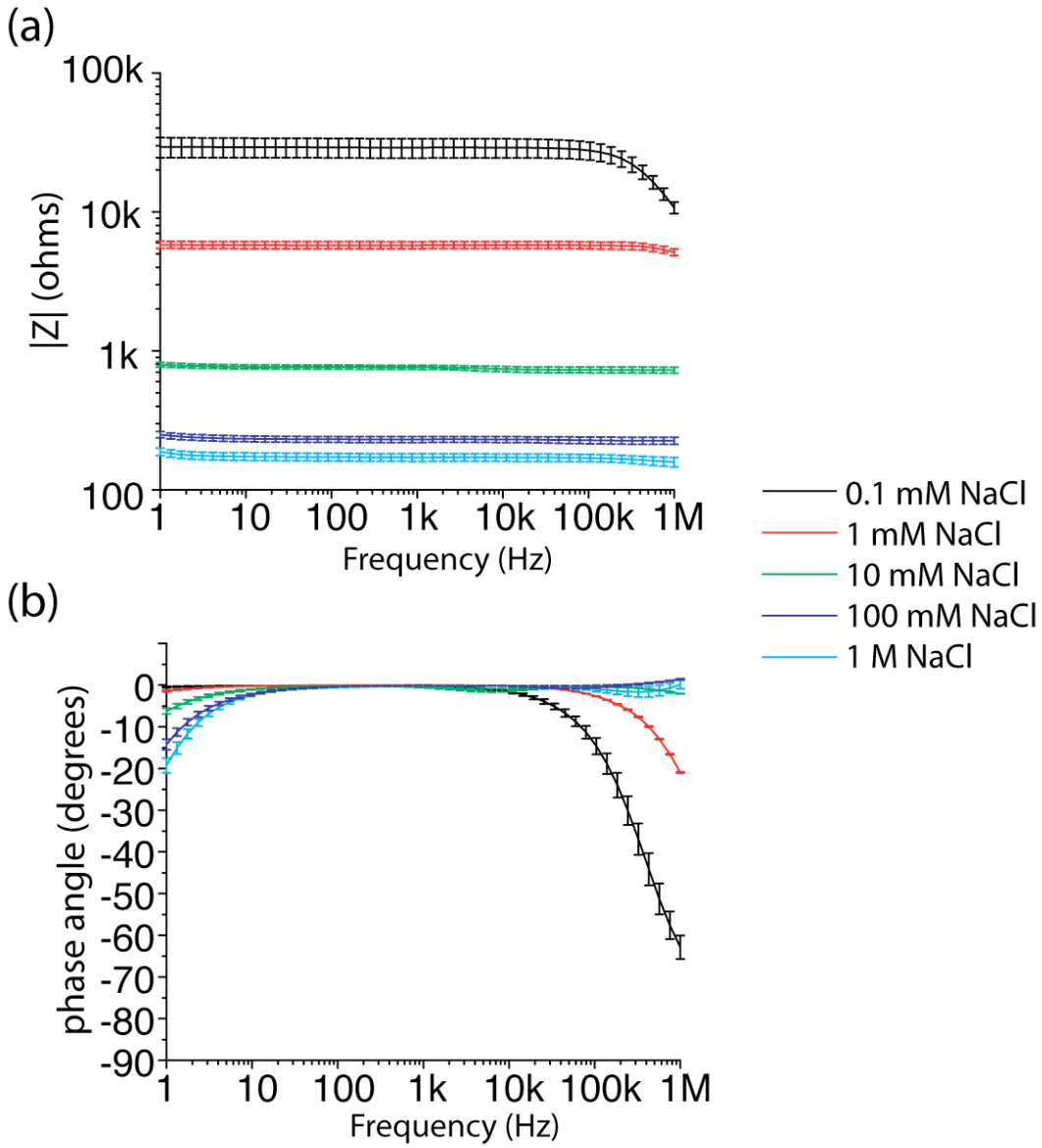

Figure 5-5 Impedance spectra acquired for platinum black in serially diluted solutions of NaCl. Error bars represent one standard deviation. (a) magnitude of impedance (b) phase.

The response of the PPy/PSS electrode is resistive across the impedance spectrum (Figure 5-6) although a slope change in the phase response at the lowest frequencies for the most concentrated solutions indicates the onset of double layer capacitance. The phase value at 1Hz for 1M NaCl is -5°. From these data, circuit parameters were extracted using equivalent circuit models. Data is shown in Tables 5-1 to 5-4.

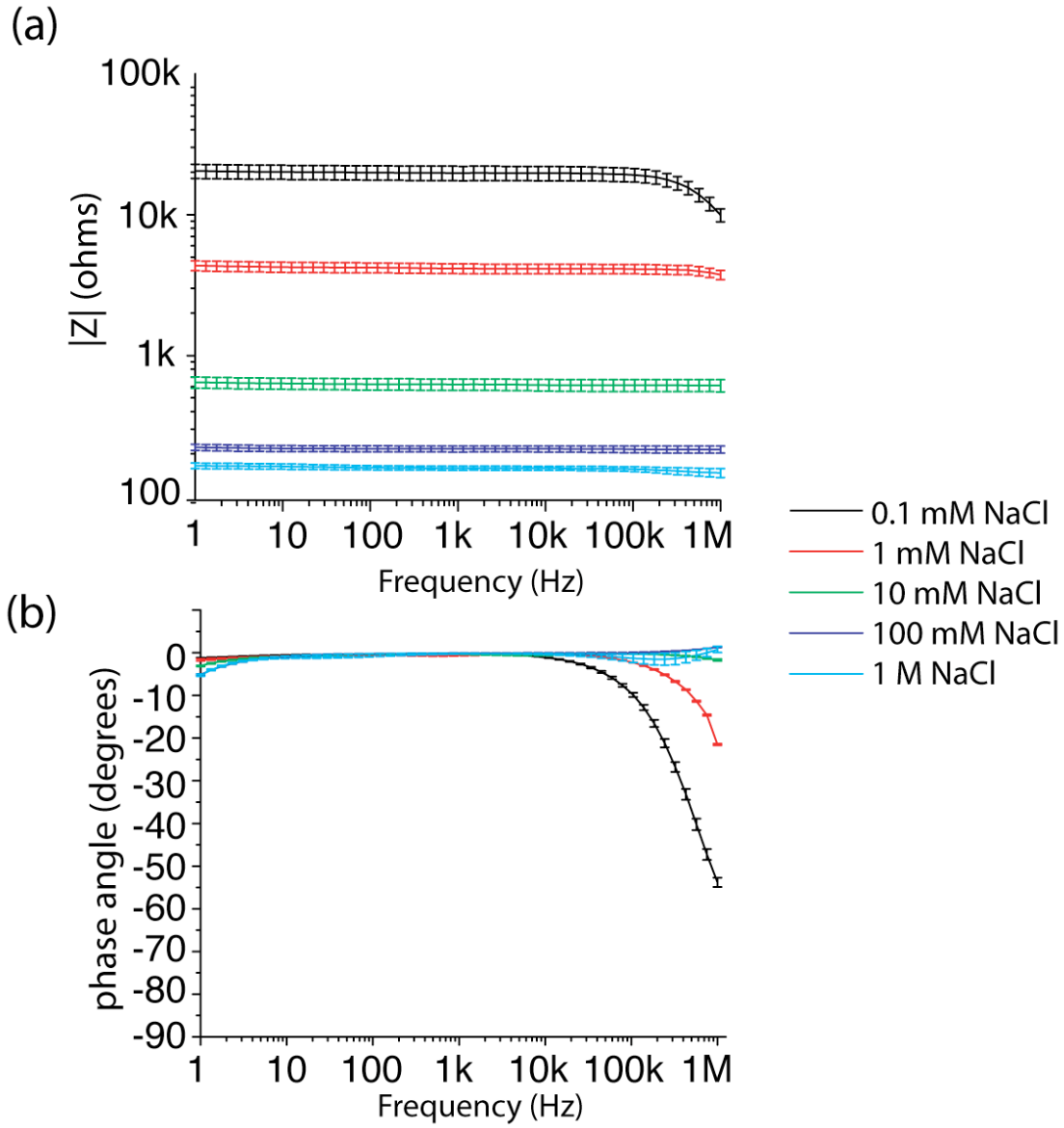

Figure 5-6 Impedance spectra acquired for PPy/PSS in serially diluted solutions of NaCl. Error bars represent one standard deviation. (a) magnitude of impedance (b) phase.

5.4.2 Measurements in PBS

Measurements were carried out in PBS solution, because it is has the same conductivity as physiological medium. The impedance magnitude and phase for four types of electrodes are shown in Figure 5-7. The conductivity of PBS is 1.6 S/m, resulting in a double layer thickness of approximately 1 nm. It is apparent from Figure 5-7 that, whereas the double layer capacitance dominates for plain platinum electrodes, the platinum black and iridium oxide electrode response is mostly resistive to 100Hz, while the PPy/PSS electrode pair is resistive to 1 Hz.

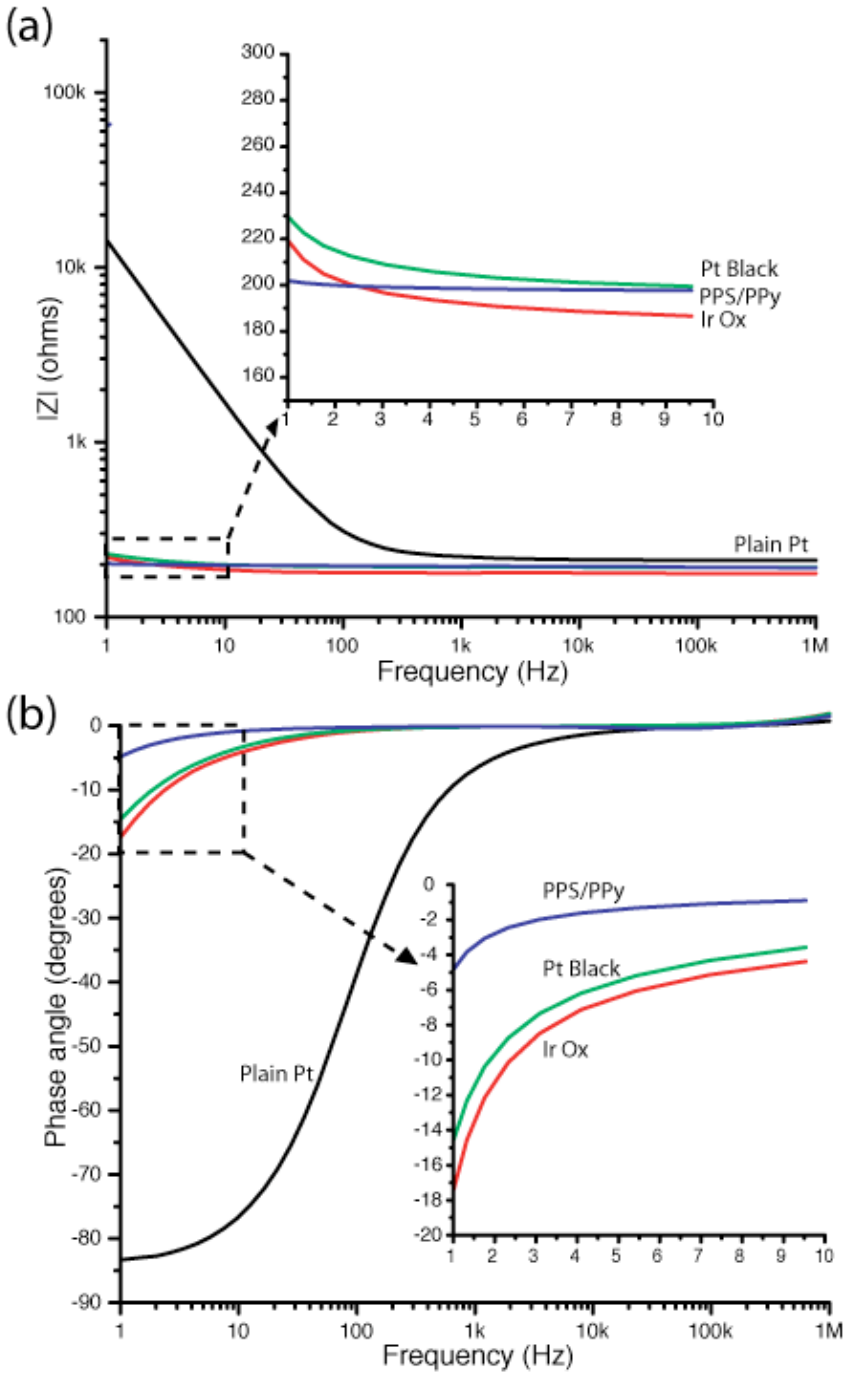

Figure 5-7 Impedance magnitude (a) and phase (b) of platinum, platinum black, iridium oxide and PPy/PSS-coated electrodes, measured in PBS (conductivity: 1.6 S/m).

5.4.3 Iridium Oxide Electrode Aging and Reactivation

Two pairs of activated iridium oxide electrodes were used to assess the stability of the impedance over time. Two methods of storage were compared: (A) 154 mM NaCl solution, and (B) rinsed in DI, dried and stored dry. The measurements were performed in the same measuring cell filled with 5 ml of 154 mM NaCl solution taken from the same stock bottle. Measurements were performed once a day, for 10 days. On day 10 the electrodes were re-activated using 50 C-V cycles, according to the procedure described in section 5.2, and their impedance measured once again.

In Figure 5-8 the impedance spectra of the dry-stored electrodes are plotted. It is apparent that the impedance changes over time become more capacitive, the larger change occurs within the first 24 hours, followed by smaller changes over the following 9 days.

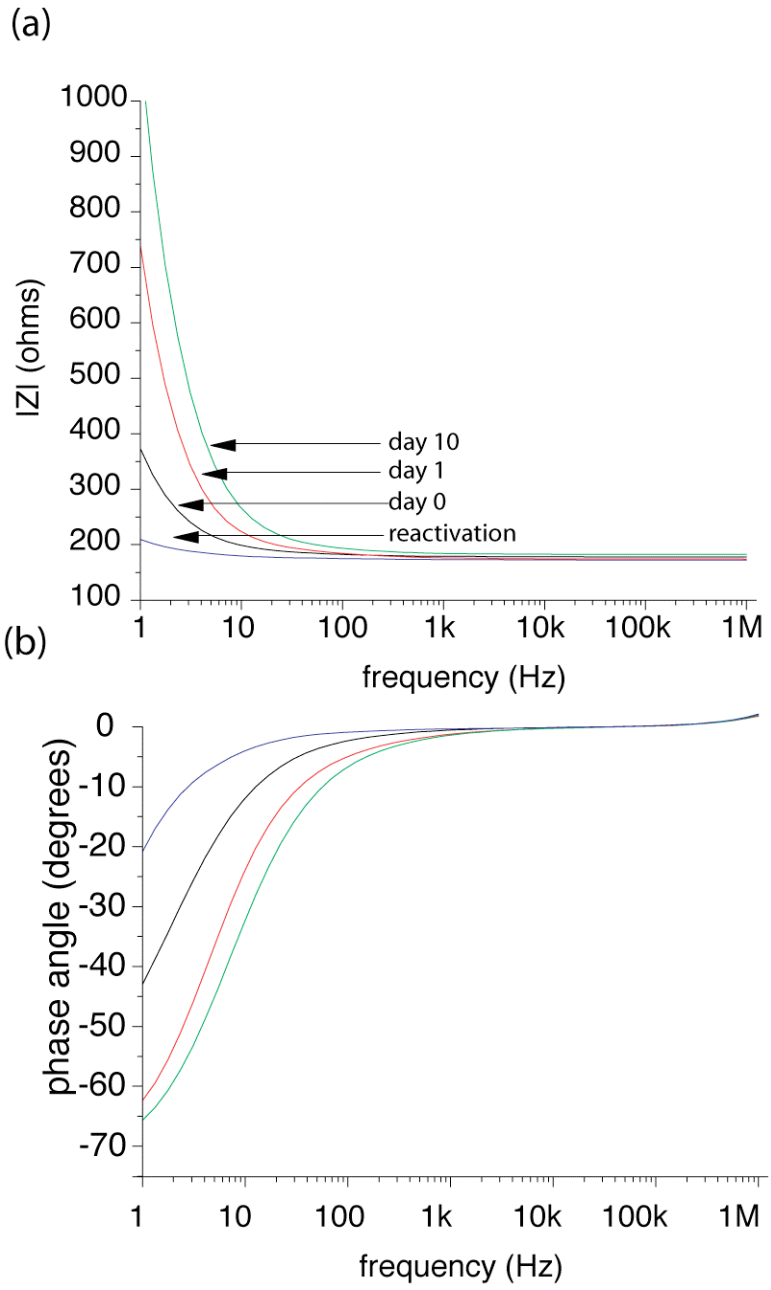

Figure 5-8 Aging effect on the impedance of iridium oxide electrodes. (a) Impedance magnitude for electrodes stored dry, measured immediately after the initial activation, one and ten days later and immediately after the re-activation process. (b) phase curves.

The stored-wet electrodes exhibited similar changes (Figure 5-9). In both cases a re-activation procedure was sufficient to return the response to a less capacitive value than recorded on day 1.

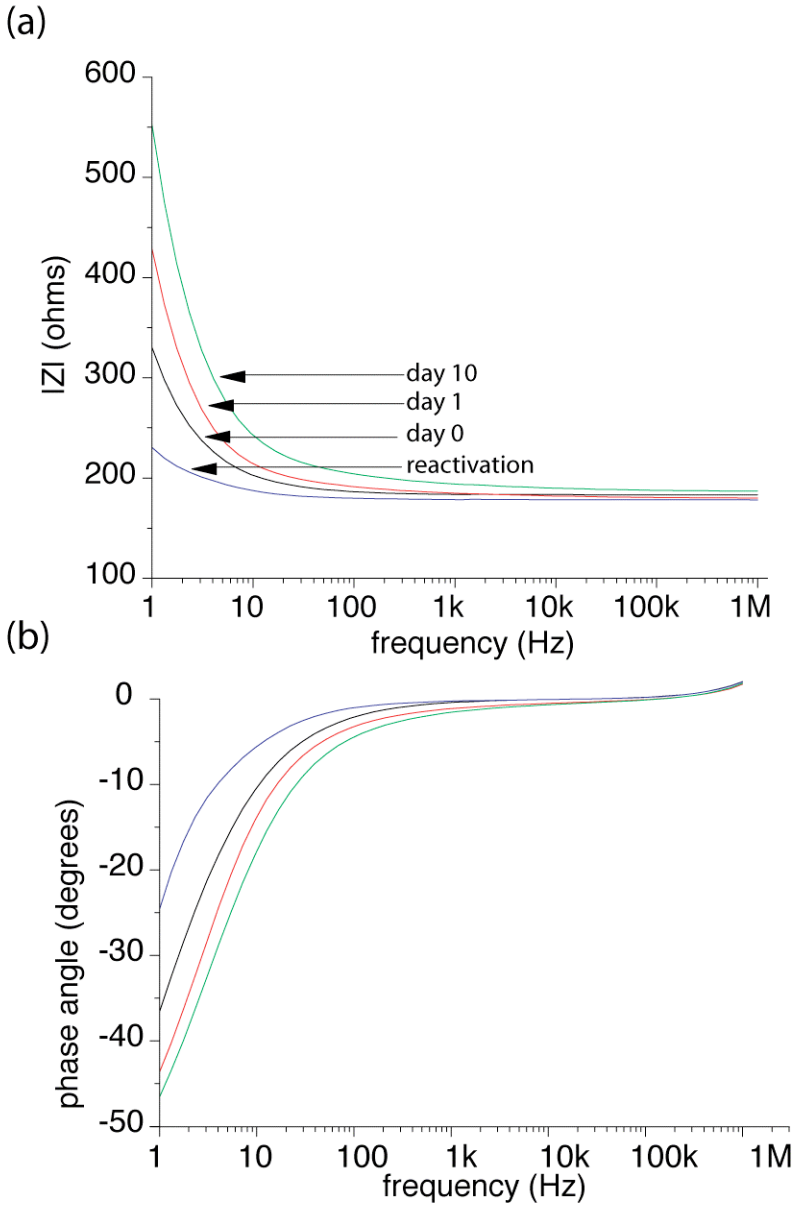

Figure 5-9 Aging effect on the impedance response of iridium oxide electrodes. (a) Impedance magnitude curves of electrodes stored in saline solution, measured immediately after the initial activation, one and ten days later and immediately after the re-activation process. (b) phase for the same days.

The changes in impedance can be quantified using the circuit parameters. In Figure 5-10, the double layer capacitance values (obtained by fitting the impedance to a series RC circuit) are plotted against time: the capacitance was found to decrease significantly in the first two days, reaching a plateau after day five. After 10 days, the reactivation procedure caused the capacitance to increase to a value higher than the initial value. In Figure 5-11 an analogous trend is shown when fitting the double layer response to constant phase elements. Whereas the power factor (P) of the CPEs tends

not to vary with time, its base value decreases with time in the same fashion as the capacitance value.

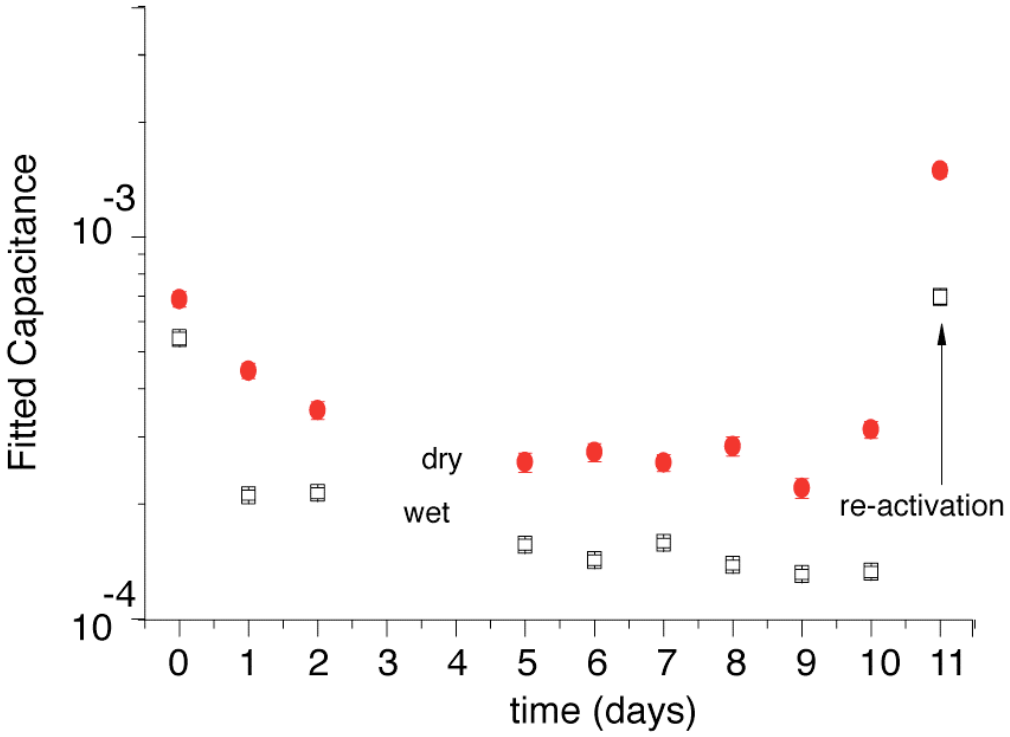

Figure 5-10 Variation of capacitance values recorded in the course of ten days after the initial activation and subsequent to reactivation for both wet- and dry- stored electrodes. The capacitance values were obtained by fitting a series R-C circuit to the measured impedance spectra.

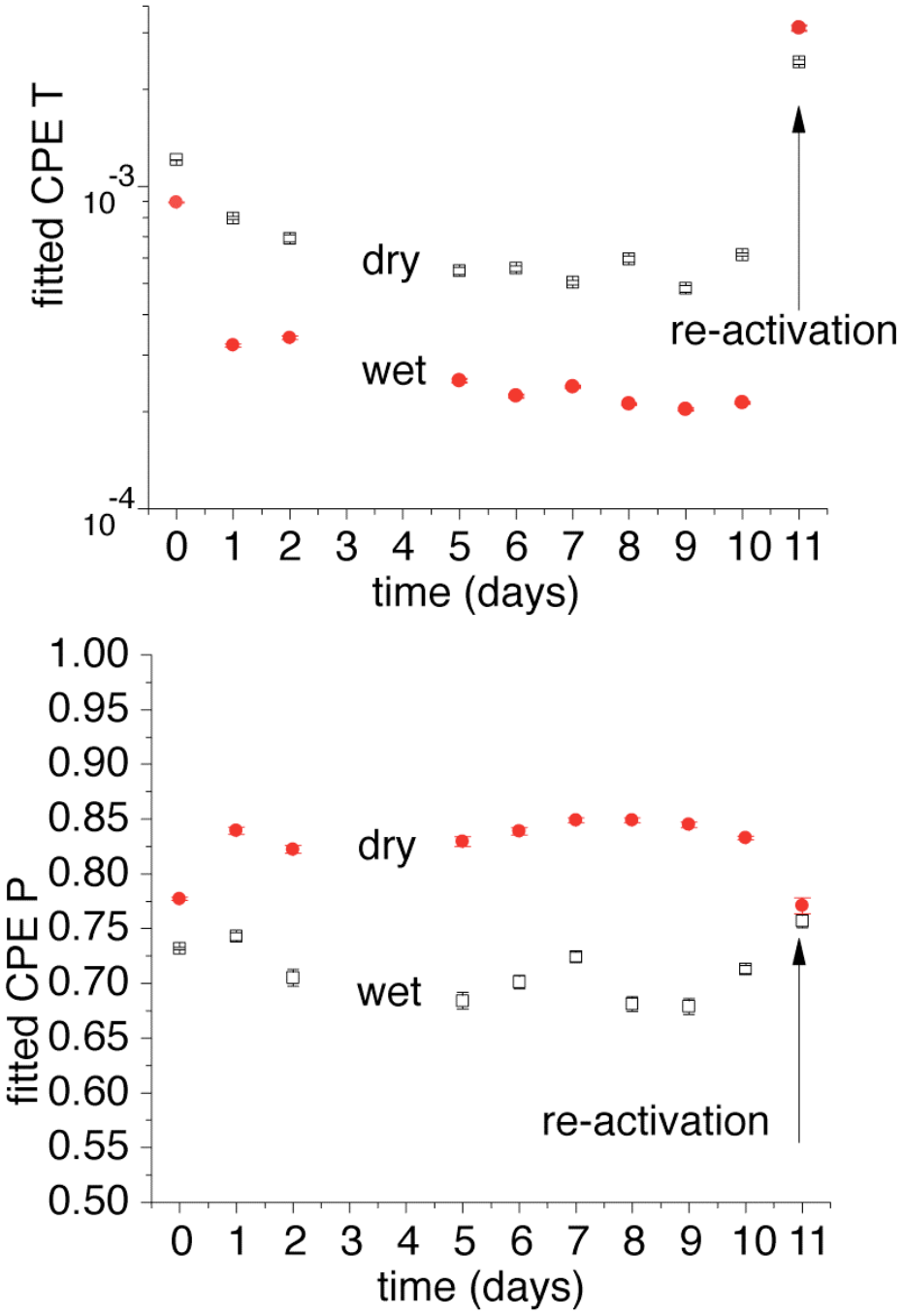

Figure 5-11 Variation of CPE values recorded in the course of ten days after the initial activation and subsequent to reactivation for both wet- and dry- stored electrodes. The CPE values were obtained by fitting a series R-CPE circuit to the measured impedance spectra. In the main plot: CPE-T values, in the inset: CPE-P values.

5.4.4 Measurement of PPy/PSS ageing

Two pairs of PPy/PSS polyelectrolyte electrodes were used to assess stability over time. The electrodes were stored in DI water or 154 mM NaCl solution. The electrodes could not be stored dry because the PPy/PSS film delaminated from the electrodes. Measurements were performed in the same measuring cell filled with 5 ml of 154 mM NaCl, once a day, for 8 days. Values of the fitted capacitance changed little, less than 1.5% over the course of 8 days.

5.4.5 Electrode surface imaging

SEM images of the electrode surfaces (Figure 5-12) show a marked contrast between the four types of electrodes. As expected, plain platinum is the smoothest. The platinum black electrode has the highest degree of disorder and self-similarity. Remarkably the iridium oxide and the PPy/PSS electrodes appear to have similar degrees of roughness, at least at the magnification used. This is somewhat surprising as visible surface roughness is generally correlated to an increase in double layer capacitance (due to a corresponding increase in effective surface area), but the measured polyelectrolyte electrode capacitance was much larger than that of the iridium oxide electrode despite a similar appearance in surface topography.

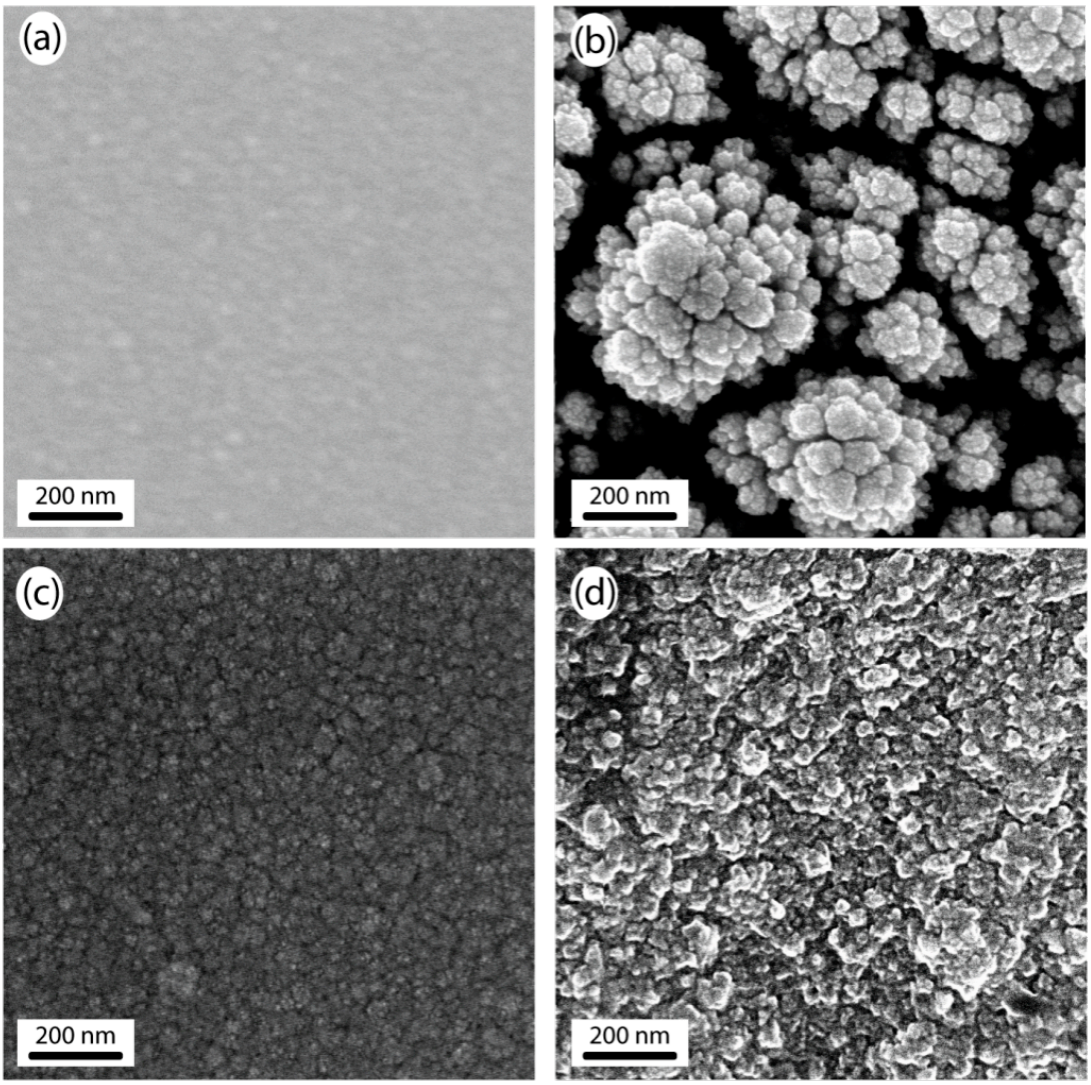

Figure 5-12 SEM images of the four electrode types investigated: (a) platinum, (b) platinum black, (c) iridium oxide (activated 60 times), and (d) PPy/PPS polyelectrolyte electrode. The SEM images were taken by Liz Wu at UC Berkeley.

5.5 Results and discussion

The capacitance values measured for the plain platinum electrodes reported in Table 5-1 are consistent with values found in the literature. Franks et al. [10] reported a value of 0.272 F/m^2 in 0.9% saline solution and Morgan et al. [25] measured 0.145 F/m^2 in PBS as compared to the values reported here ranging from 0.189 to 0.303 F/m^2, depending on the solution concentration.

The CPE-T/CPE-P fits give some insight into the topology of the electrode surface, accepting the traditional assumption that values of CPE-P lower than 1 indicate a rough surface with fractal features. However, it can be seen that the CPE-P values increase with increasing values of salt concentration (e.g. P=0.74 for 0.1 mM NaCl and P=0.93 for 1 M NaCl). This trend has been measured with several different electrodes made of different materials (metals, oxides, semiconductors as discussed in chapter 4), and although this has not been reported or discussed in the literature before, it is an indication that the CPE power factor should not be used to indicate a surface roughness quality without taking into account the dependence on ionic concentration.

	Platinum					
	C		CPE			
NaCl (M)	C/A (F/m^2)	error (%)	T/A	error (%)	P	error (%)
1 x10^{-4}	0.189	5.02	0.320	0.96	0.74	0.49
1 x10^{-3}	0.233	3.48	0.378	1.23	0.82	0.47
1 x10^{-2}	0.264	2.22	0.410	0.92	0.87	0.27
1 x10^{-1}	0.302	2.14	0.443	0.59	0.90	0.14
1	0.301	1.61	0.404	0.58	0.93	0.14
DPBS	0.303	1.52	0.402	0.57	0.93	0.14

Table 5-1. Fitting Results for Platinum

The values for platinum black, immediately after the electrochemical deposition are shown in Table 5-2. Values of double layer capacitance three orders of magnitude higher than for plain platinum have been recorded, indicating a similar increase in the effective electrode-electrolyte interface area. The CPE-P values fit *increased* to a range of 0.81-0.94, contrary to the traditional assumption that a higher fractal index is

reflected in lower CPE-P values. In this instance too, the CPE-P values increase with increasing electrolyte concentration. The double layer capacitance was too high to measure at the lowest NaCl concentration, as indicated by the dashes.

	Platinum Black					
	C		CPE			
NaCl (M)	C/A (F/m^2)	error (%)	T/A	error (%)	P	error (%)
1×10^{-4}	-	-	-	-	-	-
1×10^{-3}	32.50	4.17	48.04	1.71	0.81	0.83
1×10^{-2}	53.54	4.27	80.06	2.04	0.80	0.99
1×10^{-1}	77.48	2.68	102.96	0.91	0.86	0.41
1.00	81.54	1.52	90.44	1.09	0.94	0.44
DPBS	66.87	5.37	82.90	0.51	0.74	0.25

Table 5-2. Fitting Results for Platinum Black

The values recorded for the iridium oxide electrodes, activated by 50 cyclic voltammetry cycles are shown in Table 5-3. Values of double layer capacitance are slightly lower than the ones recorded with platinum black electrodes, but still three orders of magnitude higher than the plain platinum electrodes. A similar increase in the effective electrode-electrolyte interface area can be deduced. The CPE-P values fit *decreased* to a range of 0.61-0.70, considerably lower than the ones recorded for the platinum black electrodes. Yet again, the CPE-P values increase with increasing salt concentration in the electrolyte.

	Iridium Oxide					
	C		CPE			
NaCl (M)	C/A (F/m^2)	error (%)	T/A	error (%)	P	error (%)
1×10^{-4}	-	-	-	-	-	-
1×10^{-3}	9.66	7.87	18.52	1.19	0.61	0.73
1×10^{-2}	15.60	5.82	27.30	0.35	0.70	0.18
1×10^{-1}	22.12	4.90	38.02	0.43	0.74	0.21
1	28.72	5.63	53.58	2.64	0.70	1.31
DPBS	21.74	4.34	38.44	1.54	0.68	0.78

Table 5-3. Fitting Results for Iridium Oxide

The values recorded for the PPy/PSS coated electrodes, immediately after deposition of polymer are shown in Table 5-4. Values of double layer capacitance are four orders of magnitude higher than for plain platinum. The CPE-P values fit ranged widely from 0.57 to 0.81. The fit quality of the CPE-P is noticeably worse than the other electrodes and may explain the wide range of values. This is due in part to the extremely high capacitance values, which are harder to measure. In this instance, the CPE-P values tend to increase with increasing salt concentration in the electrolyte, although an out-of-trend local maximum was measured with 100mM NaCl and PBS solutions.

	PPy/PSS					
	C		CPE			
NaCl (M)	C/A (F/m^2)	error (%)	T/A	error (%)	P	error (%)
1×10^{-4}	-	-	-	-	-	-
1×10^{-3}	-	-	-	-	-	-
1×10^{-2}	127.82	8.79	269.58	4.05	0.57	2.92
1×10^{-1}	234.16	3.76	339.58	1.89	0.81	0.92
1	312.18	6.85	574.48	6.35	0.67	4.4
DPBS	259.06	4.78	428.12	2.45	0.76	1.29

Table 5-4. Fitting Results for PPy/PSS

5.5.1 Increase in Effective Electrode/Electrolyte Interface Area

From the impedance measurements and R-C circuit fitting it can be deduced that the activation of the iridium oxide electrodes results in a double layer specific capacitance in PBS of 22 F/m^2, roughly an 80-fold increase compared to platinum. This must be attributed to an increase in electrode-electrolyte interface area or effective surface area, which occurs when the activation corrugates the surface creating microscopic fractures and crevices. Likewise, coating platinum electrodes with platinum black results in a 240-fold increase (to 77.48 F/m^2 in PBS), attributed to the granular structure of the electrodeposited platinum. Galvanostatic deposition of PPy/PSS results in a 850-fold effective surface area increase (to 234 F/m^2 in PBS).

It should be pointed out that far greater increases in double layer capacitance have been reported in the literature by optimising operational parameters, such as deposition time, deposition current and mechanical pre-treatment of the electrode

surface. For example Schwan [26] showed that by altering the deposition time and current it is possible to obtain values of specific double layer capacitance as high as 200 F/m^2 (for a deposition time of 20 minutes and a current density of 20 mA $/cm^2$) Furthermore, by mechanically roughening (sandblasting) the metal surface previous to the platinum black deposition, he reports values as high as 500 F/m^2 (for a deposition time of 50 minutes and a current density of 10 mA $/cm^2$) However such high values were found to decline rapidly.

5.5.2 Ease of Fabrication

Platinum black and the PPy/PSS electrodes start with a base of Platinum, while the iridium oxide electrode requires an additional sputtering step of iridium. All three electrodes require some sort of electrochemical treatment to either deposit or activate the surface. The iridium oxide activation requires a potentiostat while the other two just require a DC power supply. The chemicals needed for platinum black and PPy/PSS electrodes are toxic to humans, so care must be taken during the electrodeposition process. Conversely, the iridium oxide electrodes are activated in a harmless saline solution.

5.5.3 Potential for Biological Applications

According to [27] platinum black was found to be toxic to rat oligodendrocytes, most likely due to the presence to lead traces in the platinum black film. There are no known toxicity effects of iridium oxide or PPy/PSS electrodes. In fact, iridium oxide electrodes have seen a significant amount of use for *in vivo* and *in vitro* studies [12, 14, 15, 17-20].

5.5.4 Durability and Lifetime

Platinum black electrodes are fragile and easily damaged. Scratches in the surface of the film will change the effective area with undesirable effects, so care must be taken to prevent any mechanical contact with the electrode surface. In the case of macroscopic size electrodes, the black powder films can be removed by sonicating, wiping the electrode surface with a cloth and performing another deposition.

However, when stored in saline solution, platinum black electrodes did not show measurable changes in their impedance response over a period of two weeks.

Iridium oxide electrodes have proven to be very resistant to mechanical damage. In fact, the electrode surface can be wiped with a wet cloth with no apparent damage. The electrodes can be stored dry or under water, but it was found that these electrodes do exhibit a transitory behaviour. Most of the changes occurred in the first 24 hours, with apparent stead-state values reached after 5-6 days. This indicates that particular attention needs to be taken when using this material for long term electrical monitoring of samples. The use of a reference electrode should be considered. Elzanowska et al. suggest that alkaline storage of iridium oxide electrodes may prevent the transient behaviour measured here. An additional point is that iridium oxide electrodes can be re-activated at any point to yield a predetermined impedance value.

The PPy/PSS electrodes provide a very stable electrode/electrolyte interface area over extended time periods, making these the electrodes of choice for long term experiments. However, they are more fragile than platinum black electrodes. These electrodes must be stored wet or delamination occurs. These surfaces are also sensitive to mechanical damage. But, as for platinum black electrodes, the damaged film can be removed from the surface and re-deposited.

	Platinum Black	Iridium Oxide	PPy/PSS
Effective increase in area with respect to plain platinum	239x	77x	854x
Ease of fabrication	Toxic chemicals but only a low voltage DC power supply needed	No toxic chemicals, but a potentiostat is required for activation	Initial chemicals are toxic, however once mixed are non-toxic, and DC power supply can be used
Toxicity	Some known toxicity to cells, presumably due to presence of lead [27]	No known toxicity issues, and can be used *in vivo*. [11, 18]	No known toxicity issues, is *used* in vivo [24, 28]
Durability	Easily damaged by mechanical contact	Extremely robust – can be wiped with a lint-free cloth and sonicated in acetone, but values drift over time	Cannot be dried, and is damaged by mechanical contact, but no significant drift in capacitance over time

Table 5-5 Comparison of electrode attributes.

5.6 Discussion

Many factors beyond just the low frequency impedance response should be considered when choosing the *optimal* material for impedance-based lab-on-a-chip devices. These factors are: bio-compatibility, stability of the response over time, both in the short and long term, mechanical robustness, compatibility of fabrication steps with common microfabrication techniques, requirement for activation (or re-activation if necessary) once a microdevice is fully assembled.

Platinum black deposition has been performed for decades; it is a relatively simple and well documented procedure and can easily be performed on patterned microelectrodes. Many protocols have been detailed in the literature (see for example Schwan [26]). However, the use of lead in the deposition protocol has been proven to be toxic to some cell lines [27] and the deposited films are mechanically fragile, unless steps are taken such as repeated ultrasonication during the deposition, which might be damaging to a fully assembled microdevice. Fragility of deposited films might not be an issue in devices such as flow cytometers, where cells usually do not contact the electrode surface, but should be carefully considered in the case of microelectrode arrays used for ECIS (electrode-cell impedance spectroscopy), where cells adhere to the electrode surface.

Another point of concern is the variability in impedance response with time, and degradation of the electrode surface. Such effects are rarely monitored, although Schwan has pointed out that platinum black treatments that yield the largest increases in double layer capacitance (increases as high as 500x the capacitance of plain platinum electrode can be obtained), are those most susceptible to fast degradation of response [26].

Iridium oxide is an electrode material commonly favoured for neural stimulation and recording electrodes due to the increased charge injection capacity that results from the activation process. Curiously, although impedance spectroscopy has been used to characterize the activation process, the use of iridium oxide electrodes for impedance spectroscopic studies has not yet been proposed. Activation requires cyclic voltammetry with saline solutions or PBS, avoiding the introduction of toxic chemicals. The activation process is relatively quick; it can be performed in a matter of minutes, and is very repeatable. The electrode characteristics have been found to degrade with

time, over the first three to five days after activation. However the response stabilises after five days, and reactivation restores the original properties.

This (long-term) time-dependent characteristic is not necessarily detrimental but it needs to be considered if iridium oxide is used for long term impedance monitoring. Modern cyclic voltammetry workstations can also perform impedance spectroscopy, therefore impedance analysis of the electrodes could be used to provide feedback to determine the optimum number of voltammetry scans for a given set of electrodes. Iridium oxide is mechanically very robust; it will therefore be an ideal material for use with adherent and non adherent cell lines.

Polypyrrole/polystyrenesulphonate (PPy/PSS) is a novel electrode material for impedance spectroscopy. The material has been used for neural signal recordings [28-30] and as an electro-mechanical actuator [31, 32]. PPy/PSS deposition can be performed using a DC power supply, as for platinum black. Because it is non-toxic [24, 28] it may be more convenient to use than Pt black, as it also exhibits higher values of specific double layer capacitance. Most importantly, the impedance response is extremely stable both in the short and long term, making it an ideal choice for time-dependent studies. A drawback of the material is that it needs to be kept wet at all times for the coating to be preserved: drying the electrodes causes delamination and lift-off of the polyelectrolyte coating. The protocol for the polyelectrolyte film formation and deposition used in this work can probably be further optimized to yield a even larger electrode capacitance and more durable films that are resistant to delamination.

5.7 Conclusions

Iridium oxide and PPy/PSS polyelectrolyte electrodes are compelling alternative materials to platinum black for impedance spectroscopy. The robustness of iridium oxide and lack of toxicity make it a useful material compare to the potentially toxic platinum black. PPy/PSS electrodes offer the highest electrode/electrolyte interface area and lowest variation over time, making it an extremely valuable material for low frequency impedance analysis over long periods of time, however it must be stored with care.

References

[1] H. P. Schwan, G. Schwarz, J. Maczuk *et al.*, "On Low-Frequency Dielectric Dispersion Of Colloidal Particles In Electrolyte Solution," *Journal of Physical Chemistry,* vol. 66, no. 12, pp. 2626-&, 1962.

[2] Takashima S, "Effect Of Ions On Dielectric Relaxation Of DNA," *Biopolymers,* vol. 5, no. 10, pp. 899, 1967.

[3] Takashima S, "Mechanism Of Dielectric Relaxation Of Deoxyribonucleic Acid," *Advances in Chemistry Series*, no. 63, pp. 232-&, 1967.

[4] J. Baker-Jarvis, R. G. Geyer, J. H. Grosvenor *et al.*, "Dielectric characterization of low-loss materials - A comparison of techniques," *Ieee Transactions on Dielectrics and Electrical Insulation,* vol. 5, no. 4, pp. 571-577, Aug, 1998.

[5] M. Sakamoto, H. Kanda, R. Hayakawa *et al.*, "Dielectric-Relaxation Of DNA In Aqueous-Solutions," *Biopolymers,* vol. 15, no. 5, pp. 879-892, 1976.

[6] F. Bordi, C. Cametti, and R. Colby, "Dielectric spectroscopy and conductivity of polyelectrolyte solutions," *J. Phys.: Condens. Matter,* vol. 16, no. 49, pp. R1423-R1463, Nov 30, 2004.

[7] I. Ermolina, H. Morgan, N. G. Green *et al.*, "Dielectric spectroscopy of Tobacco Mosaic Virus," *Biochimica Et Biophysica Acta-General Subjects,* vol. 1622, no. 1, pp. 57-63, Jun, 2003.

[8] M. Tirado, and C. Grosse, "Conductivity dependence of the polarization impedance spectra of platinum black electrodes in contact with aqueous NaCl electrolyte solutions," *Colloids and Surfaces a-Physicochemical and Engineering Aspects,* vol. 222, no. 1-3, pp. 293-299, 2003.

[9] A. Norlin, J. Pan, and C. Leygraf, "Investigation of interfacial capacitance of Pt, Ti and TiN coated electrodes by electrochemical impedance spectroscopy," *Biomolecular Engineering,* vol. 19, no. 2-6, pp. 67-71, Aug, 2002.

[10] W. Franks, "Impedance Characterization and Modeling of Electrodes for Biomedical Applications " *IEEE Transactions On Biomedical Engineering,* vol. 52, Jun 6, 2005.

[11] J. S. Alessandro G.A. Bufalo, Martin Fromer, Lukas Kappenberger, "Acute and Long-Term Ventricular Stimulation Thresholds with a New, Iridium Oxide-Coated Electrode," *Pacing and Clinical Electrophysiology,* vol. 16, no. 6, pp. 1240-1245, 1993.

[12] A. Blau, C. Ziegler, M. Heyer *et al.*, "Characterization and optimization of microelectrode arrays for in vivo nerve signal recording and stimulation," *Biosensors & Bioelectronics,* vol. 12, no. 9-10, pp. 883-892, 1997.

[13] Y. Chen, P. Shi, and D. Scherson, "Supported iridium oxide films in aqueous electrolytes: Charge injection dynamics as monitored by time-resolved differential reflectance spectroscopy," *Electrochemical And Solid State Letters,* vol. 11, no. 6, pp. F5-F8, 2008.

[14] S. Cogan, T. Plante, and J. Ehrlich, "Sputtered iridium oxide films (SIROFs) for low-impedance neural stimulation and recording electrodes," *Engineering in Medicine and Biology Society, 2004. IEMBS '04. 26th Annual International Conference of the IEEE,* vol. 2, pp. 4153-4156 Vol.6, 2004.

[15] I. S. Lee, J. C. Park, G. H. Lee *et al.*, "Neural cells on iridium oxide," *Key Engineering Materials*, 2004.

[16] Y. Lu, Z. Cai, Y. Cao *et al.*, "Activated iridium oxide films fabricated by asymmetric pulses for electrical neural micro stimulation and recording," *Electrochemistry Communications,* vol. 10, no. 5, pp. 778-782, 2008.

[17] R. D. Meyer, S. E. Cogan, T. H. Nguyen *et al.*, "Electrodeposited iridium oxide for neural stimulation and recording electrodes," *Ieee Transactions On Neural Systems And Rehabilitation Engineering,* vol. 9, no. 1, pp. 2-11, 2001.

[18] G. Papeschi, S. Bordi, M. Carla *et al.*, "An Iridium-Iridium Oxide Electrode For Invivo Monitoring Of Blood-Ph Changes," *Journal of Medical Engineering & Technology,* vol. 5, no. 2, pp. 86-88, 1981.

[19] S. S. Thanawala, R. J. Baird, D. G. Georgiev *et al.*, "Amorphous and crystalline IrO2 thin films as potential stimulation electrode coatings," *Applied Surface Science,* vol. 254, no. 16, pp. 5164-5169, Jun, 2008.

[20] J. D. Weiland, D. J. Anderson, and M. S. Humayun, "In vitro electrical properties for iridium oxide versus titanium nitride stimulating electrodes," *IEEE Transactions On Biomedical Engineering,* vol. 49, no. 12, pp. 1574-1579, 2002.

[21] I. A. Ges, B. L. Ivanov, A. A. Werdich *et al.*, "Differential pH measurements of metabolic cellular activity in nl culture volumes using microfabricated iridium oxide electrodes," *Biosensors & Bioelectronics,* vol. 22, no. 7, pp. 1303-1310, 2007.

[22] I. A. Ges, and F. Baudenbacher, "Microfluidic device to confine single cardiac myocytes in sub-nanoliter volumes for extracellular pH measurements," *Journal Of Experimental Nanoscience,* vol. 3, no. 1, pp. 63-75, 2008.

[23] C. A. Marrese, "Preparation Of Strongly Adherent Platinum Black Coatings," *Analytical Chemistry,* vol. 59, no. 1, pp. 217-218, Jan, 1987.

[24] P. M. George, A. W. Lyckman, D. A. LaVan *et al.*, "Fabrication and biocompatibility of polypyrrole implants suitable for neural prosthetics," *Biomaterials,* vol. 26, no. 17, pp. 3511-3519, Jun, 2005.

[25] H. Morgan, T. Sun, D. Holmes *et al.*, "Single Cell Dielectric Spectroscopy," *Journal of Physics D-Applied Physics,* vol. 40, no. 1, pp. 61-70, Jan, 2007.

[26] H. P. Schwan, "Linear And Nonlinear Electrode Polarization And Biological-Materials," *Ann Biomed Eng*, 1992, pp. 269-288.

[27] M. Schuettler, T. Doerge, S. L. Wien *et al.*, "Cytotoxicity of Platinum Black," *Proceeding of the 10th Annual International Conference of IFESS*, 2005.

[28] X. Y. Cui, J. F. Hetke, J. A. Wiler *et al.*, "Electrochemical deposition and characterization of conducting polymer polypyrrole/PSS on multichannel neural probes," *Sensors And Actuators A-Physical,* vol. 93, pp. 8-18, 2001.

[29] R. Green, C. Williams, N. Lovell *et al.*, "Novel neural interface for implant electrodes: improving electroactivity of polypyrrole through MWNT incorporation," *Journal of Materials Science: Materials in Medicine,* vol. 19, no. 4, pp. 1625-1629, 2008.

[30] M. R. Warren, and J. D. Madden, "A structural, electronic and electrochemical study of polypyrrole as a function of oxidation state," *Synthetic Metals,* vol. 156, no. 9-10, pp. 724-730, 2006.

[31] K. Kaneto, Y. Sonoda, and W. Takashima, "Direct measurement and mechanism of electro-chemomechanical expansion and contraction in polypyrrole films," *Japanese Journal Of Applied Physics Part 1-Regular Papers Short Notes & Review Papers,* vol. 39, pp. 5918-5922, 2000.

[32] D. Preethichandra, A. Thakur, W. Takashima *et al.*, "A combined bi-ionic polymer actuator with unidirectional extension against bipolar excitations," *Sensors and Actuators B: Chemical,* vol. 122, no. 2, pp. 587-590, 2007.

Chapter 6 Nanogap sensor

6.1 Introduction

Impedance spectroscopy is gaining importance as a label-free detection tool for biomolecular structure and binding events [1-6]. Shrinking the sensing system to the nanoscale means that the volume occupied by the electrical double layers is a significant fraction of the sample volume, thus potentially amplifying the effect of binding events on the signal by reducing the contribution of the bulk solution impedance [7, 8]. Devices based on this principle, called nanogap capacitors have been fabricated and characterised. The devices were fabricated using conventional semiconductor IC technology. However, due to the type semiconductor materials used (i.e. doped single crystal silicon, poly-silicon, and silicon dioxides) the sensors have complex behaviour that requires detailed analysis. In order to extract relevant dielectric parameters for the biomolecules of interest, models that describe the dependence of the impedance signals on sample permittivity are required. Modelling can also aid geometry optimization and determination of what kind of biomolecular binding event is within the sensor's detection limits.

In the first part of this chapter, a number of air-filled nanogap capacitor geometries are presented and modelled, and the models evaluated against impedance spectroscopy data. The detection limit is determined by etching away (at a controlled rate) the dielectric material between the measuring electrodes. The capacitance is measured to determine the system's sensitivity to changes in sample permittivity. It is demonstrated that such devices could function as tools for monitoring the rate of removal/deposition of material in nanocavities. The sensitivity of the measured parameters $|Z(\omega)|$ (impedance magnitude) and $\Phi(\omega)$ (phase shift) to changes in permittivity was measured and compared to model. In conjunction with standard deviation of $|Z(\omega)|$ and $\Phi(\omega)$ data over a number of devices (3-6), sensitivity values are used to determine the limit of detection for these sensors.

In the second part of the chapter the models are expanded to include the effect of an electrolyte in the sensor. It is found that analysis of the sensor provides insight into the behaviour of double layers constrained in cavities of dimensions comparable to the Debye length.

6.2 Previous work in the field

Over the last 10 years, as technology advances have made the fabrication of micro- and nano-structures possible, there has been an increasing interest in the use of nanocavities as sensors, and a substantial number of contributions have appeared in the literature. These devices are commonly referred to as 'nanogap sensors' and can be classified according to a number of criteria: the fabrication approach (top down vs. bottom up), the specific fabrication technique or their intended use. It is also possible to classify the devices according to their topology/geometry. The sensors can be classified according to the number of dimensions along which the sensing nanocavity exists; 'broken nanowires' are 1-D, 'fractured planes' 2-D and nanocavities are 3-D sensors. Where electrical DC or AC voltages are used, the nanogap sensors are classified as resistive or capacitive sensors, respectively. The topological distinction chosen here (1-D, 2-D, 3-D), overlays well with the resistive/capacitive distinction: 1-D and 2-D are resistive, 3-D are capacitive. The work in this thesis is limited to 3-D devices, whose sensing principle is capacitive.

To maximise sensitivity, it is advantageous to have large active areas and small inter-electrode distances, maximizing device capacitance. In the particular case where biomolecules are sensed as they bind to the surface and modify the double layer, it is also convenient to minimize the contribution of the bulk solution to the overall impedance, which leads to a sensitivity response that is inversely proportional to the inter-electrode distance. Defining ξ as a sensitivity factor, the two dependencies can be formulated as follows:

For a generic parallel-plate capacitive sensor, the measured quantity is capacitance, while the sensed parameter is the permittivity ε. The two are related by the well-know expression:

$$C = \varepsilon \frac{A}{d} \tag{6-1}$$

where A is the area of the electrodes, d the distance separating them and ε the permittivity of the dielectric between the two plates. It is convenient to define the ratio of A/d as ξ_1

$$\xi_1 = \frac{A}{d} \tag{6-2}$$

For the specific case of sensors sensitive to surface binding events, where bulk contributions (due to the total volume enclosed by two parallel electrodes) are to be minimized

$$\xi_2 = \frac{A}{A \cdot d} \tag{6-3}$$

Combining (6-2) and (6-3),

$$\xi = \xi_1 \cdot \xi_2 \tag{6-4}$$

$$\xi = \frac{A}{d^2} \tag{6-5}$$

This dimensionless parameter can be used to compare different nanogap sensors, as well as to optimize the design of new sensors.

For the 3-D nanogap sensors found in the literature, most are used as resistive sensors, and do not exploit the potential advantage of a large electrode surface area coupled with a short inter-electrode distance. For example, the Choi group presented fabrication methods and experimental results for nanogap sensors with gaps of 5, 10 and 15 nm to demonstrate label-free electrical detection of biotin-avidin interactions [9]. They used

the sensor as a resistive (not capacitive) sensor, with a DC voltage (0-2 V), reporting that the current increased dramatically following biotin-streptavidin binding.

Wheeler et al. used an analogous measuring technique (I/V response) for a silicon-based 7nm gap device [10]. The conduction across the gap was shown to change after functionalization with a conducting organic/gold nanoparticle film, thus implying the bridging of the 7 nm gap. Bengtsson presented a silicon- based device, with the spacer between the two silicon 'plates' made of a sacrificial oxide layer selectively wet-etched [11]. The device was characterized with I/V measurements but not shown to work as a bio-sensor. Tornow et al. introduced a biosensor made of a pair of closely spaced metal electrodes on the cleaved plane of a GaAs/AlGaAs heterostructure [12]. The device was engineered for molecular-conductance studies (I/V measurements).

A very promising nanogap capacitive sensor, presented by the Lohndorf group, is technologically very attractive (metal electrodes, integrated reference sensing on-chip) but the use of a single excitation frequency for analysis prevents full dielectric characterization of the samples. They detailed the fabrication of 64 individual capacitors of 12 μm2 area with a 150 nm gap between the electrodes [14]. The individual sensing elements could be addressed in parallel, resulting in a single capacitor of 768μm^2 area. It is worth noting that the single sensing elements have a dimensionless sensitivity factor of 533, whereas for the parallel combination of 64 electrodes the sensitivity is 34133. The device was used for detection of thrombin [13, 14]. The device has an inter-electrode distance of 68 nm and only 8 sensing elements are connected in parallel (6 pairs are used for reference measurements). The sensitivity factor of this combination is 20761. A single frequency (1.26 GHz) AC voltage is used as an excitation signal. To monitor side-effects of the bulk solution, temperature drifts, and parasitic capacities, additional planar reference sensors were patterned onto the sensor-chips. Most recently, the device was used to study the interaction of the Rev peptide (2.4 kDa) with a corresponding RNA anti-Rev aptamer (9.2 kDa), using a device with six sensing elements, 75nm gap (sensitivity factor: 12800) and a different excitation frequency (980 MHz) [14].

6.3 Microfabrication

The nanogap sensor was fabricated by K. H. Jeong at BSAC, University of California at Berkeley. It was integrated in a functional setup, as shown in Figure 6-1, by Dino Di Carlo, Cristian Ionescu Zanetti, Tanner J Nevill and Daniele Malleo.

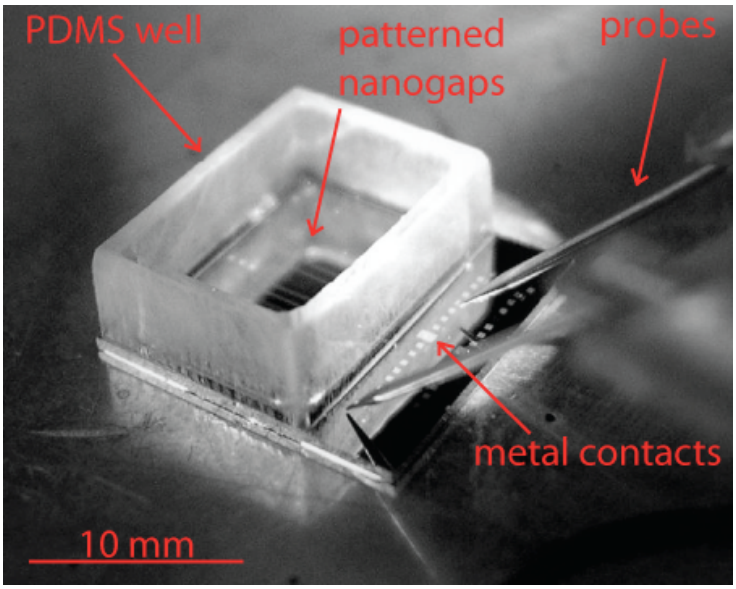

Figure 6-1. A diced chip on which 10 different nanogap devices was fabricated. The bonded, laser-cut PDMS well is the solution reservoir. Also visible are the microcontact probes which connect the gold pads on the edge of the chip to the off-chip impedance analyzer. Courtesy of J. Tanner Nevill.

The active part of the device consists of a heavily doped silicon electrode and a polysilicon electrode vertically separated by a fixed distance of 20-300 nm, defined by a deposited silicon dioxide spacer (Figure 6-2).

The first step was the creation of the bottom electrode. Starting with a four inch silicon wafer, a 1 μm thick layer of phosphosilicate glass (PSG) was deposited by low pressure chemical vapour deposition (LPCVD). The wafer was then brought to a high temperature to allow diffusion of phosphorus from the PSG into the silicon wafer, which resulted in a heavily doped silicon wafer. The PSG was then removed in an HF bath; the wafer was electrically conductive enough to act as the bottom electrode. The next step was to create the gap spacer. The surface of the wafer was thermally oxidized to create a very thin and uniform SiO_2 layer with precisely known thickness. Multiple versions of the nanogap sensor were fabricated; gap sizes ranged from 20 nm to 300 nm. For the data presented in this chapter, devices with a nanogap of 90 nm and 20 nm were used. Heavily doped poly-silicon at a thickness of 300 nm was then deposited onto the SiO_2 using LPCVD. The poly-Si was electrically conductive and acted as the

sensor's top electrode. The shape and position of the top electrodes was defined in the poly-Si using standard photolithography techniques. The poly-Si was etched using reactive ion etching. Finally, the SiO_2 layer was selectively etched with buffered 5:1 HF so that the top electrodes were undercut on all sides. However, the SiO_2 was not completely etched, so that the remaining SiO_2 acted as a mechanical spacer. The total area of the overhanging top electrodes in each device was approximately 15μm x 7mm. The final step involved evaporating and patterning gold onto the contact pads using a standard lift off procedure. This was done to help minimize the variability in contact resistance when the devices were probed.

The ξ factor of these device ranges from 262.5×10^6 (gap: 20 nm) to 12.9×10^6 (gap: 90 nm), much higher than any other 3D nanogap sensor presented in the literature.

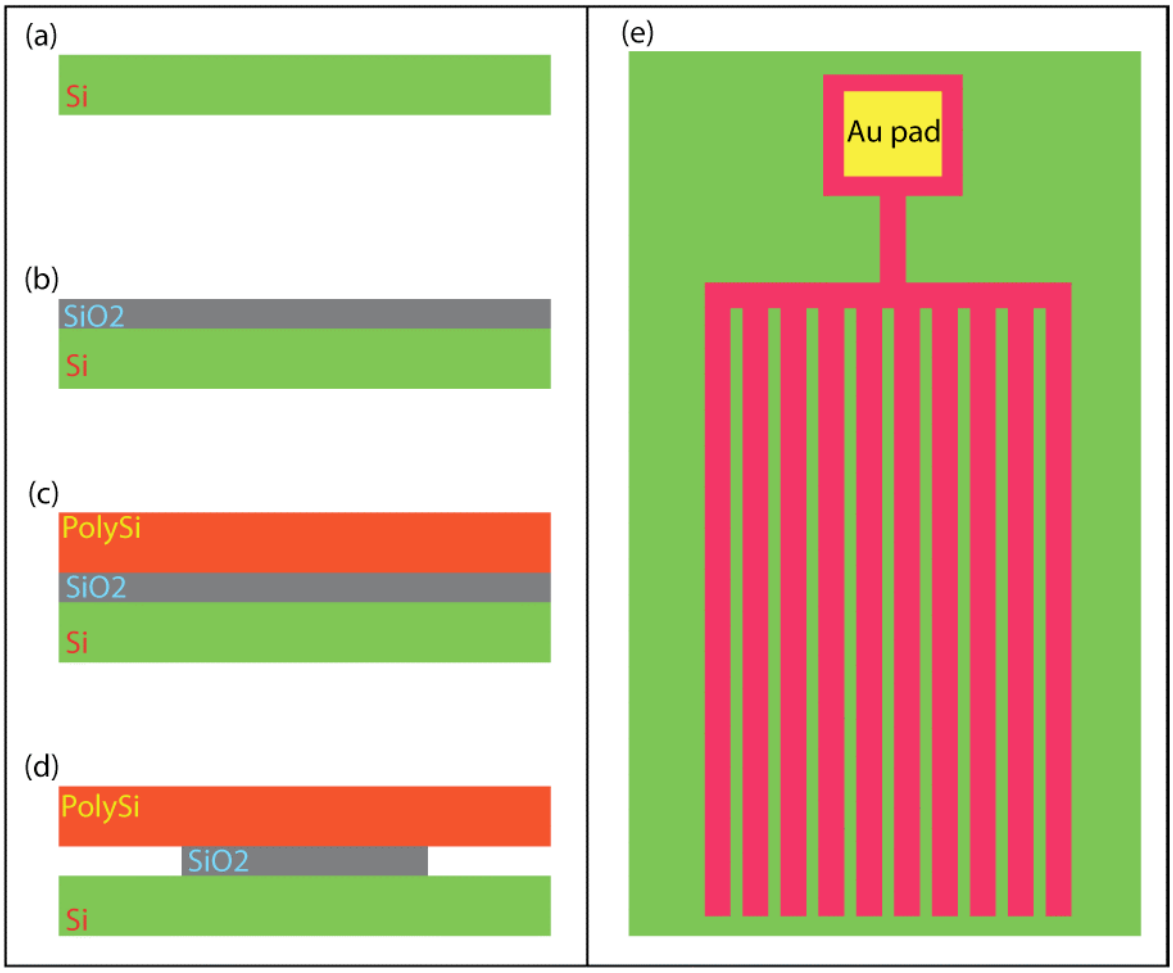

Figure 6-2 Fabrication process steps. (a) PSG was annealed on top of n-type Silicon wafer, then removed with HF. (b) SiO_2 was thermally grown on the silicon layer. (c) Polysilicon was deposited by LPCVD. (d) Polysilicon was defined with standard photolithography and patterned with reactive ion etching (RIE). (d) The oxide layer was undercut by wet etching with HF. (e) top view of the Polysilicon electrode structure. Gold was evaporated and patterned onto the contact pad to reduce contact resistance.

6.4 Experimental Setup

A solution reservoir was made from a laser-cut PDMS well bonded on top as shown in Figure 6-1. A glass coverslip was used to cap the well and prevent evaporation. Before each set of experiments, the device was put in an O_2 plasma asher for cleaning and to facilitate wetting (vacuum level: 1 Torr, Power: 50W, exposure time: 20 seconds).

6.4.1 Electrical system

Electrical impedance was measured with an Alpha-K Impedance Analyzer (Novocontrol GmbH & Co), controlled by software, WinDeta (Novocontrol GmbH & Co). Coaxial cables were used to connect the impedance analyzer to a Signatone H-100 Probe Station. Signatone probes were used to contact the electrical pads on the Nanogap devices. A Microscope mounted on the probe station was used to inspect the nanogap device for damage/contamination.

6.4.2 Measurements of electrolyte solutions

Serially diluted KCl solutions ranging in concentrations from 1M to 1μM were used. Impedance measurements with KCl solutions were always performed starting with the more diluted concentrations first. The device was copiously rinsed with DI water between experiments.

6.5 Dry characterization

A detailed equivalent circuit model was constructed to predict the behaviour of the system. As described in this section, whenever possible, circuit elements were assigned values measured individually using test structures (Figure 6-3) or extracted from geometrical parameters. The remaining parameters were optimized for best fit, by applying a least square fitting routine to minimize the error between the model prediction and the measured impedance response. With the resultant equivalent circuit model (Figure 6-4) the response of the device could be predicted to within 2% in |Z| and phase across a frequency spectrum from 1 Hz to 1 MHz.

6.5.1 Measurement of macroscopic parameters

Building a device capable of consistent measurement on the nanoscale requires the development of a robust interface between nanogap elements and macroscopic measurement apparatus. This section describes experimental improvements in device design. First of all devices were optimized to minimize the effects of contact resistance.

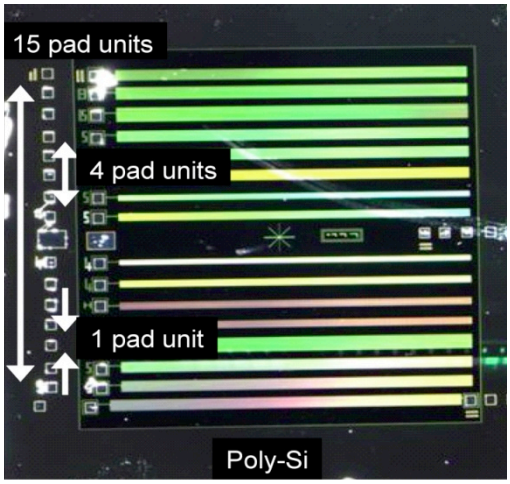

Figure 6-3 Interface to macroscale. Measurement pads patterned to the two plates of the nanogap capacitor are contacted by probe tips for connecting to impedance analysis equipment. Contact resistance measurements were performed by contacting test structures (pads) on both electrode surface types. Courtesy of J. Tanner Nevill.

The contact between the impedance spectrometer and nanogap devices was made using gold tip probes, giving good contact to the metal pads ($R < 1\Omega$). However, it was

essential that contact resistance from the metal pad to the Si substrate was also below $10^3\,\Omega$. Contact resistances were measured using test structures as follows: a set of metal pads was patterned directly onto the conductive silicon wafer at a set distance from one another, as shown in Figure 6-3. Probe tips were used to measure total resistance between different pads. The resistance of one pad unit was defined as the resistance between adjacent pads. Using this structure, resistance along the wafer could be differentiated from the pad-wafer contact resistance. The fact that there was no discernible dependence on distance between pads (or distance along the wafer) showed that the overall resistance was dominated by the contact resistance between the pad and the wafer. Two different metals (gold and silver) were tested. In summary, silver pads exhibited an average contact resistance of 0.4±0.9 MΩ, while gold pads exhibited an average of 185±35 Ω. Based on these measurements, all silicon devices used in subsequent experiments were fabricated using Au pad contacts, as these introduce a resistive element that is an order of magnitude below the lowest nanogap impedance recorded.

Another possible source of error was the parasitic capacitance and inductance of the experimental system. These were quantified by open-circuit and short-circuit measurements: the measured values were a parasitic capacitance of 0.6 pF, and a parasitic inductance of 1.5 H.

Probe contact resistance was averaged for a number of repeated probe contact experiments ($R_{c1} = R_{c2} = 0.6\ \Omega$), while the contact resistance between the Au pads to poly Si and to the doped silicon were measured using test structures ($R_{cSi} = 61\ \Omega$, $R_{cWafer} = 17\ \Omega$). For both the top poly Si fingers and the bottom wafer, sheet resistance was measured by using appropriate test structures ($\rho_{\text{sheet Poly}} = 17\Omega$/square, $\rho_{\text{sheet Si}} = 110\Omega$/square).

6.5.2 Equivalent Circuit Model

Because of the significant resistance along the top poly Si capacitor plate ($\rho_{\text{sheet Si}}$ = 110Ω/square), a ladder network was used to model the nanogap capacitor. Each finger was divided into N elements consisting of a top access resistance ($R_{t(i)} = \rho_{\text{sheetPoly}}$ X (finger length) / (finger width) / N), a bottom access resistance ($R_{b(i)}$) and a nanogap capacitive element,

$$C_{g(i)} = \frac{A_{top}}{d_{gap}} \frac{\varepsilon_{device}}{N} \tag{6-6}$$

where ε_{device} is the average nanocapacitor permittivity (see below). Three parameters were optimized, employing a least square error optimization routine: ε_{SiO2}, the dielectric constant of SiO_2, R_{leak} the leak resistance between the top and bottom plates, and the silicon dioxide etch rate. The parameters were found to be in agreement with literature, and the same values were used for all model results.

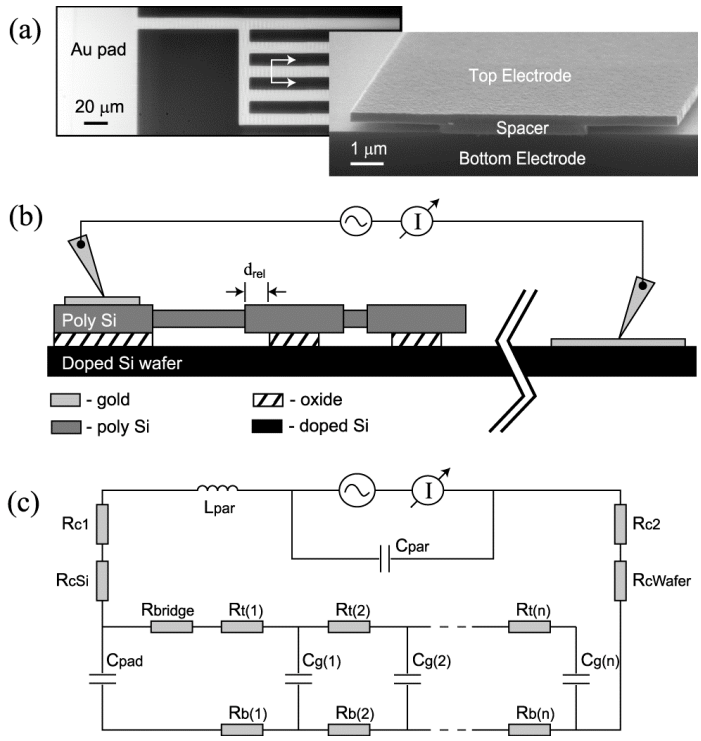

Figure 6-4. Device geometry and model description. (a) A top-view optical image of the polysilicon top electrode containing a contact pad and sensing 'fingers' illustrates the general device geometry (left). The detailed morphology of the 10 μm wide fingers is shown in a cross-sectional SEM micrograph (right). The gap size shown is ~300 nm for clarity, while data was reported from devices with 90 nm gaps. (b) Schematic representation of materials used in the device fabrication process. Dielectric measurements are taken using probes between the top polysilicon electrode (left) and the bottom conductive wafer (right). The measured space consists of a silicon oxide spacer as well as an under-etched nanocavity for sample introduction. (c) A detailed electrical model of the nanocapacitor system. The ladder network uses 100 RC elements. Taken from [9].

The functionality of the model was tested and optimized by comparing predictions for the four different un-released device geometries with impedance data, as shown in Figure 6-5. Impedance magnitude ($|Z|$) and phase (Φ) were measured as a function of frequency from 1 to $3 \cdot 10^6$ Hz, with the inside of the sensing region filled with silicon dioxide (no undercut).

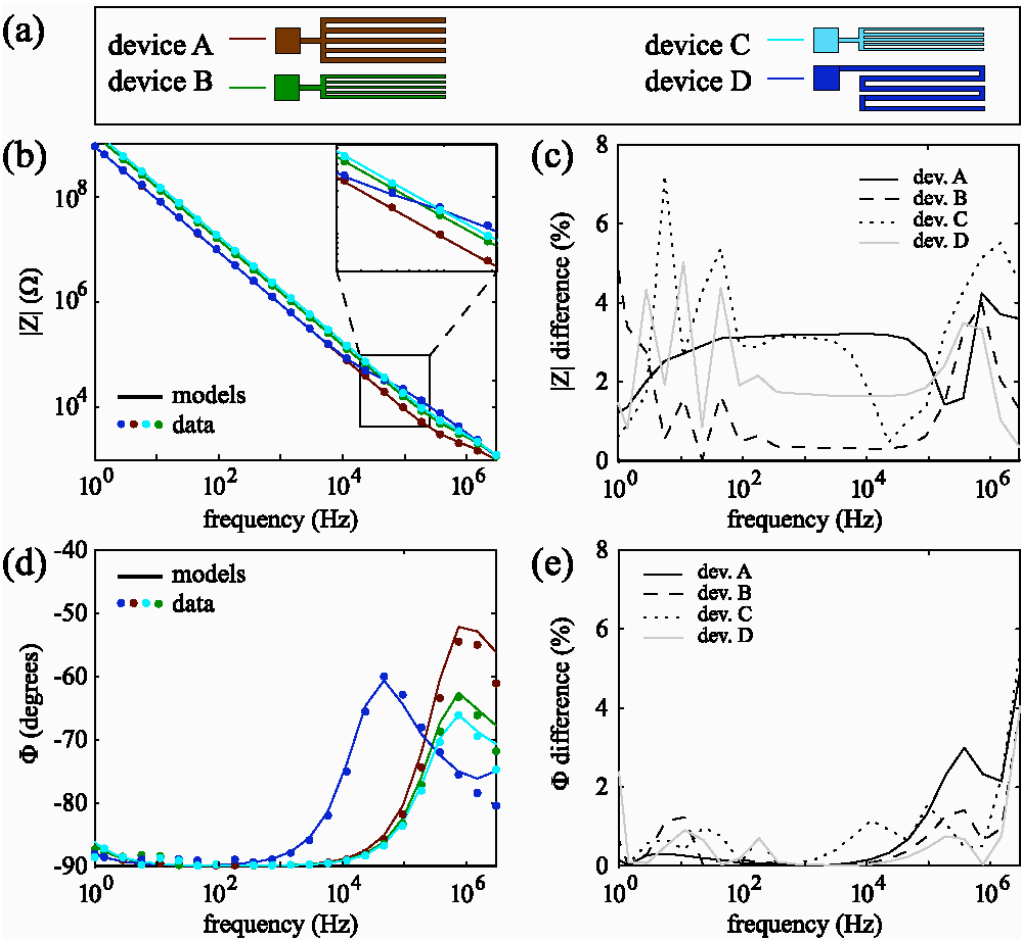

Figure 6-5 Predictions (from model) compared with data for various device geometries of un-released devices. (a) Depiction of the four different device geometries. Three devices have a comb geometry with various finger widths, from 10 μm (red) down to 5 (green) and 4 μm (cyan). The fourth device has a serpentine geometry with a single 10 μm wide finger (blue). (b, d) Model predictions (lines) for the magnitude of the impedance (|Z|) and phase shift (Φ) are compared to data (scatter) from the same four devices. (c, e) The percent difference between the predicted and measured values for both |Z| and Φ are plotted to illustrate quality of fit across the frequency spectrum. Taken from [9].

Four different geometries for the top electrode were tested, as depicted in Figure 6-5 (a). Device A has 5 fingers each 10 μm wide (red), devices B and C have 5 fingers each 5 μm and 4μm wide (green and cyan), and device D has a 10 μm wide serpentine geometry (blue). The predictions from the model (lines) are compared to impedance data for each device in Figure 6-5 (b) and (d). Moving along the frequency spectrum, the total impedance is dominated by various elements of the circuit model. For a pure capacitor, $|Z|$ varies in a straight line on a log-log graph (slope of -1), while a resistor is a horizontal line. For phase, pure capacitors phase shift to -90^o, while resistors have a 0^o phase shift. For most devices, the response is purely capacitive in the region from 10 Hz to 10 kHz. At lower frequencies, the high impedance leak starts to play a role,

leading to a slight departure from the capacitive behaviour. At high frequencies the sheet resistance along the polysilicon top electrode leads to a reduction in the slope of $|Z|$ and changes in Φ from -90° to around -60°. This effect is more important in the serpentine geometry (blue data), where the polysilicon resistance along a single long finger is higher. Finally, in the MHz range, parasitic capacitance of the macro contacts starts to dominate, moving back toward a capacitive response. The quality of the fit is shown in Figure 6-5 (c) and (e), where the percentage difference between model and data is plotted.

The model parameters were measured using test structures. However, two of the model parameters were not measured independently, and had to be optimized. These were the dielectric constant of the oxide (ε_{SiO2}) and the large leak resistance across the nanogap. The leakage is probably due to small imperfections in the oxide layer, since it is present even in un-released devices. Both parameters were set by minimizing the impedance magnitude and phase shift mean error, to yield the best correlation between the data and the model across all four device geometries tested (Figure 6-6). Optimization was performed by varying both parameters and minimizing over a 2D parameter matrix. The optimized value of ε_{SiO2} was found to be $4.25\varepsilon_o$ (Figure 6-6a), and used in all subsequent modelling. This value agrees well with reported values for ε_{SiO2}, which range from $3.81\varepsilon_o$to $5.0\varepsilon_o$ [17]. In the same manner, the leak resistance was found to be R_{leak}= 26.6 GΩ (Figure 6-6 (b)) and the etch rate of the sacrificial SiO_2 113 nm/min (Figure 6-6(c)); Error plots are presented along one dimension only for clarity. The ε_{SiO2} plot was made for the optimal R_{leak} value, and vice versa. All other model parameters were measured directly using test structures.

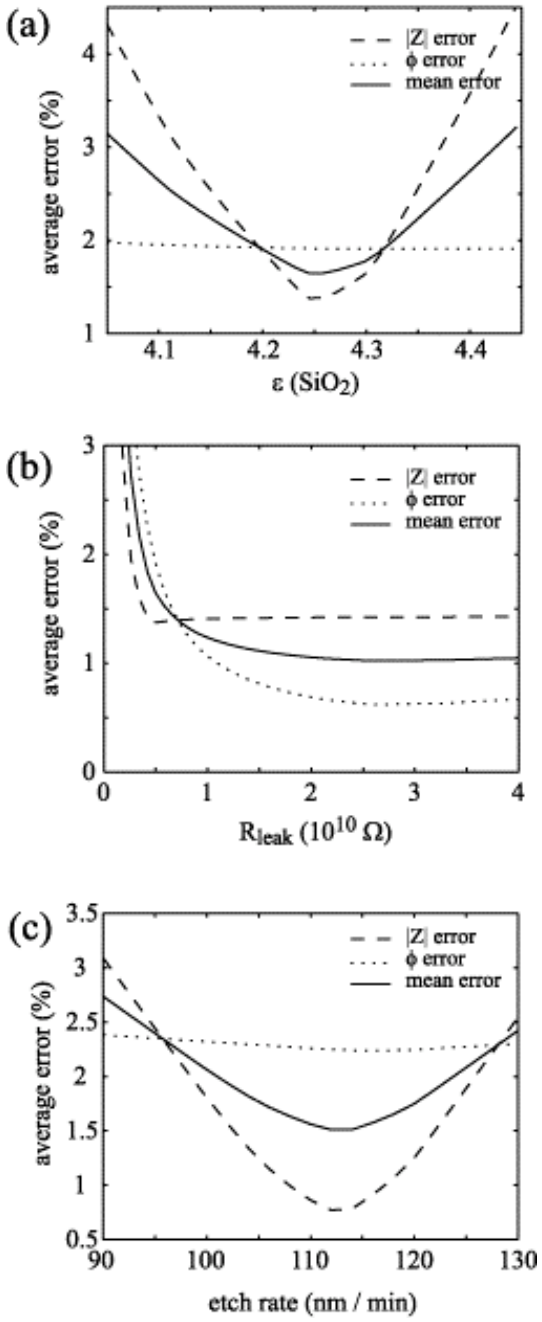

Figure 6-6 Optimization of ε_{SiO2} and R_{leak} was performed simultaneously by averaging errors over all unreleased devices geometries. One dimensional plots of the average model error as a function of parameter value (a, b) are shown for simplicity (the second parameter was fixed at its optimal value). The etch rate was optimized using ε_{SiO2} and R_{leak} from unreleased devices, and by minimizing errors for partial release experiments. The parameter values at the point of minimum error were determined to be 4.25, 2.5 x 10^{10} Ω, and 113 nm/min for relative oxide permittivity, leak resistance, and oxide etch rate, respectively. Taken from [9].

6.5.3 Determination of device sensitivity and detection limit

Determination of the sensitivity of the nanogap sensor to changes in the permittivity of the capacitor material was a principal aim of this work. Permittivity changes were introduced by successively under-etching the SiO_2 spacer. This results in replacement of high dielectric material ($\varepsilon_{SiO2} = 4.25\ \varepsilon_o$) with lower permittivity air ($\varepsilon_{air} = \varepsilon_o$) over a distance d_{rel}. The under-etched length was determined by timed etches and confirmed using test structures. The expected etch rate for the HF concentration used was 100 nm/min. However, the partial release data has a best fit with a slightly different etch rate of 112 nm/min (Figure 6-6 (c)). Etch rate was optimised while all the other parameter were fixed to fit with the unreleased device model. Using this etch rate, the average difference between the model and experiment is below 2% for the 5 μm comb finger devices tested (Figure 6-7).

The percentage change in measured parameters as a function of ε is plotted for three representative frequencies in Figure 6-8 (a and b). Average nano-capacitor permittivity was calculated from

$$\varepsilon_{device} = \left(w - 2d_{rel}\right) \varepsilon_{SiO2} + 2d_{rel} \cdot \varepsilon_o \tag{6-7}$$

where w is the finger width. From un-released devices to the last etch step, the dielectric constant ε_{device} varied from $4.25\varepsilon_o$ down to $2.2\varepsilon_o$. Plots at different frequencies illustrate differences in sensitivity regimes and measurement standard deviation across the frequency spectrum. In the low frequency region, standard deviation is high due to measurement noise with very high system impedance. At high frequency, the system response is dominated by parasitic capacitance and the dependence on ε_{device} is greatly reduced. Sensitivity to permittivity changes is a critical parameter in evaluating the possibility of using nanogap capacitors in order to map changes in protein structure, which result in small changes in the permittivity of sample proteins. The device sensitivity was defined as the percentage change in $|Z|$ and Φ over the percentage change in ε. The sensitivity results are plotted in Figure 6-9 for all four device geometries. The model was also used to predict device sensitivity, and these results are plotted alongside the measured values in Figure 6-9, showing a good fit. Note that the phase is more sensitive in the region where the impedance magnitude sensitivity decreases. At these higher frequencies, the system is less dominated by the capacitance, and phase sensitivity increases with the increase in overall system resistance.

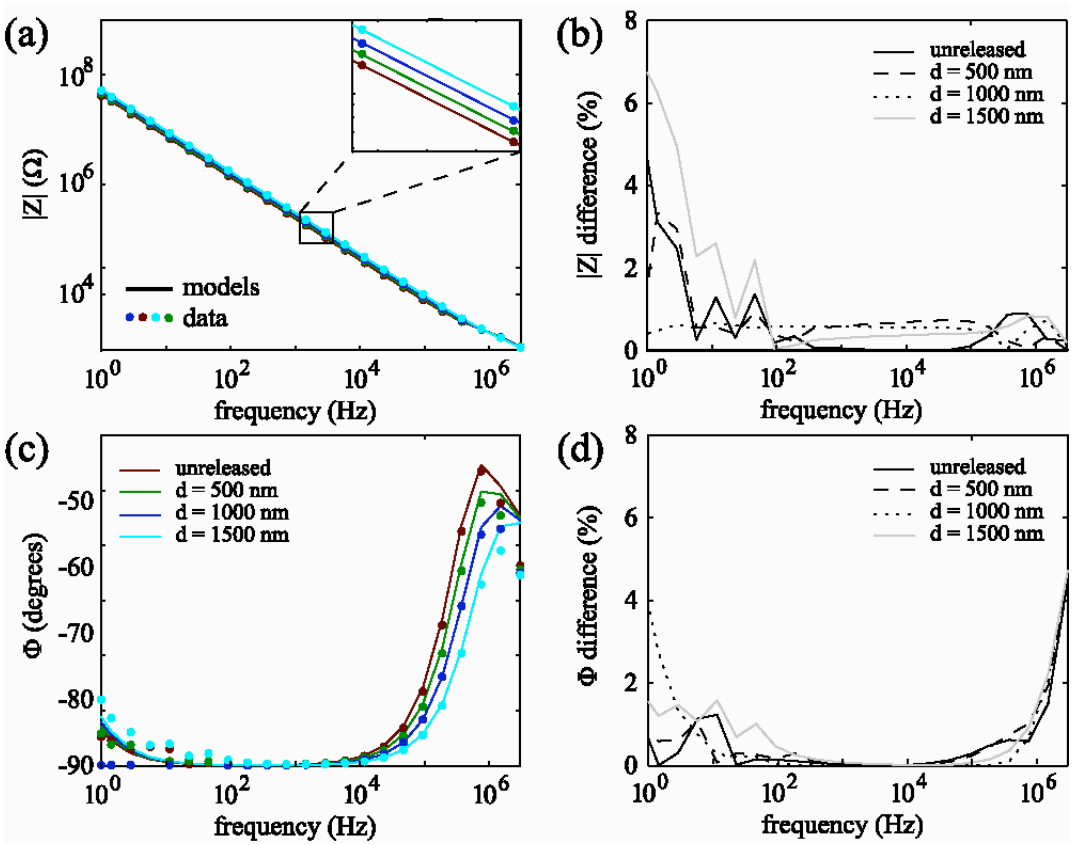

Figure 6-7 Model predictions and device data for varying permittivity. The impedance magnitude (a) and phase shift (c) are plotted as a function of frequency for varying permittivity values (release amounts) for the 5 μm nanogap geometry. Model predictions (lines) agree with data (scatter) within 1 standard deviation (standard deviation not shown). (b-d) A plot of percent difference between the data and model for |Z| (b) and Φ (d). Incremental permittivity changes of approximately 10% ε were obtained by replacing part of the SiO2 spacer material with air through successive etch steps. Taken from [9].

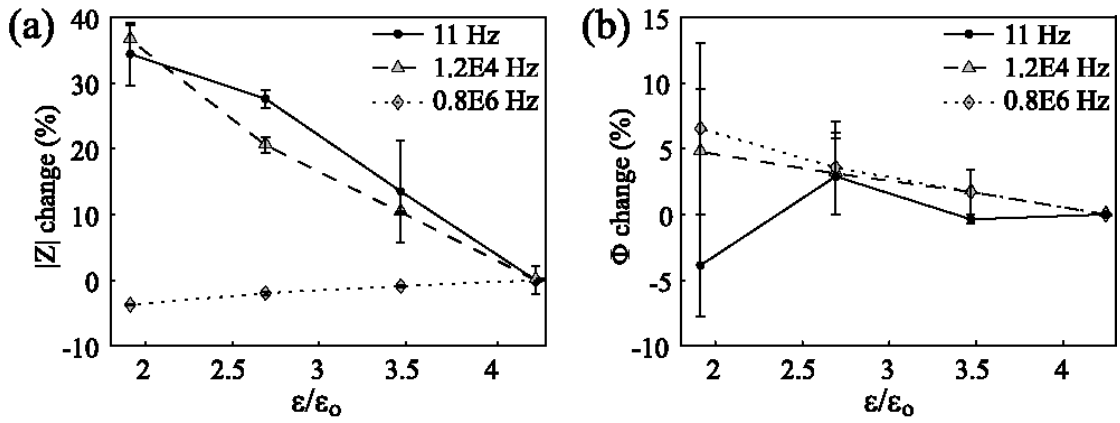

Figure 6-8 Changes in measured impedance, |Z| (a) and Φ (b) as a function of relative permittivity inside the nanogap. Three representative frequencies were chosen: a low frequency (11 Hz), a mid range frequency (1.2×10^4 Hz), and a high frequency (0.8×10^6 Hz) are

presented. The data illustrates the frequency dependence of sensitivity for such devices. Taken from [9].

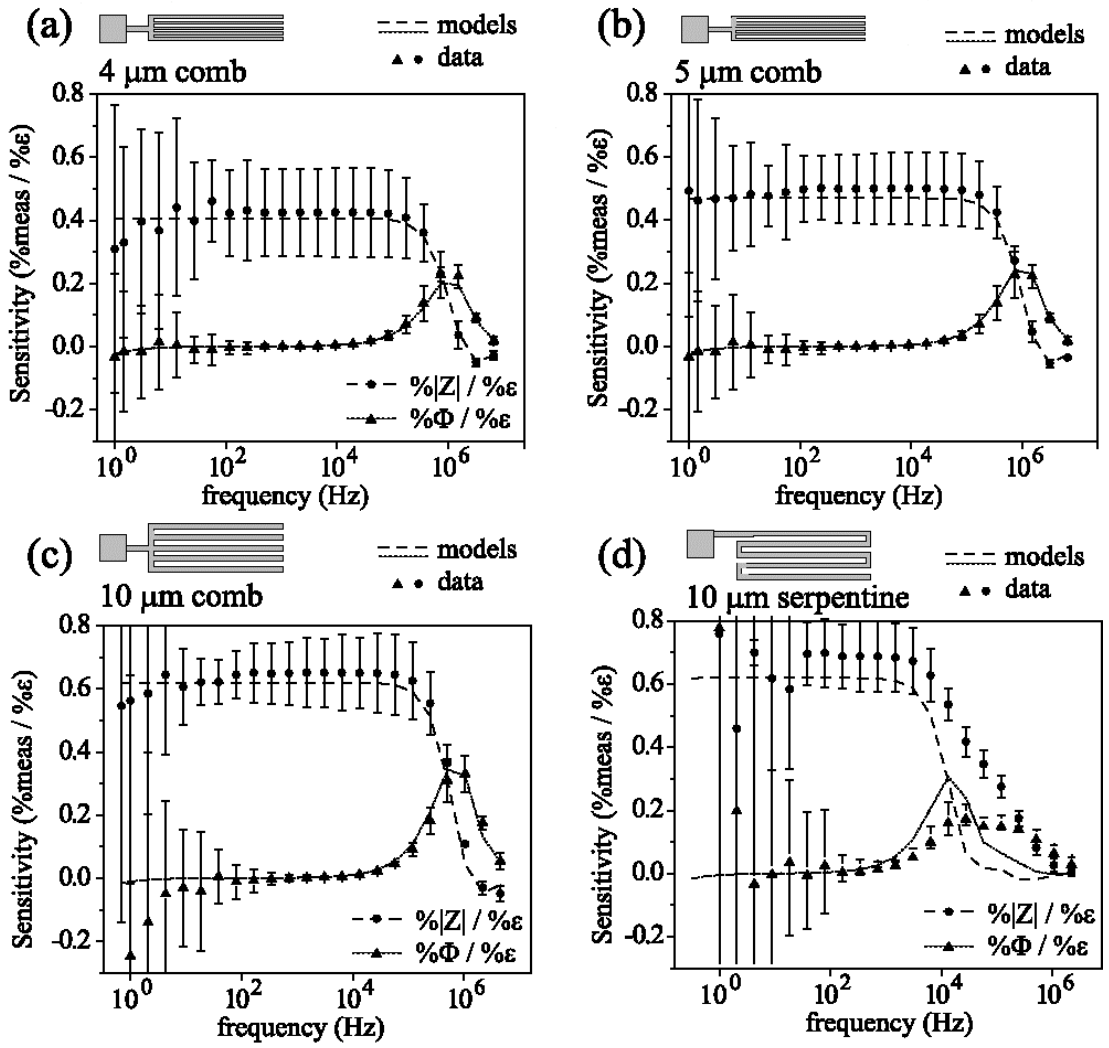

Figure 6-9 Sensitivity to changes in permittivity for four different device geometries: Device A with 5 μm fingers (a), device B with 4 μm fingers (b), device C with 10 μm fingers (c) and device D with a 10 μm serpentine (d). |Z| (●) and Φ (▲) are plotted for each geometry, as well as the predicted sensitivity based on the model (dashed and solid lines). The error bars represent one standard deviation and are based on the calculated sensitivity resulting from the three partial releases described in the experiment section. Taken from [9].

The limit of detection is an important parameter for device characterization. In this work, the detection limit is defined as the smallest change in sample permittivity that

produces a detectable change in the measured quantities |Z| and Φ, equal to the standard deviation of the measurement:

$$\varepsilon_{dlimit} = \frac{d\varepsilon}{dX} \cdot \text{stdev}(X) \tag{6-8}$$

Where X represents the measured quantity and *stdev(X)* represents the standard deviation. The lowest detection limit for |Z| is below 2% of ε in the region from 10^2 to 10^5 Hz when the standard deviation is taken from one device to another. If the same device is used repeatedly, and the standard deviation is defined as the difference between measurements of the same device on different days, the limit of sensitivity is reduced by about one order of magnitude. Consequently, detection limits are also decreased by the same factor, down to below 0.2% ε. For Φ, the low detection limit range is $2x10^4$ to 10^6 Hz and measured to be 1.5% across multiple devices.

6.6 Measurements in KCl electrolyte

6.6.1 Controlling nanogap wetting phenomena

An important parameter that can affect the reliability of nanogap impedance spectroscopy is 'wetting' of the gap, or penetration of buffer into the nano-cavity. Because the top polysilicon electrode is thin, an upright microscope was used to observe the presence of air pockets from changes in refractive index. Nanogap structures did not spontaneously fill completely. Furthermore, the amount of capacitor surface area filled with buffer solution varied with each successive filling of the experimental well. The differences were confirmed by impedance measurements in solution. Successive measurements differed from one another by as much as 40%. Filling efficiency was also observed to depend on device age: Freshly released devices (by HF etching) were highly hydrophobic, with contact angles of 90°-100°. Devices that were stored in ambient conditions for more than 1 week had contact angles in the range of 40°-60°.

A surface treatment that increases hydrophilicity of the surface did improve the filling of nanogap cavities: oxygen plasma treatment is known to create a thin oxide surface that is charged, therefore highly hydrophilic. After subjecting devices to O_2 plasma treatment (80 W, 15 s.) the device surfaces became highly hydrophilic (contact angle 1°-5°) and complete filling was observed. Reliable filling was confirmed by repeated application of buffer solution to the device surface and impedance spectroscopy measurements. For plasma treated devices, variability for successive filling was shown to be below 1%. It was concluded that the devices should be plasma treated immediately before each experimental run.

6.6.2 Impedance measurements

Impedance measurements were performed on nanogap devices of 90nm and 20nm gaps. The response to six serial dilutions of KCl electrolyte (ranging from 10 μM to 1M) was measured. Typical impedance data (|Z| and Φ) are plotted in Figure 6-10. From the data it is apparent that parasitic capacitance elements dominate the response

at frequencies above 10^5 Hz. Also, somewhat surprisingly the capacitive slopes at low frequencies tend to overlap and are not spaced apart as expected if the double layer capacitance depended on solution conductivity. This response is attributed to the spontaneous formation of a nanometer-thick native oxide layer on the surface of the polysilicon and silicon electrodes.

Also it is notable that in the mid-range frequencies (i.e. between 10^3 and 10^5 Hz), where the spectrum is expected to be resistive, the |Z| slope is not perfectly flat and the phase angles are less than 20 degrees, indicating a complex response that necessitates the use of distributed RC elements in the equivalent circuit model.

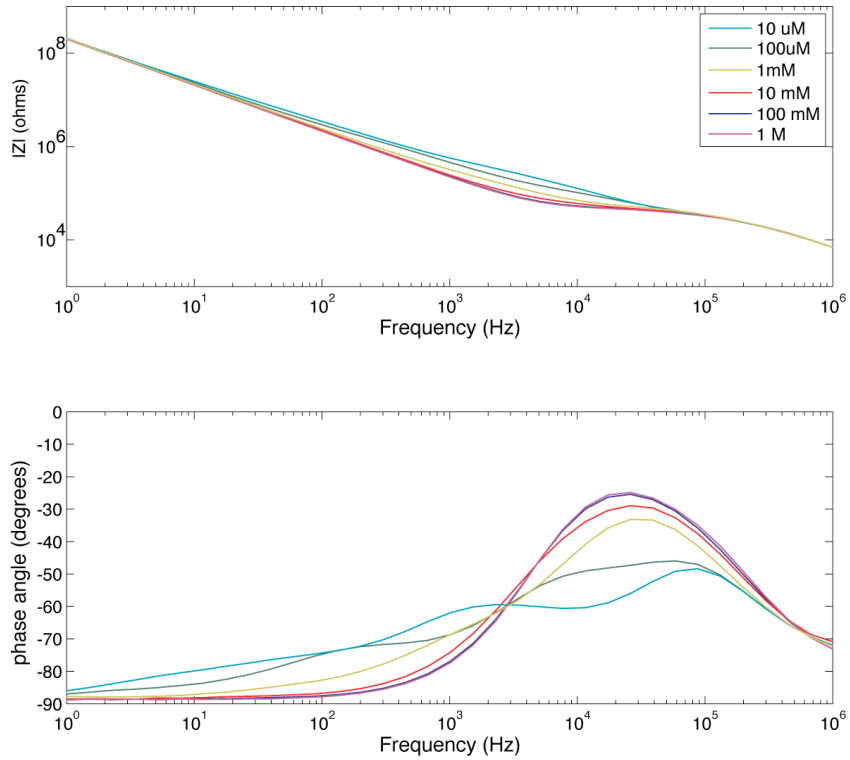

Figure 6-10 Impedance and phase response of KCl solutions in a 20nm gap device

6.6.3 Equivalent circuit model

When buffer solution is introduced into the nanogap device, numerous circuit elements are required for an equivalent model. Whilst it would be desirable for the buffer solution to only wet the inside of the nanocavity (i.e. the lower surface - but not the upper or side surface of the top electrode and the bottom electrode –but only within the confines of the gap), experimental results proved that double layers forms all over the wetted device surfaces because all conductive surfaces are exposed. This generates an extensive network of parasitic circuit elements which make the equivalent circuit model extremely complex and reduce the sensitivity of the impedance response of the device.

Data gathered from experiments conducted with solutions of 5 different molarities (100μM, 1mM, 10mM, 100mM, 1M) of KCl were used to establish and optimize an equivalent circuit model for the solution-filled device. The model builds on the bottom-up model of nanogap behaviour in air (described in the previous section), with a few important changes: First, double layer capacitors are formed on all surfaces that are in contact with solution inside the PDMS well. This happens not only inside the nanogap volume, but away from the gap wherever polysilicon or doped silicon (top and bottom electrode surfaces) are exposed to buffer solution. The top surface double layer capacitance is connected to the bottom surface double layer capacitive elements through solution resistance which is dependent on the molarity of the solution used, as well as the distance between the two. A schematic representation of this model is shown in Figure 6-11.

A correct model of nanogap behaviour requires determination of double layer capacitance values for both the top (polysilicon) and bottom (silicon) electrodes. Single surfaces were prepared for the two materials and used for double layer capacitance measurements. The measurement results reported in Chapter 4 were obtained using a test cell consisting of a standard Ag/AgCl reference electrode and an opposing surface of the same material as the nanogap electrode of interest. The double layer response is calculated from the capacitive (i.e. low frequency) region of the spectra. Even for a simple surface test cell, a number of different capacitive elements are required to fit experimental data (data not shown).

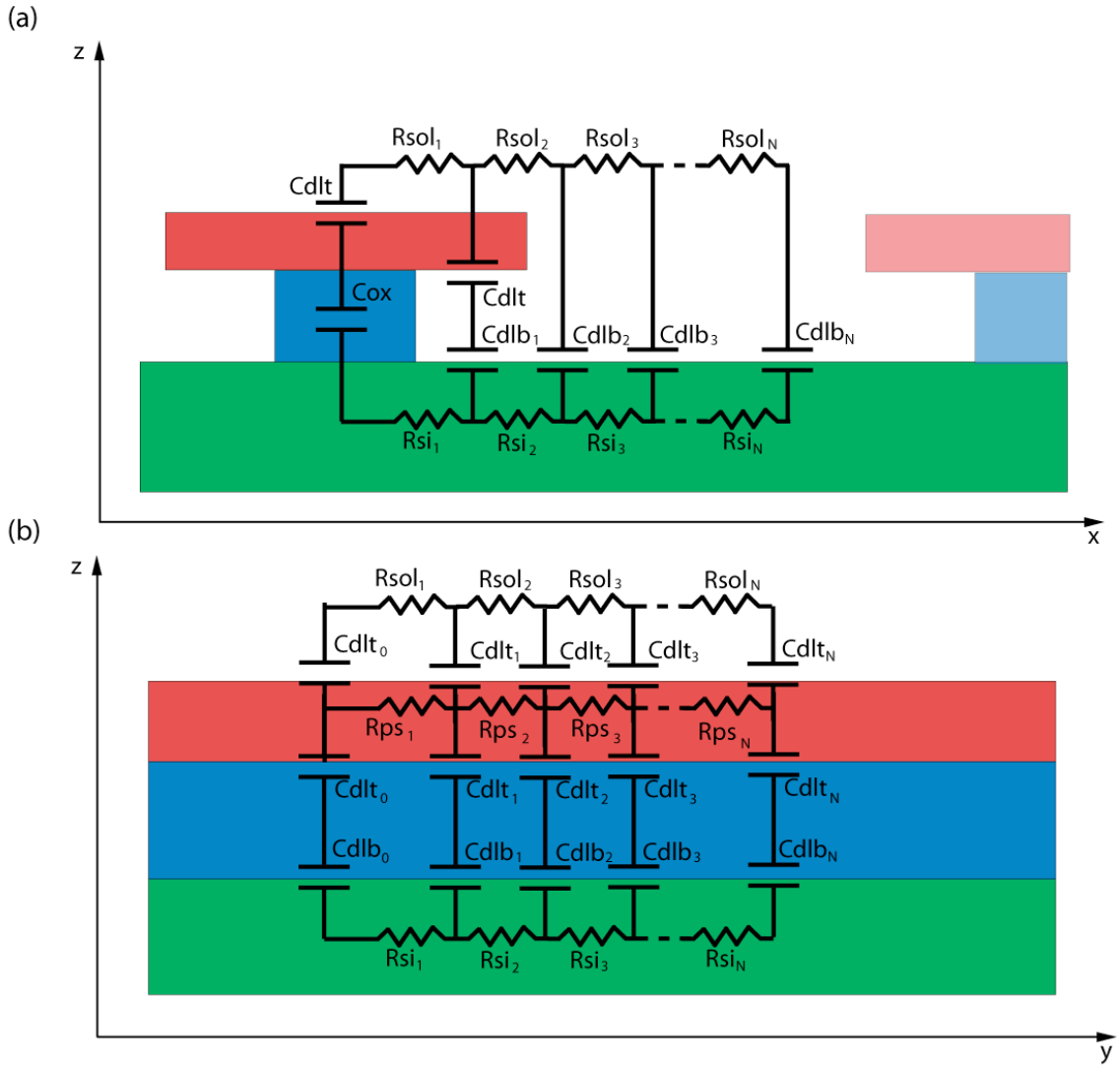

Figure 6-11 A model for nanogap device behaviour in solution. Both the small top electrode and the large bottom electrode have surfaces exposed to buffer that form double layer capacitors (Cdl) outside the nanogap volume. These capacitors are connected via a distributed solution resistance (Rsol). Each element along the device length contains is represented by the circuit model shown above. *x*-direction is along device width, *y*-direction is along device (finger) length.

The equivalent circuit model is distributed along two dimensions (i.e. along the comb fingers because of the finite conductivity of the doped silicon and polysilicon, and at a 90 degree angle far from the finger because of the finite conductivity of the buffer solution). The number of elements found to give a convergent solution (within 1%) is equal to 2000. To save computing iterations, the distribution is not nested, so

there are 2000+2000 rather than 2000^2 elements. This however comes at the cost of decreased accuracy.

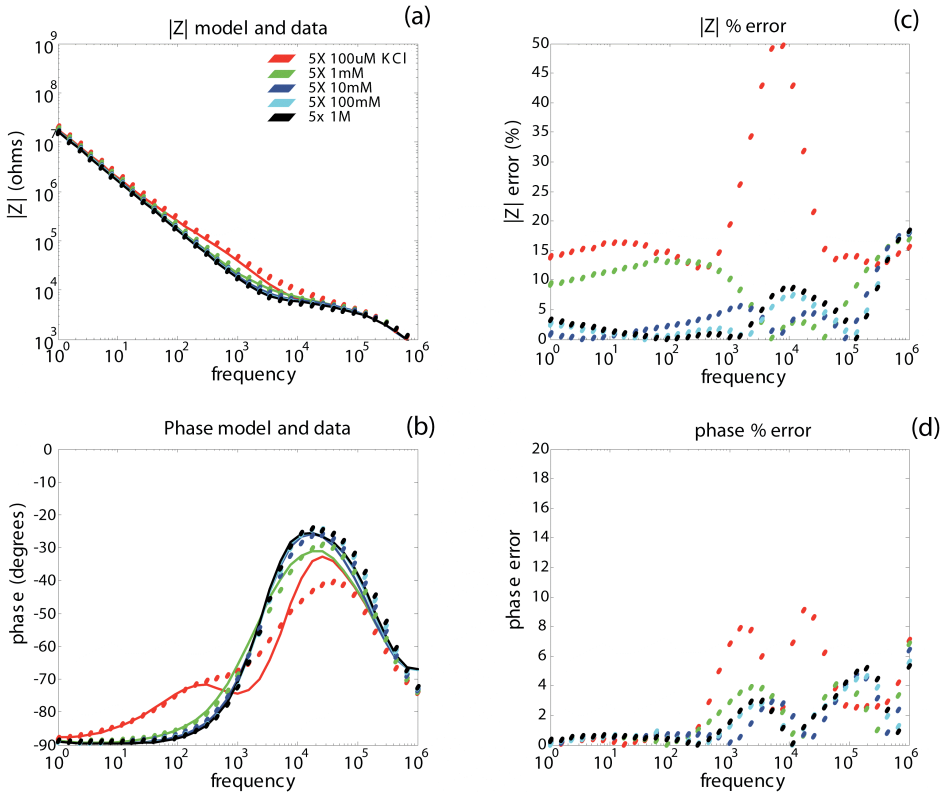

Figure 6-12 Model predictions (lines) for the magnitude of the impedance (|Z|) and phase shift, compared to data (dots) from the same four devices (a) and (b). The percentage difference between the predicted and measured values for both |Z| and Φ are plotted in (c) and (d) to illustrate quality of fit across the frequency spectrum.

The modelled response is compared to the measured response for different molarities of KCl solutions in Figure 6-12 (|Z| and Φ). The corresponding error (evaluated as the percentage difference between modelled and measured response – point by point) is shown in (c) and (d) of the same figure. Data (dots) was averaged over four different devices for each buffer concentration point, but standard deviation bars are not visible because of the log scale of the plot. It was observed that for the higher molarities (>10mM and up) the model works quite well, exhibiting a mean percent error within 5%. However the error increases for frequencies above 10 kHz when the response becomes mainly resistive. Also lower molarities (100μM and 1mM) (where the solution resistance is higher) exhibit significantly higher mean percent errors. The higher percentage error results because at lower molarities, the double layer occupies a larger fraction of the interelectrode distance (nanogap). As explained in the next section, a 'nanogap correction factor' was introduced to account for this.

6.6.4 Capacitance of a constrained double layer

The overall device impedance response results from a combination of:

1. Parasitic elements
2. Double layers on the top and bottom electrode outside the gap
3. Double layer on the electrode inside the gap

Having measured the response due to the parasitic elements, and having quantified the capacitance values of the double layer for the top and bottom electrodes, the circuit elements that model the double layer capacitance inside the gap were optimized. As shown in Chapter 4, the impedance responses of silicon and polysilicon macroscopic electrodes were measured at different concentrations of KCl, thus establishing good models for the response of the double layer on these materials. Yet, the measured values of double layer capacitance of the nanogap device differed from the expected values of silicon and polysilicon electrodes in a macroscopic parallel plate arrangement.

The modelling error, at least in part, could be due to the fact that the value of double-layer capacitance measured inside the gap might differ from the values measured in experiments on large area electrodes, where the double layer is not constrained. This would suggest that the double layer in the gap behaves differently and hence exhibits different capacitance/impedance.

A 'gap factor' with values ranging between 0 and 1 is used to correct for this phenomena and multiplied by the double layer impedance for the area where the top and bottom electrode overlap. As seen in Table 6-1, different molarities require different factors to minimize the error. This is to be expected as different electrolyte concentrations give rise to different double layer thicknesses. It can be speculated that for a measured impedance to diverge significantly from the theoretical prediction, the double layer thickness has to be close or comparable in size to at least half the inter-electrode distance.

For example, for the case of a 90 nm gap device, a value for C_{dl} (double layer capacitance in the gap for the lower molarity 100μM), for minimum error was 70% of the value in bulk solution (for the same molarity). For 100μM KCl, GCS theory predicts that the double layer thickness is about 30nm. The ratio between the double layer thickness (building on both bottom and top electrode) and the inter-electrode distance is therefore 2/3.

The constrained double layer capacitance measured at 1mM needs to be adjusted to 85% of its value in bulk, while the capacitance for 10 mM solution is unchanged, as

for higher concentration solutions. These values make sense intuitively as, for 10 mM and higher the diffuse layer is much thinner than the 90nm gap of the measuring device; while at 1mM and 100μM, the ionic cloud of the diffuse layer occupies a sizable portion of the nanogap influencing the resulting capacitance.

In Figure 6-12(b) the measured and 'gap-corrected' modelled responses are shown. The gap-factor correction lowers the overall error in the model noticeably when compared to the unadjusted model results (Figure 6-12(a)).

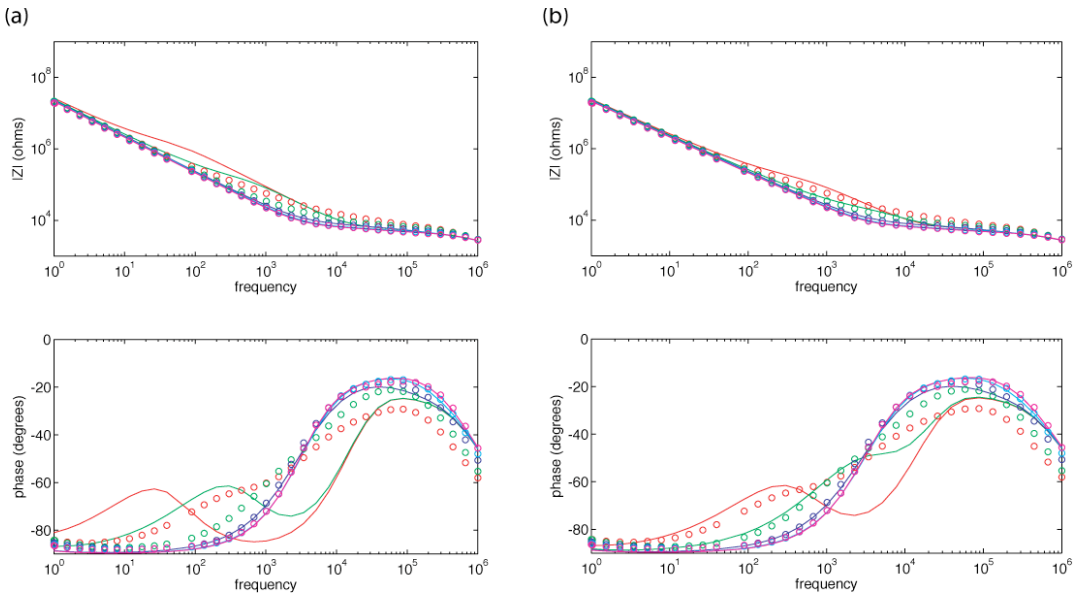

Figure 6-13 (a) Measured (dotted) and modelled (solid) impedance response curves for the 90nm gap device, *before* nanogap correction factor has been introduced. (b) Measured (dotted) and modelled (solid) impedance response curves for the 90nm gap device, *after* nanogap correction factor has been introduced. It is evident that the modelled response

Measurements from a 20 nm gap device gave a similar trend, although the gap factors needed to optimize the model resulted in much more pronounced differences in the gap double layer capacitance. In a 20 nm device, the double layers at 100μM and 1mM do overlap (since the diffuse layers at those concentration are of 30 nm and 10 nm thickness respectively), resulting in a smaller double layer capacitance (0.1% and 5% of unconstrained values respectively).

Although this is certainly not conclusive proof that a constrained double layer behaves differently from a double layer formed in bulk solution, this result warrants further investigation.

KCl concentration	double layer thickness	90 nm device		20 nm device	
		2xDL/gap ratio	gap factor	2xDL/gap ratio	gap factor
0.1 mM	30nm	0.667	0.70	1.5	0.001
1 mM	10nm	0.222	0.85	1.0	0.050
10 mM	3nm	0.07	1	0.3	0.8
100 mM	1nm	0.02	1	0.1	1
1 M	0.5nm	0.01	1	0.05	1

Table 6-1 Nanogap correction factors for 20nm and 90nm gap devices. DL gap ratios higher than one indicate overlapping double layers.

6.6.5 Sensitivity to proteins in solution

For experiments involving proteins the aim is to be able to measure biochemical events involving proteins in a novel and highly sensitive way. Biochemical events that could be explored by impedance spectroscopic methods include protein conformational changes, antibody-antigen binding, or enzymatic reactions. A sizeable amount of effort has been devoted by investigators toward the sensing of biochemical events using impedance spectroscopy at single surfaces [15-21]. Because experimental and fabrication complexity is high for nanogap devices, it is first necessary to demonstrate that such devices are more sensitive to the presence of protein in solution compared to single surface capacitive cells. Therefore the sensitivity of silicon-based nanogap devices was assessed and compared directly to experiments using flat electrodes.

Experiments set up was as follows: A high salt concentration buffer solution (1M KCl) was used such that the effects of added protein on the overall solution conductivity would be minimized. Then, experimental cells (nanogap or surface) were exposed to increasing protein concentrations in solution over seven orders of magnitude (0.1 nM to 100 μM). After a 10 minute incubation period impedance spectra were acquired for each concentration point. Additional control experiments were done using the same cell containing only buffer solution, measured at the same time intervals. Measured changes due to increasing protein concentration were small, of the order 0.5% per decade increase in concentration. More importantly, the control experiment (time dependant changes for 1M KCl solution alone), revealed changes similar to those observed for protein. This result was verified for a number of surfaces (silicon, polysilicon and gold) for two different proteins solutions (lysozyme and human serum albumin). It is concluded from this data that, without specific attachment, experiments with flat surface cannot detect changes in solubilized protein up to concentrations of 0.1 mM.

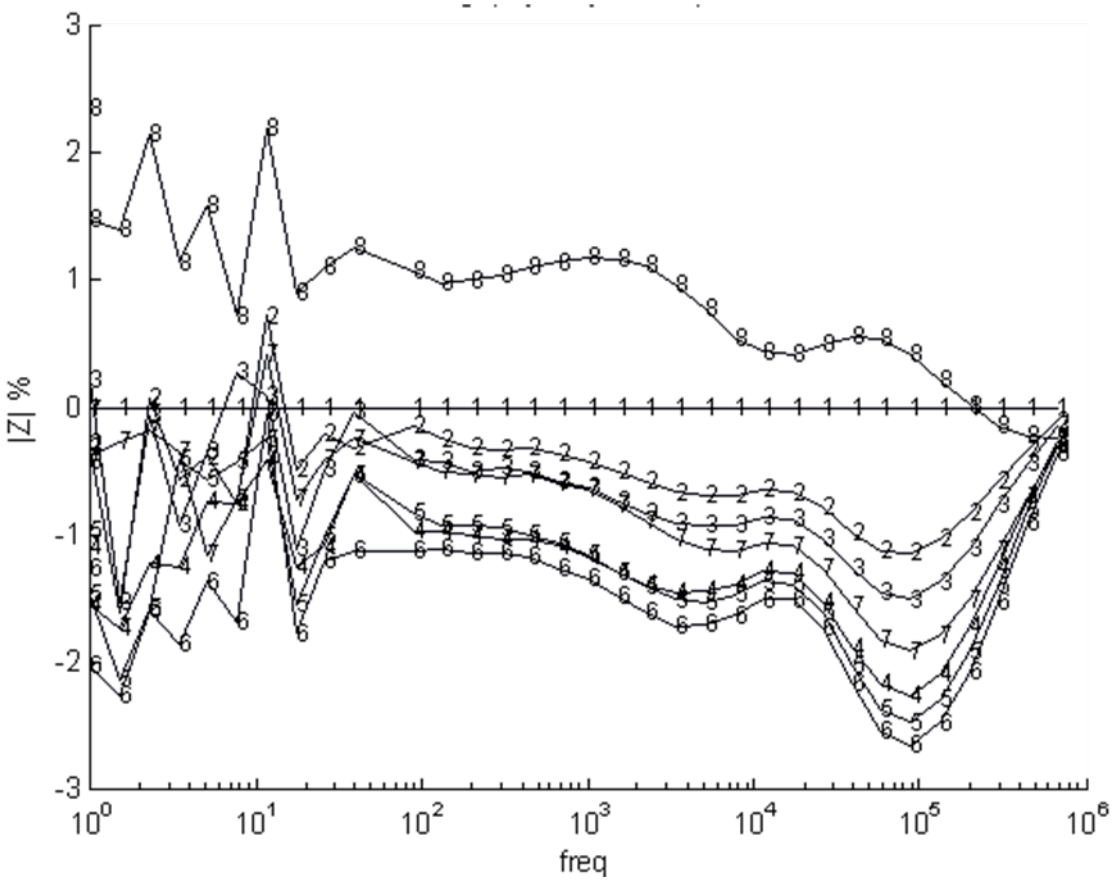

Figure 6-14. Nanogap impedance for different lysozyme concentrations. Percentage change in impedance for different lysozyme concentrations in solution from 1M KCl solution only ('label = 1'). Protein concentration was increased over 7 orders of magnitude from 0.1 nM to 100 μM lysozyme in 1M KCl ('2' to '7'). Results are averaged from two different 91 nm gap devices.

Nanogap devices were next tested to assess whether the sensor could measure protein concentration, and the results for one set of experiments is presented in Figure 6-14. For all but the last concentration point (100 μM), the impedance decreases in successive steps by about 0.3%, while the last step shows an increase in impedance of about 2%. Time-dependent control experiments were also carried out, showing a steady decrease of about 0.2% in impedance over time in the higher frequency region (Figure 6-15). The results suggest that for all but the highest protein concentration (100 μM) the device does not produce a signal above the baseline. Therefore, it is concluded that the semiconductor-based device is not sensitive enough to quantitatively detect the presence of protein in KCl solution.

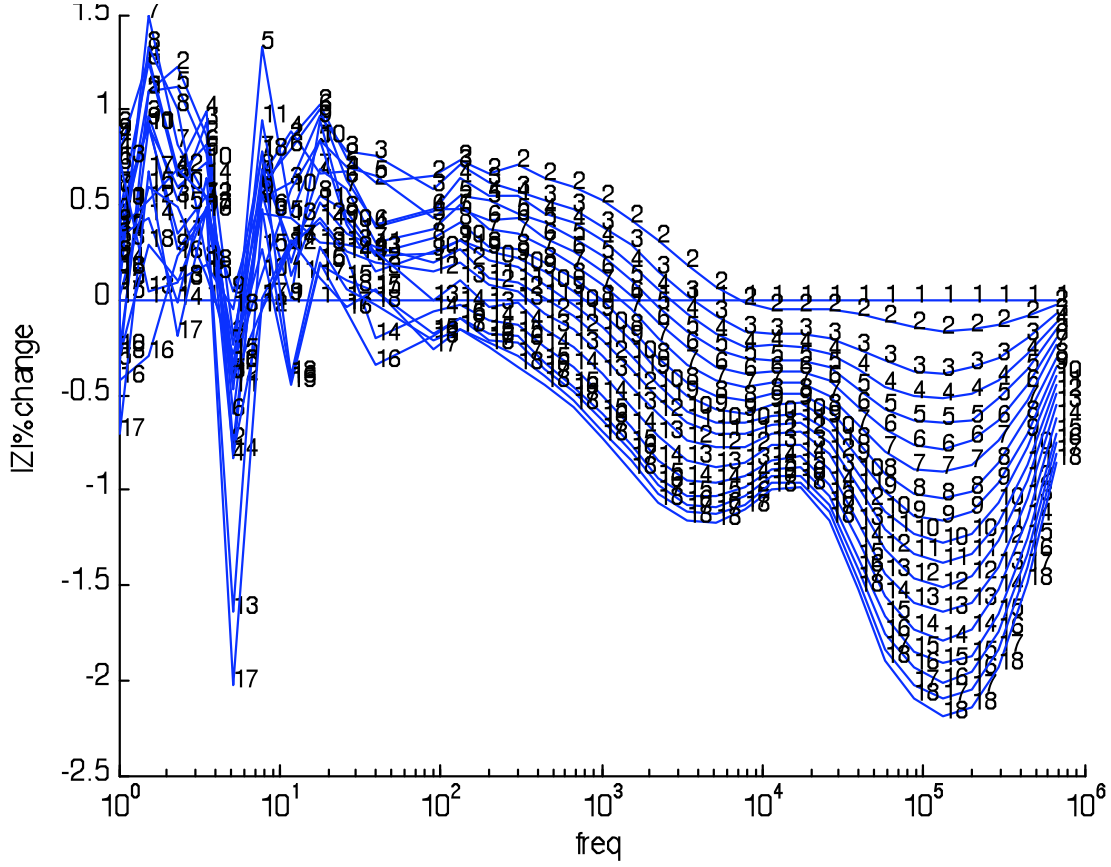

Figure 6-15 Stability of nanogap response over time. Percent change in impedance spectra taken every 10 min. for three hours. Results are averaged from two different 91 nm gap devices containing 1M KCl.

6.7 Conclusions

This device has been extensively and rigorously characterized and a complex equivalent circuit model has been constructed to predict the response of the device with less than 2% error across the spectrum when dry, and with less than 10% error across the spectrum with solution wetting the surfaces.

The ability to explore the response of overlapping ionic double layers by impedance spectroscopy is in itself quite unique and impedance spectroscopy is an attractive option to unravel the structure of the diffuse layer when confined in a cavity of comparable size. Additionally, the combination of a small sample volume, and large area-to-volume ratio make this device potentially very effective for electrochemical detection of biomolecular events, such as protein folding.

Unfortunately, the experiments revealed three fundamental problems with current nanogap devices which severely limit their use as biosensors:

(i) Double layer capacitance – electrical double layers forms on all electrode-electrolyte interfaces. The devices have semiconducting surfaces (both top and bottom) that are exposed to the electrolyte. Because of the large surface area of these electrodes relative to the active area of the nanogap, the capacitance resulting from these parasitic double layers tends to mask the capacitance of the nanogap. This translates into lower device sensitivity.

(ii) Semiconductor electrodes - even though the electrodes are made from highly doped semiconductors, the resistance of the electrodes is significant enough to mask some of the device impedance. Advantages gained by reducing the complexity of the microfabrication process are lost due to the resistive contribution of the semiconductor electrodes.

(iii) Native oxide layer – the silicon-based electrodes develop a native oxide layer on all surfaces. Not only does this oxide layer change over time, but it tends to mask changes in capacitance of the active region. Essentially, this oxide layer acts as an insulator that decreases the device sensitivity.

Increased sensitivity (defined as a percentage change in $|Z|$ for a given percentage change in the capacitance of the nanogap) to events in a nanocavity could be attained by addressing these limitations including reduction of resistivity of electrode materials and wetting of nanocavity-only surfaces. Figure 6-16 shows how metal electrodes (to decrease resistivity) and insulation of surfaces outside the nanogap would increase the sensitivity of the sensor by almost 500% across the entire spectrum of frequencies. It is evident from the experimental data that semiconductor electrodes are unsuitable for the development of a sensitive nanogap biosensor. The semiconductor electrodes should be replaced with metal electrodes and the area outside the gap insulated with photoresist. Also microfluidic channels should be used for sample delivery.

Finally, given the pronounced sensitivity of impedance spectroscopy to changes in solution acidity, temperature, conductivity, it would also be advisable to include a reference electrode in the design to take into account such changes and correct for them either at the acquisition stage or when post-processing the acquired data.

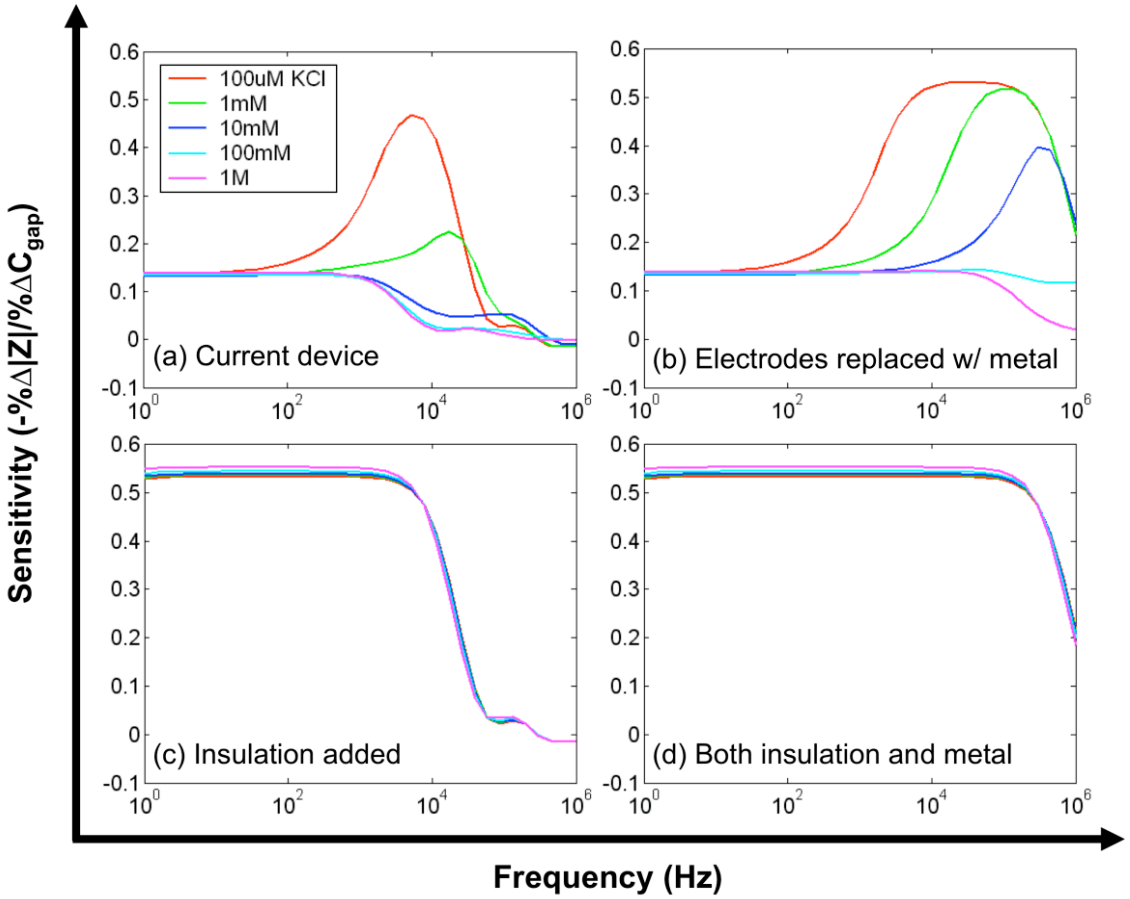

Figure 6-16 Sensitivity curves defined as a percent change in |Z| for a given percent change in the capacitance of the nanogap. (a) The sensitivity of the current device based on the developed equivalent circuit model for 5 different molarities of KCl. (b) The sensitivity of a theoretical device if the semiconductor electrodes were replaced with metal. Note that the sensitivity increases at the higher frequencies. (c) The sensitivity of a theoretical device if insulation is added to the device to cover all electrode surfaces outside of the nanogap. Note that low frequency sensitivity is drastically improved. (d) The sensitivity of a theoretical device if both the electrodes are replaced with metal and insulated from parasitic double layer capacitance. Courtesy of J. Tanner Nevill.

References

[1] C. Berggren, B. Bjarnason, and G. Johansson, "Capacitive biosensors," *Electroanal*, 2001, pp. 173-180.

[2] A. Bonincontro, "Dielectric spectroscopy as a probe for the investigation of conformational properties of proteins," *Spectrochimica Acta Part A: Molecular and Biomolecular Spectroscopy,* vol. 59, no. 12, pp. 2677-2684, Oct 1, 2003.

[3] Y. Feldman, I. Ermolina, and Y. Hayashi, "Time domain dielectric spectroscopy study of biological systems," *Dielectrics and Electrical Insulation, IEEE Transactions on,* vol. 10, no. 5, pp. 728- 753, 2003.

[4] Y. Hayashi, Y. Katsumoto, I. Oshige *et al.*, "Comparative study of urea and betaine solutions by dielectric spectroscopy: liquid structures of a protein denaturant and stabilizer," *The Journal Of Physical Chemistry B,* vol. 111, no. 40, pp. 11858-63, Oct 11, 2007.

[5] E. Katz, and I. Willner, "Probing biomolecular interactions at conductive and semiconductive surfaces by impedance spectroscopy: Routes to impedimetric immunosensors, DNA-Sensors, and enzyme biosensors," *Electroanal*, 2003, pp. 913-947.

[6] A. Oleinikova, P. Sasisanker, and H. Weingartner, "What can really be learned from dielectric spectroscopy of protein solutions? A case study of ribonuclease A," *J Phys Chem B*, 24, 2004, pp. 8467-8474.

[7] F. Patolsky, B. Filanovsky, E. Katz *et al.*, "Photoswitchable antigen-antibody interactions studied by impedance spectroscopy," *J Phys Chem B*, 1998, pp. 10359-10367.

[8] O. A. Sadik, H. Xu, E. Gheorghiu *et al.*, "Differential impedance spectroscopy for monitoring protein immobilization and antibody-antigen reactions," *Anal Chem,* vol. 74, no. 13, pp. 3142-50, Jul 1, 2002.

[9] D. Y. Jang, Y. P. Kim, H. S. Kim *et al.*, "Sublithographic vertical gold nanogap for label-free electrical detection of protein-ligand binding," *Journal of Vacuum Science & Technology B,* vol. 25, no. 2, pp. 443-447, Mar 1, 2007.

[10] S. Howell, S. Dirk, K. Childs *et al.*, "Mass-fabricated one-dimensional silicon nanogaps for hybrid organic/nanoparticle arrays," *Nanotechnology,* vol. 16, no. 6, pp. 754-758, Apr 5, 2005.

[11] J. Berg, F. Che, P. Lundgren *et al.*, "Electrical properties of Si–SiO 2–Si nanogaps," *Nanotechnology,* vol. 16, no. 10, pp. 2197-2202, Aug 16, 2005.

[12] S. M. Luber, F. Zhang, S. Lingitz *et al.*, "High-aspect-ratio nanogap electrodes for averaging molecular conductance measurements," *Small (Weinheim an der Bergstrasse, Germany),* vol. 3, no. 2, pp. 285-9, Feb 1, 2007.

[13] M. Lohndorf, U. Schlecht, T. Gronewold *et al.*, "Microfabricated high-performance microwave impedance biosensors for detection of aptamer-protein …," *Applied Physics Letters*, Dec 31, 2005.

[14] U. Schlecht, A. Malave, T. Gronewold *et al.*, "Detection of Rev peptides with impedance-sensors — Comparison of device-geometries," *Biosensors and Bioelectronics,* vol. 22, no. 9-10, pp. 2337-2340, Apr 15, 2007.

[15] J. Drexler, and C. Steinem, "Pore-suspending lipid bilayers on porous alumina investigated by electrical impedance spectroscopy," *Journal Of Physical Chemistry B,* vol. 107, pp. 11245-11254, 2003.

[16] B. Menz, R. Knerr, A. Gopferich *et al.*, "Impedance and QCM analysis of the protein resistance of self-assembled PEGylated alkanethiol layers on gold," *Biomaterials,* vol. 26, pp. 4237-4243, 2005.

[17] W. Romer, Y. H. Lam, D. Fischer *et al.*, "Channel activity of a viral transmembrane peptide in micro-BLMs: Vpu(1-32) from HIV-1," *Journal Of The American Chemical Society,* vol. 126, pp. 16267-16274, 2004.

[18] W. Romer, and C. Steinem, "Impedance analysis and single-channel recordings on nano-black lipid membranes based on porous alumina," *Biophysical journal,* vol. 86, pp. 955-965, 2004.

[19] C. Steinem, A. Janshoff, W. P. Ulrich *et al.*, "Impedance analysis of supported lipid bilayer membranes: A scrutiny of different preparation techniques," *Biochimica Et Biophysica Acta-Biomembranes,* vol. 1279, pp. 169-180, 1996.

[20] H. Huang, Z. Liu, and X. Yang, "Application of electrochemical impedance spectroscopy for monitoring allergen-antibody reactions using gold nanoparticle-based biomolecular immobilization method," *Analytical Biochemistry,* vol. 356, no. 2, pp. 208-214, 2006.

[21] F. Lisdat, and D. Schäfer, "The use of electrochemical impedance spectroscopy for biosensing," *Analytical and Bioanalytical Chemistry,* vol. 391, no. 5, pp. 1555-1567, 2008.

Chapter 7 Conclusions and Outlook

Even finding nothing is significant. Science is about shining a light into the unknown; and while that light might show you something you haven't seen before, not finding anything also tells you something about the world. Our job as experimentalists is to push the boundaries of the conditions under which you can confidently say, "It isn't there".

Jorge Cham

In this final chapter, the main contributions of this thesis are summarized and possible directions for future research, based on the findings presented, are laid out.

In chapter three, a novel device for capturing and analysing single cells was presented. With proof-of-principle experiments it has been shown that it is possible to continuously measure the impedance spectra of single cells challenged by chemical cues, and that this technique can be used to gain insights into the biological mechanisms that regulate cellular activity. The unique capability of this type of device enables observation of changes occurring to cells in real-time and in physiological media, continuously and for long periods of time without decay in measurement sensitivity. It could be exploited to investigate the kinetic effect of (potentially toxic) chemicals on single cells, as well as to study the ability of cells to undergo transient changes and recover from intermediate states of 'injury'. Current limitations in the device sensitivity should be addressed by utilising alternative electrode materials to reduce low frequency parasitic effects (such as the ones characterised in chapter five) and more sensitive electronics to extend the measured impedance spectra to a higher frequency range.

In chapter four, impedance spectroscopy has been used to study the characteristics of the double layer on metal and semiconductor electrodes with low (i.e. and high (i.e. > 10 kT) applied voltages and with a range of ionic concentrations. At low applied voltages, it is demonstrated that measurements performed with the same electrodes and under the same measuring conditions (excitation voltage amplitude, frequency range, dc bias, and temperature) resulted in CPE-P values that depended on electrolyte concentration. This behaviour has not been reported in the literature and the reasons behind this observation are not clear. These results however demonstrate that impedance data cannot be used to define surface characteristics through the fractal index. At high applied voltage, it is shown that the same double layer capacitance is measured irrespectively of the ionic concentration, and that the CPE power factor tends to decrease, directly contradicting theoretical predictions. These findings are especially relevant for modelling the response of AC electro-osmotic pumps, where the application of voltages as high as 100 kT, at frequencies below 1 kHz, is commonplace. These observations further our understanding of the ionic double layer and provide a starting point to design further experiments to clarify the behaviour of the double layer in non-linear conditions.

The materials characterised in chapter five could be used as replacements for materials traditionally utilized for microelectrodes in impedance measurements. The use of conductive polymer coatings is especially promising and thus far, their use in the field of impedance spectroscopy has not been explored. The full characterization presented in this thesis demonstrates that PSS/PPy-coated electrodes could be successfully employed to study α-relaxations, finding use not only in the measurement of cells, but also in the study of the dielectric characteristics of DNA and RNA molecules, and charged polymer proteins such as microtubules.

In chapter six, a silicon-based 'nanogap' capacitor device has been extensively and rigorously characterized and a complex equivalent circuit model has been constructed to predict its response. The capacitance of the double layer constrained in a cavity of dimensions comparable to its Debye length has been measured and its value was found to be much smaller than that predicted by theory for an unconstrained double layer. These results, albeit not conclusive, warrant further investigation of the behaviour of the double layer in nanocavities and nanochannels.

Impedance spectroscopy has been exploited as a non-invasive method to monitor cells continuously, in real time and for extended periods of time. However its limitations in resolving the level at which changes occur in a cell as a whole cannot be ignored as they severely limit its usefulness as a 'total analysis system' technique.

Some of the technological limitations can be and are being addressed, by employing more sophisticated electronic acquisition tools and novel signal processing techniques (e.g. MLS). As shown, the adoption of novel electrode materials can also bring significant advances. However, impedance spectroscopy cannot produce results that can be unequivocally interpreted, and should be considered a complementary technique, to be used in conjunction with more established techniques and tools, such as bright field and fluorescence microscopy.

Experimental observations presented here on the response of the ionic double layer under linear and nonlinear conditions and on materials with different surface characteristics provide some insight into the elusive nature of the double layer and indicate starting points to develop a new theoretical framework to accurately predict its behaviour in conditions where Gouy-Chapman-Stern theoretical predictions fail: high ionic concentrations, high voltages, micrometer- and nanometer- sized cavities.

A. Appendix – Lithography Masks

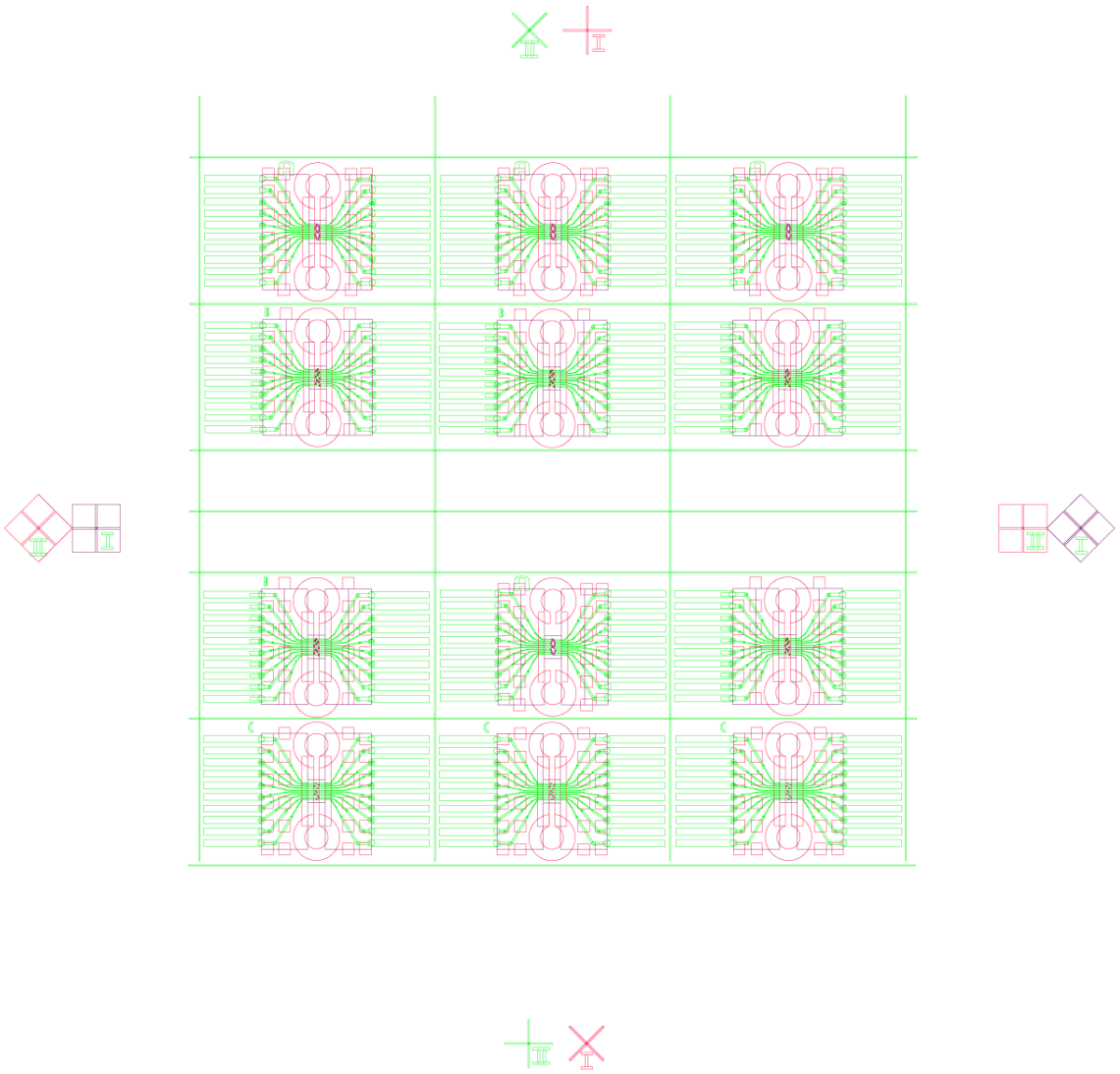

Figure A-1. Layers for bottom substrate (metal in green, SU8 in red and mauve). Wafer-level view

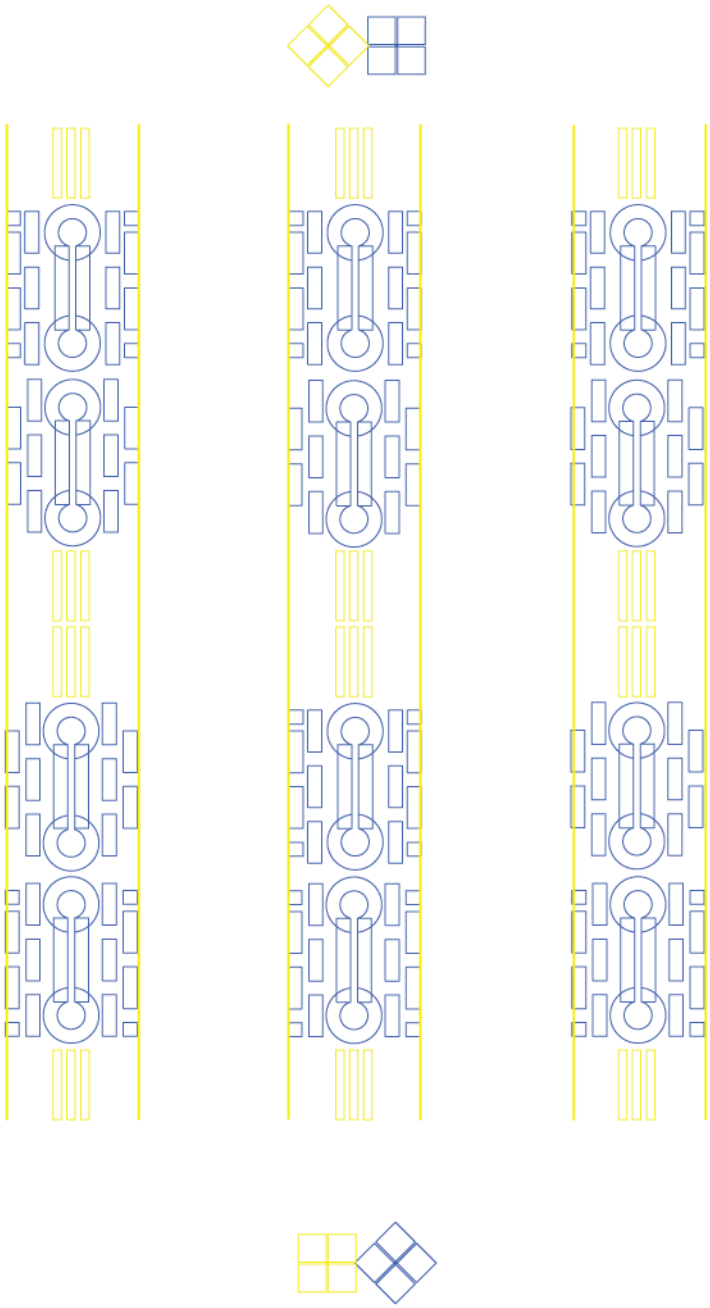

Figure A-2. Layers for top substrate (metal in yellow, SU8 in blue). Wafer-level view

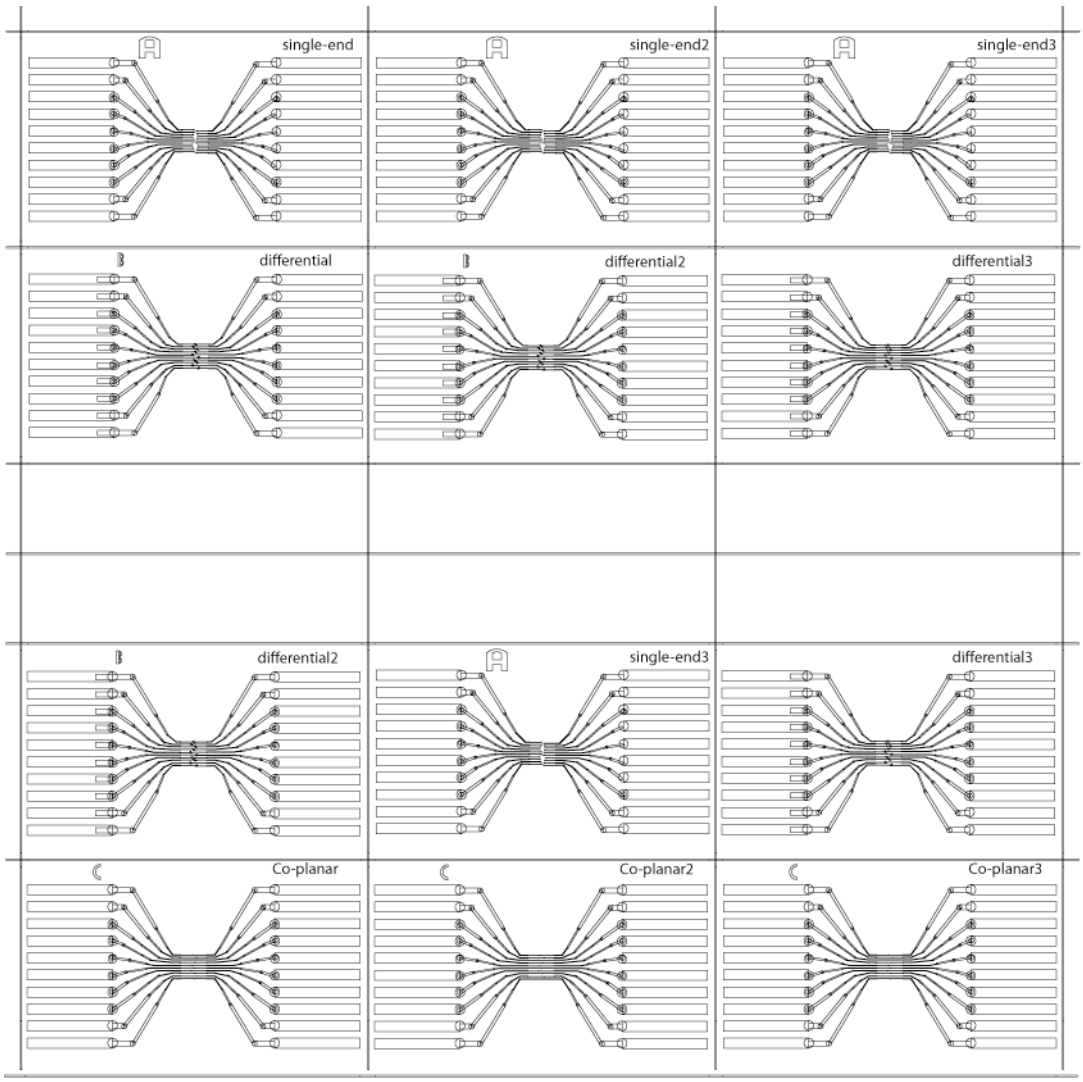

Figure A-3. Metal layers for bottom substrate. Designs for differential, single-ended and coplanar arrangements have been patterned. Wafer-level view.

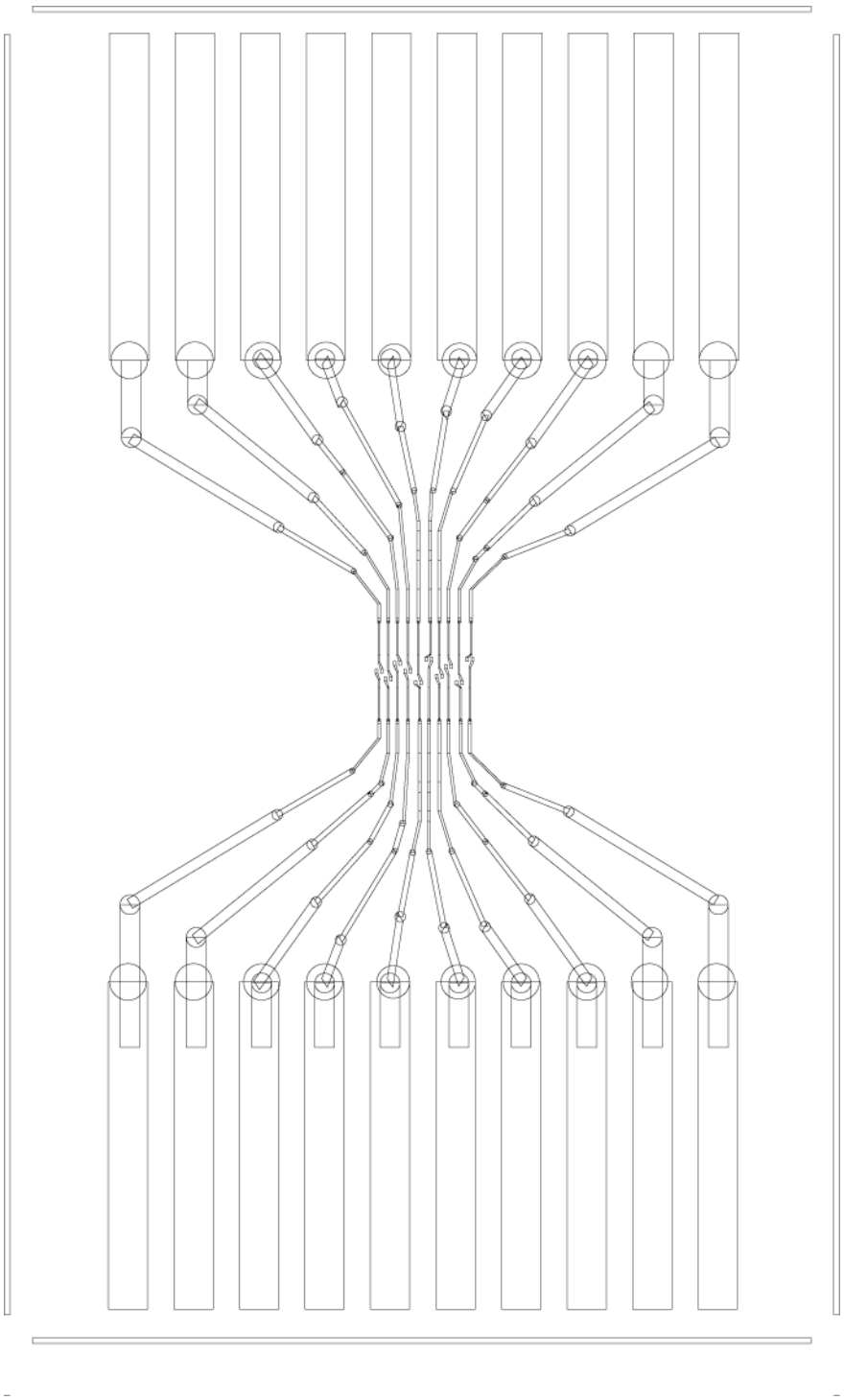

Figure A-4. Metal layer for bottom substrate: detail of differential arrangement design. Whole chip view.

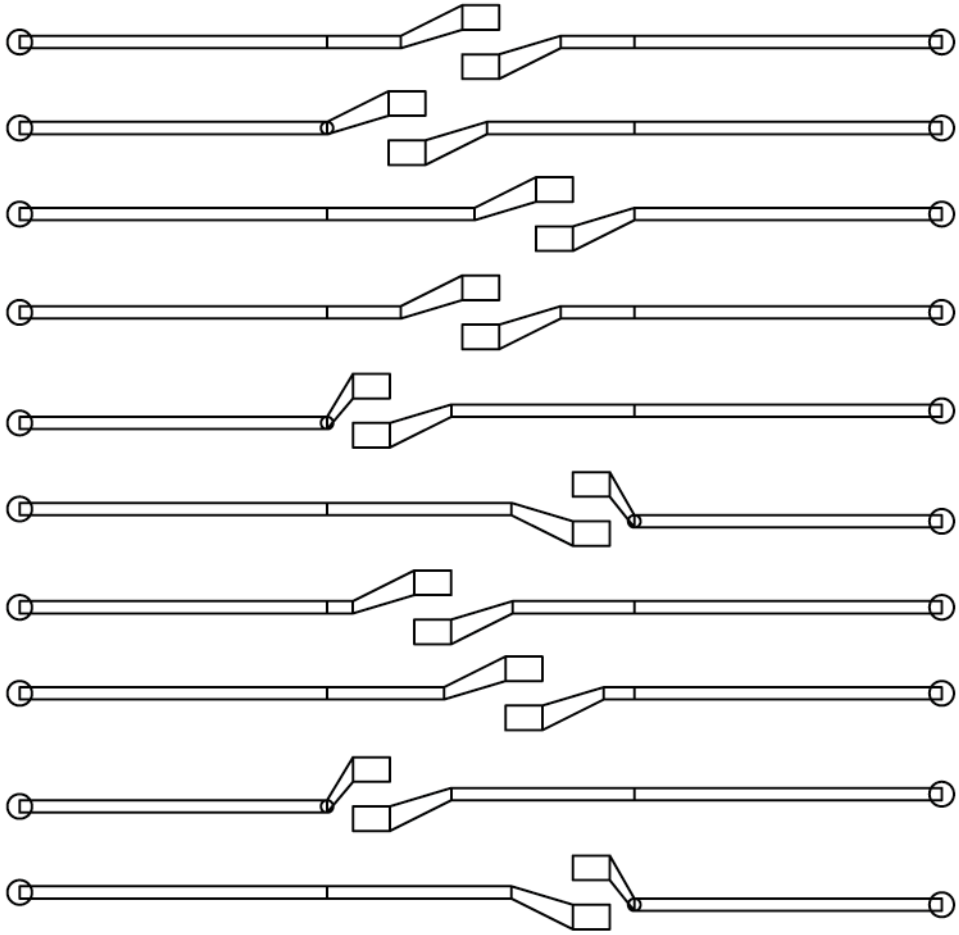

Figure A-5. Metal layer for bottom substrate: detail of differential arrangement design. Active area view.

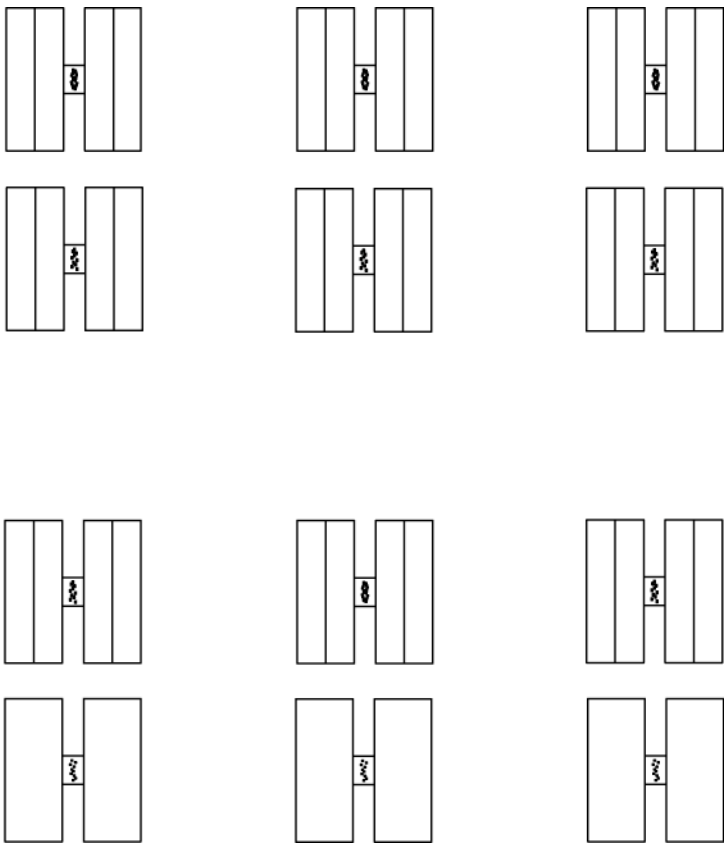

Figure A-6. First (insulation) SU8 layer for bottom substrate. Wafer level view

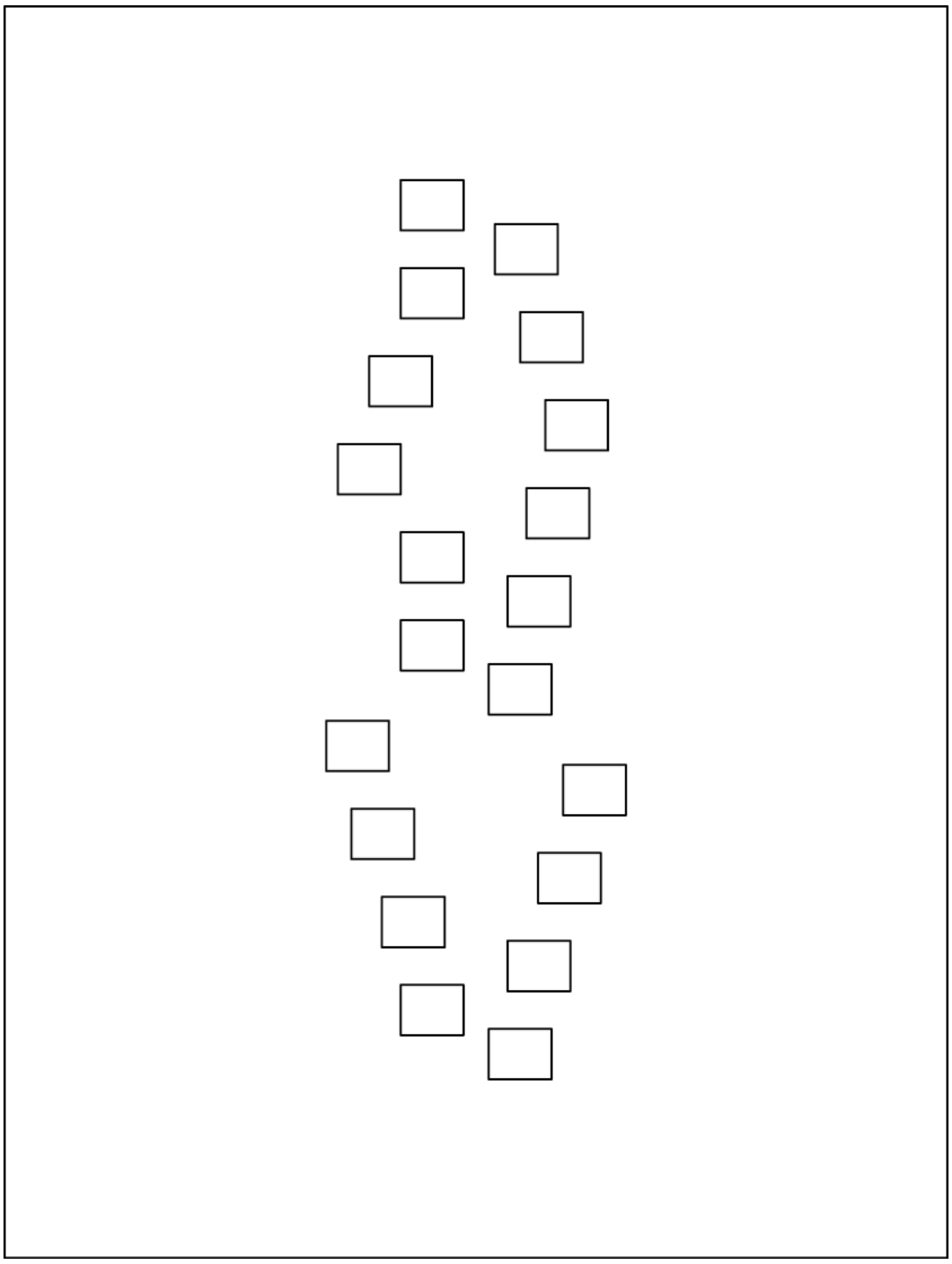

Figure A-7. First (insulation) SU8 layer for bottom substrate. Active area view.

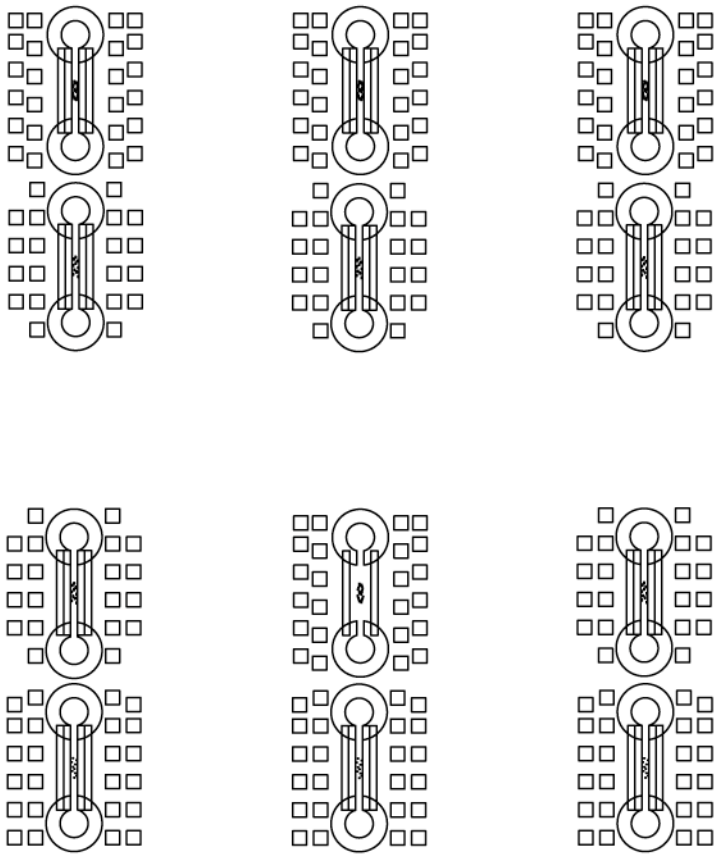

Figure A-8. Second (structural) SU8 layer for bottom substrate. Whole wafer view.

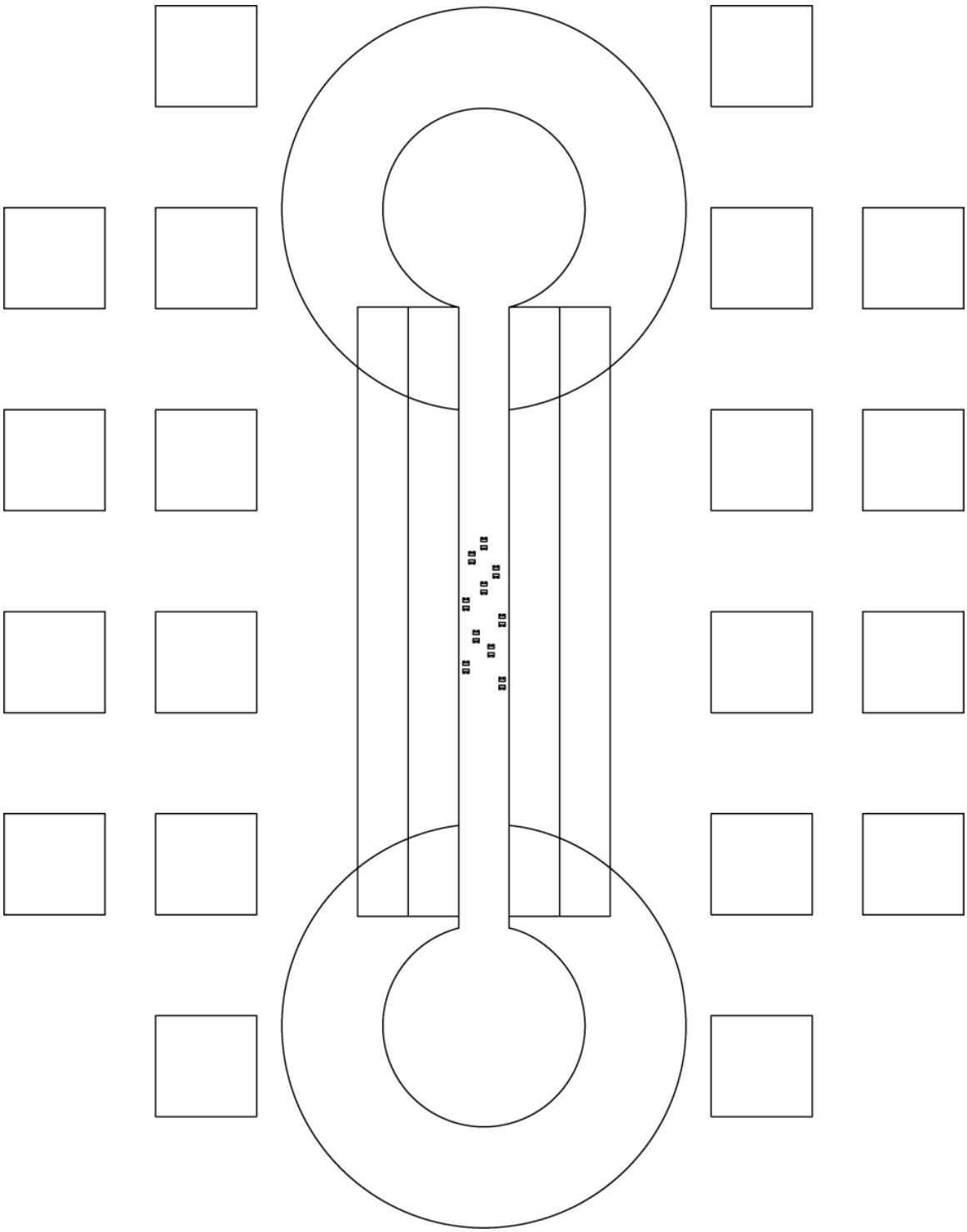

Figure A-9. Second (structural) SU8 layer for bottom substrate. Whole device view.

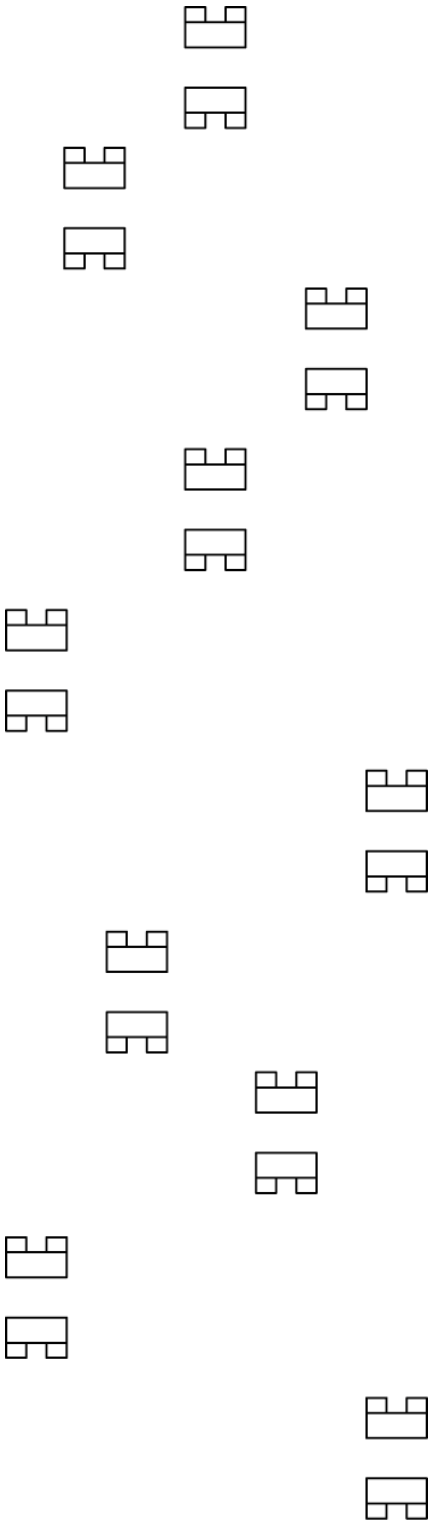

Figure A-10. Second (structural) SU8 layer for bottom substrate. Active area view.

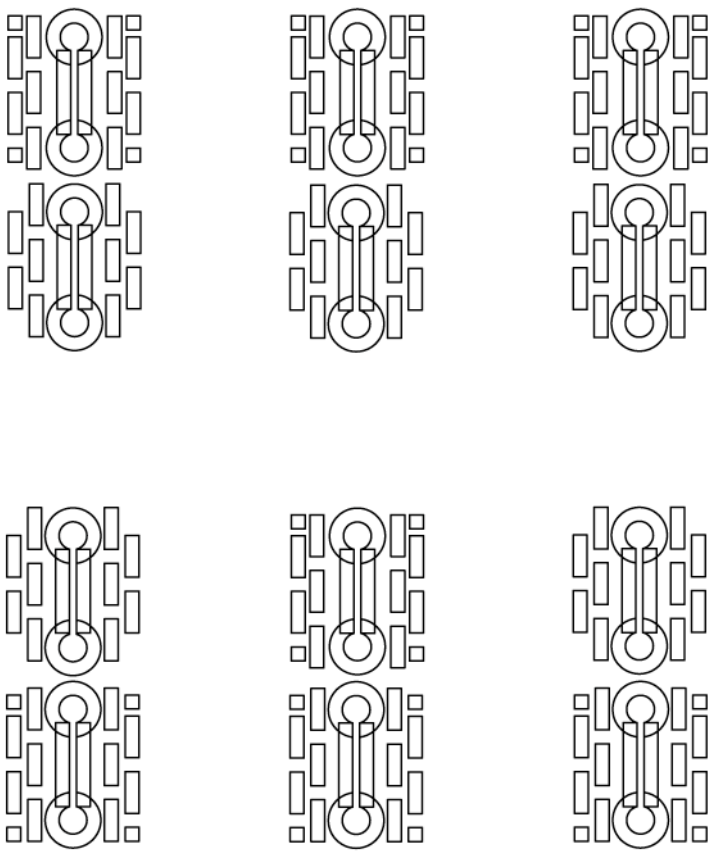

Figure A-11. SU8 layer for top substrate (spacing layer). Whole wafer view.

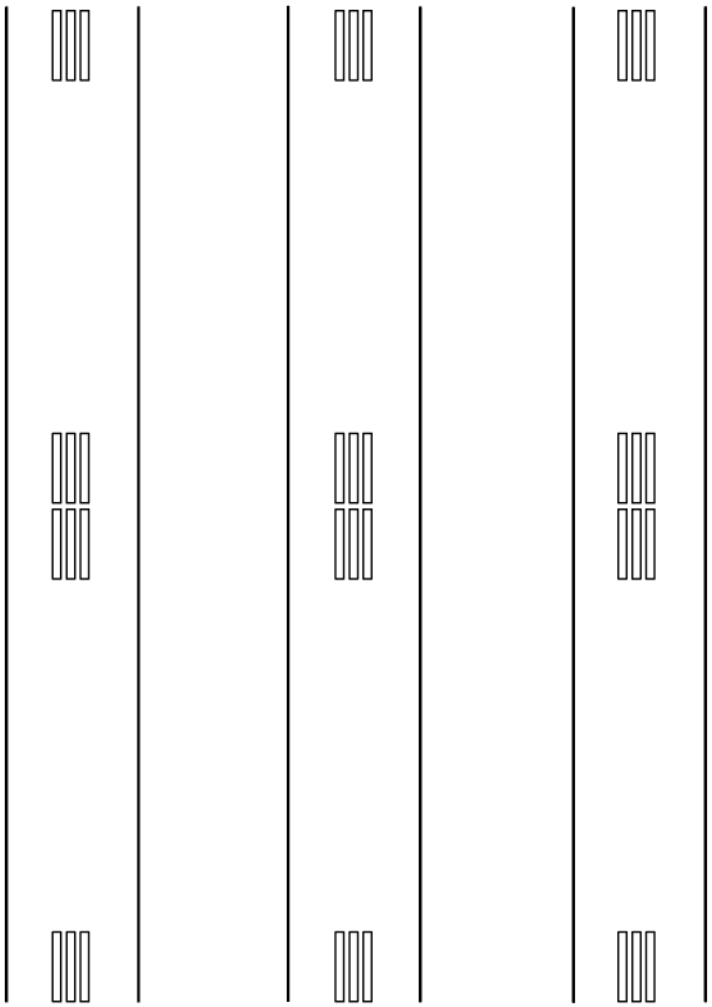

Figure A-12. Metal layer for top substrate (contact pads) . Whole wafer view.

Contents

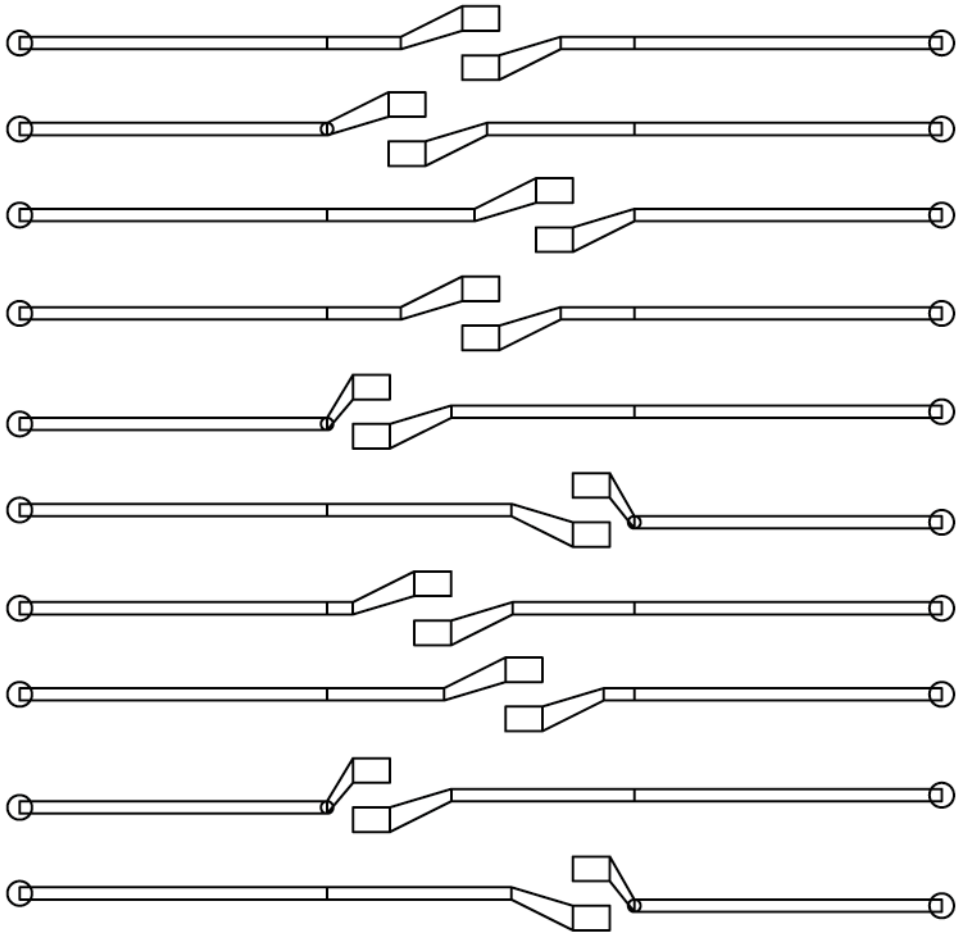

Publications

Submitted Manuscripts

D. Malleo, JT Nevill, LP Lee, and H Morgan, *A device for hydrodynamic capture of single cells and and label-free kinetics assays*, Lab On A Chip

D. Malleo, JT Nevill, Van Ooyen , U Schnakenberg, H.Morgan,*Comparison of Platinum, Platinum Black, Iridium Oxide and PPy/PSS Polyelectrolyte Electrodes for Impedance Spectroscopy*, IEEE Trans. Biomed.Eng.

Peer-reviewed Conference Papers

NG Green, D. Malleo, H Rouabah and H Morgan, *AC electroosmotic micropumps: novel designs and fundamental experimental investigations* , MIT Workshop on Electrokinetics, Cambridge, MA, October 2008

D. Malleo, JT Nevill, LP Lee, and H Morgan, *Label-free,single cell cytotoxin kinetics assay by differential impedance spectroscopy*, Proc. MicroTAS 2008, San Diego, USA

M. Tsaloglou, M. Dymond, D. Malleo, G. Attard, *A lipid mass spectrometry investigation on the effect of non-bilayer forming amphiphiles to the phospholipid metabolism of hela cells*, 33rd FEBS Congress & 11th IUBMB Conference - Biochemistry of Cell Regulation, Athens, June 2008

D. Malleo, JT Nevill, D Di Carlo, LP Lee, and H Morgan, *Examining Cytotoxic Effects on Single Cells using an Impedance Spectroscopic Platform*, Proc. MicroTAS 2007, Paris, France, pp. 1083-1085, 2007.

D. Malleo, N.G. Green, *Non-linear AC charging effects on the Electrical Double Layer*, Gordon Research Conference on Microfluidics, Waterville Valley, NH, July 7-15 2007.

D. Malleo, D Di Carlo, JT Nevill, D Holmes, LP Lee, and H Morgan, *Single Cell Differential Impedance Spectroscopy Analysis Using High Density Hydrodynamic Cell Trapping Arrays*, Proc. MicroTAS 2006, Tokyo, Japan, pp. 1292-1294, Nov. 5-9, 2006.

D. Malleo, J Tanner Nevill, Hywel Morgan, Luke P. Lee, *Impedance Spectroscopy Studies of the Electric Double Layer*, Proceedings of the 50th Biophysical Society Annual Meeting, Salt Lake City, UT, February 18-22, 2006

M. Sandison, D. Malleo, D. Holmes, R. Berry and H. Morgan, *Artificial bilayer lipid membranes (BLMs) on-chip for single molecule sensing*, Proceedings of Microtechnologies for the New Millennium 2005 SPIE, pp. 252-257, Seville, Spain, 2005

Manuscripts in preparation

D. Malleo, NG Green, *Non-linear AC charging effects on the Electrical Double Layer*, Journal of Applied Physics

D.Malleo, JT Nevill, *A review of nanogap capacitive sensors,* TBD